The switching paths of spin transfer torque magnetic random access memories

Paul Bouquin

université PARIS-SACLAY

The switching paths of spin transfer torque magnetic random access memories

Thèse de doctorat de l'université Paris-Saclay

École doctorale n° 575 : electrical, optical, bio : physics and engineering (EOBE)
Spécialité de doctorat : Electronique et Optoélectronique, Nano- et Microtechnologies
Unité de recherche : Université Paris-Saclay, CNRS, Centre de Nanosciences et de Nanotechnologies, 91120, Palaiseau, France
Référent : Faculté des sciences d'Orsay

Thèse présentée et soutenue à Palaiseau, le 14 septembre 2020, par

Paul BOUQUIN

Composition du Jury

André THIAVILLE Directeur de recherche CNRS, Université Paris-Saclay (LPS)	Président
Catherine GOURDON Directrice de recherche CNRS, Institut des Nanosciences de Paris	Rapporteure & Examinatrice
Ricardo SOUSA Chercheur (HDR), SPINTEC CEA Grenoble	Rapporteur & Examinateur
Yves HENRY Chargé de recherche CNRS, IPCMS	Examinateur
Siddharth RAO Chercheur, Institut de microélectronique et composant (IMEC)	Examinateur
Thibaut DEVOLDER Directeur de recherche CNRS, Université Paris-Saclay (C2N)	Directeur de thèse
Sébastien COUET Chercheur, Institut de microélectronique et composant (IMEC)	Invité
Claude CHAPPERT Directeur de recherche CNRS, Université Paris-Saclay (C2N)	Invité

Thèse de doctorat

NNT : 2020UPAST009

Pour toi Maman, Papa

Remerciements

Je tiens tout d'abord à te remercier Thibaut pour ces quatre années passées en ta compagnie. Tu as su me laisser me développer quand j'en avais besoin, me pousser quand il le fallait, et toujours su prendre du temps pour qu'on puisse faire avancer ensemble ce sujet. Dix fois merci. Je remercie également les autres membres de l'équipe Nomade, en particulier Joo-Von pour m'avoir servi de point de départ dans mes calculs, mais aussi Jean-Paul et Claude.

En Belgique à l'IMEC j'ai eu la chance de travailler avec Sid. Je le remercie pour son accueil au cours de mes séjours là-bas, mais surtout pour avoir su me reconcentrer sur les aspects technologiques de ma thèse lorsque je m'en suis trop éloigné. Je remercie mes autres collègues de l'IMEC, Sébastien, Kévin, Johan, Woojin, Gouri pour les échanges qu'on a pu avoir.

Merci à André Thiaville de m'avoir fait l'honneur de présider ma thèse. Merci également aux autres membres du jury, Catherine Gourdon, Ricardo Sousa et Yves Henry pour leur relecture très enrichissante de mon manuscrit.

Je remercie mes collègues devenus amis, qui furent comme moi de passage au C2N ou à l'IMEC, Jeremy, Louise, Christian, Jérôme, Myong-Woo, Shamin, Eline.

Et enfin je remercie mes proches pour leur soutient pendant ma thèse et au cours de mes études en général. Maman pour m'avoir toujours fait confiance et soutenu dans mes choix, Claire, Rémi. Mes amis Paul, Hugo, Louis, Léo.

Merci à toi Justine, pour ce qu'on a vécu et pour ce qui nous reste à vivre ensemble.

Contents

Introduction

Magnetic materials can be used to store information in a non-volatile manner. Magnetization has first been used for memory applications by the late XIXth century. The magnetic wire recording was based on a steel wire pulled across a recording head allowing an analog information to be written or read. This principle of an in-line magnetic memory was found in others technologies: the very successful magnetic tapes, the not so successful bubble memories or the under development racetrack memories. The discovery of the giant magnetoresistance effect (GMR) by Albert Fert and Peter Grünberg in 1988 was a breakthrough for magnetic memories. The conductance of a stack comprising two ferromagnetic films depends on the relative orientation of their magnetization. With this property, it became possible to access information from simple electrical measurements, opening the age of spintronics. Based on GMR magnetic random access memories (MRAM) were developed. In a MRAM device the magnetization of a layer (called the free layer, FL) can be reversed by an external field, while the magnetization of the second layer (the reference layer) is kept constant, as illustrated in figure 1. The MRAM are commercialized and occupy a niche in the memory market. One of their main drawback is the writing that is done by a current-induced magnetic field: this is not energy-efficient and limits the scaling down of the MRAM because of the possible cross-talks. An alternative for writing has been under study for the past 20 years: the spin transfer torque (STT). Under this effect, predicted by John Slonczewski in 1996, the magnetization of a thin ferromagnetic layer can be reversed by a polarized spin current through transfer of angular momentum. The STTMRAM are based on these two effects: reading through tunnel giant magnetoresistance and writing through STT.

Compared with their semi-conductors based counterparts, the STTMRAM have the advantage of being non-volatile. But still some improvement are being made on their scaling down and their speed. A state of the art STTMRAM device now has a diameter of a few tens of nm and can operate in a few tens of ns. To keep improving these performances it is necessary to have a deep understanding of their dynamics in this nano scale, namely of how the switching of the free layer occurs. Indeed several different scenarios can be imagined leading to the reversal of the free layer: coherent reversal, domain wall based reversal, nucleation of a subvolume. These possible switching scenarios are called the switching paths of the STTMRAM. They correspond to the different intermediate configurations that the magnetization can

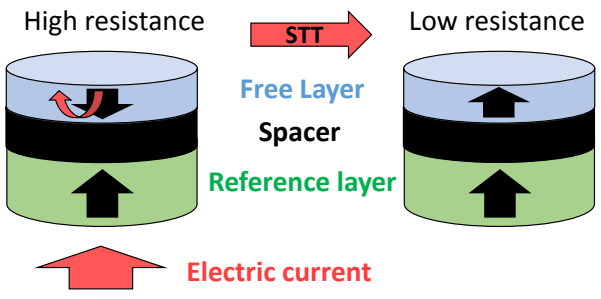

FIGURE 1: STTMRAMs in a nutshell. The represented device corresponds to an out-of-plane geometry with an insulating spacer between the two ferromagnetic layers. The information is read through the TMR effect and is written using the STT by applying a current.

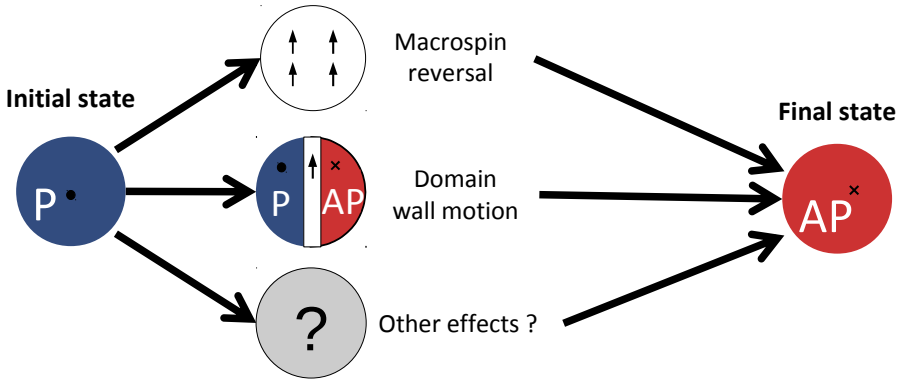

FIGURE 2: The switching paths in STTMRAM devices. Two possible paths are represented, the macrospin reversal and the domain wall based reversal.

take between its initial and final states (figure 2). The question I intend to answer in this manuscript is the following: what is the switching path in latest STTMRAM devices?

This work is the result of a close collaboration between two teams: the novel magnetic devices group (NOMADE) of the centre de nanosciences et nanotechnologies (C2N) and the memory team of the Interuniversity microelectronics centre (IMEC). The NOMADE group is a CNRS-Université Paris-Sud mixed unit that is specialized on the understanding of magnetization dynamics in next generation magnetic devices. The resources of this group include high-frequency electrical measurements, ferromagnetic resonance measurements, Kerr microscopy and a numerical calculation cluster. I worked under the direction of Thibaut Devolder, while Joo-Von Kim provided much help on the theoretical and numerical simulations aspect of this study. IMEC is a public Belgian institute financed by many industrial partners. The aim of the memory team of IMEC is to develop the next generation of memories for industrial applications. IMEC is providing the samples presented in this manuscript. The development of the stack, the patterning, the reliability study, the integration are performed at IMEC. NOMADE performs the high frequency measurements and help with the physical understanding of the device's dynamics. My PhD was a direct result of this collaboration since I am a Université Paris-Sud student financed by IMEC. I worked mostly at the C2N, spent two full months at IMEC for specific measurements and of course made a lot of shorter visits there. Through this work we try to understand the physical effects occurring in a STTMRAM free layer, while keeping in sight what are the consequences of our insights for the development of higher performance devices.

To study the switching path, we organise this manuscript as follows: in the first chapter we present the basic concepts necessary for the rest of this manuscript. It includes the energies at stake in a STTMRAM free layer, the presentation of the tunnel giant magnetoresistance, the spin transfer torque and the basic equations of magnetization dynamics. The second chapter is our state-of-the-art. We present what was known about the switching path before the beginning of this PhD. We discuss models of the coherent and domain wall based reversal and how they compare with measurements. We also present briefly the state-of-the-art of devices performances and finally what measurements were made to directly observe the switching path. Our first result chapter focuses on micromagnetic simulations of the reversal. The

idea is to solve numerically the basic equation of the magnetization dynamics presented in our first chapter in a simulated STTMRAM free layer. The switching path obtained is discussed while we vary the size of the system. We also study the impact of thermal fluctuations on the switching. In the micromagnetic simulations, it is found that the domain wall dynamics inside the free layer are complex and that they can be detrimental to the performances of the device. As a result we develop in the next chapter chapter a model for domain wall dynamics based on the existing ones presented in our state-of-the-art. At the end of this chapter we have an almost complete understanding of the domain wall behaviour inside the free layer as it was simulated micromagnetically. Then starts the experimental part of this manuscript. First we present our samples and their characterization. We show basic characterization measurements such as loops obtained by vibrating sample magnetometer and by sweeping the external field or the voltage. We then present a more complex ferromagnetic resonance measurement from which we can extract key parameters of the devices. The final chapter discusses time-resolved electrical measurements of the reversal. Such measurements give information on the switching path, while we vary the diameter of the device and the voltage applied. The experimental findings are compared with our different models to conclude on the switching path in our STTMRAM devices.

Chapter 1

Magnetic tunnel junction and magnetization dynamics basics

In this chapter we introduce the basic concepts necessary for the rest of the manuscript. We start with the most simple model for the STTMRAM free layer, a ferromagnetic thin film, and describe the energies at play. We then introduce spintronics by presenting the magnetic tunnel junctions. We discuss the basics of magnetization dynamics and introduce the spin transfer torques. Finally we solve the obtained equations and present the coherent dynamics.

1.1 Energy potential in thin ferromagnetic films

1.1.1 Introduction

Let us consider a thin ferromagnetic film. The magnetization is described by the unit vector $\overrightarrow{m}$ and the saturation magnetization M_s. The different micromagnetic energy densities $u_{\mu\text{mag},\,i}$ that are at play in such a film are related to the total energy of the system following:

$$U_{\text{tot}} = \sum_i \int_{\text{Vol}} u_{\mu\text{mag},\,i}\, d^3r \tag{1.1}$$

Each energy contribution gives rise to an effective field $\overrightarrow{H_{\text{eff}}}$ following:

$$-\mu_0 M_s \overrightarrow{H_{\text{eff},\,i}} = \frac{\delta u_{\mu\text{mag},\,i}}{\delta \overrightarrow{m}} \tag{1.2}$$

1.1.2 Zeeman energy

The magnetization tends to align with an external field $\overrightarrow{H_{\text{ext}}}$:

$$u_{\text{Zeeman}} = -\mu_0 M_s \overrightarrow{H_{\text{ext}}} . \overrightarrow{m} \tag{1.3}$$

this contribution is called the Zeeman energy.

1.1.3 Heisenberg exchange energy

The exchange energy causes adjacent magnetic moments (or spins) to align parallel (for a ferromagnet) or antiparallel (for an antiferromagnet) to each others. Following the Heisenberg model the contribution of exchange of a pair of atoms (i, j) to the total energy of the system is written:

$$U_{\text{ex}} = -\sum_{i,j} J_{ij}\, \overrightarrow{S_i} . \overrightarrow{S_j} \tag{1.4}$$

Where $\overrightarrow{S_i}$ and $\overrightarrow{S_j}$ are the spins of two different atoms and J_{ij} the interatomic exchange constant between them. In this work we study only ferromagnets and the exchange constant is positive. If we assume that the magnetization is varying slowly in space compared to the interatomic distance, the exchange energy density becomes at the first order:

$$u_{\text{ex}} = A_{\text{ex}}[(\overrightarrow{\nabla} m_x)^2 + (\overrightarrow{\nabla} m_y)^2 + (\overrightarrow{\nabla} m_z)^2] \tag{1.5}$$

Where A_{ex} the exchange stiffness (in J/m) can be expressed from the J_{ij} of two adjacent atoms and the interatomic distance. In practice it is the exchange stiffness that is directly obtained experimentally.

1.1.4 Dzyaloshinskii-Moriya interaction

The exchange energy discussed previously also has an antisymmetric contribution called the Dzyaloshinskii-Moriya interaction (DMI) [37, 74]. The DMI can arise when the inversion symmetry is broken in the material, for instance in the presence of asymmetric interfaces between layers. It can therefore be present in the STTMRAM free layers we consider. Similarly to the symmetric exchange, the total contribution of DMI to energy density is written:

$$U_{\text{DMI}} = -\sum_{i,j} \overrightarrow{D_{ij}}.\overrightarrow{S_i} \times \overrightarrow{S_j} \tag{1.6}$$

In the same approximation of slowly varying magnetization in space, the DMI density energy for our thin film can be written:

$$u_{\text{DMI}} = D[m_z \frac{\partial m_x}{\partial x} - m_x \frac{\partial m_z}{\partial x}] + D[m_z \frac{\partial m_y}{\partial y} - m_y \frac{\partial m_z}{\partial y}] \tag{1.7}$$

Where D is the DMI constant (in J.m^{-2}). The DMI is ignored in most of this manuscript. We will consider its effect only while extending our domain wall models in the corresponding chapter.

1.1.5 Magneto-crystalline and surface anisotropy

The magneto-crystalline anisotropy accounts for the interaction between the crystal lattice and the magnetic moments. This creates a preferential direction for the magnetization along what is called the easy axis. If we note θ the angle between the easy axis and the magnetization, then the first order magneto-crystalline anisotropy contribution in the uniaxial case can be written as:

$$u_{\text{K, m-c}} = K_{\text{m-c}} \sin^2 \theta \tag{1.8}$$

The magneto-crystalline anisotropy is a volume effect and $K_{\text{m-c}}$ is expressed in J.m^{-3}. As the thickness scales down in a thin film another contribution to the anisotropy called the surface anisotropy becomes of great importance. This anisotropy accounts for the interactions between the magnetic moments and the orbitals of the layer adjacent to the studied thin film. This adjacent layer is not necessarily ferromagnetic or even metallic (in our case it is MgO). The amplitude of this surface anisotropy depends on the materials of the two layers as well as on the quality of their interface. Similarly to the magneto-crystalline anisotropy, the surface anisotropy defines an easy axis along which the magnetization tends to align itself

following:

$$u_{\mathrm{K}} = \frac{K_s}{d}\sin^2\theta \tag{1.9}$$

where d is the thickness of the magnetic film and K_s the surface anisotropy constant is expressed in J.m^{-2} (positive with our MgO interface). In this work, we shall group these two anisotropy contributions into a single anisotropy constant K (in J.m^3) assuming they share their easy axis. We often use the corresponding anisotropy field $H_K = \frac{2K}{\mu_0 M_s}$. The anisotropy easy axis is out of plane in our modern STTMRAM devices (Perpendicular Magnetic Anisotropy or PMA) and is therefore responsible for the out of plane magnetization.

Higher order anisotropy terms exist for both the surface and the magneto-crystalline contributions. We have only presented the uniaxial anisotropy energy as it is the one relevant in our system, but non-uniaxial terms can be written to define more than one easy axis. Both the higher order anisotropy or non-uniaxial anisotropy are not considered in this work.

1.1.6 Demagnetizing effects

General considerations

The magnetization of the thin films creates a dipole field which acts on itself. This field is called the demagnetizing field $\overrightarrow{H_d}$ and its direction depends on the direction of the magnetization and on the shape of the system. The demagnetizing field contribution to the total energy is written as a Zeeman contribution:

$$u_{\mathrm{d}} = -\frac{\mu_0 M_s}{2}\overrightarrow{H_d}.\overrightarrow{m} \tag{1.10}$$

with a $1/2$ factor to avoid double counting of the self interaction. To better understand the meaning of the demagnetizing field, it is useful to introduce the notion of magnetic surface charges and magnetic volume charges by analogy with their electrical counterparts. The volume charges are given by $-M_s \mathrm{div}\,\overrightarrow{m}$ and the surface charges (for a surface of normal $\overrightarrow{n}$) by $M_s\,\overrightarrow{m}.\overrightarrow{n}$. The demagnetizing field is proportional to the total magnetization. The magnetization tends to follow the demagnetizing field in order to minimize the magnetic surface and volume charges. The calculation of $\overrightarrow{H_d}$ is complex in most geometries and this fields is almost never uniform in space. In the most general case the demagnetizing field is written through a potential given by integrating the magnetic surface and volume charges.

For example, let us consider that a strong anisotropy forces the magnetization of the thin film to be uniformly out of plane, namely along the z direction. Then the demagnetizing field which is also along z and of opposite direction simply reads $\overrightarrow{H_d} = -M_s\,\overrightarrow{e_z}$.

Demagnetizing field in patterned devices

It can be proven [81] that in the case of an uniformly magnetized ellipsoid, the demagnetizing field is uniform and can be expressed through a demagnetizing tensor $\overrightarrow{H_d} = -M_s\bar{\bar{N}}.\overrightarrow{m}$.

To obtain devices the thin film is patterned into disks of varying diameter. During this PhD typical diameters are between 20 and 200 nm, for a thickness of about 2 nm. Let us consider a disk perpendicularly magnetized by a strong surface anisotropy (see inset of figure figure 1.1.a). Then the demagnetizing field is not homogeneous

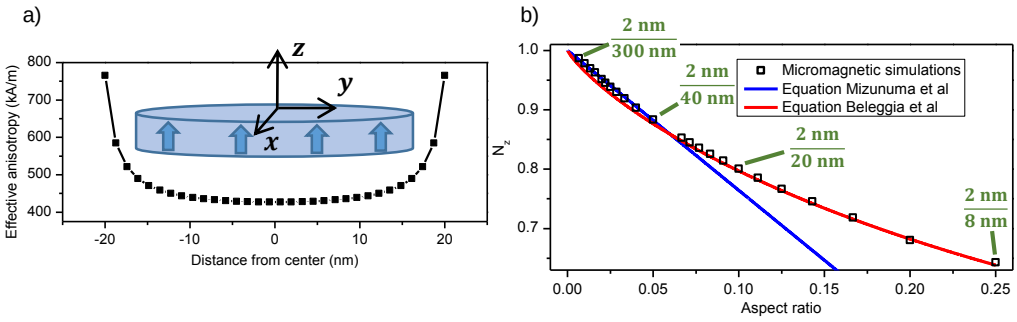

FIGURE 1.1: Demagnetizing effects in a thin perpendicularly magnetized disk. a) Effective anisotropy field profile resulting from the demagnetizing contribution along z. b) N_z determined from micromagnetic simulations of the free precession or from equation 1.12 (Mizunuma) and 1.13 (Beleggia).

since it is not an ellipsoid. We recover the exact demagnetizing profile using micromagnetic simulations. The effective anisotropy field is shown in figure 1.1.a, it corresponds to the anisotropy field minus the z component of the demagnetizing field. The demagnetizing field is stronger at the center of the disk than on the edges. This is explained by the fact that a magnetic moment in the center is surrounded by more neighbours exerting a demagnetizing field upon him than the same magnetic moment placed near the edges.

Now we make a simplification and describe this complex demagnetizing field profile by a uniform demagnetizing field whose amplitude is chosen to yield the correct total demagnetizing energy. We introduce the demagnetizing factors of the disk (N_x, N_y and N_z) which are the diagonal elements of the demagnetizing tensor given in the uniformly magnetized ellipsoid case. With this approach, the disks is under a uniform effective anisotropy of:

$$H_{k,\,\mathrm{eff}}^{\mathrm{disk}} = H_k - (N_z - N_x)M_s \tag{1.11}$$

$N_z - N_x$ appears because the energies in the fully in plane and the fully out-of-plane cases are compared. In the case of the disk, $N_y = N_x$ and by definition of the demagnetizing factors $N_x + N_y + N_z = 1$. Therefore we only need to determine N_z to obtain the demagnetizing field along z. This problem has been studied in literature and several formula are available to us. Mizunuma et al [72] propose:

$$N_z = 1 - \frac{3}{4}\pi\tau_{\mathrm{aspect}} \tag{1.12}$$

where $\tau_{\mathrm{aspect}} = thickness/diameter$ is the aspect ratio of the disk. This formula for the demagnetizing factors assumes a flat disk.

In reference [3] the equivalent ellipsoid of a magnetic body is studied, the following formula is given for N_z:

$$N_z = 1 + \frac{\tau_{\mathrm{aspect}}}{\pi}\left(1 + \ln\left(\frac{\tau_{\mathrm{aspect}}^2}{16}\right)\right) \tag{1.13}$$

To estimate the validity of these two formulas, we performed micromagnetic simulations. We do not detaild here the principle of this method since it is done in the state of the art chapter and in the micromagnetic simulations of the switching path chapter. The idea is to simulate a disk of fixed thickness (2 nm) and of varying

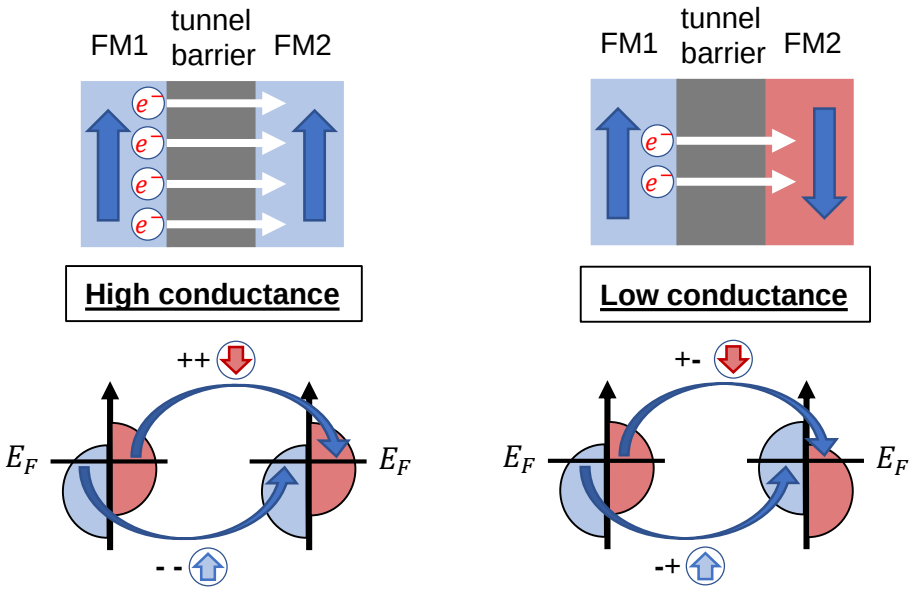

FIGURE 1.2: Schematic illustration of the TMR effect in a MTJ. The magnetization of the two ferromagnetic layers are represented, as well as the density of states of each spin bands in the parallel and antiparallel configurations. Inspired from ref. [120]

diameter. For each disk we let the magnetization precess following equation 1.23 with a small tilt angle of 5 degree. The frequency of the precession is related to the effective anisotropy over the full disk following Kittel's formula of ferromagnetic resonance [57]:

$$\omega_{\text{FMR}} = \gamma_0 H_{k,\,\text{eff}}^{\text{disk}} \tag{1.14}$$

where $\gamma_0 = \gamma\mu_0$ with γ the gyromagnetic ratio of the electron. From Kittel's equation and equation 1.11 we recover a N_z corresponding to the micromagnetic simulations. This demagnetizing factor is compared to equation 1.12 and 1.13 in figure 1.1.b. There is a very good agreement between the micromagnetic simulations and equation 1.13 at larger aspect ratio, while for the smaller one equation 1.12 gives a better estimate.

Using the demagnetizing factors of the disk always assumes that the demagnetizing field along z profile can be replaced by a homogeneous field. In some cases such as the micromagnetic simulations of the full reversal of a 50 nm disk, the exact demagnetizing profile must be considered (see section 3.2.1).

We don't consider here the in plane component of the demagnetizing field since the magnetization was assumed to be uniformly out of plane. These terms are of great importance in other magnetic configurations as will be highlighted in our domain wall models.

Finally there exists a calculation obtaining the demagnetizing factors of a cylinder in reference [18]. In this study tables are computed for the demagnetizing factors but no approximate analytical expression are given, we did not compare this result with our micromagnetic simulations and with equation 1.13 and 1.12.

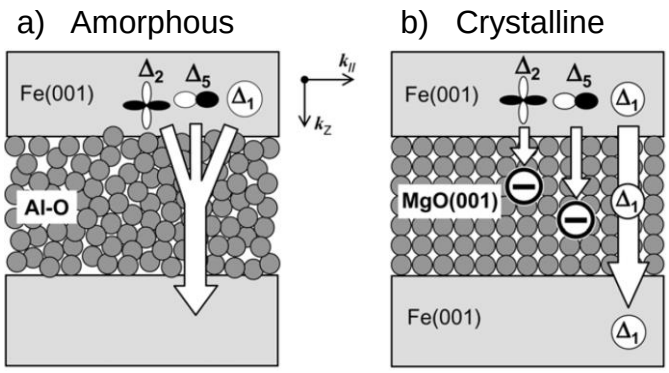

FIGURE 1.3: From reference [120]: schematic representation of the orbitals tunnelling through a amorphous (a) or crystalline (b) barrier. The Bloch states are of symmetry: Δ_1 spd hybridized, Δ_2 d and Δ_5 pd hybridized.

1.2 Transport in magnetic tunnel junctions

1.2.1 Jullière's model for tunnel giant magnetoresistance

When two metallic layers are separated by an insulator, some electrons can still flow across the barrier through the tunnel effect. In the case of two ferromagnets separated by an insulator, the conductance through the barrier depends on the relative orientation of the magnetizations of the two layers [54]. Such a stack is called a magnetic tunnel junction (MTJ). In the parallel configuration the conductance is generally higher than in the antiparallel configuration (see figure 1.2). This is due to the non-zero spin polarization of the ferromagnetic electrodes at the Fermi level E_F. In the model of Jullière [54] the variation of the conductance is deduced from the polarization of the two ferromagnetic electrodes at the Fermi level:

$$\frac{G_P - G_{AP}}{G_P} = \frac{2P_1P_2}{1 + P_1P_2} \tag{1.15}$$

and the polarization are obtained from the density of states at the Fermi level [120]: $P_i = (D_{i\uparrow} - D_{i\downarrow})/(D_{i\uparrow} + D_{i\downarrow})$. These equations link two different conductances to the four respective densities of state at the Fermi level.

The strength of this effect is often expressed by the tunnel magnetoresistance (TMR given absolute or as a ratio in %). It is defined from the resistance in the parallel and antiparallel configurations:

$$TMR = \frac{R_{AP} - R_P}{R_P} \tag{1.16}$$

If the MTJ is symmetrical $P_1 = P_2 = P$ and we recover:

$$P = \sqrt{\frac{TMR}{TMR + 2}} \tag{1.17}$$

In Jullière's model only the spin resolved density of states at the Fermi level matters. The nature of the barrier (amorphous or crystalline) has no impact on the TMR. A measurement of the TMR in such an amorphous barrier MTJ ($CoFeB/Al_2O_3/Co$) can be found in reference [73].

1.2.2 Tunnel giant magnetoresistance in Fe/MgO/Fe stacks

Qualitative understanding

In 2001, Butler et al predicted very high TMR in Fe/MgO/Fe MTJ from first-principle based calculation[12]. The tunnelling through the crystalline MgO barrier is orbital dependent: some of the Bloch states tunnel at a faster rate than the other Bloch states. This is due to the orbital overlap through the barrier that is not the same for each Bloch state symmetry. As the Bloch states at a Fe/MgO interface are spin-polarised the tunnelling through the barrier becomes spin dependent. Most notably the Δ_1 spd hybridized state is 100% spin polarized and present a great overlap through the barrier because of its s-like symmetry (figure 1.3). In cristalline MTJs, the tunnelling is now conserving the symmetry of the Bloch states. If the tunnelling was involving only the Δ_1 states, the effective spin polarization would be unity and the TMR would be infinite. Minor contributions from other Bloch states decrease the TMR value but in practice it can be much larger than the one predicted for the amorphous MTJ discussed in Jullière's model. One can recover equations similar to the one of Jullière's model using effective spin polarization P_1^{eff} and P_2^{eff} instead of the P_1 and P_2.

Equivalent circuit for a MTJ

To recover such equations one starts from the equivalent circuit of the MTJ shown in figure 1.4. Here the current densities $J_{\sigma\sigma'}$ corresponds to the four different spin-channels (two in each configuration) with $\sigma\sigma' = \pm\pm$, where the signs indicate majority or minority spin channels at the Fermi level. The MTJ can also be described by four corresponding spin-channel conductance defined by [92]:

$$\frac{dJ_{\sigma\sigma'}}{dV} = G_{\sigma\sigma'}\langle\sigma|\sigma'\rangle^2 \tag{1.18}$$

where $\langle\pm|\pm\rangle = \cos\frac{\theta}{2}$ and $\langle\pm|\mp\rangle = \pm\sin\frac{\theta}{2}$. These four spin-channel conductances are related to the conductance of the parallel and the antiparallel states introduced in Jullière's model following:

$$G_{\text{P}} = G_{++} + G_{--} \ , \ G_{\text{AP}} = G_{+-} + G_{-+} \tag{1.19}$$

In this model instead of expressing the two conductances from the polarization P_i which are obtained from the densities of states, we express the conductances by computing each $J_{\sigma\sigma'}$ for each Bloch states and by summing them to obtain the total spin-channel current. The expressions of the spin-channel conductances are going to be discussed again in the following section in order to express the spin transfer torque in such Fe/MgO/Fe MTJ.

Once the spin-channel conductances are known, they can be used to define the effective polarizations P_i^{eff} for each layer[92]:

$$P_i^{\text{eff}} = \sqrt{\frac{G_{\text{P}} - G_{\text{AP}}}{G_{\text{P}} + G_{\text{AP}}}} \tag{1.20}$$

This is simply a convenient notation in order to recover the same expression for the TMR as in Jullière's model. This is necessarily an assumption because we reduced a system described by four variables to only two, it is valid when $G_{++} \gg$

$G_{+-}, G_{-+} \gg G_{--}$ which corresponds to a high TMR assumption, for instance when the transport is dominated by the Δ_1 states.

Conductance for any arbitrary angle

For any angle θ between the magnetizations of the two layers, it was found experimentally that the conductance through the MTJ can be described by the general form [90]:

$$G(V,\theta) = G_{\perp}(V)(1 + \iota(V)\cos(\theta)) \tag{1.21}$$

Where $G_{\perp}$ is the conductance when the two layer's magnetizations are perpendicular and $\iota(V)$ the coefficient of magnetoconduction. This coefficient can be expressed from the effective polarization $\iota(V) = P_1^{\text{eff}}(V)P_2^{\text{eff}}(V)$ if we assume that the transport properties of the MTJ ensemble can be separated in the properties of each electrode. All along this manuscript we choose to disregard the bias dependence of the TMR for the sake of simplicity. Namely we assume that $P_i^{\text{eff}}(V) = P_i^{\text{eff}}(V=0)$. The bias dependence was notably studied in references [90, 101]. Since we shall predict that the switching path depends little on voltage, this assumption is not of great impact as long as our study focuses on this aspect of MTJs. In the specific case of a symmetrical junction, we can write $P_1^{\text{eff}} = P_2^{\text{eff}} = P$ and then the conductance for any given angle θ is simply

$$G(\theta) = \frac{1 + P^2\cos\theta}{R_{\perp}} \tag{1.22}$$

where $R_{\perp} = \frac{2R_{\text{P}}R_{\text{AP}}}{R_{\text{P}}+R_{\text{AP}}}$ is the median resistance. This expression for the conductance is going to be used throughout this manuscript to link the magnetization dynamics $\theta(t)$ with the conductance that can be measured electrically.

1.3 Magnetization dynamics in magnetic tunnel junctions

1.3.1 Landau-Lifshitz-Gilbert equation

In this section we introduce the Landau-Lifshitz-Gilbert (or LLG) equation, which is commonly used to describe magnetization dynamics.

The Landau-Lifshitz model describes the dynamics of the magnetization under an effective field $\overrightarrow{H_{\text{eff}}}$:

$$\frac{\mathrm{d}\overrightarrow{m}}{\mathrm{d}t} = -\gamma_0 \overrightarrow{m} \times \overrightarrow{H_{\text{eff}}} \tag{1.23}$$

The total effective field seen by the magnetization is obtained from the micromagnetic potential described in the previous section following equation 1.2. If the magnetization is aligned along the effective field, its derivative is zero and it remains unchanged. If that is not the case the magnetization remains forever along a given cyclic trajectory. The instantaneous precession frequency is $\gamma_0 H_{\text{eff}}$.

To better predict the observed magnetization dynamics, a damping term (called the Gilbert damping) was added to this equation. This gives the LLG equation:

$$\frac{\mathrm{d}\overrightarrow{m}}{\mathrm{d}t} = -\gamma_0 \overrightarrow{m} \times \overrightarrow{H_{\text{eff}}} + \alpha \overrightarrow{m} \times \frac{\mathrm{d}\overrightarrow{m}}{\mathrm{d}t} \tag{1.24}$$

where α is called the Gilbert damping constant (or simply "Gilbert damping" or "damping"). This term is phenomenological and is added by analogy with a viscous drag (it is proportional to $\dot{\overrightarrow{m}}$). The origin of damping is multifold. The coupling

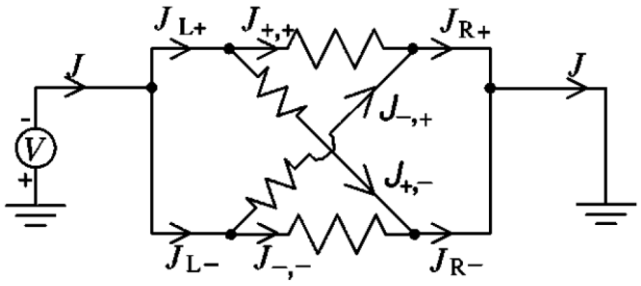

FIGURE 1.4: From reference [90]: equivalent circuit of a magnetic tunnel junction. The current in the P state is given by J_{++} and J_{--}, in the AP state by J_{+-} and J_{-+}.

of the magnetization with the others degrees of freedom of the system are a cause of damping (magnon-phonon, magnon-electron, defects, interfaces ...). Under the effect of this term the magnetization relaxes until it aligns along the effective field, while it precesses around it. The angle of precession and the frequency are no longer constant.

It is sometimes useful to write LLG in an explicit manner. This is done by multiplying the equation by $\overrightarrow{m}\times$ and injecting it back into itself to eliminate the derivative term in the left side, one can obtain:

$$(1+\alpha^2)\frac{\mathrm{d}\overrightarrow{m}}{\mathrm{d}t} = -\gamma_0\overrightarrow{m}\times\overrightarrow{H_{\text{eff}}} - \alpha\gamma_0\overrightarrow{m}\times(\overrightarrow{m}\times\overrightarrow{H_{\text{eff}}}) \tag{1.25}$$

1.3.2 The spin transfer torque

Effect of a spin polarized current on a ferromagnetic thin film

A spin polarized current can transfer its angular momentum to the ferromagnetic layer it is flowing through. This effect known as spin transfer torque was first predicted by Slonczewski in 1996 [93]. This effect can be understood as follows: the spin current loses its coherence as it flows through the ferromagnet by interacting with its magnetic moments, since the total angular momentum is conserved, a torque is applied to the magnetization. This torque can be used to change the magnetization direction of a thin film. Like any other torque, the STT can be decomposed in two orthogonal torques providing two additional terms within LLG [121]:

$$\frac{\mathrm{d}\overrightarrow{m}}{\mathrm{d}t} = -\gamma_0(\overrightarrow{m}\times\overrightarrow{H_{\text{eff}}} + b_j\overrightarrow{m}\times\overrightarrow{p}) + \alpha\overrightarrow{m}\times\frac{\mathrm{d}\overrightarrow{m}}{\mathrm{d}t} + \gamma_0 a_j\overrightarrow{m}\times(\overrightarrow{m}\times\overrightarrow{p}) \tag{1.26}$$

where $\overrightarrow{p}$ is the polarization vector of the spin current (namely the direction of the magnetization of the reference layer in STTMRAM context), b_j the field-like torque efficiency and a_j the Slonczewski-like torque efficiency. In our system, the spin current is polarized out of plane such that $\overrightarrow{p} = \overrightarrow{e_z}$. At the remanance the effective field is also along z through a strong perpendicular anisotropy. Then the b_j term is called the field-like torque as it simply adds to the effective field. In this configuration the a_j term is going to be responsible for the switching by acting as an anti damping early during the reversal, it is called the Slonczewski-like torque.

Slonczewski spin transfer torque through a tunnel barrier

The Slonczewski-like term through a crystalline MTJ is studied in references [90, 92], we discuss some findings of these two studies here. The magnetic tunnel junction is represented by its equivalent circuit shown in figure 1.4. The aim is to express the STT exerted on the right layer, which plays the role of the free layer. This torque

depends on transport properties through the crystalline tunnel barrier similarly to the TMR calculations of section 1.2.2.

Assuming that all the angular momentum carried by the current is deposited within the right layer, the torkance applied on the right layer takes the general form, following the geometry of figure 1.4:

$$\frac{\mathrm{d}\overrightarrow{\tau_{\mathrm{STT}}}}{\mathrm{d}V} = \frac{\hbar}{4e}(G_{++} - G_{--} + G_{+-} - G_{-+})\,\overrightarrow{m} \times (\overrightarrow{m} \times \overrightarrow{p}) \tag{1.27}$$

where $G_{\sigma\sigma'}$ are the spin-channel conductances defined in section 1.2.2. The $\frac{\hbar}{2e}$ factor converts the electrical current carried by an electron into a spin angular momentum applied to the magnetization. Now what is left to obtain the STT is to express the spin-channel conductance by considering the tunnelling of the different Bloch states through the barrier. In reference [92] the elastic tunnelling of the different Bloch states is first considered. From this approach, the predicted voltage dependence of the conductance in the antiparallel state takes the asymmetric form $G_{\mathrm{AP}} = a + bV$. This is an issue because the measured conductance is rather voltage-symmetric and presents what Slonczewski and Sun call a "broken-linear" dependence on voltage, namely $G_{\mathrm{AP}} = a + b|V|$. To obtain such a voltage dependence in the model, they consider the inelastic tunnelling through the barrier without detailing the nature of such a tunnelling (maybe electron traps at oxygen vacancies). From these additional channels, one obtain the broken-linear dependence of G_{AP} on voltage and a general expression for the torkance:

$$\frac{\mathrm{d}|\tau_{\mathrm{STT}}|}{\mathrm{d}V} = \frac{\hbar}{4e}[G'_{\mathrm{P}} + (U_{+-} - U_{-+})\rho_{+}\rho_{-,0} + (D_L - D_R)|V| + (U_{+-} + U_{-+})\rho_{+}\rho_{-,1}V]\sin\theta \tag{1.28}$$

Where the $U_{\sigma\sigma'}$ are the elastic tunnelling coefficients, ρ_σ the densities of states at the Fermi level and D_L , D_R inelastic tunnelling coefficient that are assumed positive and not specified. We do not detail each of these terms in this manuscript because we are going to focus on a system for which they cancel out. The conductance G'_{P} corresponds to the conductance in the parallel states corrected to account for the small G_{--} term in its expression (equation 1.19):

$$G'_{\mathrm{P}} = \frac{2P}{1+P^2}G_P(V) \tag{1.29}$$

This correction is valid if $G_{++} \gg G_{+-}, G_{-+} \gg G_{--}$, namely for a strong TMR. Equations 1.28 and 1.29 are also only valid if we assume that a single effective polarization factor P can be written. This assumption, which depends on the separability of the left and right contribution to the total tunnelling, is discussed into detail in reference [90] (see equation 16). For instance it is valid for perfect MgO barrier, but could also be valid in other cases. Here the bias-dependence of TMR is also disregarded as P does not depend on V, similarly to equation 1.22.

After obtaining these equations, Slonczewski and Sun discuss various systems in which the torkance is predicted by equation 1.28. In our STTMRAM system, we focus on symmetrical MTJs. In that case all the terms in the torkance equation are zero save for G'_P. We obtain a simple expression for the Slonczewski-like torkance:

$$\frac{\mathrm{d}\overrightarrow{\tau_{\mathrm{STT}}}}{\mathrm{d}V} = \frac{\hbar}{2e}\frac{P}{1+P^2}G_{\mathrm{P}}\,\overrightarrow{m} \times (\overrightarrow{m} \times \overrightarrow{p}) \tag{1.30}$$

According to this model there is no field like torque, if all the angular momentum is indeed deposited within the right layer.

The field like torque

In reference [101] Theodonis et al predict the current flowing through a symmetrical MTJ using tight-bindings and free-electrons calculations. The free electron model for a similar system (symmetrical MTJ) is also discussed in reference [113]. We do not detail the calculations of these models in this manuscript. The main findings of the two studies are the following: i) Two spin currents are created on the right layer, one carrying an angular moment in the plane of the layers and one out-of-plane. The two currents corresponds to the field-like torque (for the out-of-plane, perpendicular current) and the Slonczewski-like torque (for the in plane, parallel current) as defined in equation 1.26. They are of comparable amplitude. ii) The field-like torque depends quadratically on voltage. iii) The Slonczewski-like torque presents an anomalous bias dependence on voltage, i.e. it is not always proportional to the voltage. It can change sign without the voltage changing sign and follows an unexpected quadratic voltage dependence in certain regions. This last finding is in disagreement with the models of Slonczewski and Sun that we presented in the previous paragraph, which predicted a linear dependence of the STT on voltage in the case of a symmetrical MTJ.

Measurement in in-plane magnetized MTJ are performed in references [87] and [60] in order to check the theoretical predictions. In both studies the field like torque is indeed measured to have a quadratic dependence on bias, as was predicted by the free electron and the tight-bindings models. In [60] the Slonczewski-like torque voltage dependence has a good agreement with the anomalous dependence predicted by Theodonis et al. While in [87] the torkance is measured to depend little on voltage for the smaller voltage values studied (below ± 0.4 V approx), which corresponds more to the prediction of Slonczewski and Sun in the symmetrical MTJ case and therefore to our equation 1.30.

We have come to the conclusion that there is no consensus in literature. In the studies of Slonzewski and Sun the field-like torque was not predicted and the bias dependence of the Slonczewski-like torque did not correspond to the one of references [101, 113]. In our manuscript we chose to follow the approach of Slonczewski and Sun that we detailed in the previous paragraph: the field-like torque is not going to be considered and the Slonczewski-like torque (simply written STT) is considered to depend linearly on voltage following equation 1.30. In our out-of-plane systems the field-like torque would have the effect of an effective field along z at the remanance, as we already stated. The field-like torque thus has two contributions to the dynamics [105]: i)Changing the precession frequency. ii) Favoring one state compared to the other one because of the quadratic bias dependence, leading to non-symmetric switching performances. But this effect of field-like torque on switching voltage is rather weak in our system. This is shown in reference [105] and can be extrapolated from our own calculation in the following section by adding the field-like torque to the effective field. In chapter 5 we present symmetrical $R(V)$ loops, hinting a weak effect of field-like torque in our samples (figure 5.5).

Final LLGS equation

To express the Slonczewski-like torque of equation 1.30 into the LLGS equation, we multiply by the gyromagnetic constant γ and we divide by the total reversed volume

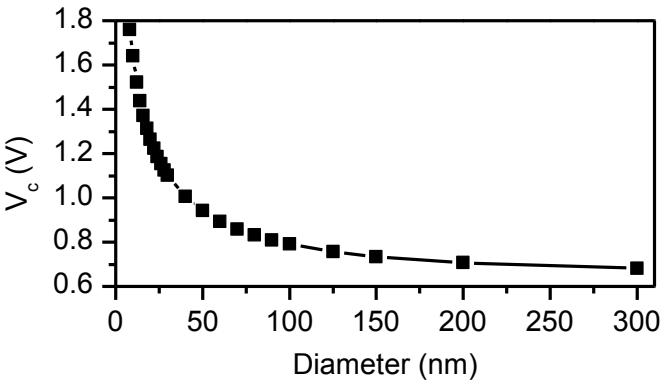

FIGURE 1.5: Diameter dependence of the macrospin critical switching voltage V_c. It is obtained from equation 1.37 using the material parameters described in table 1.1 and demagnetizing factors obtained from the free precession simulations (figure 1.1).

$\mathcal{A}d$ (d is the thickness and $\mathcal{A}$ the total free layer area). We obtain the LLGS equation that is used for all this manuscript:

$$\frac{\mathrm{d}\overrightarrow{m}}{\mathrm{d}t} = -\gamma_0 \overrightarrow{m} \times \overrightarrow{H_{\text{eff}}} + \alpha \overrightarrow{m} \times \frac{\mathrm{d}\overrightarrow{m}}{\mathrm{d}t} + \gamma_0 P \frac{V}{\mathcal{A}R_\perp} \frac{\hbar}{2e\mu_0 M_s d} \overrightarrow{m} \times (\overrightarrow{m} \times \overrightarrow{p}) \tag{1.31}$$

We give this form with $\mathcal{A}R_\perp$ and V because it is the most suited for comparing with the forthcoming measurements. Indeed as we vary the diameter of the device, the resistance changes while the area resistance product remains constant. Furthermore our measurements or simulations are performed at fixed voltage. The voltage is a more correct metric than the current to describe the STT in a MTJ context: the insulating nature of the tunnel barrier renders the voltage laterally uniform across the device, while the current density is not necessarily uniform because the magnetization can be non-uniform (for instance in a domain wall-based reversal).

To summarize, the main assumptions for this formula are: i) The field-like torque is not included. ii) No bias dependence of the TMR. iii) Symmetrical barrier tunnel. iv) Separability of the left and right contribution to the total tunnelling. v) A sufficiently strong TMR (namely $G_{++} \gg G_{+-}, G_{-+} \gg G_{--}$).

1.4 Coherent reversal of the free layer

We now solve the LLGS equation 1.31 in the single spin limit. The obtained dynamics correspond to the trajectory of the magnetization in the case of a coherent reversal of the free layer (namely within the macrospin assumption). But first we discuss how much voltage or external field should be applied to the system in order to reverse it.

1.4.1 Critical external stimuli for the reversal

Equation 1.31 can take an explicit form, similarly to the procedure used to obtain equation 1.25:

$$\begin{aligned}(1+\alpha^2)\frac{\mathrm{d}\overrightarrow{m}}{\mathrm{d}t} &= -\gamma_0 \overrightarrow{m} \times \overrightarrow{H_{\text{eff}}} - \alpha\sigma j \overrightarrow{m} \times \overrightarrow{p} \\ -\alpha\gamma_0 \overrightarrow{m} \times (\overrightarrow{m} \times \overrightarrow{H_{\text{eff}}}) &+ \sigma j \overrightarrow{m} \times (\overrightarrow{m} \times \overrightarrow{p})\end{aligned} \tag{1.32}$$

Where $\sigma j = \gamma_0 P \frac{V}{\mathcal{A}R_\perp} \frac{\hbar}{2e\mu_0 M_s d}$ is the frequency corresponding to the STT term. We consider the case of a thin disk with a strong perpendicular anisotropy uniformly magnetized, a reference layer magnetized out of plane and an external field applied

along z. Then: i) $\overrightarrow{m}$ is uniform (macrospin assumption). ii) $\overrightarrow{p} = \overrightarrow{e_z}$ namely we have a perfectly out-of-plane reference layer at all time. iii) The effective field is approximated by $\overrightarrow{H_{\text{eff}}} = (H_{k,\,\text{eff}}^{\text{disk}}\cos(\theta) + H_{\text{ext}})\overrightarrow{e_z}$, namely the demagnetizing field considered uniform and written within the effective anisotropy following the calculation of section 1.1.6. There is no exchange terms into the effective field because the system is described by a single spin.

In this system, the first two terms of equation 1.32 are precession terms: the frequency is given by the effective field corrected by a STT term multiply by α. Typically the field dynamics are faster than the STT dynamics and the damping is of the order of 10^{-2} such that the STT contribution to the precession is negligible.

The two last terms correspond to the damping and the spin transfer torque. They dictate if the magnetization is reversed or not (namely if m_z remains constant or not). Along z, equation 1.32 reads:

$$(1+\alpha^2)\dot{\theta}\sin\theta = [-\alpha\gamma_0(H_{k,\,\text{eff}}^{\text{disk}}\cos(\theta) + H_{\text{ext}}) + \sigma j]\sin^2\theta \tag{1.33}$$

For a small angle θ, we can write:

$$(1+\alpha^2)\dot{\theta} = [\sigma j - \alpha\gamma_0(H_{k,\,\text{eff}}^{\text{disk}} + H_{\text{ext}})]\theta \tag{1.34}$$

This equation shows that the magnetization moves away from the effective field when $\dot{\theta}$ is positive (for an P to AP reversal). The equilibrium corresponds to:

$$\alpha\gamma_0(H_{k,\,\text{eff}}^{\text{disk}} + H_{\text{ext}}) = \sigma j \tag{1.35}$$

This is equivalent to:

$$\frac{V}{V_c} - \frac{H_{\text{ext}}}{H_{k,\,\text{eff}}^{\text{disk}}} = 1 \tag{1.36}$$

where we introduced the macrospin critical switching voltage V_c defined by:

$$V_c = \frac{2\alpha e\mathcal{A}R_\perp\mu_0 M_s d H_{k,\,\text{eff}}^{\text{disk}}}{P\hbar} \tag{1.37}$$

To better illustrate the role of the external field and the applied voltage on the switching, it is convenient to introduce the critical external stimulus h defined by:

$$h = \frac{V}{V_c} - \frac{H_{\text{ext}}}{H_{k,\,\text{eff}}^{\text{disk}}} \tag{1.38}$$

Such that the free layer is reversed if $h > 1$ (for P to AP reversal) and otherwise it remains along the effective field. A negative field or a positive voltage favor the P to AP reversal. For the AP to P switching the same equations can be obtained and the reversal occurs for $h < -1$, a negative voltage or a positive field favor the switching.

The macrospin critical switching voltage corresponds therefore to the minimum voltage than can reverse the system if there is no external field. This voltage is notably proportional to the damping, to the area-resistance product (called $R\mathcal{A}$ product) and to the effective anisotropy of the disk. We have already shown that this effective anisotropy depends on the diameter of the disk because of the demagnetizing effects, therefore the macrospin critical switching voltage also depends on the diameter following equation 1.11. Figure 1.5 illustrates this dependence using the demagnetizing factors obtained from the free precession simulation method. The

Magnetization	Damping constant	Anisotropy field	Resistance area product (P state)	TMR	Exchange stiffness	Layer thickness
$M_S = 1.2$ MA/m	$\alpha = 0.01$	1.566 MA/m	8.55 $\Omega.\mu m^2$	150%	20 pJ/m	2 nm

TABLE 1.1: Material parameters meant to mimic a dual MgO FeCoB-based layer [21, 31]. .

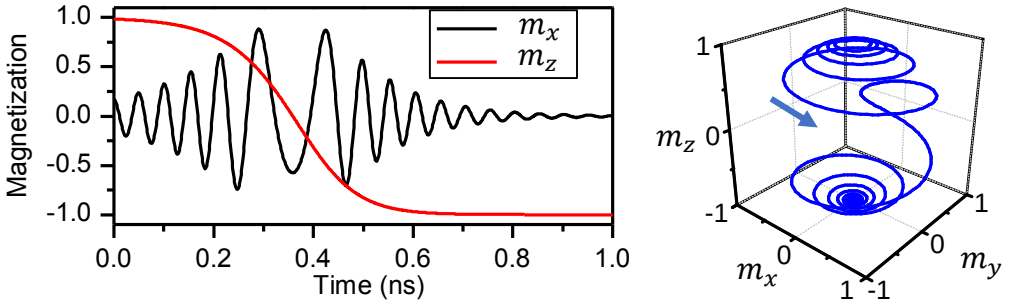

FIGURE 1.6: Macrospin trajectory. The reversal predicted by equation 1.39 and 1.40 is presented, a) m_x and m_z versus time, b) 3D trajectory over a full switching. This reversal corresponds to a 40 nm diameter disk described by the parameters of table 1.1 under an external voltage of -6 V and no external field. The initial angle θ_0 is 10 deg.

parameters that are used correspond to our best estimation of our STTMRAM devices (see the chapter on the basic properties of our devices) and are presented in table 1.1. We expect the largest devices that we study (200 nm diameter) to be reversed at around 0.7 V while the smallest (20 nm) at about 1.3 V. This highlights the strong expected effect of the demagnetizing field. But of course this approach is valid only for a coherent reversal and at 0 K, the temperature greatly affects the measured switching voltage.

With no external voltage applied, the free layer is reversed for $-H_{\text{ext}} > H_{k,\text{ eff}}^{\text{disk}}$ (P to AP). The coercive field as predicted by the macrospin model at 0 K is the total effective anisotropy field.

1.4.2 Trajectory of the magnetization

We now assume that the external stimulus is sufficiently strong to initiate a reversal from P to AP. The magnetization follows equation 1.32. The reversal is described by the dynamics of m_z and ϕ_m obtained from equation 1.32:

$$\dot{m_z} = \frac{\gamma_0 \alpha H_{k,\text{ eff}}^{\text{disk}}}{1+\alpha^2}(m_z + h)(1 - m_z^2) \tag{1.39}$$

$$\dot{\phi_m} = \frac{\gamma_0 H_{k,\text{ eff}}^{\text{disk}}}{1+\alpha^2}(m_z + \alpha^2 \frac{V}{V_c} + \frac{H_{\text{ext}}}{H_{k,\text{ eff}}^{\text{disk}}}) \tag{1.40}$$

ϕ_m is the azimuth such that $m_x = \cos\phi_m \sin\theta$. The notation ϕ is preserved for domain wall models.

Note that the individual contributions from the applied voltage and the external field cannot be grouped in a generalized stimulus h in the second equation. This time both a positive field and a positive voltage increases the precession frequency. The voltage contribution is bound to be weaker because of the damping square prefactor.

These equations are solved and the obtained trajectories are presented in figure 1.6. The figure corresponds to a 40 nm diameter disk described by the parameters from table 1.1 under a voltage of -6 V and no external field. A very high voltage was chosen in order to observe less oscillations during the full reversal, which gives an easier to read figure. For more reasonable voltage values (between 1 and 2 V since $V_c = 1$ V at 40 nm) the trajectory is qualitatively the same, but with slower m_z drift and therefore more oscillations of the in plane component of the magnetization.

The z component of the magnetization first decreases slowly because the STT and the damping are opposed. Once the equator is reached (namely $m_z = 0$), both the STT and the damping term push the magnetization down and therefore the rate of reversal is increased compared to the first part. This can be seen in the left graph of figure 1.6.

Concerning the oscillations, the frequency first decreases as m_z decreases following equation 1.40. Once the equator is reached the magnetization precess in opposite direction with a frequency increasing as m_z decreases.

From this approach, we cannot give an absolute switching time since it is strongly dependent on the chosen initial angle θ_0. In the first section of the following chapter we shall discuss the implications of this macrospin trajectory for STTMRAM devices, as well as compare this model with stability diagrams measurement from literature.

1.5 Conclusion

In this chapter we have introduced the basic concepts used in this manuscript and necessary to understand the forthcoming state of the art chapter: the relevant energies of the system, the transport properties through a tunnel barrier, the effect of spin transfer torque and finally the basic magnetization dynamics in the macrospin approximation.

Other basic studies are kept for later. The introduction to domain wall models is done in the state of the art chapter, while their basic calculation with our parameters is presented in the *Modelling the domain wall motion* chapter 4. The design and the basic properties of our STTMRAM devices are presented in chapter *STTMRAM devices and their basic properties* 5.

Chapter 2

State of the art on free layer dynamics

In this chapter we present what was the common understanding of the switching path of the free layer at the beginning of this PhD. First we discuss the predictions of the macrospin model and its comparison with stability or switching time measurements. Second we present results obtained from micromagnetic simulations of the switching path. Third the domain wall models applied to STTMRAM are shown. The last two parts of this chapter focus on the design of state-of-the-art STTMRAM devices and on the possible direct observations of the switching path in such devices.

2.1 Spin transfer torque induced coherent reversal

This section focuses on the use of the macrospin model to explain two types of measurements: stability diagrams and switching time studies. The basics of the macrospin model were presented in the previous chapter both in term of critical switching external stimuli and of magnetization trajectory.

2.1.1 Stability diagram measurement compared to the macrospin model

Predicting the stability diagram

The macrospin model predicts that an external field along the out of plane axis or an external voltage can reverse the magnetization of the free layer if they are sufficiently strong, following equation 1.36. A stability diagram is a measurement of the possible states of a STTMRAM device (P only, AP only, or both states possible) in the (H_{ext}, V) space. These diagrams can be directly compared with the prediction from a macrospin model such as the one we presented in the previous chapter.

The shapes of the stability diagram have been derived for different geometries and external stimuli by Bernert and al in reference [5]. Their study is more complete than the macrospin model we derived previously. It includes the effect of the field like torque, of an external field applied in plane and study the case of an in-plane-magnetized free layer. The phase diagram they predict for a fully perpendicular system are shown in figure 2.1.a. Similarly to what is obtained from equation 1.36 the diagram is symmetrical with P to AP and AP to P switching being equivalent. The limits are given by a straight line.

In reference [62] Lavanant et al predict stability diagrams in out-of-plane STTMRAM from a different method. They use a power dissipation approach where only the dissipative terms (damping and Slonczewski-like STT) are included in a dissipation function. Then the Euler Lagrange equation is solved. Lavanant et al obtain the same result as from the LLGS approach, as shown in the third figure of [62]. They

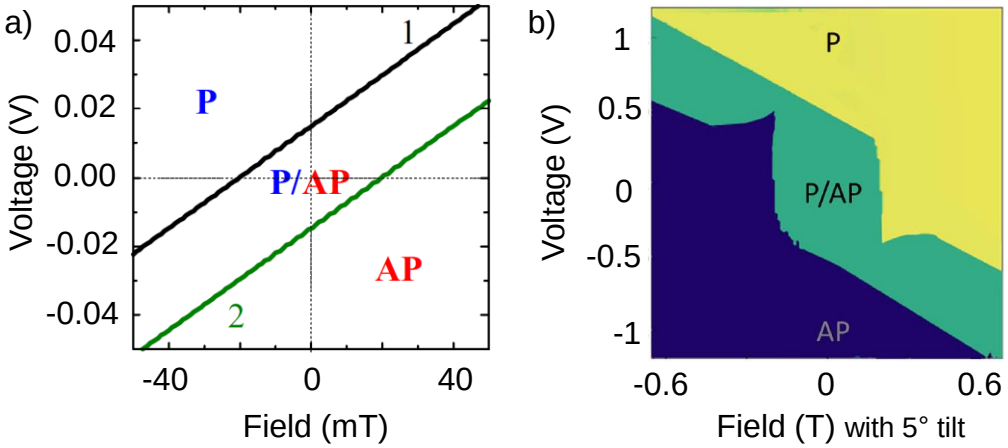

FIGURE 2.1: Predicted stability diagrams for a perpendicularly magnetized STTMRAM device from the macrospin model. a) From reference[5]: diagram with no in plane field and a field like torque, predicted by LLGS equation. b) From reference [62]: diagram with a tilt of 5 deg between the easy axis and the applied field, as computed by the power dissipation approach.

also extend their model to the case a strong second order anisotropy and consider a possible tilt between the easy axis of the free and the applied field. Such a tilt breaks the cylindrical symmetry of the stability diagram and even an angle as small as 5 deg leads to a case such as the diagram of figure 2.1.b. They predict a strong impact of a tilt or of second order anisotropy on the stability diagrams. This more complete model will prove useful to understand experimental state diagrams.

Comparing with measurements

In reference [105] Timopheev et al study stability diagrams of perpendicularly magnetized STTMRAM through macrospin modelling, micromagnetic simulations and direct measurements at room temperature. In their model the influence of the field-like torque is discussed. The obtained diagrams are similar to the one predicted in reference [5] save for the vertical lines delimiting the $H_{\text{ext}} = \pm H_{k,\,\text{eff}}^{\text{disk}}$ regions. The field-like torque has a weak effect on the state diagram if the Slonczewski-like torque is sufficiently strong. This is confirmed in micromagnetic simulations. The simulations also discuss the effect of being at room temperature on the stability diagrams: the overall shape is conserved but the switching voltage or field are reduced. Their measurement is shown in figure 2.2.a. There is a good qualitative agreement between the measured diagrams and the one predicted by the macrospin model or the micromagnetic simulations in the case of a weak field-like torque.

In reference [95] Strelkov et al study the state diagrams of similar devices while varying the tilt angle between the applied field and the easy axis of the free layer. For the case of an out-of-plane field, they recover diagrams similar to the one predicted by the macrospin model and presented in figure 2.1. But for an in plane applied angle a stability diagram such as the one presented in figure 2.2.b is measured. Strelkov et al then show that the macrospin model can account very well qualitatively for the change of shape of the diagrams while the tilt angle varies.

Measurements of stability diagrams in out-of-plane spin valves (with a metallic spacer) are compared with macrospin models by Le Gall et al in reference [63]. In

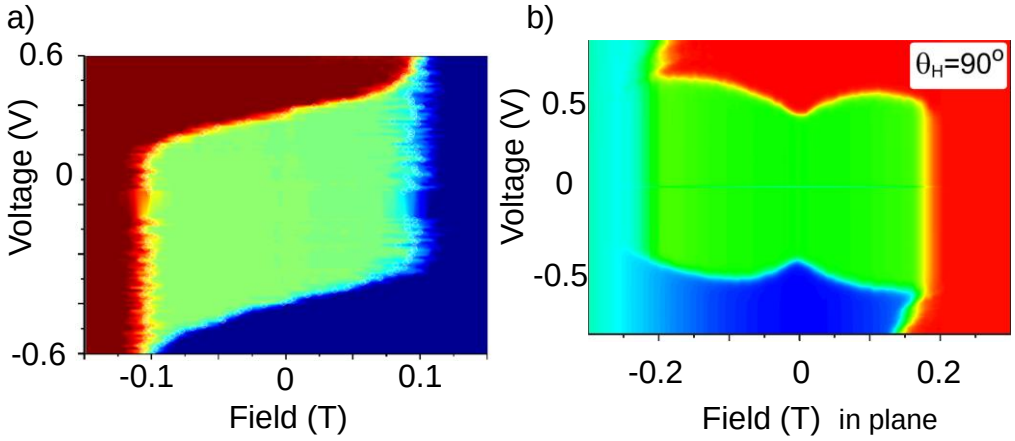

FIGURE 2.2: Measured stability diagrams in perpendicularly magnetized STTMRAM devices. a) From reference[105]: diagram in the field-voltage space. The device is a disk of 36 nm diameter. b) From reference [95]: diagram obtained for an external field applied in plane.

this paper the macrospin model fails to predict all the features observed in the measurement. A tilt between the field and the easy axis of the free layer and/or a second order anisotropy term are necessary to explain the experimental observations. In some region of the diagrams neither the P nor the AP state are stable and Le Gall et al attribute this signal to dynamical states.

In MTJs based devices the macrospin model can fail to account for all the observed features of a stability diagram. In reference [22] some features of the stability diagrams are explained by considering the existence of intermediate states between P and AP existing through domain walls.

Other groups studied stability diagrams, we here reviewed only out-of-plane devices but similar studies were performed for the in-plane configuration such as reference [86]. Those devices are less similar to the one we study throughout this manuscript.

Discussion: what the macrospin model could and could not explain from the stability diagrams ?

The macrospin model could explain the shape of the stability diagram qualitatively. Several elements should be added to the model compared to the basic one that we presented in the first chapter in order to explain all the measured features. Most notably a tilt between the easy axis of the free layer and the applied field or a second order anisotropy both have a very strong impact on the shape of the diagrams. This was both predicted and measured in the case of a tilt. Without this tilt the limits of the diagrams are predicted to be infinite by the macrospin model, unlike what is measured. However diagrams with a strong breaking of symmetry where measured while no tilt angle or second order anisotropy are expected (such as figure 11 of reference [62]). To make a more quantitative prediction of the diagram boundaries, temperature should be added to the model similarly to what is done in reference [105]. Otherwise the macrospin model overestimates greatly the voltage or field needed to reverse the device. Thermal activation in STTMRAM devices is discussed in the following subsection within the macrospin assumption.

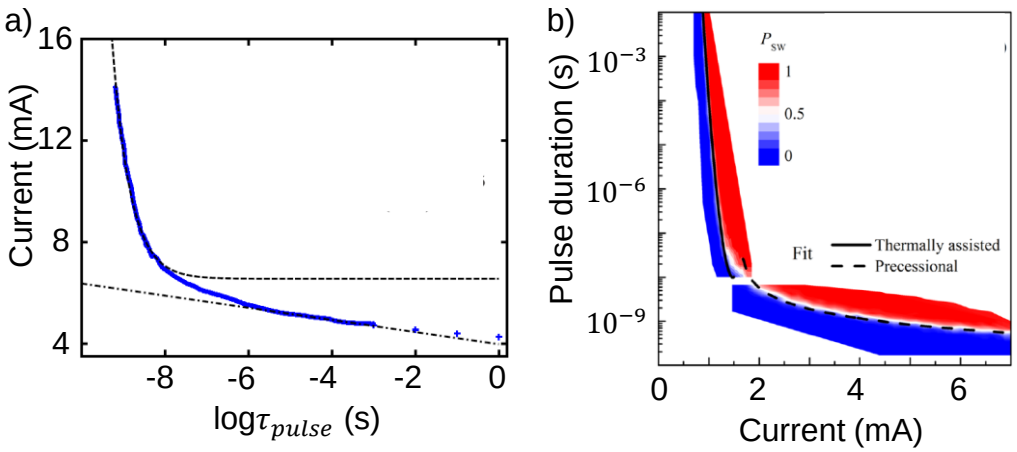

FIGURE 2.3: Probability of reversal in the pulse duration - applied current space. a) From reference[2]: the plotted line corresponds to 50 % probability of reversal. The sample is a fully metallic spin valve. b) From reference [106]: the red corresponds to a high probability of reversal and the blue to a low one. The black curves are fit from their models. The sample is a PMA-MTJ.

There are also some other experimentally observed features that cannot be described by the macrospin model: possible dynamical states or domain wall based intermediate states.

2.1.2 Prediction of the switching time through the macrospin model

Switching time measurement: two regimes are observed

A pulse-induced switching measurement consists in sending a voltage pulse through a STTMRAM device with no external applied field and checking whether the free layer has switched or not. The reversal is stochastic, the same pulse can sometimes reverse the free layer and sometimes not. The probability of reversal is obtained by repeating the experiment many times. Such probability of reversal measurements can be done while varying the duration of the pulse as well as the applied voltage. It is convenient to describe the obtained statistics of the switching time through the voltage dependence of the average switching time $\tau_{sw}(V)$.

Such measurements have been performed early on the older STTMRAM stacks. Here we present more recent studies where the devices are perpendicularly magnetized. In reference [2] Bedau et al discuss such a measurement performed in a fully metallic spin valve. In such samples a larger current range can be explored because there is no tunnel barrier to break down, but the physics of the switching remain essentially the same. Similar results are presented in reference [106] by Tomita et al in a PMA-MTJ samples. Their results are shown in figure 2.3 a) and b) respectively. It is observed that the switching time depends very strongly on the applied switching voltage, especially at low voltages/long switching time. Both studies also present two distinct regimes for the pulse duration versus voltage graphs. Those regimes are called the precessionnal (or ballistic) regime at high current and the thermally activated regime at low current.

In the two papers we presented, macrospin models are compared to the experimental results. We now discuss these models origins for both regimes before going back to the measurements and compare each others in the discussion paragraph.

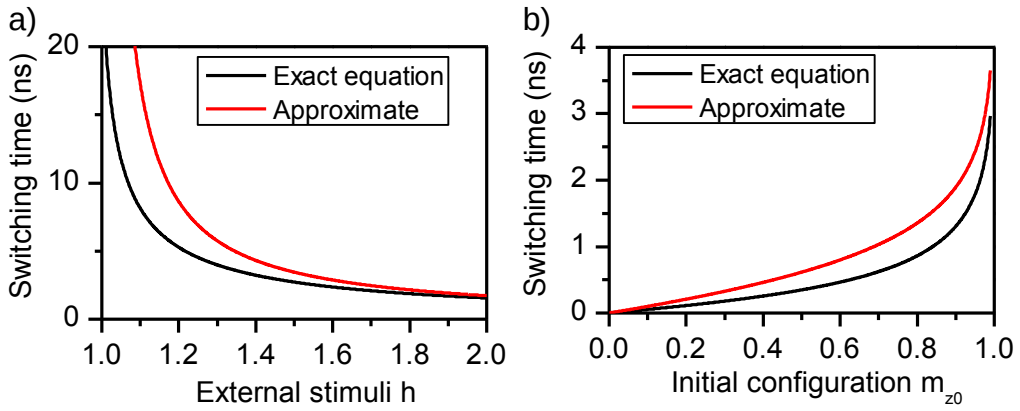

FIGURE 2.4: Switching time as predicted by the macrospin dynamics in the precessionnal regime. a) Switching time versus external stimuli h for a fixed initial tilt angle of 10 deg. Are compared the exact equation 2.2 and the approximate expression proposed by J. Sun (equation 2.1) taken at $m_z = 0$ to obtain the switching time. b) The same equations are compared while varying the initial tilt angle between $m_{z0} = 0$ (in plane) and $m_{z0} = 1$ (out of plane) for a fixed external stimuli of $h = 1.5$.

Switching time in the precessional regime

The first prediction of the switching time in a device reversed by STT was proposed by J. Sun in reference [97]. This study concerns the general case of a parallelepiped uniformly magnetized and reversed by a spin current. It is therefore within the macrospin assumptions. J. Sun derives equations similar to the LLGS equation that we presented in the previous chapter and predicts a critical switching current as well as the magnetization trajectory in a similar manner. Several geometries are discussed as well as the influence of an external field. This paper integrates the $\dot{\theta}$ dynamics and gives an approximate switching time for small θ. For a uniaxial anisotropy only system, the time needed to go from θ_0 to θ is given by equation (27) of reference [97] which translates with our notations into the "first Sun's law":

$$t(m_z) = \frac{1+\alpha^2}{\alpha\gamma_0 H_{k,\,\mathrm{eff}}^{\mathrm{disk}}} \frac{1}{h-1} \ln\left(\frac{\theta}{\theta_0}\right) \tag{2.1}$$

We define the switching time as the time needed to reach $m_z = 0$ (because if from this point we stop sending external stimuli the free layer still switches). The switching time is proportional to $\ln\theta_0$ and the inverse switching time is linear with h following equation 2.1.

This equation is obtained considering only the leading order of the h dependence, namely is valid for small θ. To have a more precise formula, we can integrate our equation 1.39 on the dynamics of m_z. This has already been done in reference [7] and lead to the following equation:

$$t(m_z) = \frac{1+\alpha^2}{\alpha\gamma_0 H_{k,\,\mathrm{eff}}^{\mathrm{disk}}} \frac{1}{2(h^2-1)} \left[(1-h)\ln\left(\frac{1-m_z}{1-m_{z0}}\right) + (1+h)\ln\left(\frac{1+m_z}{1+m_{z0}}\right) - 2\ln\left(\frac{h+m_z}{h+m_{z0}}\right)\right] \tag{2.2}$$

This equation gives the switching time corresponding to our basic LLGS equation. The exact formula and the approximate expression derived by Sun are compared in figure 2.4 while varying the generalized stimuli or the initial tilt angle. Even

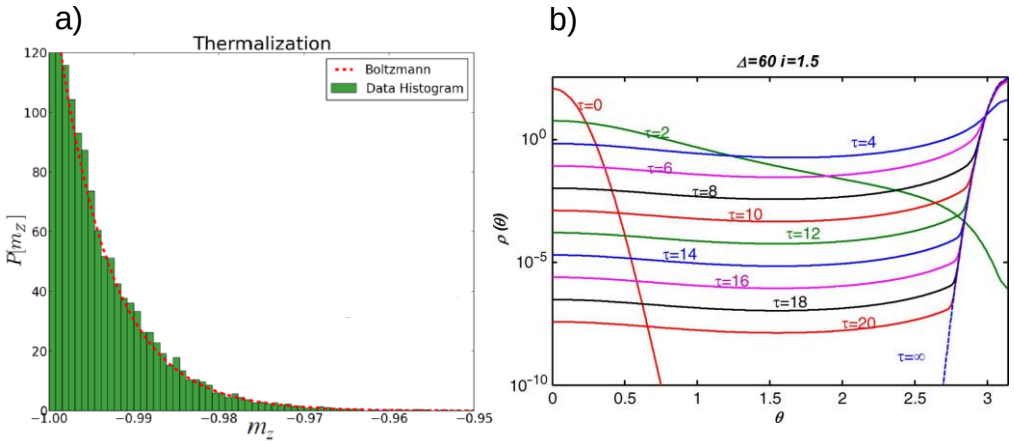

FIGURE 2.5: Probability density of the magnetization's destribution as predicted by a Fokker-Planck equation. Both figures concern PMA-MTJs. a) From reference[83]: distribution histogram at equilibrium before any STT is applied. The histogram is obtained by solving numerically the Fokker-Planck equation (equation 2.3) while the ref line is a Boltzmann distribution fit (equation 2.6). The thermal stability factor is $\Delta_T = 80$. b) From reference [13]: distributions of the magnetization obtained from the Fokker-Planck equation at different normalized time for an applied external stimuli of $h = 1.5$ and a thermal stability factor $\Delta_T = 60$.

though the approximate expression overestimates the switching time, there is a good qualitative agreement on the effect of h and m_{z0} on the switching time. Since the macrospin models will prove once again to be only qualitative when compared with measurement of the switching time, the approximate expression proposed by J. Sun finds use in literature.

In a measurement of the switching time, we have a good control of the applied external stimuli but we have no control on the initial state m_{z0}. This initial state depends on the temperature of the device: the thermal fluctuations have the effect of tilting overall the magnetization away from the effective field by an angle θ_0. This angle can be derived from a Fokker-Planck equation and by considering that the magnetization aligns itself with the Boltzmann distribution obtained around the effective field. This approach is shown after the next paragraph since it is necessary to introduce the Fokker-Planck equation to estimate the thermal regime switching time.

Now if we assume that the only effect of temperature on the switching is this initial tilt, then we can predict a switching time depending on h and T using equation 2.1 or 2.2. The regime where this assumption is considered valid is called the precessionnal regime, because the switching is then described only by the precessionnal dynamics of the macrospin model. This predicted switching time can be compared with measurement, as we shall present in the last paragraph of this subsection.

Switching time in the thermally activated regime

The first theoretical studies of the impact of thermal fluctuations on the STT based reversal where proposed by Sun et al, most notably in references [98] and [45]. These studies are performed in geometries different from ours. More recent works (references [13, 83, 106]) focus on our fully out-of-plane case. In both the older and the more recent papers, the temperature is considered through a stochastic field that is

added to the effective field in the LLGS equation. Under the effect of thermal fluctuations the magnetization is described by a distribution. We note $p(\theta, t)$ the probability density that the magnetization makes an angle θ with the easy axis at time t. This probability follows a Fokker-Planck equation, in our fully out-of-plane geometry for m_z it is written [13, 83]:

$$\frac{\partial p}{\partial t} = \frac{\partial}{\partial m_z}[(m_z + h)(1 - m_z^2) + \frac{1 - m_z^2}{2\Delta_T}\frac{\partial p}{\partial m_z}] \tag{2.3}$$

where Δ_T is the thermal stability factor of the device defined by:

$$\Delta_T = \frac{K_{\text{eff}}^{\text{disk}} Vol}{k_B T} = \frac{\mu_0 M_s H_{k,\,\text{eff}}^{\text{disk}} Vol}{2 k_B T} \tag{2.4}$$

with k_B the Boltzmann constant, T the temperature and Vol the volume of the free layer. For a 40 nm disk with the parameters described in table 1.1 at room temperature, $\Delta_T = 84$.

The Fokker-Planck equation 2.3 describes the dynamics of the distribution of the magnetization. The first term in the bracket is the flow: it accounts for the dynamics of the magnetization in the absence of thermal fluctuations following equation 1.39. The second term is the diffusion: it is proportional to temperature and accounts for the diffusion of the distribution over time.

Such an equation can be solved numerically to predict the distributions of the magnetization over time as the device switches. This is done for PMA devices in reference [83]. Reference [13] gives analytical approximate expressions for those distributions and the switching time, and compares them with the numerical results. Figure 2.5.b presents distributions obtained from this reference. Note that initially it is centered around the initial state $\theta = 0$ and at the end of the reversal ($\tau = \infty$) around the final state $\theta = \pi$.

One other key result from these two papers is the estimation of the switching time in the so-called thermal regime. The thermal regime assumptions are: i) the system follows a Boltzmann distribution about the effective field before the voltage is applied; ii) the STT can be considered as a perturbation, namely the switching is considered a rare event; iii) there is no switching back to the initial state once the reversal is done. Then the mean value of the switching time (switching meaning that we crossed the barrier, namely $m_z < 0$) takes the general form [83, 106]:

$$t_{\text{sw}} = \frac{1}{\Omega}\exp[\Delta_T(1 - h)^2] \tag{2.5}$$

where Ω is the attempt frequency.

Determining the attempt frequency is a complex issue. Two different forms are proposed in reference [83] and [106]. For both references it is expected to depend on voltage as a power of 2 or 3. In all cases, the voltage dependence of the switching time is mostly given by the exponential term. A quadratic dependence of $\ln t_{\text{sw}}$ is therefore expected when analysing measurements.

Note that while references [13, 83, 106] all predict this quadratic dependence and compare it with numerical calculations and measurements, earlier studies of the thermal fluctuations predicted a linear dependence. The linear dependence on voltage of $\ln t_{\text{sw}}$ is obtained following a Fokker-Planck equation, but reduced to a standard eigenvalue problem. This approach is detailed in reference [98] and [45]. This prediction of the switching time is compared to measurements in reference [2].

Predicting the initial tilt angle

The Fokker-Planck approach of thermal fluctuation can be used to obtain the θ_0 that is necessary to predict the switching time in the precessionnal regime following equation 2.2. This is simply done assuming a Boltzmann distribution (see figure 2.5.a) around the effective field [13]:

$$p(m_z, 0) = C \exp[-\Delta_T(1 - m_z^2)] \tag{2.6}$$

where C is a constant that is obtained by normalizing the probability density function. If we assume that initially the magnetization is fully distributed between $m_z = 1$ and $m_z = 0$, then:

$$C^{-1} = \int_0^1 \exp[-\Delta_T(1 - m_z^2)]\, dm_z \tag{2.7}$$

Once C is obtained we have the full initial probability density function. The initial average magnetization m_{z0} is simply given by the expected value of $p(m_z, 0)$.

$$m_{z0} = \int_0^1 p(m_z, 0) m_z\, dm_z \tag{2.8}$$

For a disk of 40 nm diameter at room temperature ($\Delta_T = 84$), we obtain $\theta_0 = 6.4$ deg.

In reference [64] a formula is proposed to estimate the typical initial tilt based solely on energy considerations (i.e. disregarding the entropic contribution linked to the energy degeneracy within the ϕ_m degree of freedom). Within the macrospin assumption the energy is written as $U_{\text{tot}} = \frac{1}{2}\mu_0 M_s H_{k,\,\text{eff}}^{\text{disk}} \sin^2\theta$ (with no external field or DMI). The initial tilt angle is given by the standard deviation of θ around its equilibrium position, which is obtained by expanding the energy:

$$U_{\text{tot}}(\theta_0) = \frac{1}{2} k_B T = \frac{1}{2} \frac{\partial^2 U_{\text{tot}}}{\partial \theta^2} \theta_0^2 \tag{2.9}$$

Which is equivalent to $\theta_0 = \sqrt{\frac{1}{2\Delta_T}}$. This equation gives $\theta_0 = 4.42$ deg, in reasonable agreement with the calculation from the Boltzmann distribution.

Discussion

Usually the average switching time versus voltage graphs are fitted using a h^{-1} dependence for the precessionnal regime and either a $\exp(1-h)$ or $\exp(1-h)^2$ in the thermal regime. Reference [2] uses the $(1-h)^1$ model while [106] the $(1-h)^2$ model and a more complex formula for the precessionnal regime switching time. Even though there is no clear consensus in literature regarding the power factor, the more recent studies in the PMA geometry all gave $(1-h)^2$.

For all measurements in literature or performed during this PhD, a fit can be obtained only by leaving numerous free parameters: the thermal stability Δ_T, the attempt frequency Ω and the critical macrospin switching voltage V_0. There is no study to our knowledge obtaining these three quantities in a unrelated measurement and then using it to fit switching time graphs. Qualitatively the fit obtained in both regimes are satisfactory, the macrospin model with thermal fluctuations could indeed predict two regimes and predict the overall voltage dependence of the switching time in both regimes. But because of these free parameters, the macrospin model is once again only qualitative and by no means can be quantitative. Using the

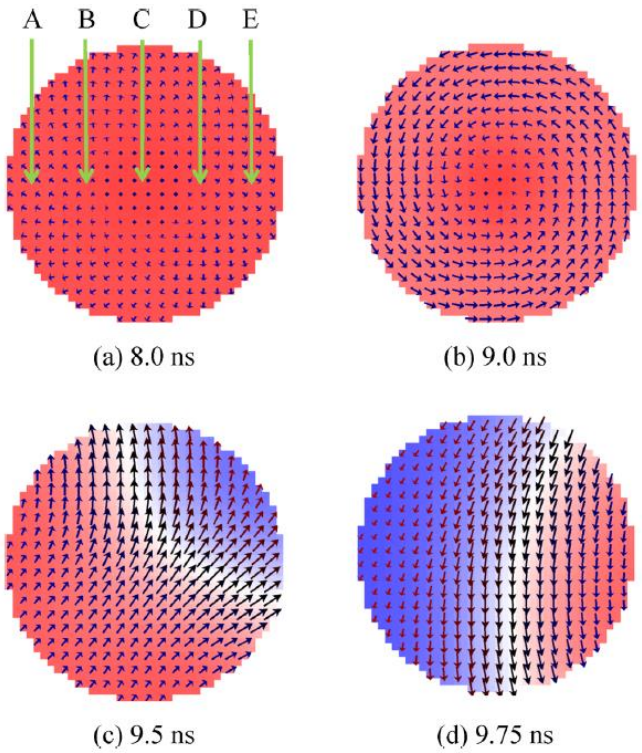

FIGURE 2.6: From reference [118]: snapshots of the magnetization during the reversal of a 40 nm diameter disk by STT. This system simulates a perpedicularly magnetized free layer. The corresponding material parameters and applied current are given in the corresponding reference.

macrospin-predicted value for Δ_T, Ω and V_0 gives switching times longer than the measured one.

The macrospin approach that we have presented here gives expression only within the thermal or precessional limits, they are bound to be invalid in between. In the ballistic regime we assume that the thermal fluctuations only influence the initial state but have no effect on the dynamics. On the contrary in the thermal regime we assume that the STT is a perturbation to the system and that the switching is a rare event. In our micromagnetic simulations at 300 K and in our time-resolved measurement, the macrospin model fails to predict the switching time partly because of these limitations.

2.2 Micromagnetic simulations to study the switching path

So far we have compared the macrospin model with different measurements of the reversal. In this section we discuss the switching path in micromagnetic simulations of the reversal found in literature.

2.2.1 Simulated dynamics under spin transfer torque

Through a grid, the free layer is divided into small elements where the magnetization is considered uniform. This approach is possible because of the exchange energy: at small size scale we expect a small volume to behave as a macrospin. Therefore the LLGS equation can be solved for each of those single elements. This method includes the exchange energy between each macrospins as well as the demagnetizing effects that they exerts on each others into the effective field, in addition to the terms already presented in equation 1.31 from the previous chapter.

The oldest micromagnetic studies of the STTMRAM dynamics were performed for in plane systems, such as in reference [67]. In this work, Li and Zhang consider a

thin ferromagnetic film with in plane anisotropy. Temperature is included as a thermal field added to the total effective field in the LLGS equation. The impact of the STT on the field hysteresis loop is discussed. In this paper, for their 64x64x2.5 nm system, the switching path is mostly coherent as the angle between each individual moments never exceeds 5 degrees during the reversal. In spite of this simple switching path, the system can still undergo complex precessionnal states in the right field and voltage conditions. These precessionnal states are studied into details in this paper. They can persist in this in-plane geometry because energy keeps being pumped into the system by STT. In their study, they also discuss the switching time dependence on voltage in both the precessionnal and the thermal regime. They found that in the precessionnal regime t_{sw} is proportional to $(h-1)^{-1}$ as predicted from the macrospin models (equation 2.1). In the thermal regime, they recover the $\exp(1-h)$ dependence that was predicted and measured in earlier STTMRAM literature. In their work, micromagnetic simulations could be used both to check whether the predictions of the macrospin model still hold beyond this assumption, but also to predict more complex dynamics (precessionnal states) that are outside of the scope of the macrospin model. For a more recent study in in-plane-system, one can consider reference [117], where both the free layer and the reference layer are simulated.

Micromagnetic simulations for the out-of-plane anisotropy are performed by Chun-Yeol You in reference [118]. The aim of this study is to reduce the switching current by elongating the shape of the free layer, or by tilting the easy axis compared to the polarization vector. It is found that breaking the circular symmetry of the system does the job. Additionally to this critical current study, this paper present a switching path of the free layer through snapshots of the magnetization configuration at different times during the reversal. It is found that during the first few ns of the reversal of a disk the out-of-plane plane component of the magnetization decreases almost uniformly across the disk under the effect of spin transfer torque. The center of disk reverses slightly faster. During this phase the in plane component adopts a vortex-like state (see figure 2.6.b). Once a certain critical angle θ is obtained, there is a nucleation of a 180 degree domain wall. Then the switching occurs by domain wall motion. This more complex switching path is related to the one we obtain with our own micromagnetic simulations and that is detailed in the corresponding chapter of this manuscript. This work from You does not focus specifically on understanding the free layer dynamics therefore a more complete study is necessary. In this manuscript we focus on the size dependence of the switching path and compare each reversal steps with appropriates models.

2.2.2 Minimum energy reversal path

Introduction to the nudged elastic bands method

The simulations of the switching path that we presented so far relied on solving the LLGS equation. Another method called the Nudged Elastic Bands method (NEB) [52] can give the switching path in the thermal regime, namely when the switching is a rare event. The free layer is simulated as a grid of magnetic moments, just like in the LLGS equation based method. The idea is to fix the initial and the final states, then an initial path is assumed between those states. This initial path is then described by a finite number of configurations of the magnetization M_i linked together by springs. The minimum energy reversal path is obtained if each M_i is connected by a minimum energy transition, in other words if the gradient of the potential U_{tot} always leads from M_i to M_{i+1}. To obtain the minimum energy reversal path from

the initial path an iterative scheme can be used, the sum of all the configurations being relaxed towards a lower energy.

Once the minimum energy path is obtained, it is assumed to be the path that the magnetization is the most likely to follow during a reversal. Because of the thermal fluctuations the actual switching path is of course slightly deviated from this minimum energy path. This method is only valid in the thermal regime where the switching is a rare event. For instance it is appropriate to study a spontaneous switching due to thermal fluctuations and with no STT applied.

Older results for in plane systems

Earlier uses of this method are presented in references [38] and [36]. For these two papers the considered systems are in-plane devices. In the first reference the obtained switching path is domain wall based for the thinner geometry considered (200x200x10 nm) and vortex based for the thicker one (200x200x50 nm). In the second paper it is shown that the switching path depends on the strength of the applied external field. The stronger is this field and the more inhomogeneous is the minimum energy path.

Recent studies on out-of-plane systems

The NEB method has been applied in out-of-plane systems more recently, for instance in reference [85]. In this work Sampaio et al study a disk of 32 nm diameter and a thickness of 1 nm, with material parameters close to ours. The main focus of their work is on the effect of the DMI on the switching performances, but they also details the minimum energy path. For all DMI values (from 0 to large), this path includes a domain wall within the system. Concerning the impact of DMI on the switching, it is greatly detrimental. Indeed the DMI both decreases the thermal stability factor Δ_T and increases the critical switching voltage V_c.

In reference [24] the thermal stability of out-of-plane system is studied. The importance of carefully selecting the Arrhenius prefactor is discussed. The minimum energy path is a domain wall based reversal.

Discussion

The NEB method, as we already stated, computes a minimum energy switching path that the magnetization can follow under thermal fluctuations. The STT and the damping terms are not included in this picture. Therefore if too much energy is brought to the system through STT, the magnetization is more likely to stray away this path. For this reason the switching paths obtained from solving the LLGS equation in the ballistic regime can be different from the one obtained from the NEB method. Conversely, if we could perform Langevin dynamics (namely solving the LLGS equation with a thermal field included) for a small excitation and a very long time scale, we should recover the minimum energy switching path predicted by NEB. Such simulations are hard in practice because of the computation time necessary for Langevin dynamics.

However for both methods, when the system is similar to our devices both in term of geometry and of material parameters (reference [118] for LLGS and [85] for NEB), the predicted switching path is domain wall based. This highlight the importance of understanding the domain wall nucleation and domain wall motion to elucidate the dynamics in STTMRAM free layers.

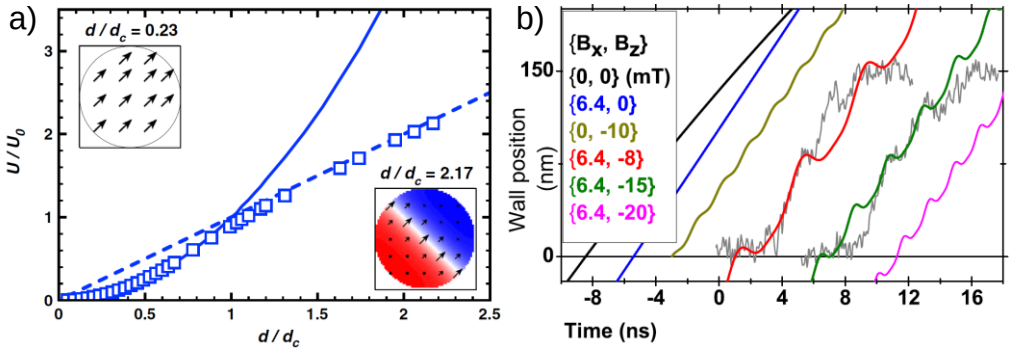

FIGURE 2.7: a) From reference [17]: energy barrier in the macrospin (straight line) or domain wall (dotted line) configurations versus aspect ratio of the considered disk. This is predicted by energy considerations for a perpendicularly magnetized system. The squares correspond to the result from micromagnetic simulations. b) From reference [30]: comparison between a time resolved pulsed induced reversal (gray lines) and the (q, ϕ) model computed for different applied fields in a stripe geometry.

2.3 Modelling the domain wall based reversal

2.3.1 Predicting the critical size for domain wall based reversal

Micromagnetic simulations predict that domain walls are generally involved in the switching path of a perpendicularly magnetized STTMRAM free layer. Only if the considered free layer is sufficiently small (typically 20 nm), then the magnetization is expected to remain homogeneous because of the exchange energy. It exists therefore a critical diameter for which domain wall based reversal starts to become more energy efficient than the fully coherent reversal.

The prediction of such a diameter is done by Chavez-O'Flynn et al in reference [17]. It is based on energy considerations: the energies of the system when a domain wall is placed at the center of the disk and when the magnetization is coherently in-plane are compared. The diameter dependences of these two energy barriers are compared in figure 2.7.a, taken from reference [17]. In our section 3.2.2 of the chapter on micromagnetic simulations we apply their critical diameter formula and proposed an improved version of it that is compared with the simulated result (see figure 3.9).

In reference [17], the influence of the external field is then studied using a NEB simulation. The dynamics of the domain wall isn't discussed.

2.3.2 Domain wall dynamics within the free layer

The domain wall dynamics in a simple geometry (namely an infinite stripe or an infinite nanowire) have been well predicted by the so called (q, ϕ) model, or 1D model. Early calculations of such a model can be found in reference [91] while the STT is considered in the work of Thiaville et al for instance [102, 103]. The derivation of the (q, ϕ) model in our geometry and with our parameters will be the focus of the chapter 4 of this manuscript. Therefore the basic calculations of this model are not presented in this state of the art. In a nutshell the (q, ϕ) model within a stripe predicts that the domain walls has a drift velocity proportional to the current. On

top of this drift, oscillations of the domain wall positions are predicted with a frequency and amplitude depending on the total field seen by the domain wall (Walker oscillations). We now focus directly on the existing comparison between free layer dynamics and domain wall dynamics predicted by the (q, ϕ) model.

In reference [30], Devolder et al performed time-resolved electrical measurements of the reversal. This technique, detailed later in our state of the art, gives a direct signature of the free layer switching path through the spatial average value of $m_z(t)$. In this study, such time traces are compared with the predicted domain wall dynamics in figure 2.7.b. The oscillations predicted by the model are somehow found in the time-resolved reversal signatures. The (q, ϕ) model has been used in other works such as reference [22] to predict the influence of STT on the domain wall depinning or nucleation in PMA free layers.

The 1D model as existing in literature at the beginning of this PhD is not sufficient to account for the dynamics observed experimentally, or even for the one predicted by micromagnetic simulations (are we shall prove in this manuscript). There is a need for an improved domain wall dynamics model in STTMRAM free layers. In particular the approximation made in the existing models that consider the finite geometry of a device as an infinite stripe needs to be better evaluated.

2.3.3 Modelling the domain wall nucleation

We have seen the existing models for predicting the critical diameter for domain wall-based reversal and for predicting the domain wall dynamics. Another important effect to be studied for understanding domain wall-based reversals is the domain wall nucleation. The nucleation is a long standing issue in magnetic bodies [94, 1], we present here more recent theoretical works on the nucleation of domain walls in an STTMRAM PMA free layer.

In the already discussed reference [118], the nucleation predicted by micromagnetic simulations is occurring from a coherent state that reached a certain critical θ angle after amplification of a quasi-coherent precession. The nucleation is changing the magnetization all over the free layer, such that it is going back up in some regions and all the way down in other regions, creating a 180 degree domain wall. In reference [77] and [110] Munira and Visscher give a possible origin for such a nucleation mechanism. They prove that beyond a certain θ angle for the coherent precession (which corresponds to $m_{z,\,c} \approx 0.875$ with their parameters), there exists a non-uniform perturbation that grows exponentially creating a domain wall. In their work they predict that such a non-uniform perturbation occurs spontaneously during the precessionnal switching, they call this perturbation the magnetostatic instability.

This means that the nucleation is a global process similarly to what was reported in micromagnetic simulations in reference [118]: the magnetization is changing everywhere within the system during the nucleation (see figure 3.6 for the same result obtained in our simulations). Therefore the domain wall is nucleated **near** the edges but not **from** the edges. Indeed during the nucleation the mean m_z value across the disk cannot change abruptly (it is only amplified by STT), such that the reversed domain is smaller than the non-reversed domain after nucleation around $m_{z,\,c} \approx 0.875$, leaving a domain wall near the edges. Concerning the impossibility of nucleating a domain wall from the edges, in reference [110] Visscher et al confirm it by being unsuccessful in forcing the reversal from such a nucleation.

The nucleation is a global process, bound to happen once the system reaches a certain critical angle after a coherent precession if the disk diameter is sufficiently

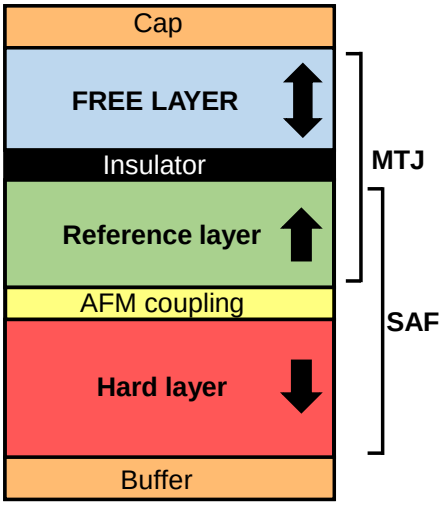

FIGURE 2.8: Typical design for a perpendicularly magnetized STTMRAM stack. Such a stack is grown from bottom to top, it is called a bottom-pinned design. Each of the layers can be composed of several sub-layers as described in the main text. The Magnetic Tunnel Junction (MTJ) and Synthetic AntiFerromagnet (SAF) are shown.

large. This critical angle is not predicted. In this manuscript we shall perform micromagnetic simulations to recover the switching path described in reference [118]. Concerning the nucleation we check that it is indeed a global process with a nucleation near the edges as predicted by the magnetostatic instability approach. We do not propose a different model for the nucleation than the one of Munira and Visscher.

2.4 Perpendicularly magnetized STTMRAM stack

2.4.1 Overall stack design

Early STTMRAM devices were magnetized in plane through shape anisotropy, until the emergence of PMA MTJs in 2010 [50, 116] which allow for the out-of-plane geometry to exist. Early in plane devices are described for instance in reference [79]. A summary of the existing designs can also be found in the review of Khvalkovskiy et al on STTMRAMs [55] as of 2013. In this review the performances of the in-plane and of the out-of-plane geometries are compared which highlights the advantages of having the latter. It permits a better scaling down of the devices diameter as well as a larger anisotropy and an easier to switch free layer [55, 19, 41].

In this section we discuss the typical perpendicularly magnetized STTMRAM stacks as shown in figure 2.8. The devices we performed our measurement on are based on a similar design. The exact composition (material and thickness) of the stack used for our own devices is shown in the chapter 5 figure 5.1. The basic components of the STTMRAM stack is the MTJ, namely the free layer, the reference layer and the insulator separating them (figure 2.8). The reference layer is coupled antiferromagnetically to another magnetic layer called the hard layer. Such a reference system is called a Synthetic AntiFerromagnet (SAF) and limits the stray field created by the reference system onto the free layer. We now detail the state of the art for the free layer and the reference system before discussing the scaling and the device performances.

2.4.2 The magnetic tunnel junction design

The study of Ikeda et al in reference [50] was a breakthrough for the development of out-of-plane MTJs. In this work a Ta/CoFeB/MgO/CoFeB stack is reported to have 120% TMR, low damping, high thermal stability and low switching current. Following this work CoFeB/MgO MTJs became the standard approach. The perpendicular anisotropy (PMA) present in such a stack comes from the CoFeB/MgO interface [68]. The tantalum capping the CoFeB layer is suggested to absorb the boron [115, 76], which is also necessary to obtain PMA and a high TMR . Therefore the exact composition of the CoFeB layer needed to optimize PMA has been extensively studied (e.g percentage of boron).

In modern designs the free layer can be more complex than a single CoFeB layer capped by tantalum. The dual-MgO free layer which consists in a MgO/CoFeB/Ta/CoFeB/MgO stack has been proposed in reference [88] for higher PMA. In such a design there are two CoFeB/MgO interfaces creating anisotropy. The tantalum is necessary to ensure that the crystallization of CoFeB happens correctly during the annealing of the stack. Indeed since the crystallisation fronts coming the the bottom MgO/CoFeB interface and from the top CoFeB/MgO interface have to meet somewhere near the midst of the free layer, any difference in the orientation of their texture results in an (undesired) grain boundary at the midst of the free layer [32]. Such a situation would be extremely detrimental to both the anisotropy of the free layer and to the transport properties of the MTJ. A tungsten layer can play the same role as the tantalum one. The dual MgO free layer design is used in the devices studied during this PhD (see figure 5.1 for the exact stack). It must be checked that such a free layer behaves indeed as a single magnetic layer, otherwise all our modelling of the dynamics of the free layer is no longer valid since it assumes a 2D system. This assumption will be checked during our devices characterization.

More complex free layer designs have been proposed in the out-of-plane geometry. PMA as been reported in Co/Pt, Co/Pd or Co/Ni multilayer [114]. The origin of anisotropy in such a Co based multilayer is discussed for instance in reference [53]. The Co/X multilayer have the interest of being easily tunable by changing the element, the thickness or the number of layers, giving access to different M_s or H_k values. However all these systems are fcc (111) crystals (i.e. with planes of hexagonal symmetry), hence they can not be grown epitaxially on/under the MgO surface which has cubic symmetry. This absence of epitaxy prevents coherent tunnelling of the electron Bloch states, and therefore the TMR cannot be as large as when CoFeB is used. These multilayers cannot alone compete with CoFeB. But it is possible to include Co/X multilayer with CoFeB in what is then called an hybrid free layer [119, 69]. This idea results in free layer of too great volume and damping compared to the pure CoFeB case, such hybrid multilayer however find much use in the reference system.

2.4.3 The reference system design

The reference layer is based on CoFeB that is coupled ferromagnetically to a harder layer (i.e a magnetic layer with a stronger perpendicular anisotropy). Having CoFeB at the interface with MgO is necessary for high TMR and to polarize the electrical current flowing through it by exchange of angular moments (spin transfer torque effect from the layer to the current). This CoFeB layer is therefore called the polarizing layer. This also ensures a symmetrical MTJ which was assumed in our transport models of the first chapter. The ferromagnetic coupling to a harder layer ensures

that the magnetization of the polarizing layer remains perfectly out of plane. This is important both to keep the polarized current vector in the right direction, but also to avoid a loss of TMR because of an initial tilt of the reference layer. The ferromagnetic coupling can be done for instance through tungsten (3-4 Å) to a cobalt layer, the reference layer then reads CoFeB/W/Co.

The reference layer exerts a stray field on the free layer. This impacts its switching performances since the AP state is now favoured compared to the P state. Both switching are no longer equivalent which is detrimental for applications. To suppress this stray field a possible solution is to add an additional magnetic layer below the reference system, with opposite magnetization direction. Such a layer called the hard layer is coupled antiferromagnetically to the reference layer forming a synthetic antiferromagnet (SAF). This ensures that the stray field compensates at the free layer position and also strengthen the pinning of the reference layer through the coupling.

Hard layer based on Co/X (Ni, Pt, Pd) multilayer have been proposed with a AFM coupling through ruthenium [15, 14, 25]. The multilayer structure has the tunability of M_s and H_k necessary for stray fields compensation and a high coercive field for pinning. The inter-layer exchange coupling that is used in the reference layer and in the SAF have its origin discussed in reference [10]. This effect is described in term of quantum interferences due to confinement in ultrathin layers. It is predicted in this study and verified experimentally that depending on the thickness of the spacer (whether tungsten or ruthenium) the coupling strength and sign (FM or AFM) varies at the scale of the angstrom. This allows once again a good tunability of the SAF by varying the spacer thickness.

2.4.4 Scaling of patterned devices

The stack is patterned to obtain devices of diameter as low as 11 nm around 2016. The etching damages the performances of the device compared to the full stack because of damages at the edges of the pillar [107]. The TMR is reduced, the anisotropy and the damping of the free layer can also be impacted by etching.

At the beginning of this PhD, the typical values for PMA-STTMRAM devices with dual-MgO free layer were the following [88, 107, 80, 65, 100, 33]:

i) A TMR going between 150 % and 200 % at device level, up to 250 % at stack level.

ii) A thermal stability factor Δ_T around 50 to 100, going down with device diameter following equation 2.4.

iii) A area-resistance product of about 5 to 20 $\Omega.\mu m^2$, in the parallel state.

iv) Diameters scaling down to 11 nm [80]. Typical diameters studied between 20 and 50 nm.

2.5 Direct measurement of the reversal

Here we report on two experimental methods which allow a measurement of the switching path.

2.5.1 Scanning transmission x-ray microscopy

The STT induced switching in a magnetic thin film can be observed using the x-ray magnetic circular dichroism effect (XMCD). The photoabsorption of circularly polarized light by a magnetic layer depends on the spin density of the unoccupied bands [89]. Therefore by sending left and right circularly polarized light onto a magnetic

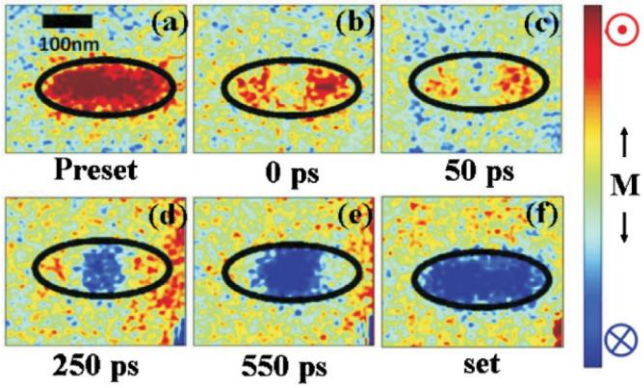

FIGURE 2.9: From reference [6]: magnetic configuration of a Co/Ni multilayer-based free layer during its reversal by STT. The free layer as an ellipse of 300x100 nm^2. The images are obtained by XMCD by averaging over numerous pulses. Between the preset and the 0 ps time, an incubation regime occurs that is not shown here.

film, we can obtain a contrast which accounts for the magnetization direction of the absorbing layer.

This method commonly used in thin film has also been used in a patterned free layer by Bernstein et al in reference [6]. Their study intends to probe the STT induced switching in the precessional regime, namely at high voltage and short switching time. Such an experiment necessitates a good temporal resolution, the typical time scale in the precessional regime being given by $\frac{1}{\gamma_0 H_{k,\,\mathrm{eff}}^{\mathrm{disk}}}$ following the macrospin assumption. A good spatial resolution is also necessary given the STTMRAM devices typical diameters, this can be obtain only with x-ray because of the diffraction limit. Finally the x-ray are able to fit into the absorption edge to ensure a strong signal. For these reasons, Bernstein et al performed their XMCD measurement of the switching path at a synchrotron light source.

Additionally to this source limitation, the stack to be measured must be adapted to the XMCD method. The free layer in reference [6] is a Co/Ni multilayer structure with strong PMA. The signal comes from the absorption of the x-ray by the nickel of the free layer. The light polarization is chosen such that the contrast gives the out-of-plane component of the magnetization. The rest of the system is also modified for x-ray transparency: there is no tunnel barrier, the reference and free layers are separated by copper. Therefore the measured sample is not a MTJ, nor it is a typical CoFeB free layer.

The obtained temporal resolution by Bernstein et al is 70 ps which is satisfying compared to the typical precessional regime time. The spatial resolution is 25 nm, which limits their study to large devices. The measurement is done only for an elliptical device of 300x100 nm^2. The dynamics in the smaller devices that are targeted for memory applications cannot be probed by this method.

The final limitation of this measurement is perhaps the most critical one: the inability of the stroboscopic techniques to perform single-shot time-resolved measurements. Indeed, to construct a time-resolved curve, the signal must be acquired at least as many times as the number points that is desired. Besides to obtain a sufficient signal to noise ratio the signal must also be averaged over numerous pulses. Therefore the obtained image shown in figure 2.9 is the average over numerous switching events. This is critical because as will be shown in the next subsection, the reversal is stochastic. The stochasticity is necessarily lost over the average in this XMCD measurement.

The results of their measurements are shown in figure 2.9. The switching is first described by an incubation period during which no domain is nucleated over the full sample. During this incubation period non-uniformities of the magnetization are still observed in the free layer. After this stochastic incubation time, a domain is

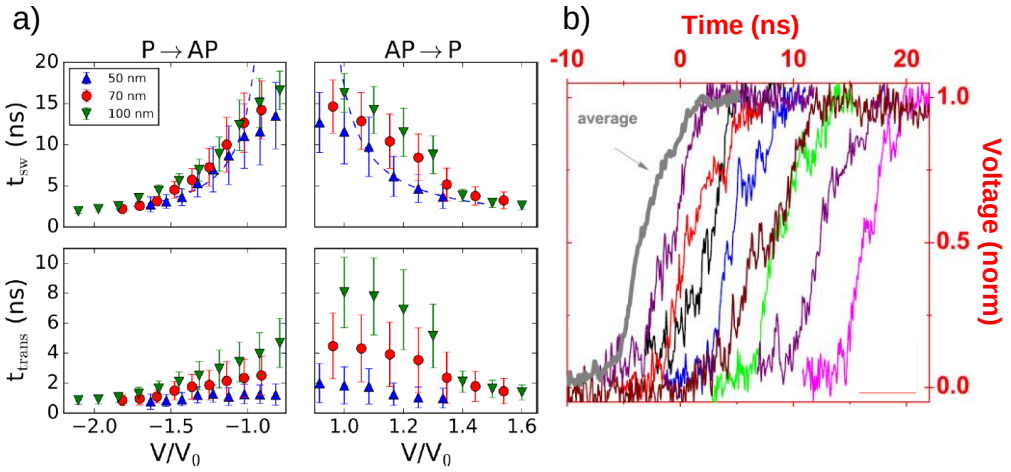

FIGURE 2.10: a) From reference [44]: voltage and size dependence of the mean transition and the mean switching times. Both times are extracted from time-resolved measurements performed on standard PMA-MTJ based STTMRAM devices. b) From reference [30]: single shots of the time-resolved measurements performed on similar devices. The devices are ellipse of 75x150 nm^2. The grey line corresponds to the average over numerous events.

nucleated near the edges around the center of the elliptical free layer. The domain wall then propagates at around 100 $m.s^{-1}$ until it reaches the edges and annihilates.

Bernstein et al finally compare the observed dynamics with micromagnetic simulations of the reversal. The qualitative agreement is good since the simulations predict the incubation time with a non-uniformity, the nucleation at the same position and the domain wall propagation with a similar velocity.

This paper, despite the numerous limitations of the XMCD method that we detailed, present several key results. i) It confirms that at large sizes the reversal is not coherent and that domain walls are expected. ii) It shows that the incubation time is still present even in the precessional regime where a strong voltage is applied. iii) It shows that stochastic non-uniformities of the magnetization are expected during this incubation time.

However the fine dynamics of the free layer is still unexplored, because of the spatial and time resolutions, but also because of the averaging over numerous reversal events. There is a need for a method able to probe a single shot reversal with a good temporal resolution, for devices with diameters more relevant for applications. This shall be possible in time-resolved electrical measurements.

2.5.2 Time-resolved electrical measurement

The principle of time-resolved electrical measurements (called "time-resolved measurements" in this manuscript) is simple: a voltage pulse is applied to the device to reverse its magnetization through STT and the conductance is recorded using a fast oscilloscope while the reversal happens. The obtained conductance is related to the mean value over space of the out-of-plane component of the magnetization in the case of an out-of-plane geometry (equation 1.22), therefore this method gives some information on the free layer dynamics and the switching path.

This method has several advantages compared to the XMCD. i) The switching can be studied in devices that are not optimized specifically for this measurement. ii) There is no spatial resolution limit. But on the smaller devices the signal to noise

ratio deteriorates. iii) A single switching event can be extracted, allowing a study of the stochasticity of the reversal.

The time-resolved measurements have also several disadvantages. i) For smaller devices the resistance is higher which reduces the signal to noise ratio and makes the reversal harder to study. This problem is reduced by a higher TMR and by the use of high gain low noise amplifiers. ii) The main issue is that the conductance is related to the mean value of m_z over the full free layer, written $\langle m_z \rangle$. Because of this it is not trivial to identify the switching path from time-resolved measurements, as an infinity of different magnetic configurations can lead to the same $\langle m_z \rangle$ (for instance a domain wall in the center of the disk and magnetization uniformly in plane both give $\langle m_z \rangle = 0$). Assumptions must be made to deduce the switching path from such a measurement compared to the more direct measurement made in XMCD.

Time-resolved measurement have been used early in STTMRAM developments, for instance in reference [59]. In this work Koch et al show how from time-resolved traces of the reversal one can extract a switching time. This switching time is then compared to the macrospin model in both regimes (precessional and thermal). This older study concerns in plane devices and does not focus on the switching path, hence we would rather detail two more recent studies performed on modern PMA-MTJ based STTMRAM devices.

The first of these studies is the work of Hahn et al in reference [44]. Their samples are standard CoFeB/MgO/SAF PMA-STTMRAM stacks similar to the one that we described in the previous section. The stacks are patterned into devices of 50, 75 or 100 nm diameter. The reversal by a voltage pulse is time-resolved by an oscilloscope giving a 50 ps resolution. The voltage applied as well as the device size vary. Here are the main results from this study: i) A smooth switching is observed for the 50 nm device, while intermediates states (conductance plateaus) can be observed for the larger devices at low voltage. These intermediate states are indicative of non-uniform magnetization states (they cannot be explained within the macrospin assumption). Hahn et al suggest that the non-uniformity is due to the non-homogeneous stray field coming from the SAF into the free layer (for a recent study of the stray field profile, see [29]). ii) The switching traces are characterized by two times: the switching time and the transition time. The transition time is related to magnetization dynamics while the switching time includes both magnetization dynamics and thermal activation (i.e the incubation time). The voltage and size dependence of these two times is shown in figure 2.10.a. iii) The transition time size dependence is compared to the macrospin model and the domain wall model predictions. They conclude that at low voltages only a domain wall based reversal can qualitatively explain the large observed dependence, while at higher voltage the weaker dependence on size could be explained within the macrospin picture. They thus emit the possibility for the switching path to depend on voltage. iv) Finally they use the formula of reference [17] for the critical diameter for macrospin versus domain wall-based reversal, obtaining a critical diameter close to 50 nm and that could therefore explain the size dependence of their measured dynamics. Hahn et al conclude their work on the importance of having more sophisticated models for the switching path.

The second study was performed by Devolder et al before my arrival in their team [30]. The stacks are similar to the one from the first study, the devices are this time elliptical shaped with 75x150 nm^2 dimensions. In contrast to Hahn et al who studied the response to a voltage pulse and thus mainly the precessional regime, Devolder et al. study the response to a slowly increasing voltage ramp, i.e. mainly the thermal regime. The main findings are the following: i) The reversal occurs at

voltages matching well the macrospin critical switching voltage V_c. ii) The reversal presents oscillations of the conductance and plateaus, which are assumed to be the signature of a domain wall based reversal. iii) This assumed domain wall based reversal is compared to the existing domain wall models, namely the (q, ϕ) model within a stripe. This comparison give a reasonable qualitative agreement since oscillations are indeed predicted, but the fitting can only be done by keeping an applied field as a free parameter and the domain wall model cannot explain the stochasticity observed in the measurements (figure 2.10.b and 2.7.b). Finally this paper discuss back-hopping, a more complex dynamical effect that is explained by failures of the reference layer. This study highlights the importance of having a better understanding of the domain wall dynamics within a STTMRAM free layer.

2.6 Objectives of this PhD

Across this state of the art, we have shown that two different switching paths are assumed to explain the various measurements done on perpendicularly magnetized STTMRAM devices: either coherent or domain wall based. In literature little work focus specifically on the study of the switching path, because the key quantities for memory applications (V_c, t_{sw}, Δ_T) monopolize most of the attention. In the field very close from application that are the STTMRAMs, we propose to answer a more fundamental question: how does the magnetization switch depending on size and voltage ? As we have seen, answering this question is of great importance because the models used to predict the devices performances must make an assumption on the switching path.

To answer this question we shall use methods that have already been presented in this state of the art and improve them. We perform micromagnetic simulations of the reversal while varying the diameter and the voltage, with a focus on the switching path. We improve the previously existing domain wall models to account for the actual geometry of a STTMRAM free layer and compare our findings with our simulations. We perform time-resolved measurements for devices with diameter ranging from 20 to 200 nm and confront our observations with our micromagnetic simulations or analytical models.

Chapter 3

Micromagnetic simulations of the reversal

In this chapter we present micromagnetic simulations of the free layer reversal. The state of the art of this method was presented in section 2.2. This model solves exactly the basic equation of magnetization dynamics for the full free layer, allowing more complex switching path than the macrospin one. An other interest of this method is the fact that thermal fluctuations are easily added. In this chapter we first discuss the method and the implementation of the micromagnetic simulations. Then we present the influence that the diameter of the free layer has on the switching path [9]. Finally we discuss the impact of temperature on the reversal.

3.1 Micromagnetic simulations methods

We implement micromagnetic simulations using the free software mumax3 [109]. This software operates on nVIDIA GPUs and the calculation was done on a dedicated cluster from the NOMADE team of the C2N. The details of the requirements, examples of code, as well as the full list of command can be found in the mumax3 website.

Let us now describe the code that we use to simulate the reversal of a STTMRAM free layer.

```
   OutputFormat = OVF2_TEXT

// grid size and geometry
sizeX := 40e-9
sizeY := 40e-9
sizeZ := 2e-9
Nx := 32
Ny := 32
Nz := 1
setgridsize(Nx, Ny, 1)
setcellsize(sizeX/Nx, sizeY/Ny, sizeZ/Nz)
setGeom(ellipse(sizeX, sizeY))

// free layer parameters
Msat = 1200e3
Ku1=1.181e6
anisU = vector (0, 0, 1)
Aex = 20e-12
alpha = 0.01
```

```
// initial magnetization state
theta:= 1
m = uniform(0, sin((theta*pi)/180), cos((theta*pi)/180))

// STT parameters
lambda = 1
Pol = 0.655
epsilonprime = 0
fixedlayer = vector(0, 0, 1)
Vext := 1.1
RAperp := 12.21e-12
jc := Vext / RAperp
J = vector(0, 0, -jc)

// managing outputs and running the simulation
autosnapshot(m, 100e-12)
tableautosave(10e-12)
run(10001e-12)
```

First the geometry is defined. The grid size is chosen such that a cell is small compared to the characteristic lengths of our system. The Bloch length is given by the exchange and the effective anisotropy for a film:

$$\Delta = \sqrt{\frac{A_{\text{ex}}}{K_{\text{eff}}^{\text{film}}}} \tag{3.1}$$

And the exchange length by the exchange and the magnetization:

$$\lambda_{\text{ex}} = \sqrt{\frac{2A_{\text{ex}}}{\mu_0 M_s^2}} \tag{3.2}$$

For instance with the material parameters presented in this code, the Bloch length is 8.5 nm and the exchange length 4.7 nm. The cell size should be smaller than Δ and λ_{ex} for the macrospin approximation to be reasonable in each single cell, therefore our cells will always be smaller than 2×2 nm^2. We assume a constant thickness of 2 nm for our free layer, therefore the simulated system is one cell thick along z.

In the second section of the code, the material parameters are entered. They mimic a dual MgO FeCoB-based free layer [21, 31], they are extracted using methods described in chapter 5. They were already used in the first chapter in table 1.1.

The magnetization is then initialized. In the given example the magnetization is uniform with a non-zero initial tilt angle to allow the start of the reversal with STT. It is possible to import arbitrary initial states in mumax3 using the .ovf matrix format as will be done in the chapter modelling the domain wall dynamics.

The STT terms entered must correspond to the torque described in the first chapter, namely equation 1.30. In mumax3, the total field torque term (Slonczewski-like and field-like torque) is described following[109]:

$$\tau_{\text{tot}} = \beta \frac{\epsilon - \alpha\epsilon'}{1+\alpha^2} \vec{m} \times (\vec{p} \times \vec{m}) - \beta \frac{\epsilon' - \alpha\epsilon}{1+\alpha^2} \vec{m} \times \vec{p} \tag{3.3}$$

$$\beta = \frac{j_z \hbar}{M_s e t_{FL}} \tag{3.4}$$

$$\epsilon = \frac{Pol\,\Lambda^2}{(\Lambda^2+1) + (\Lambda^2-1)\,\overrightarrow{m}.\overrightarrow{p}} \tag{3.5}$$

We must choose the parameters Pol, Λ, ϵ' and j_c in mumax3 such that this torque term corresponds to equation 1.30. This is achieved by taking: $\epsilon' = 0$ in order to have no field like torque; $Pol = P$ the spin polarization in mumax3 corresponds to the one we used previously; $\Lambda = 1$ to have a symmetrical torque (P to AP and AP to P equivalent); and finally $j_z = \frac{V_{ext}}{AR_\perp}$ to define the laterally uniform bias voltage, also taken constant in time.

Finally we set up the outputs, using three different formats: i) The full magnetization of the layer, which corresponds to a 3 dimensional vector for each of the cell. Mumax3 uses .ovf files to record such states. They are mainly used if all the details are necessary or to create a complex initial state, but saving it at all time uses a lot of space. ii) The magnetization over the full layer can also be saved as a snapshot. This contains the same information as the .ovf file while taking much less space but of course without giving access to the details for each cell. iii) Finally we save in a file the mean value of the three components of the magnetization over the full system. This allows to study the overall behaviour of the system: the mean value of the z component of the magnetization (written $\langle m_z \rangle(t)$) goes from 1 to -1 during the reversal of a fully out-of-plane layer, acting effectively as a reaction coordinate.

Finally we set a fixed run duration. The simulation can also be set to stop automatically when the reversal is over by tracking $\langle m_z \rangle(t)$: `RunWhile(m.Comp(3).average() > -0.94 && t < 5e-9)`.

3.2 Simulated switching path at 0 K

3.2.1 Switching path versus diameter

Here we discuss the influence of the diameter of the free layer on the switching path. The simulation are performed at zero temperature, the influence of thermal fluctuation being described later. The free layer is modelled with the parameters described in the previous section, with no external field and an initial tilt of 1 deg. To compare the reversal of two free layers of different diameters, we normalize the applied voltage using the macrospin critical switching voltage which depends on size following figure 1.5. We first compare the switching paths at $V = 1.21\ V_c$, the voltage dependence will be described later. We discuss only switching from one out-of-plane state to the other because all the torques are symmetrical, ensuring equivalent P to AP and AP to P reversals in the simulations.

Below 20 nm: macrospin reversal

For disks of 20 nm or smaller, the reversal is fully coherent (figure 3.1). The snapshots of the magnetization give an information on the in plane component through the color and on the out of plane component through the brightness (white to black corresponding therefore to a full switching). Here we can see that at all time the magnetization is uniform for all three components. To be quantitative we monitor the degree of coherence using the modulus of the mean magnetization: $||\langle \overrightarrow{m} \rangle|| = \sqrt{\langle m_x \rangle^2 + \langle m_y \rangle^2 + \langle m_z \rangle^2}$. This quantity is equal to 1 if and only if the magnetization is uniform along the disk. The value of the degree of coherence during the switching

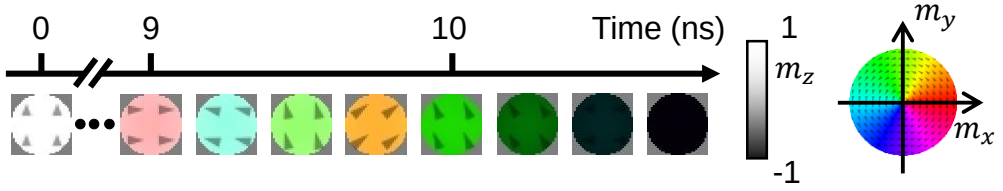

FIGURE 3.1: Snapshots of the magnetization during the switching of a 20 nm diameter disk under a voltage of $V = 1.53$ V $= 1.21\ V_c$.

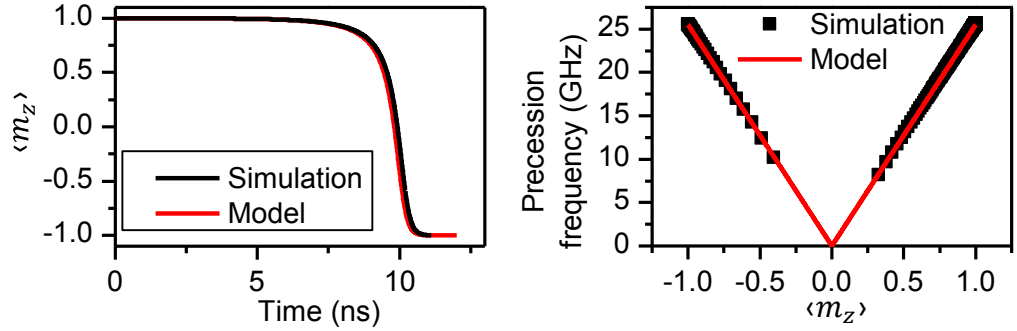

FIGURE 3.2: Comparison between micromagnetic simulations and macrospin model for the 20 nm diameter disk. $\langle m_z \rangle$ is compared to equation 3.6 on the left panel.The precession frequency extracted from the simulation is compared to equation 3.7 on the right panel.

for different sizes is shown in figure 3.8. We can observe that for the 20 nm diameter disk it remains at all time equal to 1 while for the 22 nm diameter one it drops around 10 ns.

As a reminder the macrospin dynamic is described by equations 1.39 and 1.40:

$$\dot{m_z} = \frac{\gamma_0 \alpha H_{k,\,\mathrm{eff}}^{\mathrm{disk}}}{1+\alpha^2}(m_z + h)(1 - m_z^2) \tag{3.6}$$

$$\dot{\phi_m} = \frac{\gamma_0 H_{k,\,\mathrm{eff}}^{\mathrm{disk}}}{1+\alpha^2}(m_z + \alpha^2 \frac{V}{V_c} + \frac{H_{\mathrm{ext}}}{H_{k,\,\mathrm{eff}}^{\mathrm{disk}}}) \tag{3.7}$$

The result of these equations is compared with the micromagnetic simulations for the 20 nm diameter free layer in figure 3.2. There is a perfect match both in term of $\langle m_z \rangle(t)$ dynamics and in term of precession frequency: the simulation follows the macrospin trajectory described in the first chapter (figure 1.6).

From 22 to 26 nm: growing non-uniformity

From 22 nm to 26 nm, a non-uniformity appears and grows with the diameter. This non-uniformity has the profile of a domain wall (to be discussed in the next chapter equation 4.2), but only from 28 nm onwards a 180 deg. domain wall is observed. Snapshots of the magnetization are compared for a 22 nm disk and a 28 nm disk in figure 3.3 illustrating this. The 22 nm case shows non-uniformity around 10.5 ns but no fully reversed domains.

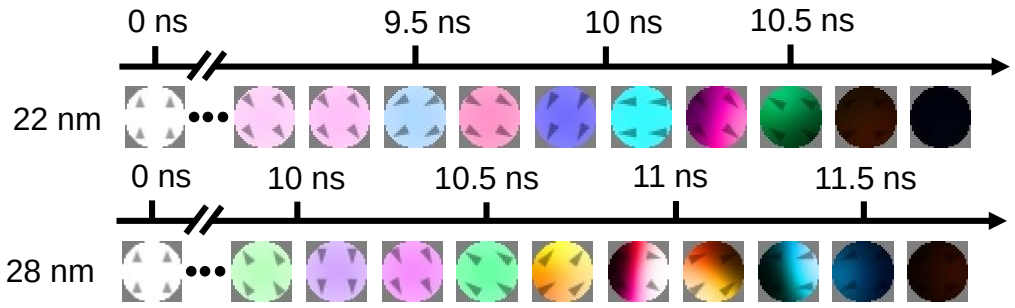

FIGURE 3.3: Snapshots of the magnetization during the switching of a 22 and a 28 nm diameter disks under a voltage of $V = 1.21\ V_c$. The color scale is the same for all simulations.

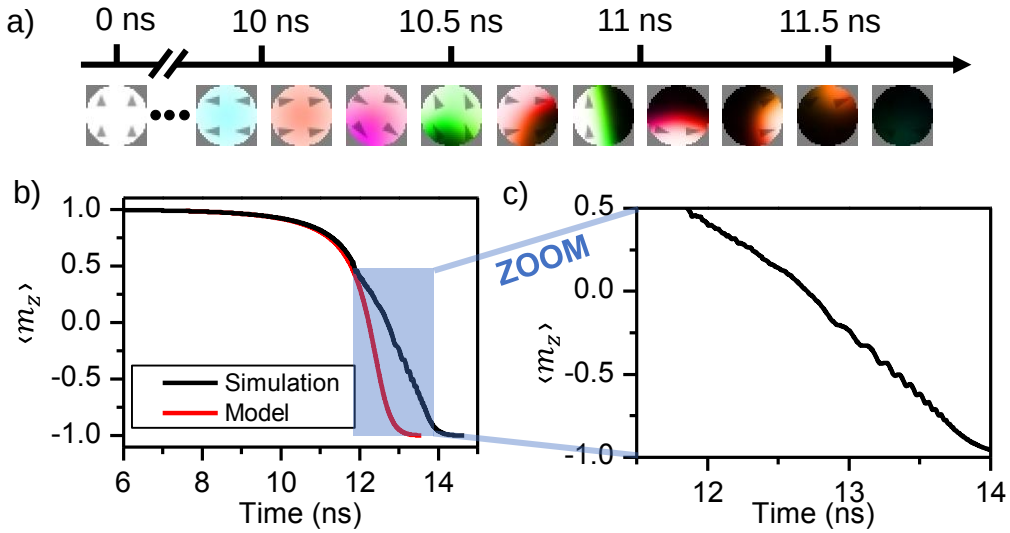

FIGURE 3.4: Domain wall based reversal. a) Snapshots of the magnetization during the switching of a 40 nm diameter disks under a voltage of $V = 1.21\ V_c$. b) Comparison between $\langle m_z \rangle$ from the simulation and from the macrospin model. The blue rectangle corresponds to the domain wall motion. c) Zoom in the domain wall motion part of the switching.

From 28 to 60 nm: single domain wall motion

We study the single domain wall based reversal observed from 28 to 60 nm by detailing the switching of the 40 nm diameter free layer.

The switching can be decomposed in two distinct phases: the magnetization remains coherent during the first 12 ns, until a domain wall is nucleated and sweeps across the disk in a non-trivial manner causing the reversal. Figure 3.4.b compares the micromagnetic simulation with the macrospin model from equation 3.6. As expected there is a good match up until the domain wall is nucleated.

However this first phase is not perfectly macrospin. During the precession the amplification of the amplitude occurs at a slightly faster rate in the center of the disk compared to the edges of the disk. This effect becomes more pronounced with increasing diameter as seen in the inset of figure 3.5. It is due to a demagnetizing effect: let us assume that the disk is fully magnetized out of plane, then on the edges of the disk the magnetization does not see the same demagnetizing field from its neighbour as in the center of the disk, because they are less of them. As a result

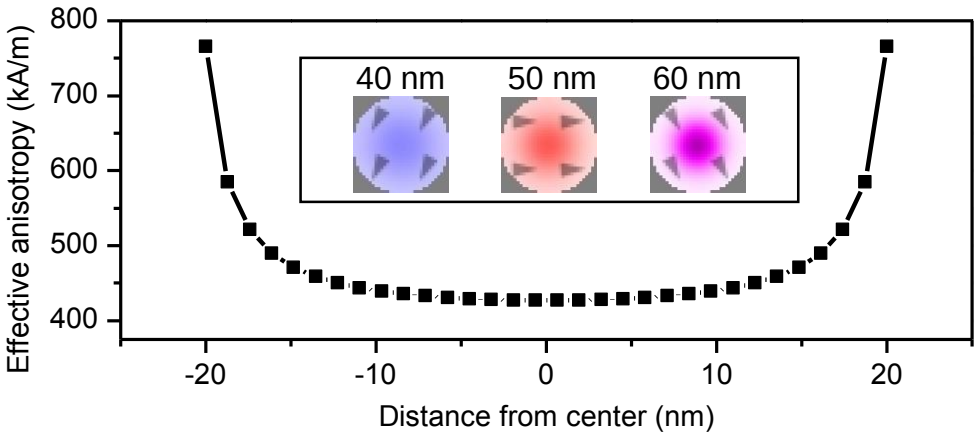

FIGURE 3.5: Effective anisotropy field versus position along the disk diameter, for a 40 nm disk. This profile was extracted using mumax3. Inset: snapshot of the magnetization right before the domain wall nucleation occurs for disks of 40, 50 and 60 nm.

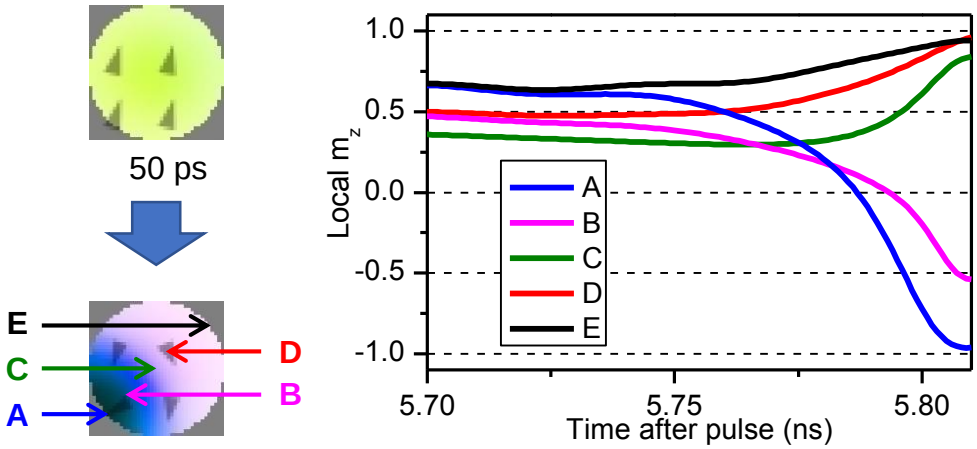

FIGURE 3.6: The nucleation. Variation of the z component of the magnetization over time during the nucleation at different positions along a disk of 40 nm diameter.

the center of the disk is more strongly demagnetized than the edges of the disk, making it easier to reverse. This translates into a stronger effective anisotropy field on the edges compared to the center in a single cell (see figure 3.5 for the 40 nm case). From the $\langle m_z \rangle$ dynamics equation of the macrospin model (equation 3.6), we see that this larger effective anisotropy field will cause a slower switching around the edges compared to the center, inducing a non-uniformity. This non-uniformity inducing effect is in competition with the exchange energy, therefore only when the disk is large enough does the non-uniformity dominates. The in plane angle remains uniform showing that the precession frequency is not as affected by this effect as the $\langle m_z \rangle$ dynamics. This non-uniformity cannot be explained within assumption of an uniform demagnetizing field that is made with the demagnetizing factors of section 1.1.6. This effect was already present in the micromagnetic simulations of reference [118] but not discussed. This effect is also related to the fundamental spin-wave eigenmode expected in the disk geometry, as seen for instance in the figure 6 of reference [78].

Once the precession angle is sufficiently large, the nucleation occurs. It creates

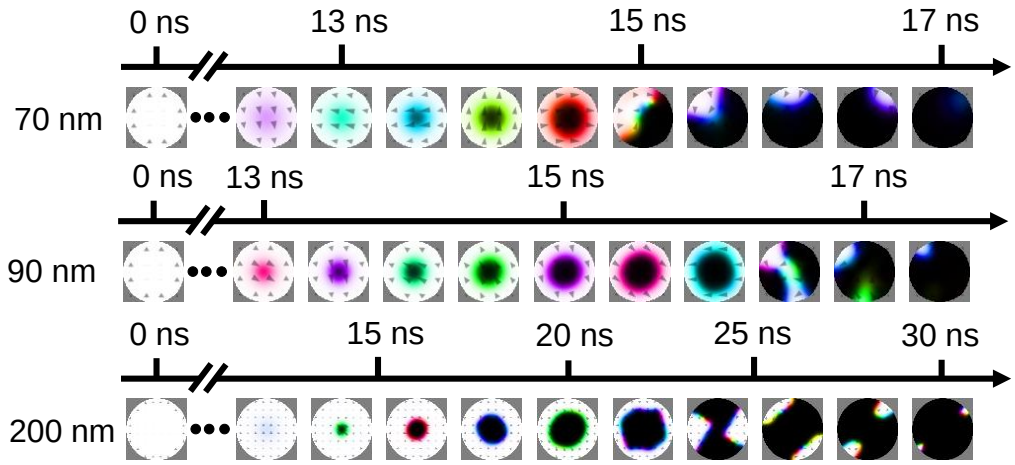

FIGURE 3.7: Snapshots of the magnetization during the switching of disks of 70, 90 and 200 diameter. Each are under a voltage corresponding to $V = 1.21\ V_c$.

a domain wall near the edges but not from the edges: the nucleation is a process changing the magnetization everywhere within the disk. This is not a domain wall profile coming unto the disk from the edges as could be assumed as a possible nucleation scenario. As seen in figure 3.6 the magnetization gets to -1 in the reversed domain while it rises back up to 1 away from it, creating a 180 deg. domain wall. It has been predicted that once we reach a certain critical angle for the precession, there exists a non-uniform perturbation within the system that can grow, causing the nucleation [77, 110] (these references are discussed in section 2.3.3 of our state of the art). In our simulation there is a non-uniformity induced by the demagnetizing field. Therefore the mechanism described in ref [77] and [110] could be responsible for the nucleation.

After the nucleation the domain wall sweeps across the free layer causing the reversal. We observe that $\langle m_z \rangle$ decays at a slower rate during the domain wall motion compared to the macrospin picture (see figure 3.4). There are oscillations of $\langle m_z \rangle$ during the second half of the reversal, which corresponds to oscillations of the domain wall position. Additionally to these position oscillations the in plane angle of the magnetization keeps oscillating, and the domain wall gyrates around the disk center. This complex domain wall motion will be the subject of the next chapter.

Above 70 nm: center domain and multiple domain walls

As we increase the diameter the radial gradient of the precession cone during the macrospin phase gets more pronounced, such that for diameters of 70 nm and larger the magnetization dips at the center creating a bubble (see figure 3.7). This central domain formation is a gradual process which induces no change in topology unlike a domain wall nucleation. Since this process is gradual it has no clear signature in the $\langle m_z \rangle(t)$ graphs as shown in figure 3.8 where the first red arrows indicates the center domain creation. But the center domain creation is noticeable in the corresponding modulus of the mean magnetization versus time plot.

Once created the domain expands in the center of the disk until it gets close enough from the edges. It then wets one or several points of the perimeter of the disk, depending on the disk diameter. Up to several domain walls are formed and

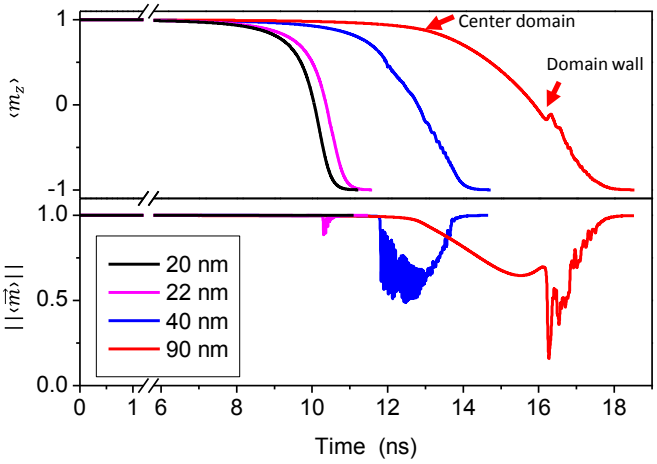

FIGURE 3.8: Comparing the different size regime. Mean value of the z component of the magnetization and of the modulus of the mean magnetization during the reversal for 4 different sizes each under a voltage of $V = 1.21\ V_c$.

will sweep across the device. The wetting induces a lot of fluctuation within the simulations. Similar to the smaller disk case the domain wall creation has a clear signature in $\langle m_z \rangle(t)$ and the domain wall motion presents the same characteristics.

We did not study free layers larger than 300 nm since the most relevant sizes for memory applications are between 100 and 20 nm.

Influence of voltage

So far we have only shown result for voltages of 1.21 V_c. The corresponding values at all sizes can be found in figure 3.10 or figure 1.5 from the first chapter. We performed the same study for voltages of 1.03 V_c and of 1.4 V_c. For those values the qualitative switching path is the same as the one we already presented for each diameters. The overall dynamics for the coherent regime, the domain wall motion, or the center domain extension are faster with increasing voltage as expected from both the macrospin model and the forthcoming domain wall models.

At zero temperature we cannot go below the macrospin critical switching voltage, but such simulations will be presented in the last section of this chapter. We did not study the reversal at higher voltages, as for applications breakdown is limiting the maximum voltage that can be applied in a real STTMRAM device. It is not clear if the switching path dependence on size that we described is still valid for voltages of several times the critical macrospin value.

3.2.2 Critical diameter for domain wall nucleation

The size study of the switching path gives access to a critical diameter for the fully coherent versus domain wall based reversal. Between 20 and 22 nm the first non-homogeneity appears, and between 26 and 28 nm the non-uniformity becomes a full 180 deg. domain wall. We call d_c the critical diameter for nucleating a full 180 deg. DW. Several expressions were proposed in the literature to predict d_c. In the minimal approach[17, 55], d_c is estimated by comparing two energies. First the energy cost of placing a domain wall along the diameter of the disk. In ref.[17], this energy is written $8\sqrt{A_{ex}K_{eff}^{disk}}R\,d$ where K_{eff}^{disk} is the effective anisotropy of the disk, R its radius and d its thickness. This expression assumes that the disk is much larger than the domain wall i.e. $2R \gg \pi\Delta$ where $\Delta = \sqrt{\frac{A_{ex}}{K_{eff}^{film}}}$. The second relevant energy is the one of the system when the magnetization is uniformly in-plane: $\pi K_{eff}^{disk} R^2 d$ which is necessary to overcome for a coherent reversal. The effective anisotropy of the

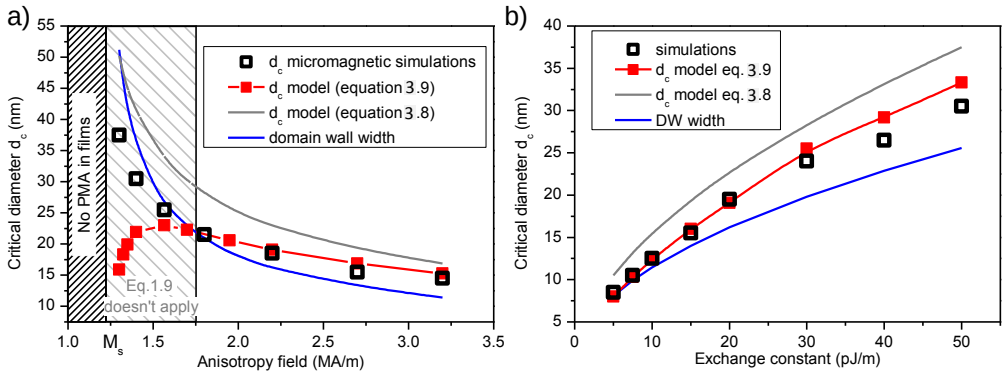

FIGURE 3.9: Critical diameter above which a 180 deg. DW is observed in the micromagnetic simulations and comparison to its analytical estimates. a) while varying anisotropy field at fixed $A_{ex} = 20$ pJ/m or b) while varying exchange stiffness at fixed $H_k = 2.2$ MA/m.

disk depends on the demagnetizing factors $N_z(R)$ and $N_x(R)$ described in the first chapter (figure 1.1). Assuming that the transition occurs when the two energies are equal, we obtain:

$$d_c \approx \frac{16}{\pi}\sqrt{\frac{A_{\text{ex}}}{K_{\text{eff}}^{\text{disk}}}} \tag{3.8}$$

Solving this equation yields a critical diameter of 33.6 nm which is larger than the domain wall width but differs substantially from 26.5 nm that we estimated from simulations.

This difference can result from one fundamental and two technical deficiencies of the minimal approach. Fundamentally, any comparison based on the energies of static configurations is bound to underestimate the energy cost of an inherently dynamical process like reversal. However in STT switching, the energy lost by damping is supposed to be compensated by STT; therefore we conjecture that we can overlook this fundamental objection. Besides, the minimal approach confuses the DW energy within a disk with that within a fictitious infinite film that would have the same effective anisotropy as the disk. Finally it neglects the dipolar energy gained when breaking the system into domains. Neglecting the domain-to-domain dipolar couping is a minute error in the ultrathin limit [49]. Conversely the imprecision in DW energy can be substantial. Indeed the demagnetizing field in thin films is essentially local within a DW [104], such that the wall energy is much more linked to the effective anisotropy of the film rather than the effective anisotropy of the disk, and therefore should be taken as $8\sqrt{A_{\text{ex}}K_{\text{eff}}^{\text{film}}}R\,d$. All together, an improved estimate of d_c is:

$$d_c \approx \frac{16}{\pi}\frac{\sqrt{A_{\text{ex}}K_{\text{eff}}^{\text{film}}}}{K_{\text{eff}}^{\text{disk}}} = \frac{16}{\pi}\sqrt{\frac{2A_{\text{ex}}}{\mu_0 M_s}} \times \frac{\sqrt{H_k - M_s}}{H_k - (N_z - N_x)M_s} \tag{3.9}$$

which has to be solved self-consistently because $(N_z - N_x)$ depends on R. Figure 3.9 compares equation 3.9 and equation 3.8 with the micromagnetic d_c in a relevant interval of anisotropy field and exchange stiffness. The values from micromagnetic simulations are extracted by monitoring the maximum and minimum values of the local m_z in order to identify a 180 deg. domain wall. The criterion for domain wall nucleation is chosen as $m_z(\max) - m_z(\min) \geq 1.9$. The diameters are changed by step of 1 nm giving us a ± 0.5 nm precision. The matching is satisfactory: as long as

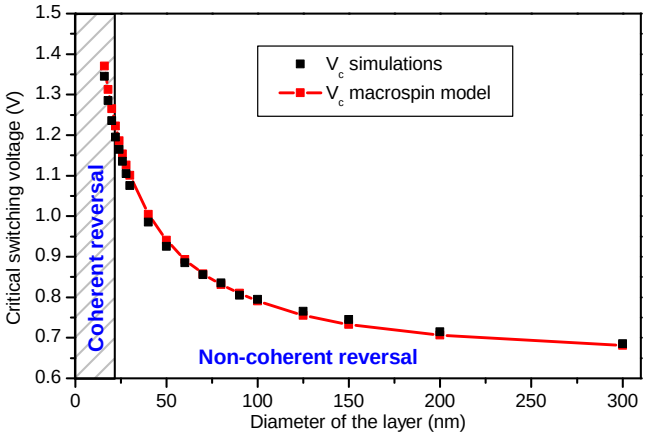

FIGURE 3.10: Critical voltages versus size. Comparison of the macrospin critical voltage and the micromagnetic switching voltage for different diameters.

the domain wall width is smaller than the disk diameter, Eq. 3.9 (red in figure 3.9) is reliable estimation of d_c extracted from simulations (black squares). Having such a good match with the simulation is a surprising result given the simplicity of this equal energy barriers approach.

3.2.3 Critical voltage from the simulations

We have shown that the macrospin model describes perfectly the coherent reversal from the micromagnetic simulations. Let us now see whether the macrospin critical voltage can account for the micromagnetic switching voltage, including for sizes that lead to non-coherent reversal. Because of our uniform initial state, a voltage stronger than V_c is a necessary condition for the reversal, but it might not be a sufficient condition. Indeed even if uniform state is unstable with finite amplitude precession, the precession amplitude could be limited by non-linearities and not lead to reversal, as observed in in-plane magnetized metallic spin-valve [56, 28], in which there is a net difference between instability and switching. We compare the V_c dependence on diameter with the actual switching voltage extracted from simulations by varying the applied voltage in figure 3.10. The macrospin and the micromagnetic switching voltage do agree for all investigated disk diameters: reaching V_c is a necessary and sufficient condition for the reversal. This approach can be extended to include an external field through the generalized stimulus: reaching $h = 1$ ensures a full reversal.

3.3 Impact of thermal fluctuations

3.3.1 Implementing thermal fluctuations in mumax3

The temperature is included by adding the following code:

```
   // thermal fluctuations parameters
SetSolver(6)
ThermSeed(1)
Temp=300

// initial run to thermalize
J = vector(0, 0, 0)
run(501e-12)
J = vector(0, 0, -jc)
```

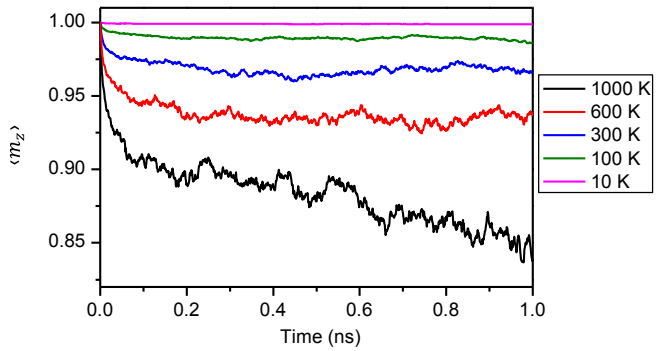

FIGURE 3.11: Thermalizing at different temperature. $\langle m_z \rangle(t)$ for a 40 nm disk, under no field or STT, with varying temperature. It is assumed that the temperature has no effect on the material parameters and that we do not reach the Curie temperature.

In the micromagnetism theory, temperature can be taken into account through a stochastic thermal field. This method is applied in mumax3. The thermal field is non-uniform, its amplitude depends on material parameters and temperature. Its direction for each cell is varying stochastically overtime following a given time step [109]:

$$\overrightarrow{B_{\text{th}}} = \overrightarrow{\eta_i} \sqrt{\frac{\alpha 2 k_B T}{\mu_0 M_s \Delta_{\text{vol}} \gamma_0 t_{\text{step}}}} \tag{3.10}$$

Where t_{step} is the time step, Δ_{vol} the cell volume and $\overrightarrow{\eta_i}$ is a random unit vector that is delta-correlated in both time and space, i.e. it changes from time step to time step and from cell to cell. With usual material parameters, at room temperature and with a time step of 1 ps, the thermal field amplitude is 22 mT. This value depends on the time step and choosing it sufficiently short is critical. To tackle this issue, we use an adaptive time step solver already implemented in mumax3 [66] and we therefore do not need to define it manually. Reference [66] discusses the validity of the adaptive time-step compared to the fixed time step method. As the stochasticity is pseudo-random the thermal seed should be changed for obtaining different sets of stochastic field for each simulations.

Additionally to adding this stochastic field, we thermalize the system in the absence of external stimuli. This is done to simulate a real STTMRAM device for which the layer is already at room temperature for a long time before the voltage is applied. The initial state for the following simulation will therefore be a thermalized system and not a system uniformly magnetized and tilted to an arbitrary angle as it was the case at 0 K. If we take a fully out of plane system and start the thermal fluctuations with no external stimuli, the mean value of the z component of the magnetization will sharply decrease until it reaches a plateau the value of which depends on the variance of the stochastic field. Such time-dependence is shown in figure 3.11 for a 40 nm disk at different temperatures. We shall first study the switching under room temperature, at which 0.5 ns is sufficient to thermalize the system as seen in figure 3.11.

In an actual STTMRAM devices the temperature is at least 300K, but there is additional Joule heating due to the current flowing through the junction. The current-induced increment of temperature depends on the device and the voltage. There is no clear consensus on the heating efficiency because a direct measurement isn't straightforward [47, 108, 64, 16]. For the sake of simplicity we will present mainly simulations at room temperature in this section, which is sufficient to give qualitative understanding of its effect on the switching.

This method for including temperature is called Langevin simulations. It is suited for cases in which the thermal activation time scale does not exceed a few μs, otherwise the simulation time is too long. For magnetic systems with longer

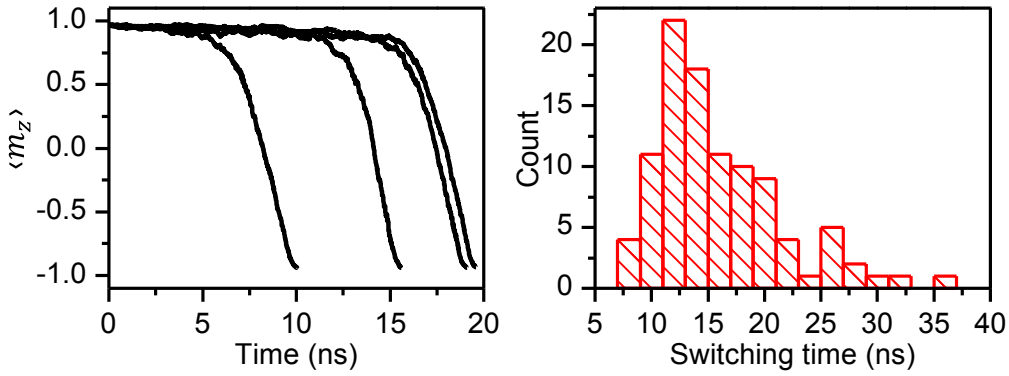

FIGURE 3.12: Example of thermally induced reversal. Left: $\langle m_z \rangle(t)$ for a 40 nm disk under $V = 0.9\ V_c$ at $T = 300\ K$. Several simulations are presented with only the thermal seed varying. Right: Corresponding histogram of the total switching time from 100 of such switching simulations.

activation delays one should consider other methods such as reaction rate theory [20], nudged elastic band method [35] or string theory [39]. In reference [23] several of those methods are compared with Langevin simulations to study the thermal stability of skyrmions, another magnetic system.

3.3.2 Qualitative impact of temperature

Temperature induces an extra delay

In figure 3.12 we simulate the reversal of a 40 nm disk at 300 K with a voltage below the macrospin critical switching voltage, while varying the thermal seed. There is a plateau of constant $\langle m_z \rangle$ with a varying duration from one run to the other before the magnetization drops and the switching occurs. This stochastic delay is called the incubation time t_{incub}. It is due to the fact that the thermal fluctuations can stochastically help or prevent the initialization of the switching. Once the precession amplitude is large enough, there is no coming back to the initial thermalized state. The right graph of figure 3.12 presents the distribution of the switching times extracted from 100 runs, showing a large standard deviation due to the incubation time distribution. This distribution depends strongly on voltage and temperature as will be discussed in the following sections. The reversal under finite temperature can therefore be described in two parts: a stochastic incubation time depending on temperature and voltage, then a transition time from the initial state to the final state which depends on the switching path. The description of the switching by two delays was proposed by Hahn in reference [44] in order to describe time-resolved electrical measurement (see our section 2.5.2).

Extracting the two delays

From the initial and the final value of $\langle m_z \rangle$ we define the initial and the final states $\langle m_z \rangle_P$ and $\langle m_z \rangle_{AP}$ (for a P to AP switching for instance). Then the incubation time is arbitrarily chosen as the time between the beginning of the voltage pulse and the moment the disk is 10 % reversed, namely:

$$\langle m_z \rangle(t_{\text{incub}}) = \langle m_z \rangle_P + 0.1(\langle m_z \rangle_{AP} - \langle m_z \rangle_P) \tag{3.11}$$

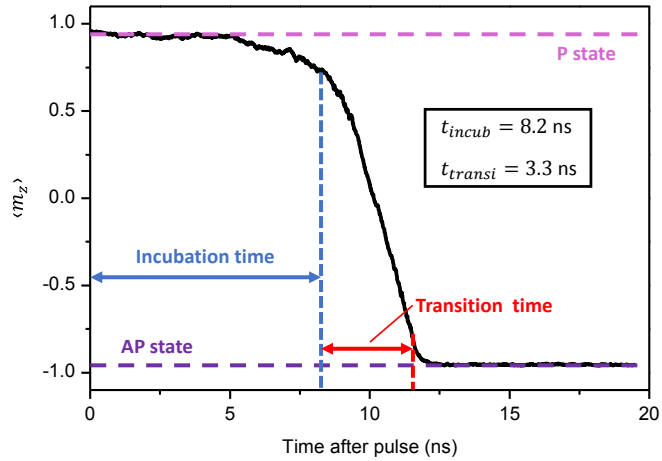

FIGURE 3.13: Defining the two delays. $\langle m_z \rangle(t)$ for a 40 nm disk under $V = 0.9\ V_c$ at $T = 300\ K$. The definitions of the delays and of the final and initial states are shown.

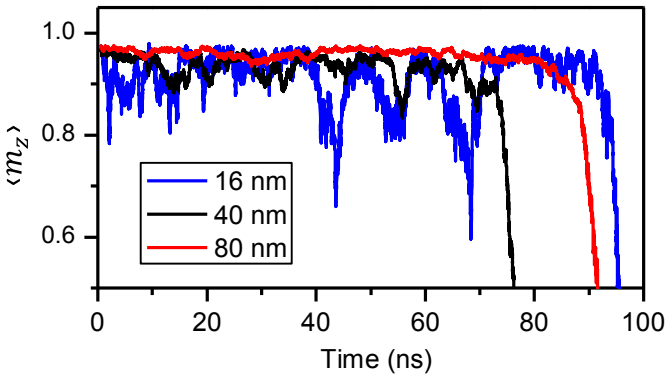

FIGURE 3.14: Size dependence of the fluctuations during the incubation period. $\langle m_z \rangle(t)$ graphs are shown for disk of 16, 40 or 80 nm diameter. The simulations where performed at respectively 1 V, 0.8 V and 1 V. For each size a reversal event with an especially long incubation time was selected in order to better highlight the fluctuations dependence.

Similarly the transition time is defined as the time needed to go from a 10 % to a 90 % reversed disk:

$$\langle m_z \rangle(t_{\text{transi}} + t_{\text{incub}}) = \langle m_z \rangle_P + 0.9(\langle m_z \rangle_{AP} - \langle m_z \rangle_P) \tag{3.12}$$

The two delays can be simply extracted using a threshold method (figure 3.13). Another extraction method that proved to be useful was the fitting of the full data set with an arbitrary function, this shall be discussed in the chapter about time-resolved measurement where two similar delays will be extracted. For this part only threshold extracted data are presented.

Dependence of the fluctuations on size

During the incubation time, the fluctuation level seen on $\langle m_z \rangle(t)$ depends on the diameter of the disk. This is observed in figure 3.14 where we performed simulations at low voltage for each diameter, inducing a long incubation period. The fluctuations of $\langle m_z \rangle(t)$ are much weaker for the 80 nm disk than for the smaller ones. The 16 nm disk presents very strong fluctuations, where the magnetization can go as low as $\langle m_z \rangle = 0.6$ and still come back up. This size dependence is due to the fact that the fluctuations are occurring independently for each cell: they are averaged over a larger number of cells in the $\langle m_z \rangle(t)$ graphs for the larger devices compared to the smaller one. This effect would be removed by simulating the different sizes with a constant number of cell.

The larger fluctuations make the extraction of the delays less precise for the smaller sizes, both in term of incubation and of transition time.

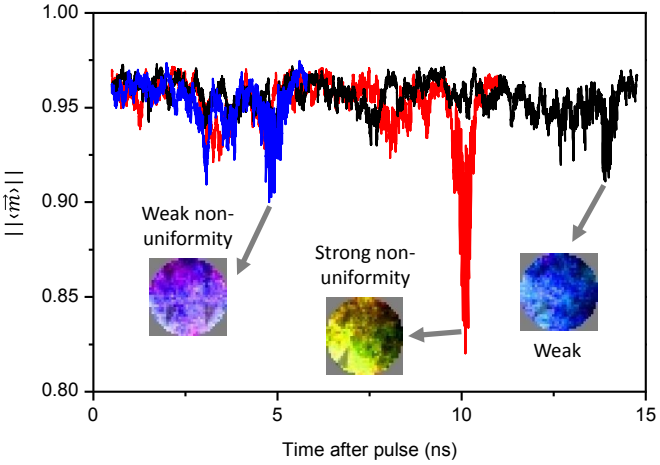

FIGURE 3.15: Thermal fluctuation within a 20 nm disk. $||\langle \vec{m} \rangle||(t)$ for a 20 nm disk under $V = 0.9\ V_c$ at $T = 300\ K$. The reversal for three different thermal seeds are shown. The curve in red with the strong non-uniformity occurred for one out of the 10 runs we simulated. All the other reversals were similar to the blue and black curves (weak non-uniformity). The snapshot are taken around the maximum of the non-uniformity.

3.3.3 Impact of temperature on the switching path

In this subsection we discuss only the impact of thermal fluctuations on the switching path, namely what happens during the transition time. We once again vary the diameter of the free layer while keeping voltage constant and a temperature of 300 K. We check if the previously described size dependence is still valid.

Temperature and coherent reversal

We simulate the reversal of 20 nm disks at 300 K and check whether or not the reversal is still coherent. Our criterion for uniformity is the modulus of the mean magnetization $||\langle \vec{m} \rangle||$. As seen in figure 3.15 it is subject to fluctuations due to temperature even during the coherent phase. Indeed during the first 10 ns of the black curve for instance while we are still within the incubation time which corresponds to a coherent state, $||\langle \vec{m} \rangle||$ is fluctuating around 0.95 instead of being constant at 1 like at 0 K. This value corresponds therefore to a disk as uniformly magnetized as possible despite thermal fluctuations. It is however clear that $||\langle \vec{m} \rangle||$ is reduced well below 0.95 for all runs, around 1 ns before the end of the reversal (each graph is plotted until the reversal is complete). Since $||\langle \vec{m} \rangle||$ goes lower than its coherent value, the reversal at 20 nm is at some point not as coherent as it is possible to be in the presence of thermal fluctuations.

It is also observed in figure 3.15 that the maximum value for the non-uniformity is stochastic, some runs (like the one in red) being less coherent than the other ones. Approximately one out of 10 runs presented a "strong non-uniformity" while most are similar to the "weak non-uniformity" cases.

The macrospin critical size got lower because of temperature. But the situation is now more complex: i) we can no longer define clearly a coherent reversal because of the fluctuations in our homogeneity criteria; ii) the maximum non-uniformity reached during the reversal is stochastic from one run to the other. We can still observe that as we decrease further down the diameter reaching a clear minimum of $||\langle \vec{m} \rangle||$ during the reversal becomes less and less likely. Consequently our discussion in the previous section about predicting the critical diameter for domain wall based switching through energy considerations is bound to overestimate the value expected in an actual STTMRAM device.

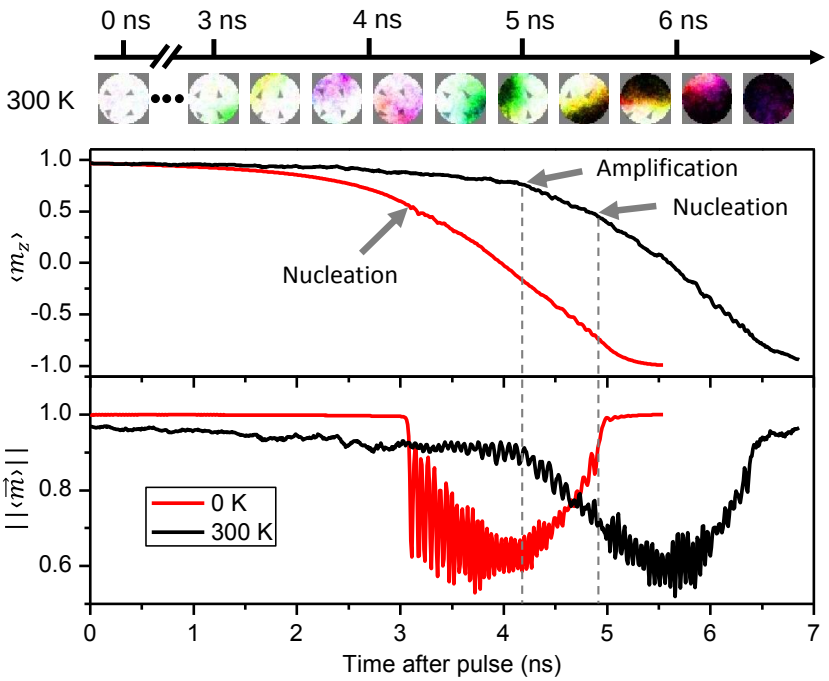

FIGURE 3.16: Thermal fluctuations impact on domain wall motion. Top: snapshots of the magnetization during the switching of a 40 nm free layer under $V = 1.21\ V_c$ at 300 K. Bottom: corresponding $\langle m_z \rangle(t)$ and $||\langle \vec{m} \rangle||(t)$ graphs and their comparison with the same simulation run at 0 K.

Temperature and domain wall based reversal

For devices between 28 and 60 nm we predicted a coherent phase followed by a domain wall motion at 0 K. Here we compare the 0 K case with the 300 K case for a 40 nm disk under a voltage of $V = 1.21\ V_c$. We performed 100 runs with different thermal seeds. Despite a large distribution of incubation time (to be discussed) the transition time distribution is very narrow and only a single switching path is observed. The median value for the transition time is 2.425 ns and its standard deviation 0.14 ns. We can therefore compare our simulation at 0 K with a single run at 300 K, which is done in figure 3.16. Apart from the incubation time at 300 K, the switching path corresponds mostly to the one previously described: amplification of an in plane precession; nucleation of a 180 degree domain wall while varying the magnetization over the full device; and finally domain wall motion presenting coupled oscillations of the domain wall position and of the in plane magnetization angle. The main difference being that at 300 K the amplified precessing part is not equally distributed across the disk, which creates an early non-homogeneity before the creation of a domain wall. This effect is illustrated in the snapshots of figure 3.16 and occurs between the "amplification" and the "nucleation" arrows. Such non-uniformities during the incubation time were already predicted in micromagnetic simulations and observed in XMCD measurement [6] (see section 2.5.1 of our state of the art).

The switching path is mostly unchanged by temperature in this regime of size at 300 K for the considered voltage values, only the amplification is done non-uniformly before nucleation.

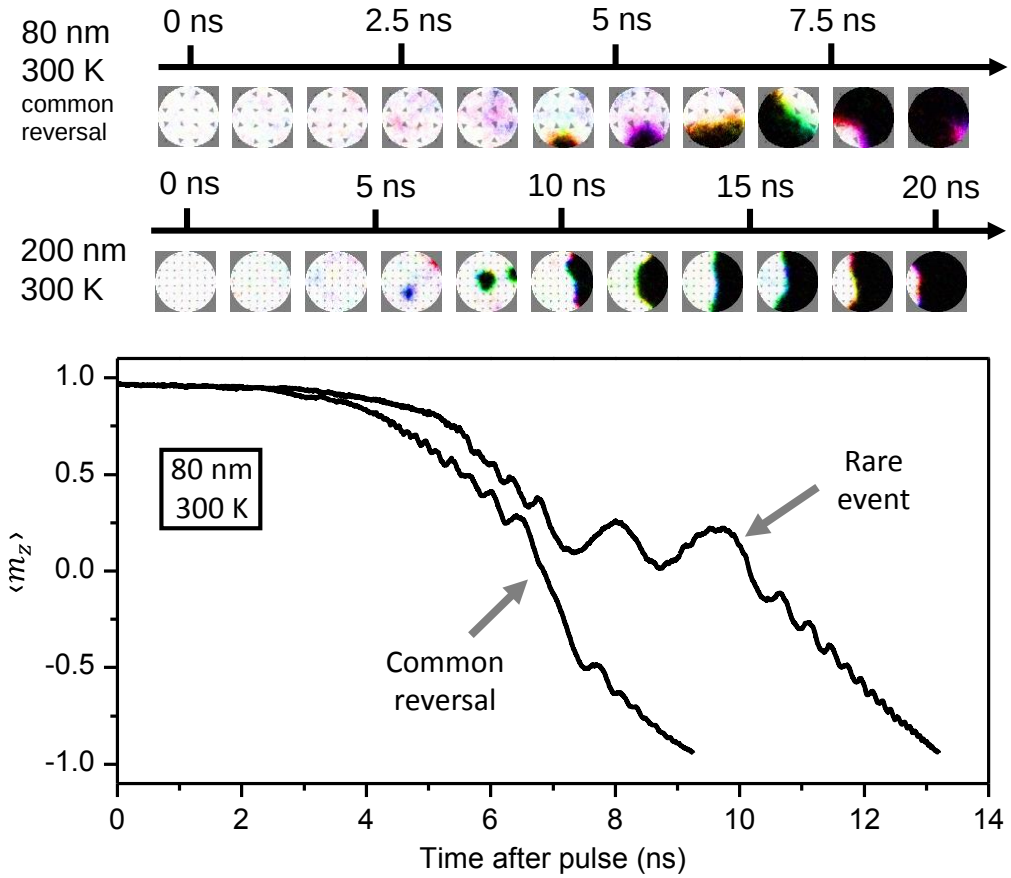

FIGURE 3.17: Thermal fluctuations impact on the center domain. Top: snapshots of the magnetization during the switching of 80 and 200 nm diameter free layers under $V = 1.21\ V_c$ at 300 K. Bottom: corresponding $\langle m_z \rangle(t)$ graph for the 80 nm case, along with a another run for the same parameters and a different thermal seed.

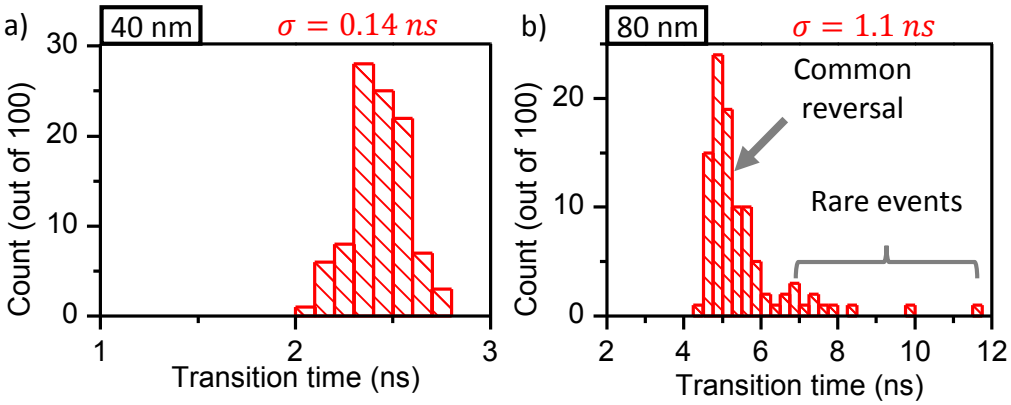

FIGURE 3.18: Transition time distribution for disks of a) 40 and b) 80 nm diameter. The standard deviation are given in red. The rare event presenting strong domain wall oscillations are highlighted.

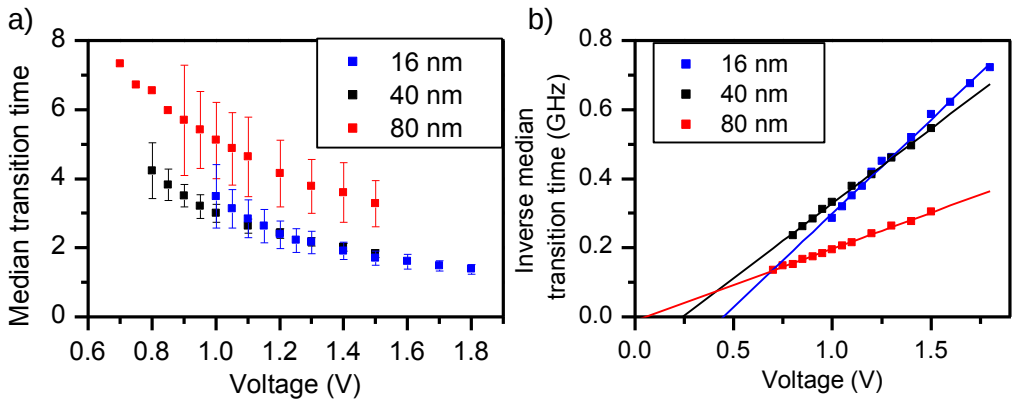

FIGURE 3.19: Voltage dependence of the transition time. a) median value for disks of 16, 40 and 80 nm diameter at 300 K, the error bar is the standard deviation. The 16 nm delay are obtained from the fitting method, while for the larger disks the threshold method was used. 100 simulations were performed for each voltage point. b) corresponding inverse median transition time versus voltage with their proportionality fit as straight lines($ax + b$).

Temperature and center domain

For disks between 70 and 300 nm at 0 K, after the amplification of the coherent precession a reversed domain appears at the center and expend until it creates a domain wall on the edges. This center domain is not as easily observed at 300 K. Indeed the thermal fluctuations break the cylindrical symmetry of the system, which has the effect of moving around the center domain. As the center domain moves it will very quickly reach the edges and create a domain wall for diameters below 100 nm, while for very large diameters it can remain far from the edges for a few ns (see snapshots of figure 3.17). As seen in the 200 nm case presented, two distinct domains are nucleated: one stays a bit at the center while the other one is quickly wetted to the edges, finally they merge creating a single domain wall.

For diameter below 100 nm, as illustrated by the 80 nm case, the domain wall is nucleated after a much shorter bubble phase at 300 K compared to the 0 K case, because of the fluctuations of the bubble position. This results in a longer domain wall motion starting from one edge all the way to the other edge, instead of starting near the center (see figure 3.7). We observe in the bottom graphs of figure 3.17 that the behaviour of the domain wall near the center of the disk ($\langle m_z \rangle \approx 0$) varies from one run to the other. In the most common reversal the domain wall seems to pass linearly through the center, while in some rarer (about 10 %) events very strong oscillations of the domain wall position are observed. This complex domain wall effect was not observed at 0 K or for the 40 nm disk, as illustrated in figure 3.18 where we can see a much more narrow distribution of the transition time for the 40 nm disk compared to the 80 nm one. This effect can be detrimental for applications (slower switching) and will be explained fully in the following chapter discussing domain wall models.

For this size regime we can conclude that the center domain becomes unstable with thermal fluctuations and is therefore only observed in the larger disks. Temperature has a clear impact on the switching path for these diameters.

3.3.4 Voltage-dependence of the transition time

Here we discuss the impact of voltage on the switching path and the transition time while thermal fluctuations are included.

At 0 K the voltage had no impact on the switching path and only accelerated the overall switching speed. This is still valid at 300 K: we varied the voltage between 0.7 and 1.8 V_c for 16, 40 and 80 nm disks and observed no change in the switching path. For the 16 nm disk the switching path described in figure 3.15 is mostly unchanged with voltage. For the 40 nm disk we still have a single, simple domain wall motion. For the 80 nm we observe the complex domain wall motion with stochastic oscillations at the center regardless of the chosen voltage within this interval.

Of course changing the voltage once again accelerates the overall dynamics. This is shown in figure 3.19.a for all three sizes. One can see that the median value for the transition time is reduced with increasing voltage, as well as its standard deviation. The standard deviation remaines low (below 1 ns) for the 40 nm disk compared to the 80 nm case even at the lower voltage we simulated. The 16 nm disk presents larger median transition times than expected from the simulations a 0 K, where the smaller was the disk and the faster was the switching. This is due to the stronger overall effect that thermal fluctuations have on the switching at small sizes compared to the larger disks (see figure 3.14). This induces longer transition time and larger standard deviation as fluctuations are still going on in the transition phase. The fact that the transition appears sometimes faster for the 40 nm disk compared to the 16 nm one is therefore an artefact coming from the constant cell size used in our simulations.

We remark that the inverse median transition time is proportional to the applied voltage (figure 3.19.b) for the three considered sizes. For the 80 nm disk the fitting is almost linear (the intercept is close to $(0,0)$). This result is not surprising given the switching path at these three sizes. For the 16 nm case, the reversal is mostly coherent. Therefore the switching time follows Sun's first law (equation 2.1) or more precisely the exact expression of equation 2.2. These expressions predicts a linear dependence (with offset voltage) of the inverse switching time on voltage for the macrospin reversal, which is indeed verified here even with thermal fluctuations. For the larger devices the issue is more complex because the switching path is composed of both a macrospin and a domain wall-based periods. In the domain wall regime, the drift velocity of the wall is proportional to the voltage (no offset voltage) in the absence of applied field (equation 4.48 to be proven next chapter). Thus the macrospin and the domain wall model both predict a linear dependence of the inverse transition time on the voltage. Note that for the 80 nm disk the intercept is closer to $(0,0)$ than in the 40 nm case, which is explained by the fact that the larger is the device and the more the domain-wall phase contributes to the total switching time. Therefore the 80 nm disk is closer from the hypothetical fully domain-wall based reversal where $(0,0)$ would be reached.

The voltage dependence of the transition time is well understood by our models of the switching path. Only the very high thermal fluctuations in smaller devices lead to the non-intuitive result of a 16 nm disk with a transition time as long as the 40 nm disk.

3.3.5 The simulated incubation time

This subsection focuses on the incubation time. We mainly discuss its dependence on voltage but also give a qualitative understanding of the impact of disk diameter

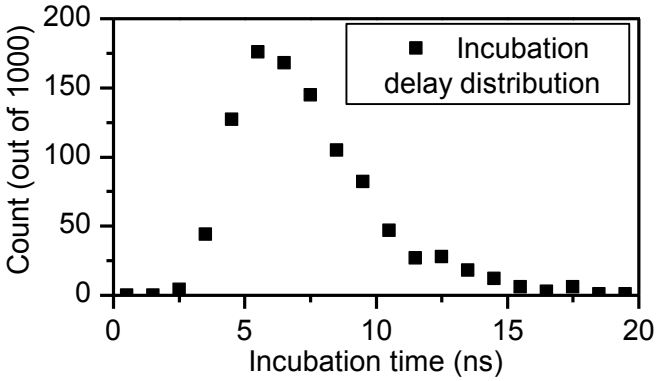

FIGURE 3.20: Typical incubation distribution. Distribution of the incubation time out of 1000 runs for a 40 nm disk under a voltage corresponding to V_c, at 300 K.

and temperature.

Typical incubation distribution

Before varying the different simulation parameters, we here detail the distribution of the incubation time obtained for a 40 nm disk at the macrospin critical switching voltage (1 V). The distribution obtained for 1000 runs is shown in figure 3.20, each delay being extracted with the threshold method previously discussed. The distribution is asymmetric. The asymmetry is due to the fact that for these parameters the time needed to amplify the coherent precession and initiate the reversal is not negligible compared to the medium incubation time. For instance in figure 3.16 we can observe that $\langle m_z \rangle$ decreases during the incubation time period (before the "amplification" arrow). This is not the case when the voltage is lower and the incubation time longer, as seen in figure 3.14 where for all three sizes the average $\langle m_z \rangle$ remains constant during the incubation. As a result when we extract the incubation from the threshold for the 1 V case (10 % reversal corresponding to $\langle m_z \rangle = 0.77$ because of the thermalized initial state), a part of the amplification is necessarily included. In other words the incubation delay as we defined it depends partly on thermal activation and partly on the beginning of the switching path. The longer is the median incubation time and the smaller is this switching path contribution. Consequently our extracted incubation delay can never go below a certain value which depends on the characteristic time of the first stage of the switching. This effect deforms the distribution for the small incubation times, explaining the observed asymmetric distribution.

Impact of voltage on the incubation time

Here we discuss the impact of voltage on the incubation time for a 40 nm disk. We apply between 0.8 and 1.5 V_c similarly to what we did in the transition time versus voltage study. As we increase V the median value of the incubation delay very sharply decreases for the three studied sizes (figure 3.21). We plot the median value since for the lowest voltage point we could not observe a full reversal for all of our switching simulations, which doesn't allow us to extract the mean or the standard deviation of the distribution but still give access to the median since more than 50% of the runs were reversed. The standard deviation of the incubation time increases very sharply as we decrease the voltage for the three disk diameters (not shown).

The inverse median incubation time depends linearly on voltage as seen in figure 3.21.b. This trend is similar to the one we just described for the transition time

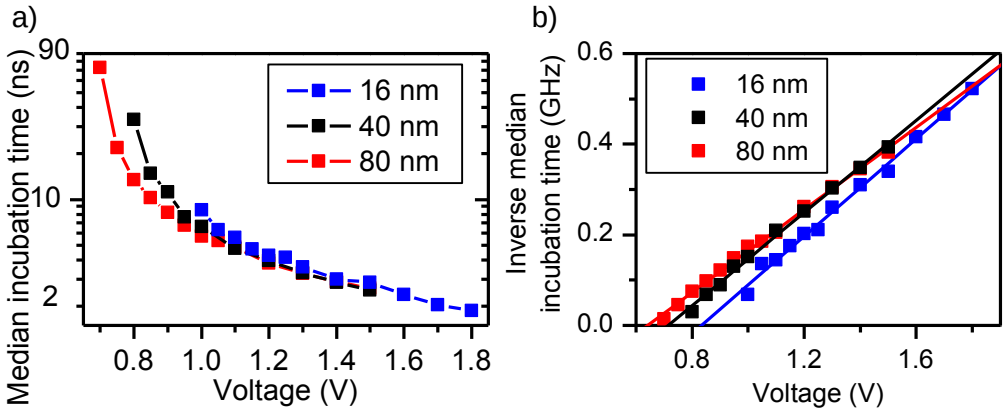

FIGURE 3.21: Voltage dependence of the incubation time. a) Median value for disks of 16, 40 or 80 nm at 300 K. The macrospin critical switching voltages are respectively 1.37, 1 and 0.83 V. b) Same data in a reciprocal scale with the corresponding proportionality fit for each sizes.

but the incubation time decays with voltage at a faster rate. In the case of the incubation time, the intercept is never at $(0,0)$ regardless of size. The intercept does not correspond neither to the macrospin critical switching voltage as seen in figure figure 3.22.b (otherwise the 3 intercepts would be 1). We believe that the linear dependence on voltage of the inverse incubation time is related to the fact that for most of our data points (typically below 10 ns) the incubation time includes the beginning of the coherent amplification. The delay of this amplification is inversely proportional to the voltage as we have discussed in the transition time section.

The incubation time does exist at high voltage, but it cannot be clearly distinguished from the transition time as it is the case in the long incubation regime. As a result the models that we discussed in section 2.1.2 of our state of the art for the switching time in the thermal regime cannot be compared to the results of our micromagnetic simulations. Despite this fact, the macrospin assumption made in these models is still valid when studying the incubation time of the micromagnetic simulations as the initial stage is coherent. Finally it is of interest that in the XMCD measurement described in section 2.5.1 of our state of the art, an incubation period was measured even at high voltage, in agreement with our simulations.

Incubation time versus diameter

The dependence on size of the median incubation time is surprising. We observe that the larger the disk, the easier it is to reverse at a fixed voltage (figure 3.21.a). The first stage of the reversal is the amplification of the coherent precession for the 3 sizes presented here, hence we can discuss the incubation time using a macrospin model at all sizes. For a macrospin system, the incubation time should depend on the diameter of the disks because of the demagnetizing factors that changes with size. For instance the demagnetizing field is included when solving the Fokker-Planck equation [13] (equation 2.3 with our notations) for the models predicting the voltage dependence of the switching time. We insist that the Fokker-Planck equation is valid even at high voltage, only the approximate formula for the switching time must assume a rare event and therefore are valid within the thermal regime only. As a result in both regimes, we expect the larger disks to be easier to reverse because they have a larger demagnetizing field, which is what we observe qualitatively. But following

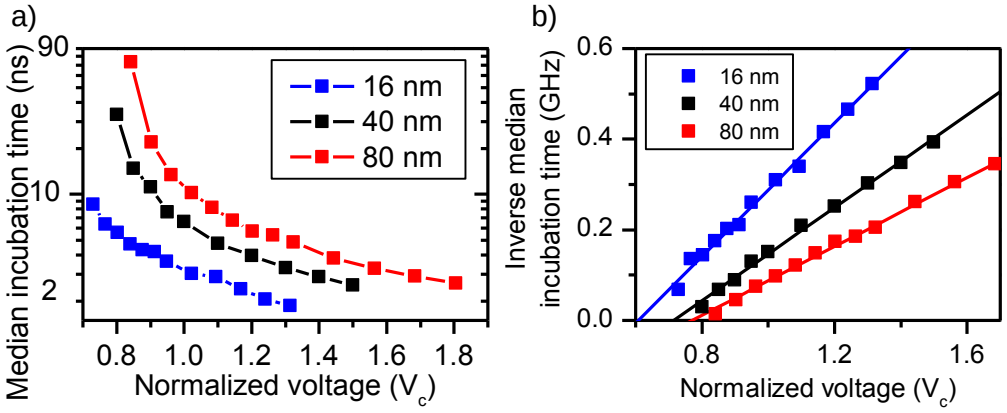

FIGURE 3.22: Dependence of the incubation time on macrospin critical switching voltage. a) Median value for disks of 16, 40 or 80 nm at 300 K. The macrospin critical switching voltages are respectively 1.37, 1 and 0.83 V. b) Same data in a reciprocal scale with the corresponding proportionality fit for each sizes.

this reasoning, we would expect that the incubation delay does not depend on size at a fixed normalized voltage value, because dividing by the macrospin critical switching voltage takes into account these demagnetizing effects. As seen in figure 3.22, this is not the case and the larger disks are harder to reverse than predicted by the macrospin picture with the normalized voltage.

To conclude this section we observed that the larger disks are easier to reverse than the smaller one, but not as easy as predicted by the macrospin model. We believe that this is due to the non-uniformity growing as the amplification starts to increase its rate (see figure 3.16). With temperature, the end of the incubation time is no longer a coherent amplification but the amplification of the precession over a smaller section. Then it is the demagnetizing effects of the smaller sections that give the size dependence of the incubation time. Qualitatively, the smaller section area increases only slightly with the diameter of the full disk. As a result the incubation time does not depend on size as strongly as in the case of a coherent amplification. We did not extract quantitatively the area of the smaller section and therefore cannot give the corresponding demagnetizing factors to normalize the incubation time data. Note that this smaller section observed in our simulation does not correspond to the subvolumes discussed in reference [96] by Sun as a possible switching path. The subvolume hypothesis of this study is compared with our experimental data in section 6.5.3.

Finally it is of great interest to notice that the incubation delays extracted from time-resolved measurement on STTMRAM devices at comparable sizes and voltage do in fact follow the macrospin-predicted size dependence (see section 6.5.2 figure 6.24) unlike the present simulations.

Impact of temperature on the incubation time

Finally in this short paragraph we change the temperature from 300 K to 600 K. The 600 K case is used as an example of STTMRAM devices reversal where Joule heating is very important (as already stated the exact expected temperature is unclear in literature). We only varied temperature for one size (40 nm) and a single voltage corresponding to 0.9 $V = 0.9\ V_c$.

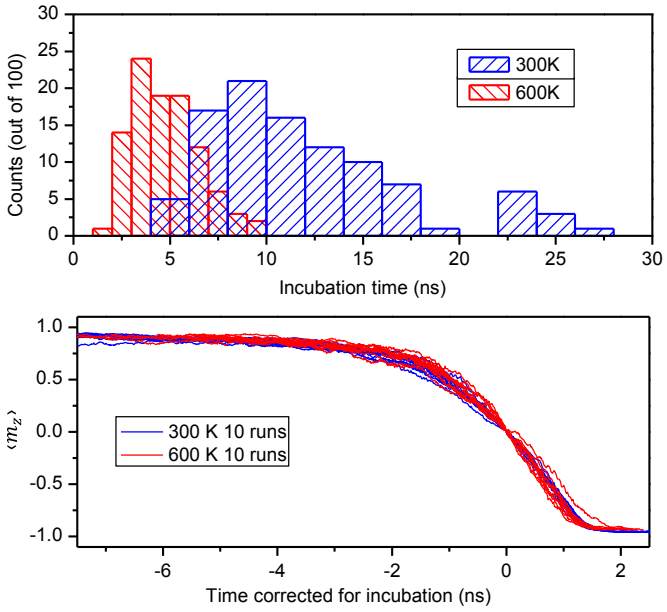

FIGURE 3.23: 300 K versus 600 K. Top: distributions of the incubation delays out of 100 runs for a disk of 40 nm under 0.9 V_c and a temperature of 300 or 600 K. Bottom: 10 $\langle m_z \rangle(t)$ graphs for each temperature. All the graphs as been stacked together to be reaching $\langle m_z \rangle = 0$ at $t = 0$ ns, thus removing the incubation time.

As expected the incubation time is significantly reduced by going at 600 K, as seen in the top graph of figure 3.23 where both distributions are plotted. If the temperature is larger, the amplitude of the stochastic field applied in our simulations is larger (equation 3.10) and therefore the typical time that should be waited for the fluctuations to accelerate the switching is shorter on average. The overall shape of the distribution (asymmetrical) is unchanged.

The transition time is however only weakly affected by the temperature. As seen in the bottom graph of the figure, we can stack together the time traces of the reversal at 300 or 600 K regardless of the temperature. At 300 K the transition time has a median of 3.52 ns and a standard deviation of 0.33 ns while at 600 K the median is 3.34 ns and the standard deviation 0.59 ns. We also checked in the magnetization snapshot that the switching path described at 300 K remained unchanged qualitatively at 600 K.

To conclude this paragraph we can observe that considering a temperature of 600 K (strong Joule heating) instead of 300 K (no Joule heating) changes only the incubation time without affecting the switching path or transition time.

3.4 Conclusion: the switching path from micromagnetic simulations of the free layer

In this chapter we have solved exactly the equation of motion for the free layer after dividing it into smaller macrospin cells. The switching path depends strongly on the diameter of the disk but is independent of voltage in a range reasonable for STTM-RAM applications. Three main size regimes are observed at 0 K(figure 3.24): below 20 nm the reversal is fully coherent and can be described by a single macrospin; from 28 to 70 nm there is a coherent phase followed by a domain wall motion; above 70 nm a domain is nucleated at the center after the coherent phase and then expands to create a domain wall near the edges.

Thermal fluctuations were added to the system. This adds an incubation time for all sizes and affects slightly the switching path. The transition between macrospin and non-uniform reversal is at lower diameters and becomes blurry because of stochasticity. The amplification of the precession is done non-uniformly but the domain wall

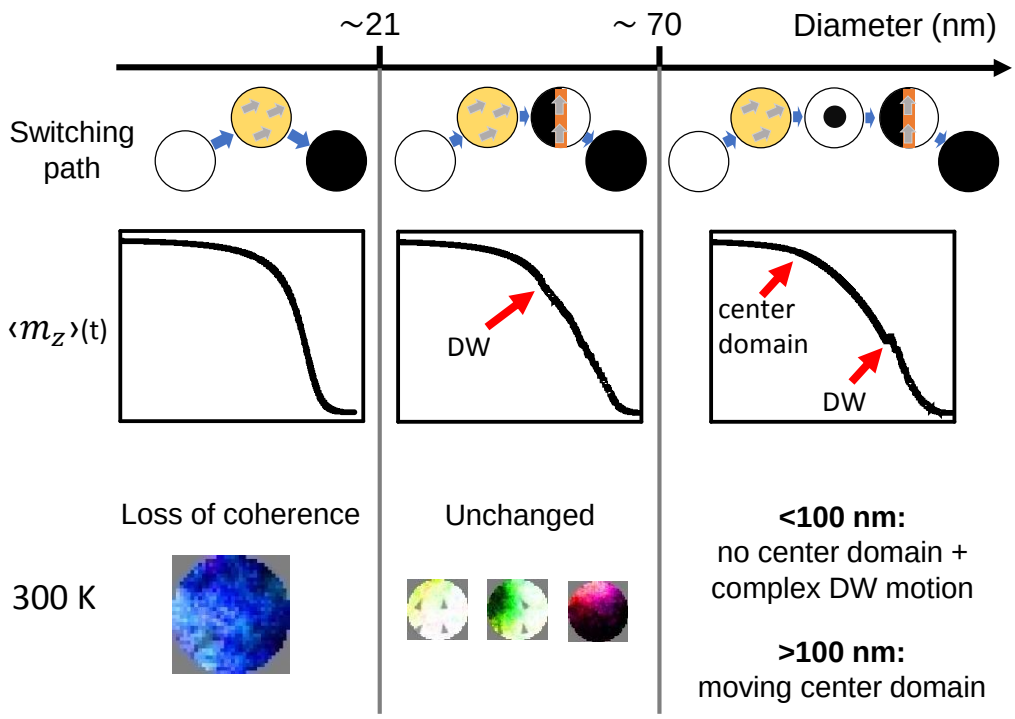

FIGURE 3.24: The switching path predicted by micromagnetic simulations. For each size regime the typical switching path is shown as well as its temporal trace and its behaviour with thermal fluctuations. The exact transition between two size regimes is more complex than what is shown in this figure.

motion is unchanged. Finally the center domain becomes unstable for disks smaller than 100 nm.

The most relevant sizes for applications are disks between 20 and 100 nm (size is scaled down to increase memory density), at a temperature of 300 K. Therefore the expected switching path in this size regime is a mostly coherent phase followed by a domain wall motion. We reported that the domain wall motion for a disk of 80 nm was more complex than what was observed for the smaller disks (figure 3.17), including rare events that slow down the overall switching speed. For this reason, we will in the next chapter focus on understanding the domain wall motion inside a perpendicularly magnetized thin disk.

Chapter 4

Modelling the domain wall motion

In the previous chapter we highlighted the importance of understanding the domain wall motion in the free layer in order to explain the switching scenario expected in actual devices. In this chapter we propose several models to elucidate the domain wall dynamics induced by spin transfer torque in a perpendicularly magnetized thin disk.

A domain wall is a collective state of the magnetization which separates two domains. The domains are fully magnetized in opposite out-of-plane directions in our case. For the thin disk that we study, the domain wall is a two dimensional object since we assume that the magnetization is uniform along the out-of-plane direction. Domain wall dynamics has been extensively studied in one dimensional object such as nanowires or in thin films under the effect of an external field [91, 102] or a spin current [103, 22]. In particular those two books were precious references for the following works [48, 46]. Most models for domain wall dynamics in literature are based on the so called (q, ϕ) approach where the parameters q the position of the domain wall and ϕ its tilt angle are used to describe its motion. Here we derive a similar model while taking into account the full geometry of our system. The geometry of the magnetic body proves to have a strong impact on the domain wall behaviour. In our analytical model the domain wall remains straight but its curvature can be used as an additional degree of freedom [43].

This chapter is organized as follows: we first present additional micromagnetic simulations to better illustrate the complex domain wall motion that was mentioned in the previous chapter. Then we recall the (q, ϕ) results in the simple case of a domain wall moving along an infinite stripe since it will prove to shed light into the more complex disk system. We propose two ways of solving the equations of the domain wall motion within a disk, either with an exact micromagnetic potential or with an effective field approach. These two approaches are compared to the micromagnetic simulations, with an emphasis on the sensitivity of the three models to the initial conditions of the system. We then discuss the impact of varying different parameters on the domain wall dynamics according to our models, in particular the external applied stimulus. Finally the limits and possible extensions of our models are presented.

4.1 Micromagnetic simulations of the domain wall motion

Even though we already encountered domain wall motions in our previous micromagnetic simulations, they were only a part of the complete reversal. To focus solely on the domain wall dynamics and disregard any perturbation due to the complex nucleation for instance, our initial state is going to be a domain wall close to the

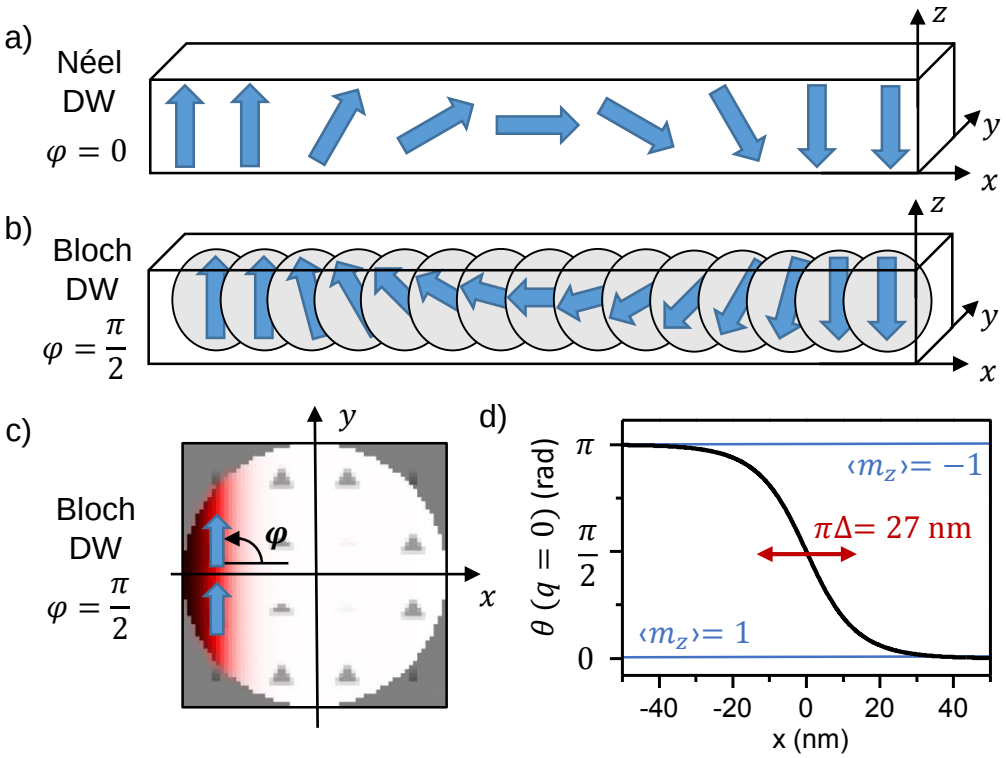

FIGURE 4.1: The initial state of the domain wall. Top: 3D representation of a a) Néel and a b) Bloch type domain walls. c) Snapshot of the initial state following the static solution as will be imported in mumax3. d) Profile of the domain wall following equation 4.2 for $q_0 = 0$.

edges. This approach also allows a better control of the initial state of the domain wall (its position q_0 and its tilt angle ϕ_0) than a full switching simulation.

4.1.1 Methods for domain wall motion micromagnetic simulations

Parameters used

We use the same material parameters and the same mumax3 code as the one presented in the previous chapter. Only the initial state is different: instead of a uniformly magnetized state with an initial tilt angle (at 0 K) or a thermalized state, we create an initial domain wall state that is imported inside mumax3 using the $m.LoadFile("initial - state.ovf")$ command.

In this chapter we will also vary the diameter of the disk, studying in particular the 40 nm and the 80 nm cases. Studying these two sizes will shed light on the full diameter dependence of the domain wall dynamics. We still use a voltage corresponding to the macrospin critical switching voltage for both of our disks. This voltage is not intrinsically related to the pure domain wall motion that we are simulating since it is a characteristic of a full switching. But we still use the normalized voltage for continuity with the previous chapter and to keep this study within the broader context of the free layer switching path.

Static domain wall profile

To create our initial domain wall state, we first need to chose a domain wall profile of minimum energy. If it is not the case (for instance if we create initially two

domains without separating them by a domain wall) the simulations present strong perturbations while the system relaxes to a more stable state. These perturbations are as many artefacts added to the intrinsic domain wall motion.

To tackle this issue we first create a straight initial domain wall with a constant tilt angle ϕ_0 (the angle between the in plane magnetization and the domain wall normal) and a profile following the static solution [48, 91]:

$$\phi(x,y) = \phi_0 \tag{4.1}$$

$$\theta(x,q_0) = 2\tan^{-1}[\exp(\frac{q_0 - x}{\Delta})] \tag{4.2}$$

where the domain wall motion is parallel to the x axis (see figure 4.1.c), q_0 is the initial position of the center of the domain wall and Δ is the characteristic width of the domain wall given by $\Delta = \sqrt{A_{ex}/K_{eff}}$ with A_{ex} the exchange stiffness and K_{eff} the infinite film effective anisotropy. Note that the width of the domain wall is given by $\pi\Delta$ rather than simply Δ (figure 4.1.d).

This static solution is obtained by assuming a one dimensional system (namely everything is constant along y and z) and by considering only the exchange and the out of plane anisotropy energy. By solving this problem we obtain the profile given by equation 4.2 and an initial tilt angle along the y axis. For our simulations we will vary ϕ_0 and q_0 and thus differ from the minimum energy state. $\phi = \frac{\pi}{2}\ [\pi]$ corresponds to a domain wall in the Bloch state (the static solution, figure 4.1.b) and $\phi = 0\ [\pi]$ to the Néel state (figure 4.1.a).

To import the profile in mumax3 we need to create an ovf file. This is done by first creating the data of the initial state in the three column format used by ovf files (one for each component of the magnetization), which we do using simple loops in mathematica. An example of final state is given in figure 4.1.d.

Curved or straight initial domain wall

During the domain wall motion observed in the previous chapter, the domain wall curves itself towards the center of the disk. This effect is still observed if we initiate a straight domain wall at any given tilt angle and position without any applied voltage: it quickly (in a few tens of ps) curves itself. This can be understood from wall energy considerations in the circular geometry: after the nucleation of the domain wall during a full switching or once we fix an initial state, the system is described by a given $\langle m_z \rangle$ value that will vary with time under the effect of spin transfer torque. This given $\langle m_z \rangle$ corresponds to a given reversed surface. The longer is a domain wall the more it costs energy to the system because both the exchange and the anisotropy are frustrated. This cost in energy is given by the domain wall surface energy density $\sqrt{A_{ex}K_{eff}}$ and is therefore proportional to the domain wall length. To minimize the energy the system minimizes the length of the domain wall while maintaining the fixed surface.

This problem becomes purely geometrical. When limited to configurations touching the edges it can be proven (calculation not shown) that the length is smaller at a fixed surface for a curved domain wall (the intercept between the free layer disk and a second circle with 90 degree angles at the edges) than for a straight domain wall [17]. This explains why the domain wall quickly relaxes from our initial straight state to a curved state.

This relaxation adds perturbations to the intrinsic domain wall motion: there are fluctuations of the domain wall shape that we call a "breathing". The domain wall

oscillates quickly back and forth between the straight configuration and the curved configuration, with a frequency of about 15 GHz.

To suppress the breathing we can use an initial state where the domain wall is already optimally curved. To obtain this new initial state we let the domain wall go across the disk from q_0 to $2R - q_0$ with R the radius while recording the magnetization configurations in ovf format. Then we take the magnetic configuration at $2R - q_0$ and we reverse the z component to obtain a curved initial state. This procedure suppresses the breathing because this artefact only occurs during the first few ns and becomes insignificant once the domain wall has crossed the center.

Consequently q_0 and ϕ_0 needs to be redefined for the curved initial state. q_0 is defined from the corresponding $\langle m_{z,0} \rangle$ assuming a straight wall (equation 4.47). ϕ_0 is defined as the tilt angle at the center of the domain wall (the point the nearest from the disk center). In fact the tilt angle is not constant along the domain wall since the in plane angle of the magnetization is constant but the domain wall normal vector varies because of the curvature.

Note that the breathing artefact is minor and cannot be spotted in the $\langle m_z \rangle(t)$ traces while comparing the simulations from a straight initial domain wall with the forthcoming curved initial domain wall case. All the micromagnetic simulations shown in this chapter are obtained from curved initial domain walls.

4.1.2 Domain wall dynamics within a 80 nm disk

The figure 4.2.a illustrates the motion of a domain wall with an optimal initial curvature, an initial tilt $\phi_0 = 30$ deg. and an initial position corresponding to $q_0 = 10$ nm within a disk of diameter 80 nm at the applied voltage V_c. As expected, the wall sweeps through the disk, acquires a straight shape when at the disk center and then bends again. The magnetic moment $\langle m_z \rangle$ reverses in a few ns (figure 4.2.b). This domain wall motion is similar to what was observed in the previous chapter for a 80 nm disk under 300 K. Let us here describe in details this dynamics.

Overall motion: domain wall drift and superimposed oscillations

The first important point is that the wall velocity and the tilt angle $\phi(t)$ (i.e. the color in figure 4.2.a) are coupled: $\phi(t)$ increases monotonously during the domain wall motion towards the disk center and this modulates the wall velocity. The wall passes periodically from the Bloch state ($\phi = \frac{\pi}{2}$ $[\pi]$) to the Néel state ($\phi = \pi$ $[\pi]$). For 80 nm diameter disks, the domain wall advances (i.e. $\dot{q} > 0$) when near the Néel state and moves backward when near the Bloch state (see the lower snapshots in figure 4.2.b), at the noticeable exception of when the wall crosses the center of the disk.

This fast back-and-forth motion of the domain wall is superimposed on the global drift of the domain wall that sweeps through the disk. The oscillation of the moment $\langle m_z \rangle$ has a more pronounced amplitude when the wall approaches the disk center (when $\langle m_z \rangle \approx 0$). As this same position the oscillation of the moment slows down and the rate of change $\dot{\phi}(t)$ of the tilt changes sign.

Sensitivity to the initial conditions

The second noticeable point is the large sensitivity of the dynamics to the initial conditions (figure 4.2.b,c,d): minute changes of either the chosen initial DW position (q_0, not shown) or the initial tilt angle (ϕ_0) alter substantially the dynamics when the

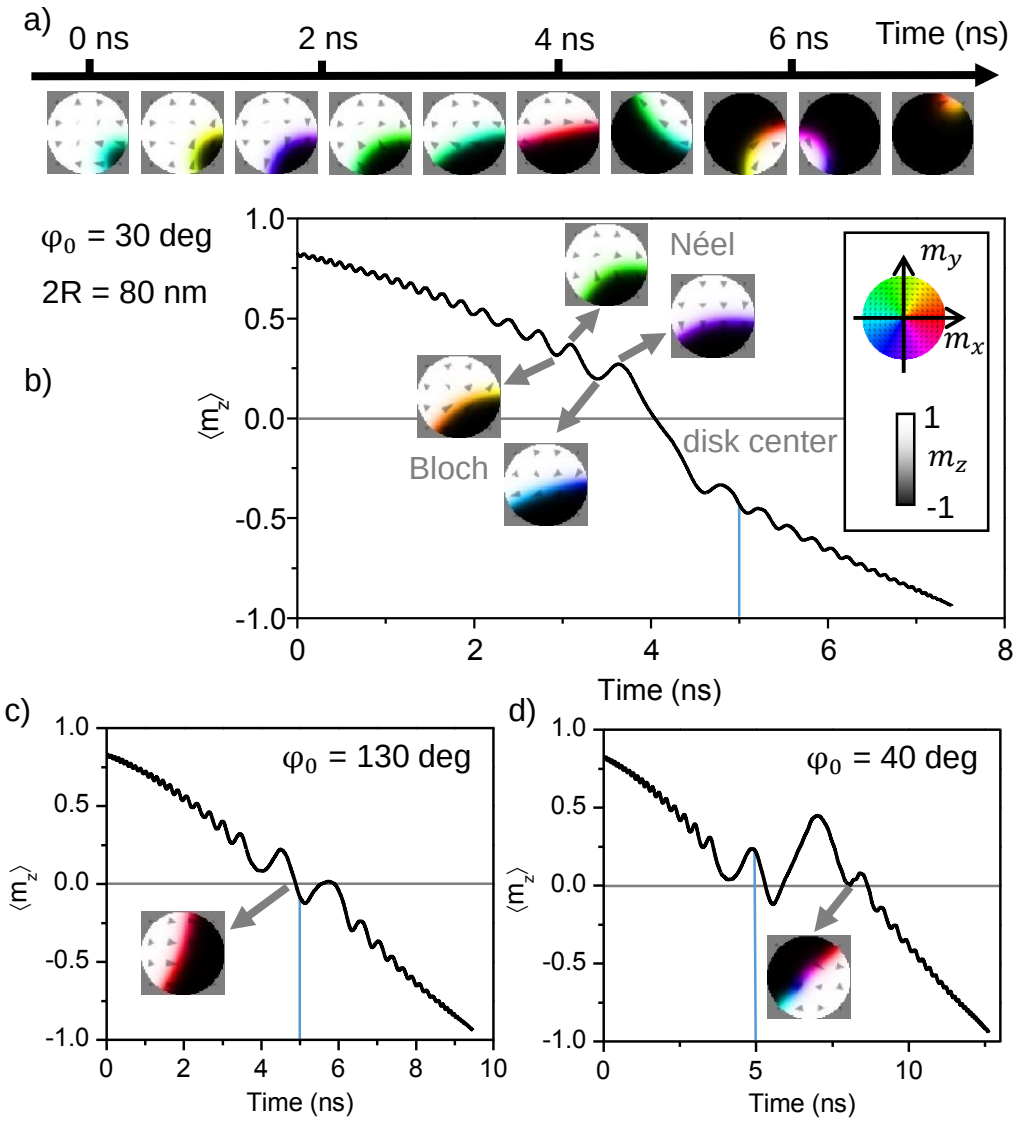

FIGURE 4.2: Micromagnetic simulations of the domain wall dynamics within a disk of diameter 80 nm for domain walls with optimal initial curvatures. a) Snapshots of the chosen initial magnetization state with $\{\phi_0,\ q_0\} = \{30$ deg., 10 nm$\}$ and its subsequent evolution under an applied voltage of 0.85 V. b) Resulting evolution of the spatial average of the m_z component of the magnetization. The micromagnetic snapshots are taken at the extrema of $\langle m_z \rangle$. They illustrate the Néel (Bloch) character of the wall when the DW velocity changes from negative to positive (positive to negative). The panels c) and d) present similar plots calculated for different initial states in which in the initial tilts were rotated by respectively $\Delta\phi_0 = +100$ deg. and $\Delta\phi_0 = +10$ deg. The vertical bars are placed at 5 ns to better reveal the resulting changes in switching duration. Inset in panel d): note that the non-uniformity of the magnetization tilt within the wall ($\frac{\partial\phi}{\partial y} \neq 0$, which is seen by a multicoloured wall) correlates with the occurrence of a switching scenario in which the DW performs multiple crossing of the disk center in a swing-like manner.

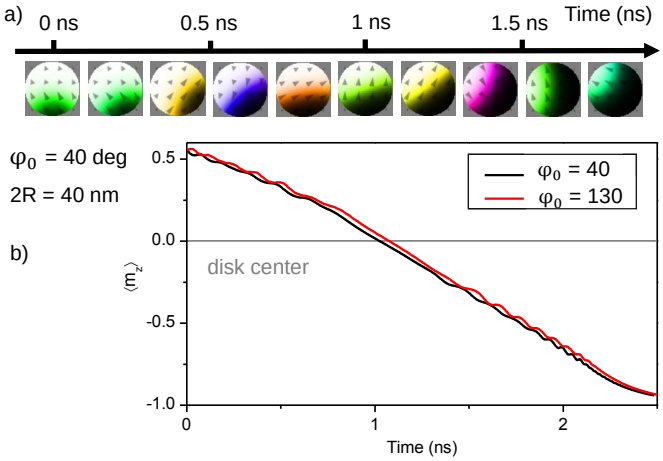

FIGURE 4.3: Micromagnetic simulations of the domain wall dynamics within a disk of diameter 40 nm for a domain wall with optimal initial curvature. a) Snapshots of an initial magnetization state with $\{\phi_0, q_0\} = \{40 \text{ deg.}, 10 \text{ nm}\}$ and its subsequent evolution under an applied voltage of 1 V. b) Resulting evolution of the spatial average of the m_z component of the magnetization for the same simulation and for one with an initial tilt angle incremented by 90 degrees.

wall later arrives in the center of the disk. The same sensitivity to initial conditions is observed when domain wall is initialized with a straight shape and was observed in the full switching at 300 K from the previous chapter (rare event versus common reversal in figure 3.17 and 3.18).

We have identified three scenarios: a drift-like one-way crossing, a one-way crossing with pre- and post-crossing pauses and a swing-like crossing with multiple attempts. Most initial conditions $\{q_0, \phi_0\}$ lead to a drift-like one-way crossing: the wall sweeps through the center without stopping there. The time-resolved magnetic moment is rather linear (figure 4.2.b). For some specific other initial conditions, the wall stops on either sides of the disk diameter before and after crossing the center (figure 4.2.c). In both scenarios the domain wall crosses the center while being essentially in a Bloch-type configuration. Note that this holds for a disk diameter of 80 nm but shall no longer hold for the smaller disk diameter. Occasionally, the domain wall swings several times back-and-forth in the vicinity of the disk diameter and crosses the center multiple times before finally leaving the center (figure 4.2.d). In this last scenario, the tilt ϕ of the magnetization within the wall gets substantially non-uniform when the wall is in the vicinity of the disk center: a partial Bloch line can even be created within the wall (inset in figure 4.2.d).

Minor features of the domain wall dynamics

Finally for the sake of completeness, let's mention additional minor facts that can be observed in the micromagnetic simulations (figure 4.2.a). In addition to its gradual drift and its fast position oscillation, the domain wall also rotates around the center of the disk. The gyration speed is minimal when ϕ is quasi-uniform; the gyration speed seems to increase with the non-uniformity of the tilt. Unfortunately the details of the gyration of the wall depend on how the (ideally perfectly circular) disk is deformed by mapping it on the square simulation grid of the micromagnetic solver. Staircase artefacts prevent an objective analysis thereof. This effect is discussed further into details at the end of this chapter (section 4.8.5).

4.1.3 Domain wall dynamics within a disk of diameter of 40 nm

The figure 4.3 presents the domain wall dynamics within a smaller disk of diameter 40 nm with an initial optimal curvature. The main qualitative features of the dynamics formerly observed in the larger disk are preserved: there is still a gradual drift of the domain wall on which a fast position oscillation is superimposed. A wall

curvature is also observed with a breathing when the wall is initialized with straight shape.

However the reduction of the diameter induces quantitative differences on the dynamics. In the 40 nm disk, the oscillations of the domain wall position are much less pronounced and can hardly be noticed in the time-resolved magnetization curves (figure 4.3.b), especially near the disk center where the motion looks very linear. The oscillatory modulation of the domain wall velocity is weaker than the domain wall drift velocity during the most part of the reversal. Among the 3 scenarios previously identified in the 80 nm disk, only the drift-like one-way crossing is still observed when the diameter is 40 nm. Another difference is that the initialization conditions $\{\phi_0, q_0\}$ do no longer have a strong impact on the dynamics of the total moment. In 40 nm disks, the walls cross the disk center in a manner that does not depend much on their Néel or Bloch character. The existence of a single type of switching event at 40 nm is consistent with the full switching simulations at both 0 and 300 K (figures 3.4 and 3.16).

Having described in details the domain wall motion as predicted by solving numerically the LLGS equation, we now present the collective coordinates approach leading to the (q, ϕ) model.

4.2 Domain wall motion within a stripe

We start our analytical models study by recalling the well known result of the spin transfer torque induced domain wall dynamics within an infinite stripe, before discussing two different (q, ϕ) models in the disk (effective field model and exact potential model). The infinite stripe results will prove useful for introducing the (q, ϕ) approach in a simple system, as well as for understanding the more complex disk case. Note that such models for a stripe were already compared to experimental data on STTMRAM devices [22, 30] with relative success (see section 2.3.2 of our state of the art). The geometry of the system is presented in figure 4.4.

4.2.1 The collective coordinate approach

Instead of solving the LLGS equation for every point within the domain wall, this collective state will be described as a soliton using collective coordinates. For a domain wall the collective coordinates are q and ϕ as defined previously (the position of its center along the propagation axis and its tilt angle). The domain wall width Δ could also be used as a third collective coordinate , but with our parameters it can reasonably be considered constant (as seen in [102] and in the micromagnetic simulations where it appears mostly unchanged).

Solving LLGS for the full domain wall is equivalent to solving the Euler-Lagrange equations for the two collective coordinates $X = q, \phi$:

$$\frac{\mathrm{d}}{\mathrm{d}t}\frac{\partial L}{\partial \dot{X}} - \frac{\partial L}{\partial X} + \frac{\partial W_G}{\partial \dot{X}} = 0 \tag{4.3}$$

Where L is the Lagrangian of the system and W_G its dissipation function.

The Lagrangian $L = L_B - U_{\text{tot}}$ of the system is the difference between the kinetic term:

$$L_B = \frac{M_s}{\gamma}\int_{\text{Vol}} \dot{\phi}(1 - \cos\theta)\, d^3r \tag{4.4}$$

and the total energy:

$$U_{\text{tot}} = \int_{\text{Vol}} u_{\mu mag}\, d^3r \tag{4.5}$$

The kinetic term is equivalent to the kinetic energy in classical Lagrange dynamics (written $L_B = \frac{1}{2}mv^2$). The form we adopt is commonly used in the case of Lagrange formalism applied to magnetism as it corresponds to the LLGS equation [112].

The micromagnetic energy density $u_{\mu mag}$ includes the conservative torques applied to the magnetization while the dissipation function corresponds to the dissipative torques. Let us detail these torques.

4.2.2 Micromagnetic energy and dissipation function

Micromagnetic energy density

The total micromagnetic energy density includes the energy terms that were discussed in the first chapter section 1.1.

The magneto-crystalline anisotropy energy is $u_{anis} = K\sin^2\theta$ with K the anisotropy constant. It is minimized by staying fully out of plane.

The exchange energy is $u_{ex} = A_{\text{ex}}(\frac{d\theta}{dx})^2$. We consider that ϕ is constant for all the system, giving us this simple form for the exchange. It is minimized by keeping the magnetization uniform.

The Zeeman energy density is $u_Z = -\mu_0 H_z M_s \cos\theta$ for an external field H_z along z. It is minimized by keeping the magnetization along the field.

The demagnetizing energy is complex in the domain wall within a stripe system. Indeed there are out of plane component of opposite directions coming from each domains and in plane components coming from the domain wall itself. In this model and in the effective fields in a disk model we incorporate the out-of-plane demagnetization into a global effective anisotropy. This term and the anisotropy energy density merges into a single $u_{anis,eff} = K_{\text{eff}}\sin^2\theta$. We will prove that this assumption is reasonable by comparing the results of the effective field and exact potential models for the disk.

The in-plane contributions of the demagnetizing field are written as a domain wall anisotropy energy density: u_{DW} [75] which reflects the fact that Néel-type domain wall have volume magnetic charges (i.e. we have $\vec{\nabla}.\vec{M} \neq 0$ within the wall) while Bloch-type domain wall have magnetic surface charges only at the edge of the stripe. The anisotropy energy density reads $u_{DW} = K_{DW}\cos^2\phi\sin^2\theta$ where $K_{DW} = \mu_0\frac{H_{N\leftrightarrow B}M_s}{2}$ with the domain wall stiffness field $H_{N\leftrightarrow B}$ being the in-plane field that one needs to apply to transform a Bloch domain wall into a Néel domain wall.

The stiffness field can be written [75] from effective demagnetizing factors of the domain wall: $H_{N\leftrightarrow B} = \frac{M_s}{2}(N_y - N_x)$. If $w \gg d$ and $w \gg \pi\Delta$ the demagnetizing factors are [81]:

$$N_x \approx \frac{d}{d+w} \quad \text{and} \quad N_y \approx \frac{d}{d+\pi\Delta} \tag{4.6}$$

For example, a stripe of width $w = 80$ nm and of thickness $d = 2$ nm would have a stiffness field of $\mu_0 H_{N\leftrightarrow B} = 34$ mT.

So far no Dzyaloshinskii–Moriya interaction (DMI) is included in the system, but such terms could be included here into the total micromagnetic energy density. This will be done briefly near the end of this chapter (section 4.7.5).

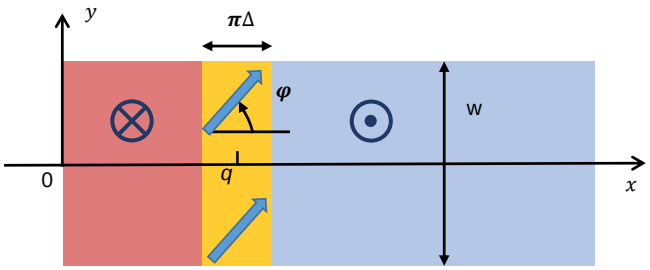

FIGURE 4.4: Geometry: a straight wall (yellow) of width $\pi\Delta$ and of tilt ϕ is at a position q within a stripe of width w. The stripe thickness is written d.

Dissipation function

The dissipation function includes the dissipative torques of LLGS equation, namely the damping and the Slonczewski-like spin transfer torque.

The damping is accounted through the dissipation density [102] $F_\alpha = \frac{1}{2}\alpha\frac{M_s}{\gamma}(\dot{\vec{m}}.\dot{\vec{m}})$ which gives by writing $\vec{m}$ into spherical coordinates: $F_\alpha = \frac{1}{2}\alpha\frac{M_s}{\gamma}(\dot{\theta}^2 + \dot{\phi}^2\sin^2\theta)$.

The spin transfer torque dissipation density is taken as $F_{\text{STT}} = -\sigma j\frac{M_s}{\gamma}\vec{p}.(\vec{m}\times\dot{\vec{m}})$ where σj is the amplitude of the spin transfer torque expressed in frequency. It can be expressed in applied voltage V as we did previously (equation 1.32):

$$\sigma j = \gamma_0 P\frac{V}{\mathcal{A}R_\perp}\frac{\hbar}{2e\mu_0 M_s d} \tag{4.7}$$

The current density to voltage correspondence is $\sigma j = 1.1$ GHz for an applied voltage of 0.85 V (namely at V_c for the 80 nm disk). Assuming a current polarized along z we obtain $F_{\text{STT}} = -\sigma j\frac{M_s}{\gamma}\dot{\phi}\sin^2\theta$ such that the dissipation function is:

$$W_G = \frac{1}{2}\alpha\frac{M_s}{\gamma}\int_{\text{Vol}}(\dot{\theta}^2 + \dot{\phi}^2\sin^2\theta)\,d^3r - \sigma j\frac{M_s}{\gamma}\int_{\text{Vol}}\dot{\phi}\sin^2\theta\,d^3r \tag{4.8}$$

4.2.3 Integrating the equations

Each term in the Lagrangian energy density and the dissipation function must now be integrated over the full volume of the system. For the stripe case following figure 4.4 the integral is:

$$\int_{\text{stripe}} = w\,d\int_{-\infty}^{\infty}\mathrm{d}x \tag{4.9}$$

These usual expression are necessary, obtained using equation 4.2 and assuming a constant domain wall profile during the motion:

$$\cos\theta = -\tanh\left(\frac{q(t)-x}{\Delta}\right) \tag{4.10}$$

$$\sin\theta = \operatorname{sech}\left(\frac{q(t)-x}{\Delta}\right) \tag{4.11}$$

$$\int_{-\infty}^{\infty}\operatorname{sech}^2\left(\frac{x}{\Delta}\right)\mathrm{d}x = 2\Delta \tag{4.12}$$

From this one can recover:

$$L_B = -2wd\frac{M_s}{\gamma}\dot{\phi}q \tag{4.13}$$

$$U_{\text{tot}} = 2wd\left(\frac{A_{\text{ex}}}{\Delta} + K_{\text{eff}}\Delta - K_{DW}\Delta\sin^2(\phi) - \mu_0 M_s H_z q\right) \tag{4.14}$$

$$W_G = wd\frac{M_s}{\gamma}\Delta\left(\alpha(\frac{\dot{q}^2}{\Delta^2} + \dot{\phi}^2) - 2\sigma j\dot{\phi}\right) \tag{4.15}$$

Finally these three expressions are injected into the Euler-Lagrange equation 4.3 for the collective coordinates q and ϕ, giving:

$$-\dot{\phi} + \alpha\frac{\dot{q}}{\Delta} = -\gamma_0 H_z \tag{4.16}$$

$$\frac{\dot{q}}{\Delta} + \alpha\dot{\phi} = \gamma_0\frac{H_{N\leftrightarrow B}}{2}\sin 2\phi + \sigma j \tag{4.17}$$

We obtain coupled equations for q and ϕ which describe their dynamics and therefore the domain wall dynamics within a stripe.

4.2.4 The Walker breakdown

From the coupled equations, it is straightforward to obtain:

$$\dot{\phi} = \frac{1}{1+\alpha^2}\left[\gamma_0(H_z + \alpha\frac{H_{N\leftrightarrow B}}{2}\sin 2\phi) + \alpha\sigma j\right] \tag{4.18}$$

$$\dot{q} = \frac{\Delta}{1+\alpha^2}\left[\gamma_0(\frac{H_{N\leftrightarrow B}}{2}\sin 2\phi - \alpha H_z) + \sigma j\right] \tag{4.19}$$

The solution of these equations depends on the relative strength of σj and the two fields H_z and $H_{N\leftrightarrow B}$. The domain wall can follow either a linear regime (or constant mobility regime) or an oscillating regime called the Walker regime. The transition between the two regimes is the well known Walker breakdown and shall be discussed here with our parameters.

Constant mobility regime

From equation 4.18 we can find a solution with $\dot{\phi} = 0$ if $\gamma_0 H_z + \alpha\sigma j \leq \gamma_0 H_W$ where $H_W = \alpha\frac{H_{N\leftrightarrow B}}{2}$ is called the Walker field.

When this condition is satisfied, the domain wall is within the linear regime. Then the tilt angle takes a constant value:

$$\phi^* = -\frac{1}{2}\arcsin(2\frac{\gamma_0 H_z + \alpha\sigma j}{\gamma_0 H_W}) \tag{4.20}$$

While the domain wall center moves with a constant velocity given directly by replacing ϕ by ϕ^* in equation 4.19:

$$\dot{q}^* = -\Delta\frac{\gamma_0 H_z}{\alpha} \tag{4.21}$$

Oscillatory regime

If we assume that $\gamma_0 H_z + \alpha\sigma j > \gamma_0 H_W$ then there is no solution of constant ϕ. The equations still admit a simple solution if we assume $\gamma_0 H_z + \alpha\sigma j \gg \gamma_0 H_W$. Then the domain wall enters the Walker regime with coupled oscillations of ϕ and q.

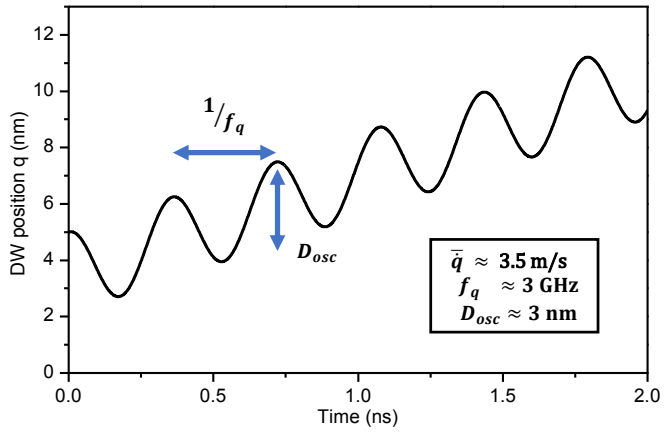

FIGURE 4.5: Dynamics of q for a domain wall within a stripe according to the (q, ϕ) model. The spin transfer torque corresponds to $\sigma j = 0.5$ GHz and the applied field is $\mu_0 H_z = 50$ mT. Inset: values of the drift velocity, the frequency and the amplitude of the oscillations using the approximate formulas (equations 4.23 4.26 4.27).

In the Walker regime within this assumption the tilt angle grows at a rather constant rate given by:

$$\dot{\phi} \simeq \frac{1}{1+\alpha^2}(\gamma_0 H_z + \alpha\sigma j) \equiv \omega_\phi \tag{4.22}$$

We thus defined the ϕ angular frequency ω_ϕ.

The q dynamics, still given by equation 4.19, is more complex. It can be decomposed into a drift part (domain wall motion of constant velocity) and an oscillating part. The drift velocity, written $\bar{\dot{q}}$, is given by the terms independent of ϕ:

$$\bar{\dot{q}} \simeq \frac{\Delta}{1+\alpha^2}(\sigma j - \alpha\gamma_0 H_z) \tag{4.23}$$

The angular frequency of q is twice that of ϕ because of the $\sin 2\phi$ oscillating term:

$$\omega_q \equiv 2|\omega_\phi| \simeq 2\left|\frac{1}{1+\alpha^2}(\gamma_0 H_z + \alpha\sigma j)\right| \tag{4.24}$$

Finally the amplitude of the q oscillations is obtained by integrating the oscillating part of equation 4.19 over half a period:

$$D_{\text{osc}} \simeq \frac{\Delta}{1+\alpha^2}\left|\frac{\gamma_0 H_{N\leftrightarrow B}}{2(\gamma_0 H_z + \alpha\sigma j)}\right| \tag{4.25}$$

4.2.5 Numerical values for the domain wall motion within a stripe

Numerical values

The parameters used for the simulations gives $\Delta = 8.5$ nm. For a stripe of 80 nm width and 2 nm thickness, then following equation 4.6 $\mu_0 H_{N\leftrightarrow B} = 34$ mT and therefore $\mu_0 H_W = 0.17$ mT.

The Walker field is very small, much smaller than the typical fields at stake in a STTMRAM free layer (stray field from the reference layers for instance [29]). In practice $\gamma_0 H_z + \alpha\sigma j \gg \gamma_0 H_W$ is verified and we can focus our study on the Walker regime.

The evolution of q over time is plotted in figure 4.5 for an external applied field of 50 mT and a external voltage corresponding to $\sigma j = 0.5$ GHz. The domain wall motion can indeed be decomposed into a constant drift with oscillations of fixed amplitude and frequency.

With our parameters, we remark that $\alpha^2 \ll 1$ and typically $\alpha\sigma j \ll \gamma_0 H_z$ since $\gamma_0 H_z$ is of the order of the GHz while $\alpha\sigma j$ of the MHz. We can rewrite the equations 4.24 4.25 into the simpler forms:

$$\omega_q = 2|\omega_\phi| \approx 2|\gamma_0 H_z| \tag{4.26}$$

$$D_{\text{osc}} \approx \Delta \frac{H_{N\leftrightarrow B}}{2H_z} \tag{4.27}$$

Discussion

The drift velocity, the frequency and the amplitude of the q oscillations are key quantities because they are the ones that can be easily evaluated from a micromagnetic simulation (through $\langle m_z \rangle$) or an electrical time-resolved measurement of the conductance. The approximate formulas we proposed give a good insight into their physics:

i) The drift velocity (equation 4.23), namely how fast the domain wall is moving overall, is proportional to the voltage applied as well as to the field applied. But the field term includes the Gilbert damping as a prefactor while the voltage do not.

ii) The frequency of both the q and the ϕ oscillations (equation 4.26) is mostly given by the field applied along the z direction to the domain wall. The spin transfer torque has little impact on it because of the damping prefactor.

iii) The amplitude of the oscillations (equation 4.27) is more complex since it involves both the applied out-of-plane field as well as the stiffness field of the domain wall. The stiffer is a domain wall (the more a Bloch state is stable) and the larger will be these oscillations even at fixed external field.

We can already compare the domain wall dynamics predicted by our (q, ϕ) model within a stripe to the micromagnetic simulations in a 80 or a 40 nm disk. In the simulations just like in this model there is a drift velocity with coupled oscillations of q and ϕ on top of it. Similar to what was described for the 80 nm micromagnetic simulations in section 1.1.2 of this chapter, the domain wall advances (i.e. $\dot{q} > 0$) when near the Néel state and moves backward when near the Bloch state in the stripe model.

The main difference with the model is that in the simulations the amplitude and the frequency of the oscillations varies with the position of the domain wall as it moves across the disk. Furthermore, the stripe model does not explain the qualitative difference between the domain wall behaviour at the center of the 40 and the 80 nm disks. Including the exact geometry and solving the same Euler-Lagrange equation within the disk will resolve all these issues.

4.3 Domain wall motion within a disk: effective fields

In this section we derive the (q, ϕ) model within a disk, while keeping an analytical potential similarly to what was done in the case of a stripe.

4.3.1 Integrating the equations

The Euler-Lagrange equation 4.3, the micromagnetic energy densities, the density of kinetic energy and the dissipation densities are the same as the ones described in the stripe model. The main difference is that now instead of integrating over the stripe,

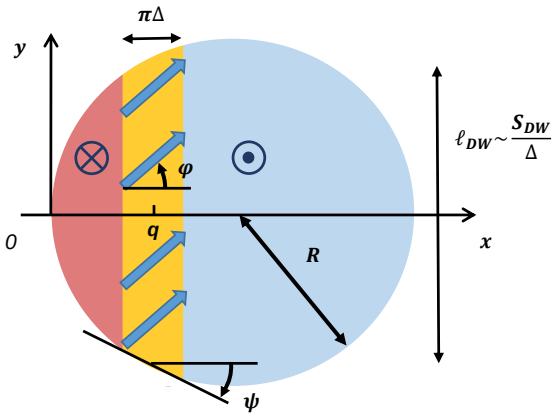

FIGURE 4.6: Geometry: a straight wall (yellow) of width $\pi\Delta$ and of tilt ϕ is at a position q within a disk of radius R. The disk thickness is written d. ψ and ℓ_{wall} are useful quantities that shall be defined later.

we integrate over the disk following (figure 4.6):

$$\int_{\text{disk}} = 2d \int_{-R}^{R} \sqrt{R^2 - x^2}\mathrm{d}x \tag{4.28}$$

Using this integral we obtain:

$$L_B = 2d\frac{M_s}{\gamma}\dot{\phi}\left(\frac{\pi}{2}R^2 + \int_{-R}^{R}\tanh(\frac{q-x}{\Delta})\sqrt{R^2-x^2}\mathrm{d}x\right) \tag{4.29}$$

$$\begin{aligned} U_{\text{tot}} = 2d\int_{-R}^{R}\text{sech}^2(\frac{q-x}{\Delta})\sqrt{R^2-x^2}\mathrm{d}x\left(\frac{A_{\text{ex}}}{\Delta^2} + K_{\text{eff}} - K_{DW}\sin^2(\phi)\right) \\ +2d\mu_0 M_s H_z \int_{-R}^{R}\tanh(\frac{q-x}{\Delta})\sqrt{R^2-x^2}\mathrm{d}x \end{aligned} \tag{4.30}$$

$$W_G = d\frac{M_s}{\gamma}\int_{-R}^{R}\text{sech}^2(\frac{q-x}{\Delta})\sqrt{R^2-x^2}\mathrm{d}x\left(\alpha(\frac{\dot{q}^2}{\Delta^2} + \dot{\phi}^2) - 2\sigma j\dot{\phi}\right) \tag{4.31}$$

The Euler-Lagrange equations gives, without injecting U_{tot}:

$$-\dot{\phi} + \alpha\frac{\dot{q}}{\Delta} = -\frac{\gamma}{2M_s d}\frac{\Delta}{S_{\text{DW}}(q)}\frac{\partial U_{\text{tot}}}{\partial q} \tag{4.32}$$

$$\frac{\dot{q}}{\Delta} + \alpha\dot{\phi} = -\frac{\gamma}{2M_s d}\frac{1}{S_{\text{DW}}(q)}\frac{\partial U_{\text{tot}}}{\partial \phi} + \sigma j \tag{4.33}$$

where $S_{\text{DW}}(q)$ has the dimension of a surface and reads:

$$S_{\text{DW}}(q) = \int_{-R}^{R}\text{sech}^2(\frac{x-q}{\Delta})\sqrt{R^2-q^2}\mathrm{d}x \tag{4.34}$$

$S_{\text{DW}}(q)$ can be viewed as the effective surface of the domain wall, as it corresponds to the integral over the disk of $\sin^2(\theta)$, the in-plane projection of the magnetization. It can be reasonably approximated in large disks (figure 4.7) by the product of the wall width Δ by the chord of a disk length, yielding:

$$S_{\text{DW}}(q) \approx 2\Delta\sqrt{R^2 - (R-q)^2} \tag{4.35}$$

If we inject the analytical potential (equation 4.30) into equations 4.32 and 4.33 we obtain:

$$-\dot{\phi} + \alpha\frac{\dot{q}}{\Delta} = -\gamma_0\left[H_z + H_{\text{stray}}(q) + H_{\text{stretch}}(q,\phi)\right] \tag{4.36}$$

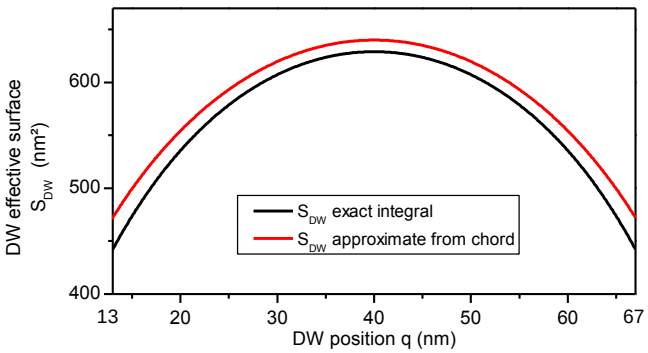

FIGURE 4.7: Effective surface $S_{DW}(q)$ of a straight domain wall in an 80 nm disk as computed exactly using equation 4.34 and as approximated using equation 4.35.

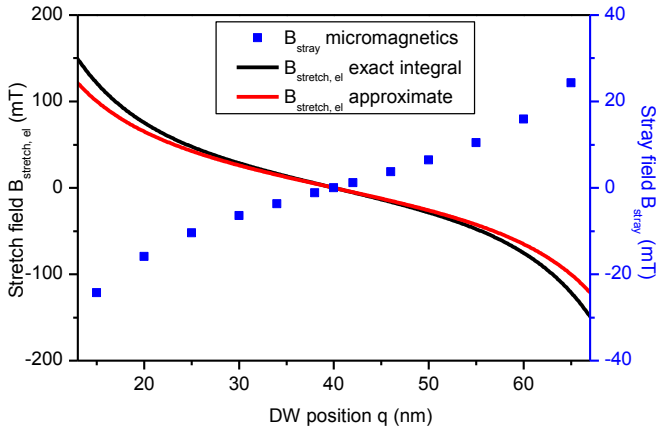

FIGURE 4.8: Elastic part of the stretch field (equation 4.39) and its large diameter approximation using the chord of a disk formula (equation 4.41). In blue: stray field $H_{\text{stray}}(q)$ of the two domains versus DW position in an 80 nm disk.

$$\frac{\dot{q}}{\Delta} + \alpha\dot{\phi} = \gamma_0 \frac{H_{N\leftrightarrow B}}{2} \sin 2\phi + \sigma j, \tag{4.37}$$

where we introduced two new fields: the stretch field (from the integrals of exchange and anisotropy) and the stray field (added in an ad hoc manner). It is of great interest that these coupled equations are exactly similar to the one computed in the case of the stripe in the previous section, apart from the disk-specific terms that we shall now discuss.

4.3.2 The disk specific terms

The stretch field

The stretch field $H_{\text{stretch}}(q,\phi)$ is the sum of two contributions: an elasticity part $H_{\text{stretch,el}}(q)$ that solely depends on the wall position and a dipolar part $H_{\text{stretch, NB}}(q,\phi)$ that depends on both q and ϕ and that is related to the Néel or Bloch (NB) nature of the domain wall.

The elasticity part of the stretch field reads:

$$H_{\text{stretch, el}}(q) \equiv \frac{2\sqrt{A_{\text{ex}}K_{\text{eff}}}}{\mu_0 M_s} \frac{1}{S_{\text{DW}}(q)} \frac{\partial S_{\text{DW}}(q)}{\partial q} \tag{4.38}$$

or equivalently:

$$H_{\text{stretch, el}}(q) = H_k^{\text{eff}} \frac{\Delta}{S_{\text{DW}}(q)} \frac{\partial S_{\text{DW}}(q)}{\partial q} \tag{4.39}$$

This term, which comes from the integrals of both the effective anisotropy and the exchange, simply illustrates that while moving within the disk the length of the wall varies and this costs energy, hence why this effect isn't found for a stripe of constant

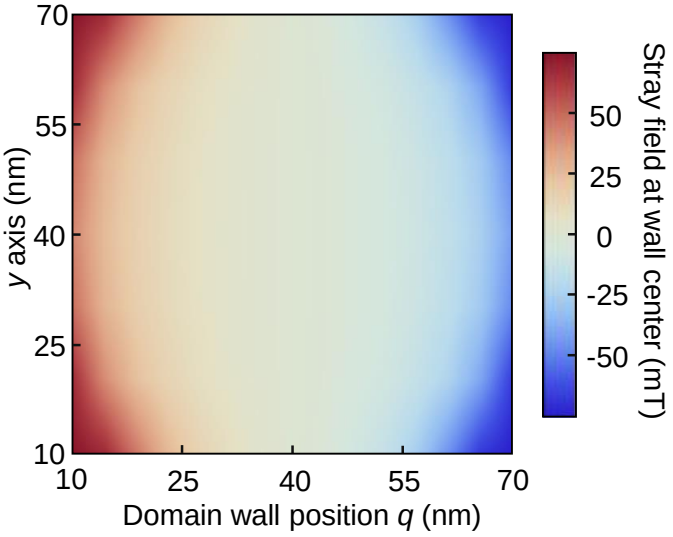

FIGURE 4.9: Stray field profile. The stray field is represented as a heat map versus the position of the domain wall q along the x axis and along the domain wall length following the y axis. The domain wall is assumed straight and therefore the data are less relevant when q is far from the center of the disk.

width. $H_{\text{stretch,el}}$ plays the same role as an out-of-plane external field: it applies a pressure on the wall. As the domain wall moves in the disk, its length first increases (leading to $H_{\text{stretch,el}} < 0$, opposed to the forward motion of the wall) then decreases once it has crossed the disk center (leading to a positive $H_{\text{stretch,el}}$ that favors the forward motion of the wall).

The other part of the stretch field depends both on the wall position q and on the wall configuration ϕ (Néel or Bloch, NB). This $H_{\text{stretch,NB}}$ accounts for the fact that when a Néel domain wall is displaced, this induces a change of the volume in which this Néel wall induces volume magnetic charges. It reads:

$$H_{\text{stretch,NB}}(q,\phi) \equiv \frac{H_{N\leftrightarrow B}}{2}\frac{\Delta}{S_{\text{DW}}(q)}\frac{\partial S_{\text{DW}}(q)}{\partial q}\cos^2\phi \tag{4.40}$$

From Eq. 4.39 and 4.40, it is clear that the spatial variations of the two parts of the stretch field are identical. However they have very different magnitudes, with a ratio being:

$$\frac{H_{\text{stretch,NB}}}{H_{\text{stretch,el}}} \leq \frac{H_{N\leftrightarrow B}}{2H_k^{\text{eff}}}$$

so that the dipole-dipole part of the stretch field is typically a tenth of the elasticity part.

For large disks with $R \gg \Delta$, the stretch field can be approximated using equation 4.35:

$$H_{\text{stretch}}(q,\phi,R\gg\Delta) \approx \left(H_k^{\text{eff}} + \frac{1}{2}H_{N\leftrightarrow B}\cos^2\phi\right)\frac{\Delta(R-q)}{q(2R-q)} \tag{4.41}$$

The elastic part of the stretch field is strong (figure 4.8) ranging from -150 mT to 150 mT from one edge to the other on a 80 nm disk. It has a cubic shape with a zero and an inflection point at the disk center. The demagnetizing part is much smaller as mentioned.

The stray field

The stray field is the dipolar field induced by the two domains onto the domain wall. Since in our finite disk geometry these two domains are not of the same size,

this field is non-zero and should be added to the potential in an ad-hoc manner, just like we did in equation 4.36. It depends on the position of the domain wall within the disk, being zero in the center and changing sign. It is maximum when the wall is at an edge because the two domains are then the most distinct.

Like most demagnetizing effects this field is non-uniform. For an accurate evaluation it has to be computed numerically, in practice using mumax3: we replace the domain wall by a straight non-magnetic gap and estimate the resulting total demagnetizing field at the center of this gap. The gap is necessary to separate the demagnetizing contributions from within the domain wall (which are already included in the stiffness field and the effective anisotropy) from the stray contributions of the two domains. This procedure is used to obtain the demagnetizing field at the center of the gap for several different gap position along the x axis (which corresponds to different q values) and for different positions along the y axis (namely along the domain wall length). The result is shown in figure 4.9. One can see that the stray field is indeed maximum at the edges and zero at the center while changing sign, for all positions along y. The y dependence of the stray field shows that it is stronger close from the edges compared to the center, but this effect is much more pronounced when the domain wall is also placed far from the center.

To incorporate the stray field into our model in a simple manner, we make the assumption that the domain wall sees a uniform stray field along its length $H_{\text{stray}}(q)$ (to keep the one dimension assumption). We chose to define $H_{\text{stray}}(q)$ as the demagnetizing field at the center of the domain wall length. This assumption is reasonable when the domain wall is placed near the center of the disk as seen in figure 4.9. When the domain wall is near the edges this assumption seems hazardous following the figure. But since this data was obtained for a straight domain wall (the straight non-magnetic gap) and since the domain wall bends itself near the edges, figure 4.9 is not relevant in this region anyway. Fortunately the stray field is a rather small effect compared to the stretch field as we will show, meaning that this causes a minute error. This is confirmed by comparing the effective fields model with the exact potential model where the stray field of a straight wall is considered exactly.

The value of $H_{\text{stray}}(q)$ are shown in figure 4.8 for a 80 nm disk. It is typically 5 times smaller than the stretch field and it is of opposite sign. This means that the stray field attracts the domain wall towards the center of the disk where it is compensated, in contrast to the stretch field. The stray field reaches 25 mT when the wall is near the edge of a 80 nm disk and has a shape that resembles very much that of the elasticity part of the stretch field. This shape similarity can be understood since in the ultrathin limit, the stray field that the two domains radiate on the wall is mostly dominated by the magnetization configuration in the direct vicinity of the wall. Qualitatively, the left and right neighbourhoods of the wall have compensating contributions, except for the parts near the perimeter; these uncompensated parts carry a total moment proportional to $\frac{\partial S_{\text{DW}}(q)}{\partial q}$ and generate a field that is diluted on the full domain wall surface S_{DW}. As a result, the stray field has q-dependence that resembles the $\frac{1}{S_{\text{DW}}(q)}\frac{\partial S_{\text{DW}}(q)}{\partial q}$ shape of the stretch field.

Position dependent stiffness field

We terminate this review of the different effective fields by a word of caution. So far we have abusively considered while computing the equations that the domain wall stiffness field $H_{N\leftrightarrow B}$ is independent from the DW position. We need to analyse the validity of this approximation. Indeed a Bloch wall generates surface charges at both

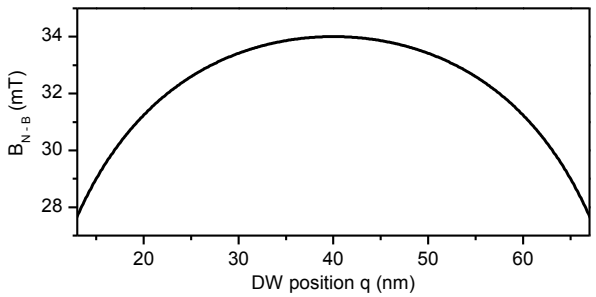

FIGURE 4.10: Domain wall stiffness field $H_{N\leftrightarrow B}$ versus domain wall position in a 80 nm disk. The graph is obtained from the demagnetizing factors approximate expressions (equation 4.6).

end of its length. As the DW length varies also with the position q, the associated internal demagnetizing field also varies and the energy difference between the Bloch and Néel configurations also does. The magnitude of this variation can be estimated from the approximate expression of the domain wall demagnetizing factors (equation 4.6) in which the stripe width w should be replaced by the wall effective length ℓ_{wall}. This would predict $\mu_0 H_{N\leftrightarrow B} = 34$ mT when the wall is at the disk center and $\mu_0 H_{N\leftrightarrow B} = 28$ mT when the wall center is 13 nm away from the edges for disk of 80 nm diameter (see figure 4.10). These numbers indicate that the error done when approximating $H_{N\leftrightarrow B}$ by a constant number is of minor importance.

4.3.3 Deriving the effective field intuitively

This subsection is a side remark: the effective fields that we obtained with the cumbersome integrals over the disk can be guessed intuitively using general domain wall consideration. We present here briefly this approach.

The Zeeman energy U_Z is simply evaluated by the surface in which the magnetization has changed by $-2M_s$. Noticing that $\ell_{\text{wall}} \equiv S_{\text{DW}}(q)/\Delta$ is the wall effective length when at position q, the Zeeman energy can be written as:

$$U_Z(q) = -\mu_0 d M_s H_z \left(\pi R^2 - 2 \int_0^q \frac{S_{DW}(x)}{\Delta} dx \right)$$

such that the Zeeman force acting on the wall is:

$$\frac{\partial U_Z}{\partial q} = 2\mu_0 d M_s \frac{S_{DW}(q)}{\Delta} H_z \tag{4.42}$$

Equivalently, the two domains at $x \geq q$ and $x \leq q$ create a dipole field $H_{\text{stray}}(q)$ which is along z at the wall position. $H_{\text{stray}}(q)$ thus simply adds to H_z in equation 4.42.

As long as the wall is constrained to keep its native profile (equation 4.2) the effective anisotropy energy and the exchange energy can simply be accounted for by multiplying the domain wall surface energy density $4\sqrt{A_{\text{ex}} K_{\text{eff}}}$ by the wall cross-sectional area $d\ell_{\text{wall}}$ to get $U_{\text{el}} = 4d\sqrt{A_{\text{ex}} K_{\text{eff}}}(S_{\text{DW}}(q)/\Delta)$. The elastic force acting on the wall is thus:

$$\frac{\partial U_{el}}{\partial q} = 4d\sqrt{A_{\text{ex}} K_{\text{eff}}} \frac{\partial S_{\text{DW}}(q)}{\partial q} \tag{4.43}$$

Finally, the energy arising from the in-plane demagnetizing fields of the wall can simply be written as the product of the effective volume in which there are volume charges $2dS_{\text{DW}}$ and its uniaxial Néel-Bloch anisotropy field $H_{N\leftrightarrow B}$, i.e.

$$U_{\phi,NB} = \frac{1}{2}\mu_0 H_{N\leftrightarrow B} M_s \cos^2(\phi) \times (2d\ S_{\text{DW}}(q)) \tag{4.44}$$

This energy term yields two forces. The first force favors the Néel to Bloch transition and reads:

$$\frac{\partial U_{\phi,NB}}{\partial \phi} = -\mu_0 H_{N\leftrightarrow B} M_s d \; S_{\mathrm{DW}}(q) \sin(2\phi) \tag{4.45}$$

The second force favors the domain wall motion only when the wall has a Néel component (i.e. when $\phi \neq \pi/2 \; [\pi]$) and reads:

$$\frac{\partial U_{\phi,NB}}{\partial q} = \mu_0 H_{N\leftrightarrow B} M_s d \frac{\partial S_{\mathrm{DW}}(q)}{\partial q} \cos^2(\phi) \tag{4.46}$$

With this intuitive approach we have recovered the potential derived exactly in equation 4.30.

4.4 Domain wall motion within a disk: exact potential

Before discussing the implications of the coupled equations that we derived with the analytical potential within the disk, we present in this section a different approach to tackle the problem. In this third model, the potential U_{tot} is obtained numerically.

4.4.1 Why is a numerical potential necessary ?

The main approximation in our estimation of the total potential is the demagnetizing effects. The demagnetizing field seen by the domain wall was split into three parts: the infinite film z component which is within the effective anisotropy, the in plane component which is considered in the stiffness field and the stray field coming from the two domains which is added ad hoc to the potential to correct the infinite film term. Within these terms more approximations are made, most notably when determining the stiffness field using the demagnetizing factor formula (equation 4.6) which are only valid for a large disk. In the following section where we will compare the three models (micromagnetics simulations, analytical potential and exact potential), we shall see that for a 80 nm disk these approximations are reasonable while they are no longer valid at 40 nm.

In this section we recover the potential from mumax3 which suppresses most of our assumptions on the demagnetizing effects (save for the one of straight domain wall). However this method necessitates more numerical tools and the physics is less transparent since we cannot access each individual terms within the potential.

4.4.2 Methods: extracting the potential

The potential is obtained using mumax3. A domain wall state is created with varying q and ϕ and for each point the total energy of the system is saved using the E_total option. The domain wall remains straight for each of the points, which is going to be a limitation when we compare this model with the micromagnetic simulations where the domain wall curves itself.

One point is taken every 15 deg. for ϕ and one each nm for the domain wall position. The obtained matrix is then extrapolated and imported into mathematica to solve equations 4.32 and 4.33.

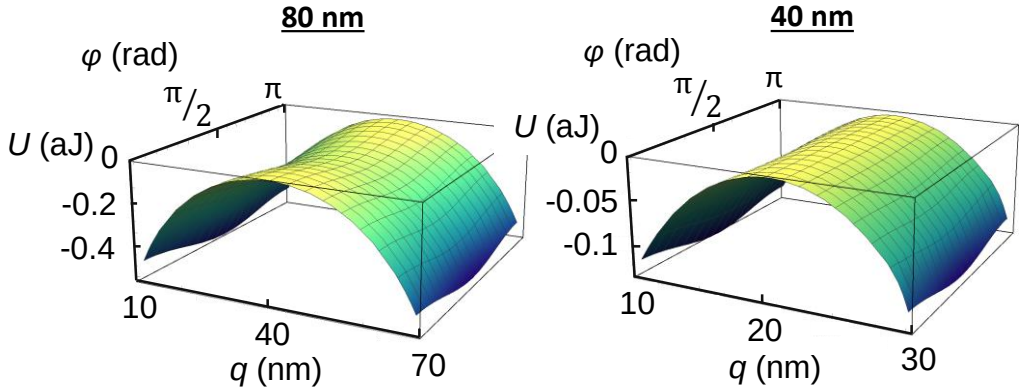

FIGURE 4.11: Energy landscapes U_{tot} extracted from micromagnetic simulations for all positions q and tilt angles ϕ for a straight domain wall in perpendicularly-magnetized disks of diameters left: 80 nm and right: 40 nm. A constant offset was added to the energy landscape to have the energy maximum be zero.

4.4.3 Discussion on the potential shape and the effective fields

The obtained energy landscape are shown in figure 4.11 for a 40 and a 80 nm disks. The 80 nm disk potential has the simpler shape: a saddle. The energy is minimum while on the edges and for a domain wall within the Bloch state. This shape was expected from our effective fields model because the stretch field minimizes energy near the edges and the stiffness field favors the Bloch configuration.

To be more quantitative on the 80 nm case, we extract different energy barrier from the graph. At a fixed angle of $\frac{\pi}{2}$ the energy barrier in the q direction, namely the energy difference between $q = 10$ nm and $q = 40$ nm, is 0.47 aJ. The one in ϕ at the center of the disk is 0.044 aJ, namely an order of magnitude lower than the one in q. In the effective field model previously derived, the stretch field is varying by 200 mT between $q = 10$ nm and the center. The stiffness field $H_{N\leftrightarrow B}$ was 34 mT at the center, which corresponds to the Néel versus Bloch transition field. The difference between these two fields gives very roughly an order of magnitude between the expected effects of varying q or ϕ. Quantitatively the significantly larger barrier in q than in ϕ seen in the potential is not surprising.

The 40 nm case is mostly similar, but the overall difference between Bloch and Néel configuration is weaker. Consequently the potential is flat at the center of the disk in the ϕ direction, meaning that no tilt angles are favored while the domain wall is near the center for this radius. In terms of effective field it would correspond to a stiffness field getting close to zero. This cannot be checked in the effective field model because the demagnetizing factor equations 4.6 are not valid for smaller disks.

4.5 Comparing the domain wall trajectories from the three models

We have proposed several different models for the domain wall motion. First the micromagnetic simulations, or LLGS model, for which the equations are solved exactly on a grid and the domain wall is not considered as a soliton. Then the domain wall model within the one dimension approximation (or (q, ϕ) model) for a stripe, this could already explain the coupled oscillations of q and ϕ seen in the micromagnetic simulations. Then we proposed the same model derived for a disk, which is

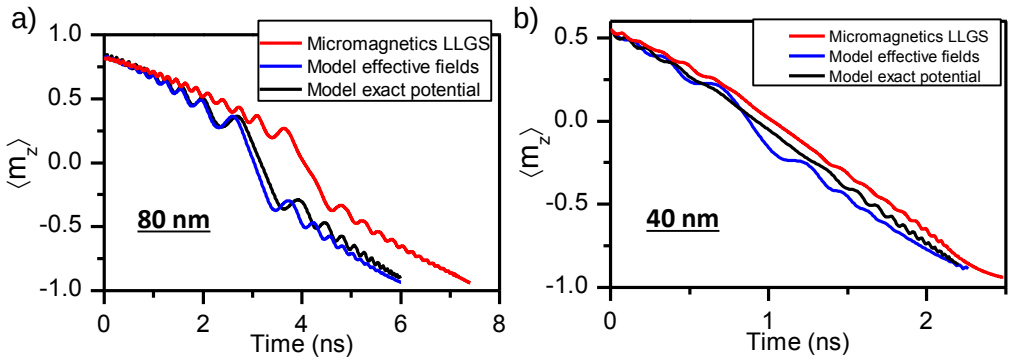

FIGURE 4.12: Comparison between the micromagnetic simulations of the dynamics of a wall with initial optimal curvature (red curves), the collective coordinate model with the exact energy landscape ($\{q, \phi\}$ model with exact U_{tot}, black curves), and the collective coordinate model with the approximate analytical effective field (blue curves). a) Mean value of the z component of the magnetization evolution during the DW motion for a disk of 80 nm diameter. The initial conditions are for $q_0 = 10$ nm and $\phi_0 = 70$ deg. There is no external field and the voltage corresponds to V_c for this diameter. b) Idem in a smaller disk of diameter 40 nm.

called the effective field model or analytical potential model. Finally we showed the same model but with the exact potential obtained numerically, called the numerical or exact potential model.

In this section we compare the trajectories predicted by the LLGS, analytical potential and exact potential model. We focus on the main features of the reversal and shall dedicate a full section to the complex dependence on the initial conditions.

4.5.1 Qualitative features

Figure 4.12 compares the three models for disks of 80 or 40 nm. For the 80 nm case depending on initial conditions several behaviours are possible for the domain wall near the center of the disk, in this figure we selected trajectories presenting the most common type of center crossing (the drift-like one way crossing). We obtain $\langle m_z \rangle(t)$ for the (q, ϕ) model from $q(t)$ using the formula:

$$\langle m_z \rangle = \frac{2}{\pi R^2} \int_{-R}^{R} \tanh\left(\frac{x-q}{\Delta}\right) \sqrt{R^2 - x^2} \mathrm{d}x \tag{4.47}$$

Concerning the 80 nm disk there is a very good qualitative agreement between the micromagnetic simulations and the two (q, ϕ) models. The same coupled oscillations on top of a drift are predicted, in the models as well the domain wall moves forward after reaching the Néel configuration similarly to the snapshots of figure 4.2. The same position dependence of the amplitude and of the frequency of the oscillations are predicted, with $\dot{\phi}$ changing sign in the center. The three models also predict that the domain wall can only cross the center in a Bloch configuration. For this large disk, there is no noticeable difference between the exact and the approximate potential models, meaning that our assumptions on the potential using the effective fields are very satisfying for this size regime.

For a 40 nm diameter, there is a good agreement between the micromagnetic model and the $q - \phi - U_{tot}$ model but the approximate $q - \phi - H_{\text{tot}}$ model is not as satisfactory: the amplitude of the oscillations are overestimated. This reveals

the limits of our analytical approximations at small disk diameters. For this size or smaller the numerical approach is necessary for the demagnetizing effects.

4.5.2 Explaining the trajectory with the effective fields

As already stated, the equations of the model with effective fields (equation 4.36 and 4.37) are similar to the one obtained in the stripe case (equation 4.16 and 4.17) if the external field H_z is replaced by the total field $H_{\text{tot}}(q) = H_z + H_{\text{stretch}}(q) + H_{\text{stray}}(q)$. Therefore all the remarks made on the stripe case considering the Walker breakdown, the linear versus oscillating regime and the description of the oscillating regime are still valid. The Walker field is of the same order of magnitude within the disk as within the stripe of equivalent width since the stiffness field $H_{N\leftrightarrow B}$ depends only very little on q (figure 4.10). Consequently the domain wall within the disk is everywhere within the oscillating regime, save for a very tiny position window near the disk center. We can use by analogy with the stripe the approximate expression that we proposed to describe the domain wall motion (equation 4.23, 4.26 and 4.27).

According to the analytical potential model and away from the position at which $H_{\text{tot}} = 0$, the drift velocity within the disk is given by:

$$\bar{\dot{q}} \approx \Delta(\sigma j - \alpha\gamma_0 H_{\text{tot}}(q)) \tag{4.48}$$

Within the same conditions the frequencies and the q oscillation amplitude can be approximated (neglecting α^2 but not $\alpha\sigma j$) by:

$$\omega_q = 2\omega_\phi \approx 2(\gamma_0 H_{\text{tot}}(q) + \alpha\sigma j) \tag{4.49}$$

$$D_{\text{osc}} \approx \Delta \left| \frac{H_{N\leftrightarrow B}}{2H_{\text{tot}}(q) + \alpha\sigma j} \right| \tag{4.50}$$

With these expressions as well as the shape of the effective fields (figure 4.8) in mind, the domain wall trajectories are easily understood. If we assume no external field the total field is basically given by the stretch field since the stray field is of the same shape and 5 times as small. The drift is composed of a constant value given by the spin transfer torque, but also varies as the domain wall advances because of the stretch field effect following $-\alpha\gamma_0 H_{\text{tot}}(q)$. The oscillations start with a large frequency and small amplitude as the stretch field is maximum near the edges; the amplitude diverges while the frequency vanishes near the center where the stretch field gets to zero and our assumptions on the oscillating regime get invalid; once the center is crossed $\dot{\phi}$ changes sign because the stretch field changes sign.

The domain wall motion seen within the simulations was well reproduced by our models and understood by our effective fields approach. Now we propose a more quantitative comparison.

4.5.3 Quantitative comparison

Figure 4.13 presents the instantaneous frequencies extracted from the micromagnetic simulations or the numerical potential models and compares it to the prediction from equation 4.49 at different domain wall positions. The good agreement between the two (q, ϕ) models proves that the approximations made writing equation 4.49 are reasonable for this diameter. The agreement between these two models and the LLGS is however far from satisfactory.

From a thorough examination of the comparisons done in figures 4.12 and 4.13 we can conclude that $q - \phi$ models only slightly overestimate the domain wall drift

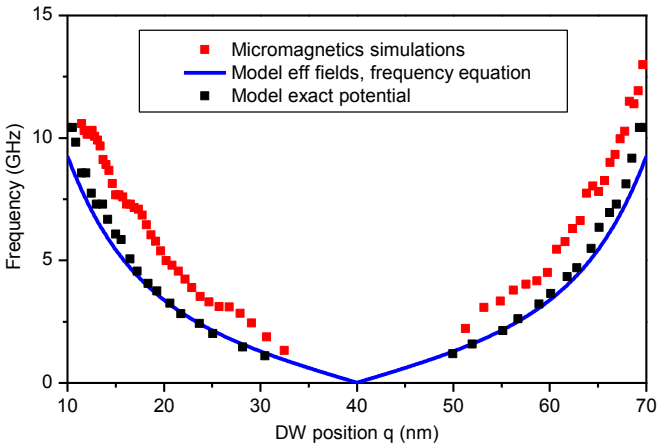

FIGURE 4.13: Characteristic frequency of the oscillatory part of the domain wall motion along its motion through a disk of diameter 80 nm. Relation between the inverse of the wall oscillation period and the mean wall position during this period as predicted by the micromagnetic simulations (red symbols) and by the $q-\phi-U_{tot}$ model (black symbols). The blue line is frequency inferred from the analogy with the infinite stripe case (equation 4.49).

velocities while they are much less accurate to account for the oscillatory part of the motion. This can be understood with the help of equation 4.48 and 4.49. Indeed σj is a constant number ($\approx$ 1 GHz) during the wall motion. The term $\gamma_0 H_{\text{tot}}(q)$ is comparatively larger as well as position dependent. For instance it varies between typically -25 and 25 GHz from one edge of an 80 nm disk to the other edge (figure 4.8).

Having in mind the typical values of $\gamma_0 H_{\text{tot}}(q)$ and σj, we find that the term $\alpha\sigma j$ is much smaller than $\gamma_0 H_{\text{tot}}(q)$ except right at the disk center, such that the dynamics of the tilt (equation 4.49) is resulting from the sole effective fields (except at the disk center). Since the effective fields depend on the exact wall shape and exact tilt state, their accuracy is directly endangered by the approximation of a straight wall with uniform tilt which is made in both our $q-\phi$ models; the frequency mismatch between the predictions of micromagnetics and of the $q-\phi$ models can thus be interpreted as a failure to account precisely enough for the stretch field.

The situation is reversed for the domain wall drift velocity (equation 4.48): the term $\alpha\gamma_0 H_{\text{tot}}(q)$ amounts to a minor fraction (e.g. circa 25% when $2R = 80$ nm) of σj. The domain wall drift velocity prediction is thus little affected by potential errors in the stretch field. (Note that the term σj is independent of the domain wall shape and of its Néel or Bloch character, hence it is reliable despite our straight wall and uniform tilt approximations). Our assumptions of a straight wall with uniform tilt are thus much less detrimental to the accuracy of the predictions of the domain wall drift dynamics than the oscillatory part of the dynamics. The equations 4.50 and 4.49 should thus be considered as indicative only.

Now that we have established the degree of accuracy with which the collective coordinate models describe the dynamics, let us see whether they can shed further light onto the origin of the sensitivity of the wall dynamics to the initial conditions.

4.6 Origin of the sensitivity to initial conditions

4.6.1 Describing the sensitivity

From the micromagnetic simulations we observed a sensitivity to the initial state (position or tilt angle) in the 80 nm disk either for an initial domain wall or for a full reversal at 300 K. The full switching simulation at 0 K does not present such variability because the center domain expands longer in the center than at 300 K and therefore after the nucleation the domain wall is already past the center. Three

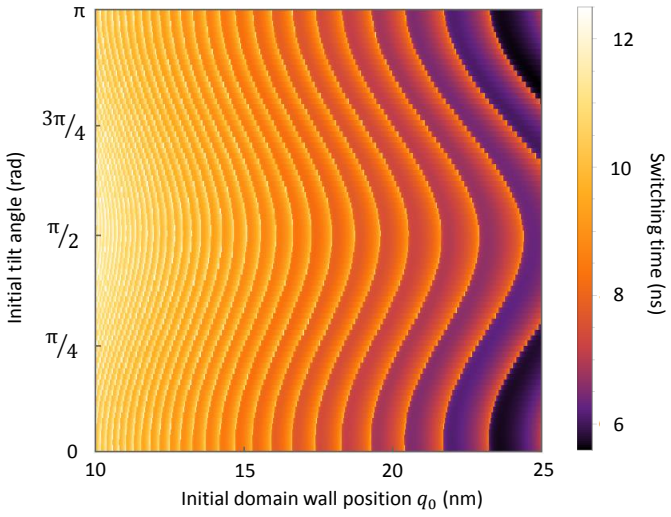

FIGURE 4.14: Plot of the total switching time while varying the initial tilt angle and initial position of the domain wall. Data obtained from the numerical potential (q, ϕ) model, on a 80 nm disk under V_c. The slower switching (bright contours) on a fixed initial position column corresponds to the one-way crossing with pre- and post-crossing pauses scenario.

scenarios are observed in the micromagnetic simulations and were described in figure 4.2: linear-like crossing ($\approx$ 85% of simulations), one-way crossing with pre- and post-crossing pauses ($\approx$ 10%) and swing like crossing ($\approx$ 5%).

Concerning the (q, ϕ) models (analytical and numerical potential within a disk), while the same sensitivity to the initial condition is seen with approximately the same probabilities, the swing-like crossing is impossible to replicate. Since computing the domain wall trajectory is several thousands time faster with these models than from micromagnetic simulations, they allow a complete mapping of the (q_0, ϕ_0) space. Such mapping is done for the 80 nm disk in figure 4.14 using the total switching time (defined as the time needed to cross the center of the disk) to differentiate the linear-like crossings from the more delayed crossings. In this figure it is shown vertically than we can vary the switching time (namely the behaviour at the center of the disk) by varying the angle at fixed initial position (single column). Horizontally two effects are observed: first the closer we are from the disk center and the faster is the overall switching; second if we move the domain wall from q_0 to $q_0 + D_{\text{osc}}(q_0)$ we recover the same crossing in the center having simply skipped one q oscillation and therefore increased the switching time. The study of the (q, ϕ) space is going to shed light into the sensitivity.

4.6.2 Phase plots and retention pond

The phase space is shown in figure 4.15 for the 80 nm case, along with two corresponding $q(t)$ plots. It is obtained by using the *streamplot* function in mathematica while solving equation 4.36 and 4.37 (the phase plot is similar to the numerical potential approach for the 80 nm disk). To understand the physical origin of the sensitivity of the dynamics to initial conditions, it is convenient to first discuss the case of a Néel wall initially placed at the center of the disk (this corresponds to $\{q_0, \phi_0\} = \{R, 0\}$). The system is in the absolute maximum of the energy landscape (figure 4.11). Some work of non-conservative torques (damping and spin-torque) is thus needed to allow the wall to move away from this energy maximum. In the collective coordinate space, the trajectory from this specific wall position is an outgoing spiral. The wall first swings about the center with an increasingly large amplitude. In this transient process, there is a back-and-forth transfer of energy between the position degree of freedom of the wall and the Néel/Bloch degree of freedom of the wall: U_{el} and $U_{NB,\phi}$ act as communicating vessels. The wall can escape from the

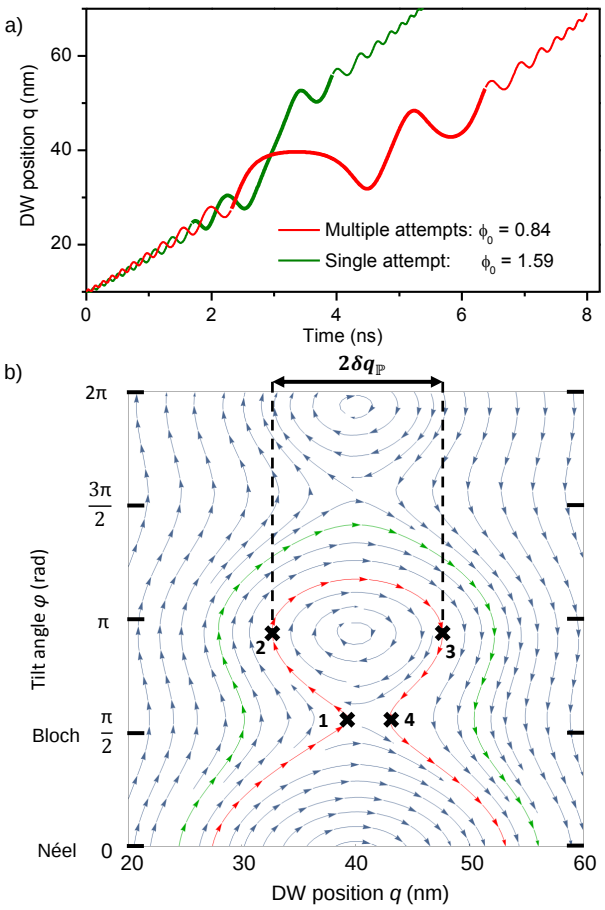

FIGURE 4.15: Domain wall dynamics within a disk of 80 nm diameter in the collective coordinate model with analytical potential. a) Time dependence of the position of the DW for two different initial tilt angles of 48 and 91 deg and the same initial positions $q_0 = 10$ nm. b) Description of the possible trajectories of the domain wall in the space of the collective coordinates. $\phi = 0$ corresponds to a Néel wall and $\phi = \pi/2$ to a Bloch wall and the landscape is π periodic in the ϕ direction. The colored trajectories correspond to the bold-colored parts of the trajectories in the top graph. The contour traced along the labels 1,2,3 and 4 of the red trajectory is very close to the retention pond frontier $\partial\mathbb{P}$.

central part of the disk and sweep to the edge only when sufficient energy has been dissipated.

This central part in which the wall is transiently stuck is a zone of the (q, ϕ) space that we shall quote hereafter as the "retention pond", written $\mathbb{P}$ and illustrated as the red contour from labels 1 to 4 in figure 4.15. Within the $q - \phi$ model, all trajectories crossing the frontier $\partial\mathbb{P}$ are *outgoing* trajectories. As a result a domain wall that exits from the retention pond will subsequently cross the disk center but it never performs so while being in a Néel configuration, in line with the conclusions of the micromagnetics study for this diameter of 80 nm. No domain wall trajectories starting from the edges can enter the retention pond. In the absence of spin-torque, $\mathbb{P}$ is centered on $\{q = R, \phi = 0\ [\pi]\}$. It is distorted for strong values of the applied spin-torque (see section 4.7.2).

Before discussing the consequence of the existence of the retention pond, we mention that for disks smaller than a threshold to be determined later (equation 4.52), $H_{N\leftrightarrow B}$ is negative and the retention pond is then centered about the Bloch configuration. Extrapolation of our arguments to that case is trivial.

4.6.3 The retention pond causes the sensitivity

Having in mind the concept of the retention pond, let us return back to our case study which is the wall dynamics after an hypothetical nucleation of a domain wall near the disk edge, i.e. out of the retention pond. The strong sensitivity of the dynamics to the initial conditions can be understood as follows. The wall progressive drift and the superimposed oscillations are rather independent phenomena such

that when the wall heads to the center of the disk, it can either approach close to the retention pond $\mathbb{P}$ or pass at a large distance from $\mathbb{P}$ depending solely on initial conditions. If the wall avoids the vicinity of the retention bond, it crosses the disk center and performs a one-way, single attempt crossing. If in contrast the wall happens to approach the retention pond, it will have to circumvent it which leads to a more complex trajectory.

These two scenarios are illustrated in figure 4.15. The green curve corresponds to a trajectory with initialization being $\phi_0 = 48$ deg.. Along its trajectory, the wall passes the disk center with a quasi-Bloch configuration, far from the retention pond. The resulting trajectory is archetypal of the drift-like one-way crossing identified in micromagnetics figure 4.2.b. If adding $\Delta\phi_0 \approx \pi/4$ to the initial tilt (red curve in figure 4.15), one obtains the antonym case: the domain wall trajectory arrives in a tangent manner to (but outside) the retention pond $\mathbb{P}$. The wall performs a single turn about $\partial\mathbb{P}$ thereby making a considerable back-and-forth motion with two pauses at either sides at the disk center. This recalls the one-way crossing with pre- and post-crossing pauses formerly identified in the micromagnetic description (figure 4.2.c).

In short, the $\{q-\phi\}$ models can explain *some* sensitivity to the initial conditions: depending on $\{q_0, \phi_0\}$ the crossing is either of the type drift-like one-way crossing, or entails pre- and post-crossing pauses. However the swing-like crossing with multiple attempts (figure 4.2.d) cannot be obtained in the framework of the $\{q-\phi\}$ models. We will discuss this case in the last section of this chapter by going beyond the one dimension approximation.

4.6.4 Size of the retention pond versus diameter

From the above discussion, we conclude that the respective probabilities of occurrence of the drift-like one-way crossing and the one-way crossing with pre- and post-crossing pauses are correlated with the size of $\mathbb{P}$ with respect to the full $\{q-\phi\}$ parameter space. If one aims at a reproducible domain wall propagation duration while not being able to control the initial wall position and tilt (or if the thermal noise is large enough to let q and ϕ diffuse with time), it is important to determine the size of $\mathbb{P}$. Let us define $\delta q_{\mathbb{P}}$ the half width of the retention pond in the q direction (see figure 4.15) and derive it in the conservative limit when the wall follows a constant energy path. We can estimate $\delta q_{\mathbb{P}}$ by comparing the energy of the saddle point of U_{tot} with that of a Néel wall $\delta q_{\mathbb{P}}$ away from the center (these two states are close to the labels 2 and 1 in the figure):

$$\left(U_{\phi,NB} + U_{stretch} + U_{stray}\right)\Big|_{\substack{\phi=0 \\ q=R+\delta q_{\mathbb{P}}}} = \left(U_{\phi,NB} + U_{stretch} + U_{stray}\right)\Big|_{\substack{\phi=\frac{\pi}{2} \\ q=R}} \tag{4.51}$$

After approximating the effective wall length ℓ_{wall} as the length of the disk chord and having neglected the dipole energy U_{stray}, a straightforward algebra leads to the size of the retention pond:

$$\delta q_{\mathbb{P}} \approx R\sqrt{\frac{H_{N\leftrightarrow B}}{H_{\text{k,eff}}}} \tag{4.52}$$

This equation leads to $\delta q_{\mathbb{P}} \approx 11$ nm for a disk of diameter 80 nm. This result should be compared to the phase plot obtained from the (q,ϕ) models in the absence of spin

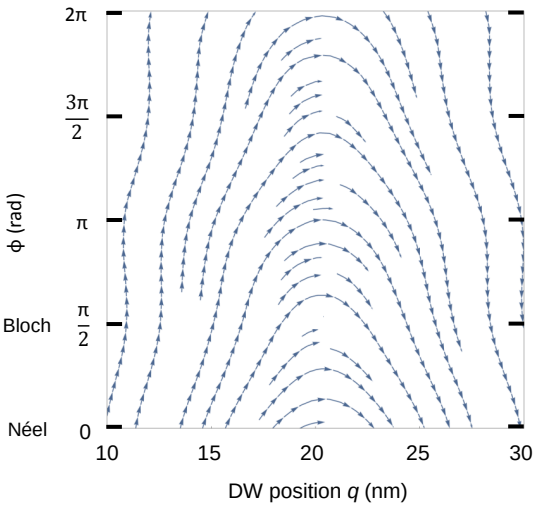

FIGURE 4.16: DW dynamics within a disk of 40 nm diameter in the collective coordinate model with the exact energy landscape for $H_z = 0$ and $V = V_c$. The streams describe all possible trajectories of the DW in the space of collective coordinates. The are interrupted when they become too dense.

torque, since it will be shown that increasing the voltage reduces the pond. Those 11 nm give a very good agreement as seen in figure 4.17.

4.6.5 Disk diameter for optimal reproducibility of the domain wall propagation

So far we have only discussed the 80 nm case. The phase space plot for the 40 nm disk is shown in figure 4.16. The overall behaviour is the same but there is no retention pond anymore. This is related to the flat energy landscape that was found in the center of the 40 nm disk (figure 4.11): in the center no tilt angle is favoured and therefore there is no longer the "forbidden Néel wall in the center" region in the phase plot.

This recalls the conclusions of the micromagnetic simulations (figure 4.3) for the 40 nm disk: the dynamics are insensitive to the initial tilt since there is no pond; the center crossing is always done linearly because no tilt angles are favoured; the center crossing can be done with any tilt angle for the same reason.

To be more general, we can determine the diameter $d_{\text{no}\mathbb{P}}$ for which the retention pond disappears. This situation happens when a wall placed at the center of the disk has the same energy when either in the Néel or in the Bloch state, i.e. when:

$$U_{\phi,NB}(q = R, \phi = 0) = U_{\phi,NB}(q = R, \phi = \frac{\pi}{2}) \text{ for } d = d_{\text{no}\mathbb{P}} \tag{4.53}$$

or equivalently when $H_{N\leftrightarrow B} = 0$. With our material parameters and using the numerical potential (since for those sizes the demagnetizing factors are unreliable), we find that the retention pond reduces indeed to a single point exactly when $d_{\text{no}\mathbb{P}} =$ 40 nm. This critical disk diameter $d_{\text{no}\mathbb{P}}$ is of interest for applications. Indeed it ensures that all the domain wall trajectories pass through the disk center in a ballistic way: the walls cross the center directly and almost independently from their Bloch or Néel character (figure 4.16). We can expect to maximize the reproducibility of the time needed for a domain wall to sweep across a disk, a feature that is of great interest for STTMRAM.

As a side remark, we mention that for diameters $2R < d_{\text{no}\mathbb{P}}$, we have $H_{N\leftrightarrow B} < 0$. As a consequence, while the retention pond formerly centered about the Néel state has disappeared, another one emerges from the central Bloch situation. However this new pond has little practical relevance with our material parameters. Indeed the

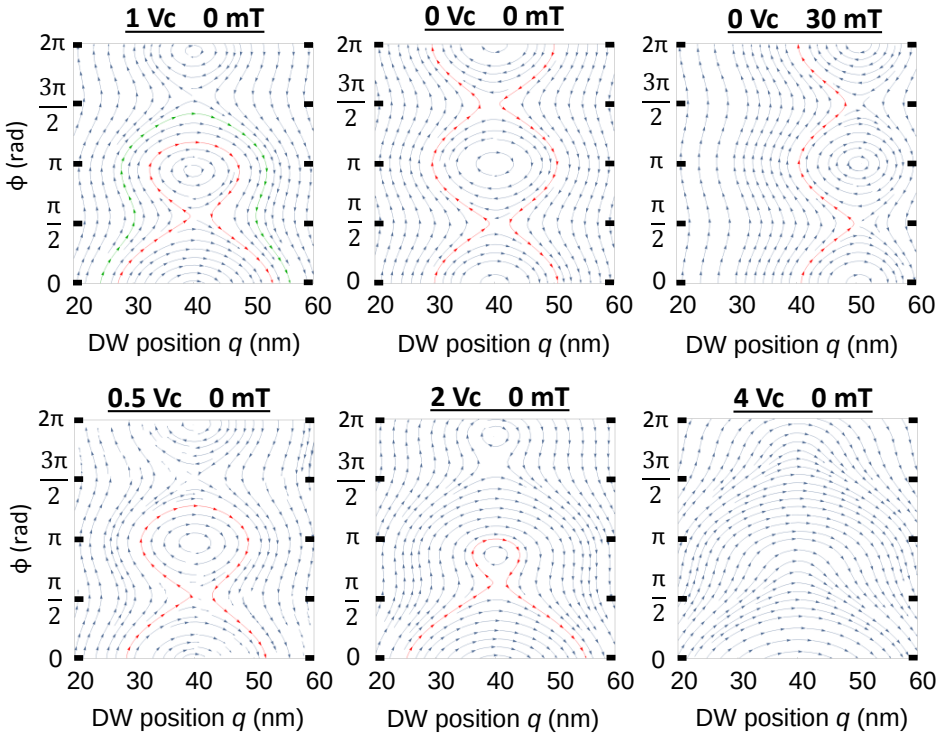

FIGURE 4.17: Domain wall dynamics within a disk of 80 nm diameter under various voltages and out of plane fields in the collective coordinate model with analytical potential. The streams describe all possible trajectories in the (q, ϕ) space. The red colored trajectories is chosen close to the frontier of the retention ponds, when existing.

energy difference between the Bloch and Néel states of a central wall for $2R < d_{\text{no}\mathbb{P}}$ stays very small, of the same order as the thermal energy $k_B T \approx 4$ zJ (25 meV) at room temperature. For comparison, the energy difference between the Bloch and Néel states for a central wall at 2R=80 nm was 44 zJ (275 meV).

In this section the study of the trajectories in the phase space allowed us to understand and predict the initial conditions dependence of the center-crossing that was observed on the 80 nm disks, but also to understand why such sensitivity isn't found at 40 nm.

4.7 Impact of the external stimulus and of each material parameter

In this section we discuss the impact of most of the parameters we used in our models. We also give an insight on how to include other terms such as Dzyaloshinskii–Moriya interaction within this paradigm. This discussion will be based mostly on the analytical potential model since it is the model for which the role of each effects is the most straight-forward to identify.

4.7.1 External field

Out of plane fields

Adding an external field along the z direction will change the total field $H_{\text{tot}}(q)$ term in equations 4.48, 4.49 and 4.50. This offset shifts the position q for which the total field seen by the domain wall is zero. This corresponds to a shift in the (q, ϕ) space of the pond position in the q direction (as illustrated in figure 4.17).

If the external field is greater than the maximum value of the stretch field (around 200 mT in a 80 nm disk), then the retention pond is pushed out of the phase space. Consequently in that case the domain wall crosses the full disk without entering strong oscillations and without being sensitive to the initial conditions. The complex dynamics that we described are only possible when the total field seen by the domain wall cancels out somewhere during its motion.

In a STTMRAM device, there are stray fields coming from the rest of the system (reference and hard layer) into the free layer. Along the z direction those fields are non-homogeneous and of the order of a few tens of mT [29] in our IMEC devices. This is smaller than the stretch field therefore the total field should be zero for at least one position during the domain wall motion (more than one position is possible because those stray fields are non-homogeneous).

In plane fields

So far we have only discussed the system in the presence of out-of-plane fields. A field along the x and y direction should be added to the Zeeman micromagnetic energy, $u_{\text{IP field}} = -\mu_0 M_s \sin\theta(H_x \cos\phi + H_y \sin\phi)$ before being integrated along the disk:

$$U_{\text{IP field}} = -2d\mu_0 M_s (H_x \cos\phi + H_y \sin\phi) \int_{-R}^{R} \operatorname{sech}\left(\frac{q-x}{\Delta}\right) \sqrt{R^2 - q^2}\,\mathrm{d}x \qquad (4.54)$$

The complex integral appearing is very similar to S_{DW} that was introduced previously, but the hyperbolic secant function isn't squared here. The overall potential is close from the stiffness contribution previously derived (equation 4.30 or 4.44). It is possible, but cumbersome, to derive the equations of motion with this additional term to obtain equations similar to 4.36 and 4.37. But from this potential alone we can already discuss the impact that the in plane field has on the domain wall dynamics. As this term depends both on q and on ϕ it will be present in the Euler-Lagrange equations for the two collective coordinates. The ϕ dependence creates $\cos\phi$ and $\sin\phi$ terms in the second equation, which will have the same role as the stiffness field term $H_{N\leftrightarrow B} \sin 2\phi$. The q dependence creates an extra component to the stretch field which still depends on ϕ just like the stiffness contribution to the stretch field, but with a 2π periodicity instead of π.

We study the exact dependence of the trajectories on H_x and H_y using phase plots, some example are given in figure 4.18 for low field along x and large fields along x or y. Overall a low in plane field (a few mT) along any direction differentiate two ponds: the system becomes 2π periodic instead of π in the ϕ direction. The position and the size of the two ponds depend on the amplitude and the direction of the applied field (figure 4.18.a). Once the in plane field is sufficiently large (a few tens of mT) only one pond remains (centered around π for H_x and $\frac{3\pi}{2}$ for H_y as seen in figure 4.18) and grows larger if we increase the corresponding in plane field. We insist that even though it is a single pond just like in the phase plots described so far, this one is 2π periodic and not π periodic. For instance for the $H_x = 50$ mT phase

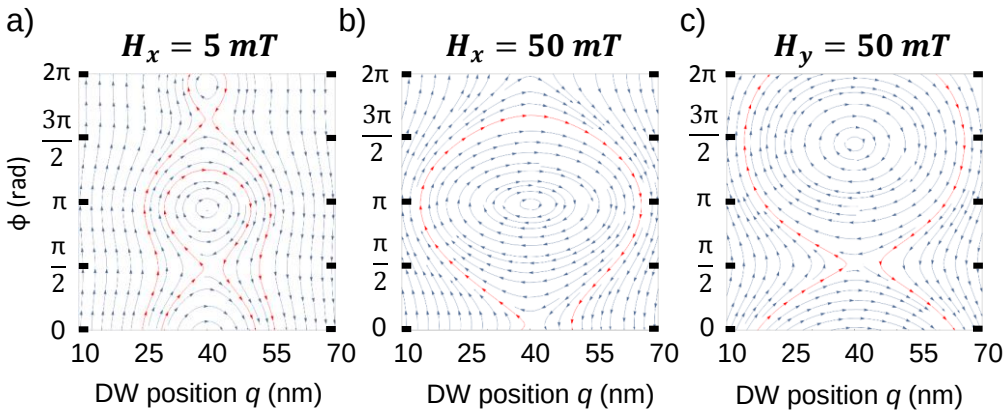

FIGURE 4.18: DW dynamics within a disk of 80 nm diameter under various in plane fields in the collective coordinate model with analytical potential. The system parameters are the usual one, there is no external field along z, the applied voltage corresponds to V_c. The streams describe all possible trajectories of the DW in the space of the collective coordinates q and ϕ. a) Typical phase plot for a low in plane field along any direction, illustrated here with $H_x = 5$mT. The two following graphs show the dependence of the position of the pond on the field direction at high applied field, with 50 mT applied along b) x or c) y.

plot in figure 4.18.b, the Néel wall at $\phi = \pi$ is inside a maximum of energy (retention pond) while $\phi = 0$ which is still a Néel wall but this time with the minimum of energy with respect to the tilt degree of freedom. With this type of single pond our discussion on the sensitivity of the domain wall dynamics to the initial condition can still be extrapolated to this system, strong Walker oscillations are expected.

Our system appears to be very sensitive to the in plane fields. This is a limitation of our model for predicting the reversal of STTMRAM devices, since the in plane stray fields from the reference system are expected to go up to a few tens of mT [29]. In a real device it is also impossible to control the direction of the in plane field since we do not know the normal of the domain wall and since it can gyrate around the center like what was seen in some of our simulations (figures 4.2 and 4.3).

4.7.2 External voltage

So far we have shown only domain wall motion under a voltage corresponding to V_c (1 V at 40 nm and 0.855 V at 80 nm). If we change the voltage it will affect linearly the drift velocity (equation 4.48) and affect weakly the amplitude and frequency of the oscillations because of the $\alpha\sigma j$ term (equations 4.49 and 4.50).

However near the disk center when those formula are no longer valid because we exit the oscillating regime, the voltage can have a more complex impact on the wall dynamics than a simple drift. This is illustrated by the phase plots given for 5 different voltages (0, $0.5V_c$, V_c, $2V_c$ and $4V_c$) in figure 4.17. The stronger is the voltage, the more all the trajectories are bent towards the center because of the drift contribution. This goes with a reduction of the size of the retention pond as the voltage increases, up until the pond totally disappears for a value between 3 and 4 V_c. This is due to the fact that the oscillating terms coming from the micromagnetic potential become less relevant as the voltage increases, this is especially true at the center where the total field cancels out in the absence of external contribution.

Consequently the larger is the voltage and the more the trajectory becomes ballistic. It could be said that increasing the voltage or reducing the size (above 40 nm) both have the effect of reducing the pond and making the switching more deterministic. A word of caution is needed: even for the 4 V_c phase plot where the pond do not exist, all the tilt angles at the center are not equivalent. Some are still more likely to be found which is illustrated in this graph by the density of trajectories in the center.

In terms of memory application this is good news: the strong Walker oscillations that we predicted in this chapter and in our micromagnetic simulations at 300 K for devices of more than 40 nm are reduced as we increase the voltage. In the fast regime that is targeted for applications we expect the voltage to be of the order of V_c at least, but smaller than the value necessary to totally suppress the pond. On the other side of this coin, if we want to observe the predicted Walker oscillations in a time-resolved measurement, we should study the reversal of a disk between 50 and 100 nm diameter, at low voltage, while sweeping the applied external field along z to make sure the total field cancel out. This approach will be presented in the time-resolved measurement chapter, but no clear Walker oscillations are to be found.

4.7.3 The annihilation critical voltage

Let us consider a domain wall nucleated near the edges at the position $q_0 = \frac{\pi\Delta}{2}$ in the 80 nm disk. The oscillations are of high frequency and low amplitude because the stretch field is maximum. Thus, we assume that the domain wall dynamics is essentially described by the equation of the drift velocity 4.48. If the voltage is sufficiently low, it does not overcome the total field term and therefore the domain wall moves backwards overall: it is annihilated. If we assume that there is no external field and if we neglect the stray field from the domains compared to the stretch field, this corresponds to an annihilation voltage of:

$$V_{\text{anni}} = \frac{2\alpha\mu_0 \mathcal{A} R_\perp e M_s t_{\text{mag}}}{P\hbar} H_{\text{stretch}}(q = \frac{\pi\Delta}{2}) \tag{4.55}$$

The stretch field at position $\frac{\pi\Delta}{2}$ is obtained from equation 4.39 (see black curve in figure 4.8): it is equal to 144 mT. This results into an annihilation voltage of $V_{\text{anni}} =$ 0.2 V.

We compared this annihilation voltage to micromagnetic simulations. The domain wall is placed 13 nm from the edges and we sweep the voltage. Annihilation is indeed observed, for a voltage equal to 0.24 V. There is a reasonable agreement between the very simple approach that we proposed (only stretch field, only drift dynamics, no bending of the wall) and the micromagnetic simulations.

The fact that the annihilation voltage is of the order of 0.2 V has strong implications for STTMRAM applications. Indeed we know that at zero temperature the memory cell is reversed by applying V_c. The diameter dependence of V_c was shown in the previous chapter (figure 3.10). It was found that from both the macrospin model and micromagnetic simulations the macrospin critical switching voltage remains above 0.7 V even for the larger disks. When thermal fluctuations are added it is possible to reverse the free layer for lower values, but not as small as 0.2 V. This is shown in the simulations with thermal fluctuations included in the previous chapter (section 3.3), or in the static measurement of our STTMRAM samples (section 5.2.3). The annihilations due to stretch field are not expected with our parameters. If we

send a voltage large enough to nucleate a 180 degree domain wall, it will propagate and cause ultimately the reversal of the full free layer.

It is also of interest to compare our predicted annihilation to other works from literature studying the STTMRAM reversals. In reference [110] micromagnetic simulations are presented in which a domain wall nucleated from the edges could not reverse the disk (this study is discussed in section 2.3.3 of our state of the art). This impossibility of nucleating a domain wall near the edges could be related to the annihilation of the initial domain wall due to stretch field that we described here. However if a *partial* domain wall (i.e. with theta spanning less than 180 deg.) is nucleated, our approach is no longer valid and the annihilation voltage could go up.

4.7.4 Impact of the material parameters

Here we discuss briefly the impact of different material parameters. We chose to stay qualitative and not to show the corresponding phase space graph for each parameter value explored.

Anisotropy and exchange

Across this chapter, we have shown the strong impact of the disk diameter on the overall domain wall dynamics. What matters is the relative value of this diameter compared to the characteristic domain wall length $\Delta = \sqrt{\frac{A_{ex}}{K_{eff}}}$. Any change on the effective anisotropy (which depends on M_s and K) or on the exchange constant will therefore affect the overall dynamics. We have also shown that the demagnetizing effects are of great importance. They are all proportional to the magnetization M_s therefore its relative value compared to the stretch field (given by exchange and anisotropy) affects the dynamics strongly.

The other main change induced by varying the effective anisotropy is the size of the retention pond, following equation 4.52. A strong anisotropy slowly reduces the size of the pond, which reduces the sensitivity to the initial conditions and the maximum amplitude of the Walker oscillations. While a small effective anisotropy increases the size of the pond, which leads to even larger Walker oscillations than the one presented with our parameters and therefore even more spectacular dynamics. In terms of memory application a small pond is preferred and therefore a strong anisotropy. The issue being of course that changing the anisotropy is affecting numerous other effects in STTMRAM devices than the size of the pond, I would suggest other methods to get rid of the pond (stronger voltage, smaller diameter, stray in plane fields).

Varying the exchange has a weaker impact on the dynamics than the effective anisotropy. It will mostly affect the stretch field (which increases with exchange) and the domain wall length. For instance a larger exchange means that the critical diameter for optimal reversal is going to be higher than the 40 nm found with our usual parameters.

Damping

The role of damping is complex. It changes the coupling between the q and ϕ oscillations. Concerning the dynamics in the Walker regime (described by equations 4.48, 4.49 and 4.50) the damping mostly impact the drift term because of the difference in order of magnitude between the spin transfer torque term and the typical fields. For a strong damping the drift velocity is more affected by the total field than for a

weak damping. For applications since the field term in the drift velocity is first positive then negative (assuming no external field), changing the damping has overall no impact on the switching time considering only the domain wall motion.

The damping also has an impact on the large Walker oscillations that can be seen around the disk center. A strong damping relaxes faster the oscillations, meaning that if we enter a strong oscillation before crossing the center its amplitude is reduced once the center is crossed. With a small damping, the oscillations before and after the center are about the same amplitude and the trajectories looks more symmetrical around the center.

4.7.5 Extending the model within the 1D approximation

Here we briefly extend the model to other geometries and systems than the STTM-RAM free layers, while remaining within the frame work of the (q, ϕ) models.

Changing the geometry

We have presented two geometries in this chapter: the stripe case and the disk case. It was found that the geometry has a very strong impact on the domain wall dynamics through an elastic term that we called the stretch field. This field accounts for the fact that varying the domain wall length as it sweeps through the geometry of the system has a cost in energy. The stretch field can be written in a more general geometry by introducing the angle ψ between the domain wall normal and the contour of the system (see figure 4.6). The equation 4.41 that was obtained with the *chord* assumption (namely by assuming that S_{DW} can be taken from the chord of a disk formula) can be re-written as:

$$H_{\mathrm{str}}(q,\phi) = \left(2H_{\mathrm{k,eff}} + H_{N\leftrightarrow B}\cos^2(\phi)\right)\frac{\Delta}{\ell_{wall}(q)}\tan(\psi(q)) \tag{4.56}$$

This equation can be generalised to any geometry where a straight wall hypothetically moves in a funnel of angular opening 2ψ. This is proven by using arguments similar to the one of subsection 4.3.3 where the effective fields were obtained intuitively, in particular equation 4.43.

Dzyaloshinskii–Moriya interaction

For the sake of simplicity, we have disregarded the interfacial Dzyaloshinskii-Moriya interaction (DMI) that may be present in ultrathin PMA films [4]. The impact of DMI for a domain wall motion within a stripe was already studied with the (q, ϕ) approach in reference [104]. The DMI should be added to the total potential as:

$$u_{\mathrm{DMI}} = D(m_z \mathrm{div}\vec{m} - (\vec{m}.\vec{\bigtriangledown})m_z) \tag{4.57}$$

Where D is the DMI constant. This density integrated over the full disks gives the potential:

$$U_{\mathrm{DMI}} = \frac{d}{\Delta}D\cos\phi\int_{-R}^{R}\mathrm{sech}(\frac{q-x}{\Delta})\sqrt{R^2-q^2}\mathrm{d}x \tag{4.58}$$

This potential is similar to the one derived for the in plane field along the x direction (equation 4.54) which is not surprising since the DMI, just like a field along x, favors one of the two Néel configurations. The DMI impact on the domain wall dynamics

is exactly the same as the one of H_x: a low DMI breaks the π periodicity creating effectively a second pond, while a high DMI recovers a very large single pond scenario which induces strong Walker oscillations (figure 4.18 is still relevant for DMI).

Just like for the in plane field case, DMI has a strong impact on our system. For our STTMRAM devices it is unclear which DMI value is expected, but it is predicted to be up to $D = 1$ mJ.m^{-2} [51, 85, 40, 42, 84] which gives a DMI field $H_{\text{DMI}} = \frac{\pi D}{2\mu_0 M_s \Delta}$ of the order of 150 mT. This field could be very strong and would change greatly the domain wall dynamics that we predicted here. At such a strong DMI or H_x the pond covers the full phase space. The domain walls are then annihilated or swept through the disk depending on their initial tilt angle in a ballistic manner, with no Walker oscillations possible. STTMRAM stacks are already optimized as to reduce the DMI, we have here given the most extreme value reported but expect way less in our own devices.

The assumption made in our models of no in-plane field and no DMI could prove to be problematic in terms of comparing our models with a measurement on our real STTMRAM devices. Having a good estimation of these two quantities is important as to predict the switching path.

4.8 Beyond the one dimension approximation

In this final section we go back to the micromagnetic simulations. We have shown that the (q, ϕ) approach can explain most of the dynamics observed in the simulations, but there are still some discrepancies. The main ones are the curvature of the domain wall, the non-homogeneity of the tilt angle along the domain wall (as seen in the snapshot of figure 4.2.d for instance) and the gyration of the domain wall around its center.

Here we give some qualitative insights into these three effects, the three of them being closely related. We focus on the 80 nm disk for a reason to be given in the Bloch lines subsection.

4.8.1 Initial non-homogeneity

As we already stated, the domain wall curves itself in order to minimize its length at a fixed reversed surface. When doing so from an initial state that is a straight wall with a constant tilt angle ϕ_0, the system keeps a constant in plane angle for the magnetization (see the initial states used in figure 4.2 and 4.3). Since the tilt angle is defined from the normal of the domain wall, the curved initial state with a constant in plane angle has necessarily a non-uniform tilt angle along its length. In the micromagnetic simulations, there is initially a varying tilt angle along the wall.

During the domain wall motion, $\dot{\phi}$ is *mostly* uniform which explains why the in plane component of the magnetization direction remains *mostly* homogeneous. We will now discuss on this *mostly* aspect by using our findings from the (q, ϕ) model within a disk with an analytical potential.

4.8.2 Effect of the stretch stiffness field

The stretch field is composed of an elastic part and a dipole-dipole part which depends on ϕ (equation 4.40). Since $\dot{\phi}$ depends on the total field through equation 4.49, the dipole-dipole part of the stretch field induces a ϕ dependence of $\dot{\phi}$. This dependence is very small since the stiffness field is smaller than the elastic part of the stretch field as already stated. Since ϕ is not homogeneous initially because of

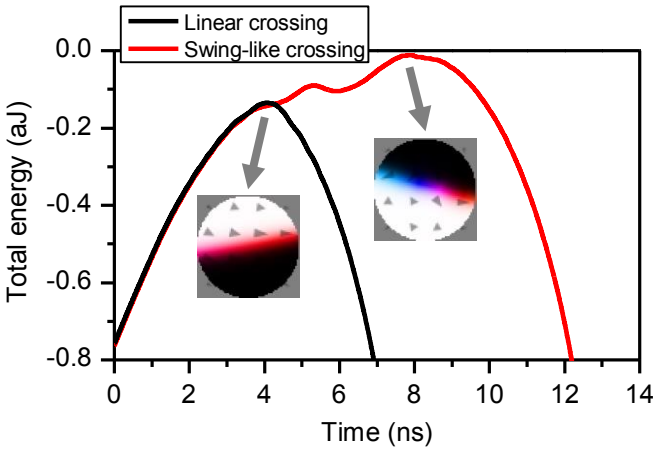

FIGURE 4.19: Total energy of the system as the domain wall sweeps across the disk. Two trajectories are represented corresponding to the linear crossing ($\phi_0 = 30$ deg) and the swing like crossing ($\phi_0 = 40$ deg) of figure 4.2. The energy values have been corrected by an offset such that the maximum energy reached is zero. The snapshots corresponds to the magnetization configuration at the maximum energy of each respective trajectory.

the domain wall curvature (previous subsection), $\dot{\phi}$ also is not homogeneous along the domain wall length. This induces slowly an increasing non-homogeneity of the in plane component of the magnetization angle as the domain moves along the disk. Once we get near the center and the domain wall becomes straight once again, it does not have a perfectly uniform tilt angle.

4.8.3 Impact of non-homogeneity on the center crossing

We have just shown that the domain wall reaches the center with a slightly non-uniform tilt angle because of intrinsic reasons (curvature + dipole-dipole stretch field). But the dynamics at the center are extremely sensitive to the initial conditions as seen in the phase trajectories (figure 4.15). In most cases (linear-like crossings) the non-homogeneity has no impact. But in some rare cases a part of the domain wall gets stuck near the center because of the vanishing precession frequency as described by the (q, ϕ) model, while the rest of the domain wall crosses the center as it was not described by the same ϕ. When this happens it induces a strong non-homogeneity of the tilt angle and the in plane angle of the magnetization since ϕ and q are coupled. This ultimately results into a domain wall with a strong gradient in ϕ along its length, that gyrates around the disk center and gets stuck near the center region without being able to cross it at first. Once the non-homogeneity in tilt angle is that strong our (q, ϕ) models do not apply at all and the exact swinging across the center is hard to predict.

The scenario that we just described corresponds to the "swing like trajectory" that we observed in figure 4.2.d and that we could not explain within the fully one dimensional frame.

4.8.4 Energy consideration: Bloch lines

So far we have focused this section on the 80 nm diameter disk. For the 40 nm case, the strong non-uniformity of ϕ and the swing like center crossing are never observed. This is related to the fact that the 40 nm disk is not as sensitive to the initial conditions, the trajectories remains ballistic (or equivalently it is due to the absence of retention pond). There is also a more fundamental reason for the absence of any non-homogeneity for the in plane component of the magnetization at small sizes versus large sizes.

Looking at the snapshots of the magnetization near the center in the simulation described in figure 4.2.d we can see that the in plane component (the color) makes

almost a full turn. A full turn of the tilt angle along the domain wall length is called a Bloch line and such objects have been studied in thin films for instance[49]. We now discuss with energy consideration the impact of the disk diameter on the possibility of creating Bloch lines.

The time-resolved system energy (figure 4.19) indicates that during the swing-like scenarios seen at 80 nm the system reaches a higher energy compared to when in the one-way single crossing scenario. In the scenario of figure 4.2.d, the systems reaches an energy that exceeds by 130 zJ (810 meV) the maximum energy in the scenario of figure 4.2.a. The energy maximum of the scenario of figure 4.2.d is reached when the wall has already passed the disk center once forth and once back for a total moment of $\langle m_z \rangle = 0.04$ namely very near the center. This extra energy cost of 130 zJ (810 meV) can be understood from the expected energy [49] of a full Bloch line: $U_{\text{B-line}} = \frac{8A_{\text{ex}}d}{\sqrt{H_k/M_s}} \approx 280$ zJ (1.75 eV).

In order to anticipate whether the tilt is likely to stay quasi-uniform or not during the domain wall motion for a given disk diameter, $U_{\text{B-line}}$ should be compared to the "domain wall energy barrier" $\Delta E_{\text{dw}}(q_0, \phi_0)$ that an (already nucleated) wall with uniform tilt needs to acquire to climb up to the saddle point in the energy landscape (i.e. the height of the potentials in figure 4.11). Since ΔE_{dw} depends on the subjectively chosen initial conditions $\{q_0, \phi_0\}$, only its order of magnitude is meaningful. For 40 nm disks, the spin transfer torque has to supply typically $\Delta E_{\text{dw}} \approx 120$ zJ (0.75 eV) to jump over the barrier (right graph in figure 4.11). This is much below $U_{\text{B-line}}$. With these energy scales in mind, we can understand why at diameters of 40 nm, the tilt is staying essentially uniform whatever the initial conditions $\{q_0, \phi_0\}$. Indeed it seems unlikely that minor changes in the reversal paths would permit a fourfold increase of the work supplied by the spin-torque with the whole of it fed into the $\frac{\partial \phi}{\partial y}$ degree of freedom. We believe that this is the reason why at diameters of 40 nm the $q - \phi$ model succeeds in describing the full wealth of the domain wall propagation: the energy cost of a strongly non-uniform ϕ is just out of reach.

Conversely for larger disks, the work supplied by the spin torque is substantially larger (e.g. $E_{\text{dw}} \approx 450$ zJ (2.8 eV) for a diameter of 80 nm and $q_0 = 10$ nm). Minor changes in the reversal path and thus in the work supplied by the spin-torque may transfer a sizable part of this work in the $\frac{\partial \phi}{\partial y}$ degree of freedom of the wall. This can induce a swing-like scenario if the wall stays long enough at the disk center for a partial Bloch line to develop like it is the case when a portion of the domain wall gets stuck.

We have shown that the non-homogeneity of ϕ seen only in larger disks can be understood on a single scenario by decomposing the complex domain wall dynamics using our (q, ϕ) models. But it can also be anticipated from purely energetic considerations by comparing the typical Bloch line energy with the heights of the total potentials we previously derived.

4.8.5 The domain wall gyration

As we already stated the domain wall gyration is seen when the tilt angle is non-uniform or when the domain wall is initially straight. Several effects cause the gyration: i) the staircase effect that is due to the grid, this turns the domain wall around until it is along a diagonal; ii) a non-uniformity of ϕ causes a gyration because $\dot{q}$ depends on ϕ, if the right side of the domain wall advance while the left side moves back, then the domain wall turns around. To treat the gyration rigorously one should

consider the domain wall as a 2D object and study its topological charge. The dynamics is then described by a Thiele equation similarly to vortex dynamics. We do not detail this approach as gyration is a minor effect that do not appear in the time traces and as we cannot extract an intrinsic gyration from our micromagnetic simulations because of the staircase effects.

To conclude this section the curvature of the domain wall induces a slight non-uniformity of the tilt angle because of the stretch stiffness field. This non-uniformity can grow near the center, but only for the larger disks. Once the non-uniformity is large it induces gyration around the disk center.

4.9 Conclusion: domain wall dynamics within a perpendicularly magnetized thin disk

In this chapter we have studied how a Slonczewski spin-torque induces the propagation of a domain wall across thin magnetic disks possessing perpendicular magnetic anisotropy. Micromagnetic simulations were first used to identify the possible domain wall motion scenarios for two representative disk diameters, 40 and 80 nm. At small disk diameters, the domain wall sweeps through the devices in an almost monotonous manner; the wall dynamics is essentially independent from the initial tilt angle. Conversely at larger diameters, the wall performs back-and-forth oscillations superimposed on a gradual drift across the disk. Depending on the initial state of the domain wall, it crosses the disk center either in a direct manner or with variably marked pauses before and after the crossing of the center. Some specific initializing conditions of the domain wall can even result in the wall crossing the disk center multiple times, which correlates with the growth of a strong non-uniformity of the wall tilt along the wall length as well as a gyration of the overall magnetic texture. Analytical modeling was then used to shed light onto the main features of the domain wall motion scenarios and their dependence with the disk diameter. We used a collective coordinate model in which the wall is described by the wall position q inside the disk and the magnetization tilt ϕ within the wall. First we remind the result in the case of an infinite stripe. We then solve the equations for the disk, introducing the concept of the stretch field whose elastic part (equation 4.39) describes the affinity of the wall to reduce its length and thereby to be repelled by the disk center, and whose demagnetizing part (equation 4.40) describes the affinity of the wall to reduce its internal dipolar energy by rotating its tilt, generally away from the Néel configuration. During the spin-torque induced motion of the domain wall, part of the system's energy flows back and forth between the energy reservoirs associated with the two components of the stretch field; the mean velocity (equation 4.48, quantitative) and the oscillation (equation 4.49 and 4.50, indicative only) of the wall propagation velocity can be understood from this picture.

To unravel the sensitivity of the wall dynamics to its initialization condition, we introduce the concept of the retention pond: a region in the $q - \phi$ space in which walls of tilt close enough to the Néel wall configuration are transiently bound to the disk center. Walls having trajectories tangent to the retention pond make two pauses before and after crossing the disk center, thereby yielding switching times longer than average. The size of the retention pond (equation 4.52) is correlated with the energy difference between Bloch and Néel walls when at the disk center. There exists a single optimal disk diameter (equation 4.53) for which the retention pond reduces to a single point. For this specific diameter, the wall crosses the disk center in a ballistic manner independently of its tilt such that the time needed for a domain

wall to sweep through the disk gets also largely independent from its tilt. This is expected to maximize the reproducibility of the wall dynamics, which is of great interest for magnetic memory applications. Our model is also useful to anticipate the respective effects of small external fields, larger spin-torques, different material parameters and weak interfacial Dzyaloshinskii-Moriya interactions.

Finally we highlighted how to observe the predicted domain wall motion in a time-resolved measurement. The strong Walker oscillations are a good target for an experiment since they can account for large changes in the total moment near the center. We know that such oscillations are stochastic (not seen systematically in each single shot); at the lower voltages (to prevent ballistic switching); at the larger disks (typically 50 to 90 nm); and that we should sweep the external field applied along z during the experiment to make sure we have a position for which the total field seen by the domain wall cancels out. We present this type of experiment in the time-resolved measurement chapter of this manuscript.

Chapter 5

Spin transfer torque random access memory devices and their basic properties

In this chapter we start the experimental part of this manuscript by presenting our devices and their basic properties. The deposition and the etching of our devices are made at IMEC. I did not take part into the stack engineering or any of the fabrication processes. The devices are optimized for STTMRAM applications. They are targeting a high TMR, low RA product and high perpendicular anisotropy. Another important requirement is to have a CMOS-compatible process, namely the device should maintain a good level of performances after a 400 °C annealing. In this chapter we first describe the most common devices we used to study the switching path. Then we show static measurements performed on these devices. Finally we discuss the results of ferromagnetic resonance measurements in order to extract key material parameters.

5.1 Presentation of our STTMRAM devices

5.1.1 Stack description

Standard stack composition

The stack used during most of this manuscript is presented in figure 5.1. It is called POR19 (for Process of Reference 2019) as it was the standard STTMRAM stack from IMEC as of 2019. It corresponds to the dual-MgO bottom-pinned designed discussed in our state of the art (see figure 2.8). The stacks are deposited by magnetron sputtering on 300 mm Si wafers. They are then annealed in vacuum at 400 °C. I am not allowed to give the full stack composition and layer thicknesses, but more details can be found in the references given for each layers. From bottom to top:

i) I cannot disclose the exact seed here. The seed composition has a great impact on the PMA of the hard layer [70].

ii) The hard layer is a multilayer based on 5 [Co (5 Å)/ Pt (3 Å)] stacks with a Co layer on top of it. The Co/X multilayer present a strong PMA as discussed in section 2.4 of our state of the art. Terminating the multilayer with Co instead of Pt permits a better antiferromagnetic coupling through the Ir layer.

iii) The reference layer reads Co / Spacer / FeB . The Co layer is present next to the Ir for the strong antiferromagnetic coupling with the hard layer. FeB is then used to polarize the spin current and to ensure a symmetrical MTJ. The spacer used in the reference layer allows a smooth texture transition between the two ferromagnetic layers and ensures a good ferromagnetic coupling [29].

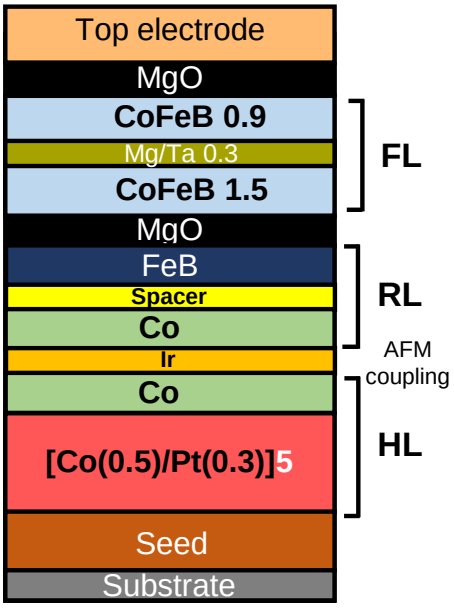

FIGURE 5.1: Stack composition used during most of this PhD. This stack is called POR19. The free layer, the reference layer and the hard layer are shown as defined in figure 2.8. I gave here as much detail as authorized for confidentiality reasons.

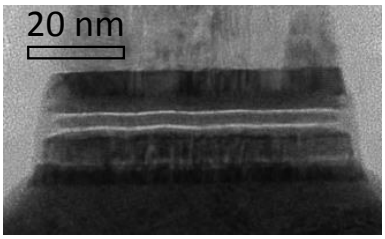

FIGURE 5.2: Transmission electron microscope image of a pillar after the full patterning process, provided by IMEC. The brighter layers correspond to the MgO. This highlight the damage at the edges of the pillar.

iv) The free layer is composed of $Fe_{52.5}Co_{17.5}B_{30}$ (15 Å)/ Mg/Ta (3 Å)/ $Fe_{52.5}Co_{17.5}B_{30}$ (9 Å). This is a dual MgO design with Ta in the center to ensure the crystalline match and to absorb the boron, as already discussed. The magnesium is a sacrificial layer protecting the already deposited CoFeB layer during the Ta deposition. The impact of this sacrificial layer and its development at IMEC are discussed in reference [99].

Variations of the stack during this PhD

In the course of this PhD, stacks slightly different from the one of figure 5.1 where studied. Indeed POR19 is the stack we did our latest and more advanced measurement on, hence our focus on this stack. Earlier we measured stacks with Co/Ni multilayer instead of Co/Pt in the hard layer and compared their performances with ferromagnetic resonance measurements. Additionally to this different hard layer, the earlier stacks had a different seed and a slightly different thickness of the free layer. Since the free layer remained mostly unchanged (only slight thickness variation) in all these different stacks, our study of the switching path inside the free layer is little impacted. Unless specified otherwise the measured stack is POR19 (figure 5.1).

5.1.2 The patterning

The stack are then patterned into pillars of varying diameters. The critical patterning step is done in-situ. It consists of the etching, cleaning, oxidation and encapsulation of the pillars without vacuum breaking. The etching is performed by ion beam etching. As the etching damages the edges of the pillar it should be performed with an energy as reduced as possible. The oxidation processes were also optimized at

IMEC so to reduce the oxygen diffusion from the edges into the magnetic pillar. Finally the encapsulation is done with SiN. The encapsulation also affects the overall performances of the devices through physical stress on the pillar.

We do not detail here the complex patterning process, in which each step is regularly improved at IMEC. However we know that there is damage on the edges of the pillar and that this could affect the free layer dynamics. An example of such damage is shown in figure 5.2 concerning the MgO layers. There is a discrepancy between the nominal etching diameter and the diameter that can be measured in electron microscope images. Knowing the diameter of a measured device is critical in the study of the switching path as we have predicted, but it is not possible to obtain it from such images in all our measured devices. Therefore we use the electrical critical dimension (electrical CD).

The electrical CD d_{e^-} is a diameter of the pillar deduced from its resistance. For a large device (for instance a nominal 500x500 nm^2) the edge damage can be reasonably neglected and we assume that the actual diameter of the pillar corresponds to its nominal one. From this assumption we obtain the resistance-area product of an undamaged pillar by measuring its resistance in the P state. This product in the P state is simply called the RA product of the stack, written RA. The diameter of any pillar is then taken from its resistance and RA:

$$d_{e^-} = 2\sqrt{\frac{RA}{\pi R_{\mathrm{P}}}} \tag{5.1}$$

For instance the stack POR19 (figure 5.1) has an RA product of $RA = 6.29\ \Omega.\mu\mathrm{m}^2$. A pillar of 100x100 nm^2 nominally was measured with no field or voltage at $R_{\mathrm{P}} = 860\ \Omega$, which gives an electrical CD of $d_{e^-} = 96.5$ nm. Usually the electrical CDs are significantly smaller than the nominal sizes, especially for the smaller devices where the edge damage are more significant. Some 60 nm diameter device nominally can have an electrical CD as low as 25 nm.

In the following chapters, we assume that the electrical CD is the diameter of the free layer disk. This is a rather strong assumption since it implies that the electrical diameter and the magnetic diameter are the same (one could imagine a part of the tunnel barrier with conduction but greatly reduced magnetic properties). On another hand the electrical CD is obtained from the resistance, which arises from the tunnel barrier, namely directly in the vicinity of the free layer. Therefore even though the pillar diameter is not perfectly constant along its height (as seen in figure 5.2), the electrical CD is an estimation at the free layer level which is the focus of our study.

5.1.3 Integration of high frequency devices

The pillars are then integrated to be connected with probes. Our measurements are performed on devices specifically integrated for high frequency measurements in a ground-signal-ground configuration (see figure 5.3). We have used only one design during this PhD in which the circular devices have nominal diameters of 50, 60, 75, 100, 120, 150 and 200 nm. Additionally elliptical devices with varying aspect ratio and diameter are also integrated for high frequency measurement, but we focused on the circular ones.

We did not study the switching path in devices fully integrated for memory applications, but we do not expect the integration to have any impact of the dynamics of the free layer.

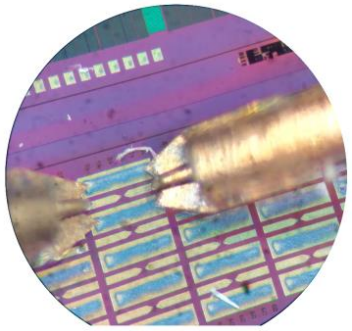

FIGURE 5.3: Picture of a device while it is measured by our probes. The probe is coplanar ground-signal-ground. Each device corresponds to a different nominal diameter.

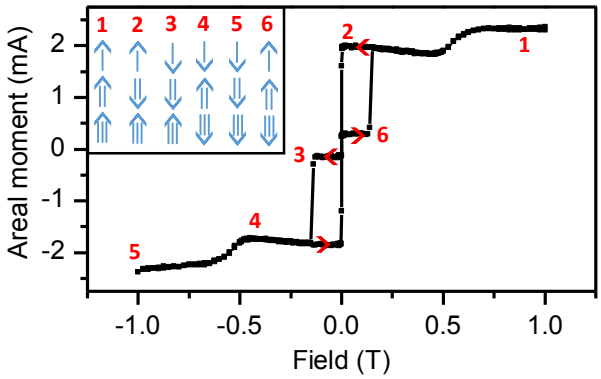

FIGURE 5.4: Full VSM loop on POR19 stack. The red arrows indicate the field sweep direction. In the legend the largest arrow corresponds to the hard layer, the middle one to the reference layer and the smallest one to the free layer.

5.2 Basic properties of the devices

Here we present briefly the loop obtained for POR19 using a Vibrating Sample Magnetometer (VSM). This measurement was performed at IMEC and I did not take any part in it. But since the M_s is extracted from such a loop we present it here in order to present the origin of all our material parameters values.

Understanding a full loop

A full VSM loop performed on POR19 is shown in figure 5.4. From such a loop we can extract the magnetization of the free layer and check that the reference system behaves adequately. A low field is sufficient to reverse the free layer (because it is a full stack); then for a field of a few hundreds of mT both the reference layer and the hard layer switch maintaining the AFM coupling within the SAF; finally for very high fields values the AFM coupling gradually breaks and all the magnetic layer are aligned along the field. This last transition presents no hysteresis. The large difference in the field needed to switching the free layer and the reference system is an indication of the robustness of the SAF. This robustness is also seen in our R(H) and R(V) loops of POR19 where no reference system failures are observed.

Extracting the magnetization

To extract the M_s of the free layer we focus on the change in the total moment when the free layer is reversed. This corresponds to transition 2 to 3 and 4 to 6 in figure 5.4. A minor loop can also be performed to study the free layer specifically (namely a loop for lower field values in which only the free layer is reversed). From a minor loop performed in POR19 we obtain a $M_s * d$ product of 2.12 mA. The total thickness of the free layer is 2.7 nm (figure 5.1) as we consider that the Ta is diluted within a pure CoFeB layer giving a free layer behaving as one unit. With this we obtain

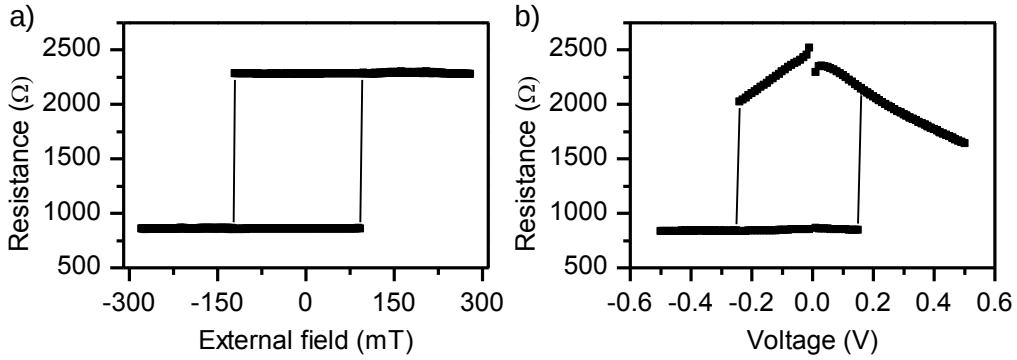

FIGURE 5.5: Static measurement performed in a POR19 device of 96 nm diameter (100 nominal). a) R(H) minor loop obtained by sweeping the external field along z at a constant applied voltage of 10 mV. b) R(V) loop obtained at zero applied field.

$M_s = 784$ kA/m for POR19. Note that this value is different from the $M_s = 1200$ kA/m that was used so far in all our models and numerical works. The 1.2 MA/m correspond to the magnetization of the older stack I measured and therefore it was the value that we started our theoretical work with. For experimental work done with POR19 $M_s = 784$ kA/m is taken.

5.2.1 Basics on static measurement

We present now static measurements performed at device level, namely loops obtained by sweeping the applied external field along z or the applied voltage. They are performed using a sourcemeter directly connected to the device under test (DUT) through ground-signal-ground probes. A field is applied in the z direction by a hand-made coil. The supply of the coil is controlled by another voltage source such that the applied field, applied voltage and measured voltage can be monitored in a single software. We used labview to pilot all our experiments, we do not give the details of our software in this manuscript.

We performed static measurements on numerous devices for each sizes and stack compositions we worked on. The resistance-field loops (R(H) loops) and resistance-voltage loops (R(V) loops) are recorded before each more complex measurement to check the performances of the individual device studied. There was a large device-to-device variability in the earlier stacks we worked on: about half of the devices presented reference system failures next to the voltage or field values necessary to reverse the free layer. But for POR19 the optimization of the seed allowed a much stronger hard layer and reduced greatly the device-to-device variability. We chose in this manuscript to present only loops of devices where everything is working as intended (strong reference layer, not too high offset field, flat P and AP level in the R(H) loops). Such loops for a POR19 device of 96 nm diameter (from electrical CD) are presented in figure 5.5.

5.2.2 Resistance versus out-of-plane field loops

From the R(H) minor loops we can extract the electrical diameter, the TMR ratio, the offset field and the coercive field. The diameter is the electrical CD obtained from the resistance value at zero field in the P state and the RA following equation 5.1. The TMR ratio is obtained from the resistance in the P and AP states at zero field following equation 1.16. We assume that it corresponds to the TMR at zero voltage,

even though a small constant voltage of 10 mV was necessary to measure the R(H) loops. The device of figure 5.5 as an electrical CD of 96 nm and a TMR of 165 %. This is a typical TMR value for our POR19 devices. The size dependence of TMR is discussed in section 5.2.4.

The offset field of the device is defined as the opposite of the field that should be added along the z direction to obtain a symmetrical R(H) loop. This offset field rises from the more complex offset field profile due to the imperfect synthetic antiferromagnet and discussed in reference [29]. In figure 5.5.a for instance the offset field is $H_{\text{offset}} = +14.5$ mT (favoring the AP state) meaning the loop can be made symmetric by applying a constant -14.5 mT field. In our time-resolved measurement we shall symmetrize the loops in order to obtain a system closer to our models where the voltage-induced reversal was studied mostly at zero field. This assumes a constant offset field but in practice the offset field varies slightly with the applied voltage.

The coercive field H_c is the field at which the reversal occurs during the R(H) loop. Because of the offset field the reversals from P to AP and AP to P do not occur at the same applied field. To have a single coercive field, it is defined as the average of the absolute values of the two switching fields. For instance in figure 5.5.a the coercive field is 108.5 mT. The coercive field value depends on the sweeping rate of the applied field during the loop, because of the incubation effects. Indeed in a static measurement the switching is done in the thermal regime in both field or voltage induced reversal, meaning that the switching time is stochastic because of the incubation delay. Performing the same loop several times gives a slight variability in the coercive field. We ignore this issue in this section and extract the performances of a device from a single loop. Note that at 0 K with a perfect device, the coercive field is expected to be the effective anisotropy of the disk $H_{k,\,\text{eff}}^{\text{disk}}$ given by the anisotropy and the demagnetizing factors (equation 1.11). While the coercive field in a R(H) loop never corresponds to this value, it still depends on size as expected from the demagnetizing factors (see section 5.2.4).

5.2.3 Resistance versus voltage loops

The R(V) loop on the same 96 nm POR19 device is shown in figure 5.5.b. Such a loop gives access to the voltage dependence of the conductance in both states (and therefore the voltage dependence of the TMR) and to the switching voltage V_{switch}.

The resistance in the P state depends very little on voltage while the resistance in the AP state presents a broken-linear dependence on voltage. This broken-linear dependence in the AP state has been discussed by Slonczewski and Sun in reference [92]. We already discussed this paper in details in our section 1.3.2 while discussing the origin of the STT terms. It is also proven in this work that the conductance of a symmetrical MTJ with asymmetrical distribution of inelastic tunnelling centers through the barrier presents such a voltage dependence in the AP state. The shape of our R(V) loops is thus understood from the transport models.

The switching from AP to P and P to AP are not equivalent since the offset field also affects the voltage induced reversal. The switching voltage V_{switch} is defined in a similar manner as the coercive field H_c by taking the average between the switching voltages from AP to P and from P to AP. Just like in the field case, the switching voltage at 0 K is predicted to be the macrospin critical switching voltage V_c and so regardless of the switching path as we proved in our micromagnetic simulations. In the case of a R(V) loop, we are very much within the thermal regime as we sweep through the voltage range in a slow manner (a full loop takes a few seconds). The switching voltage is therefore much lower than V_c, as already discussed in our state

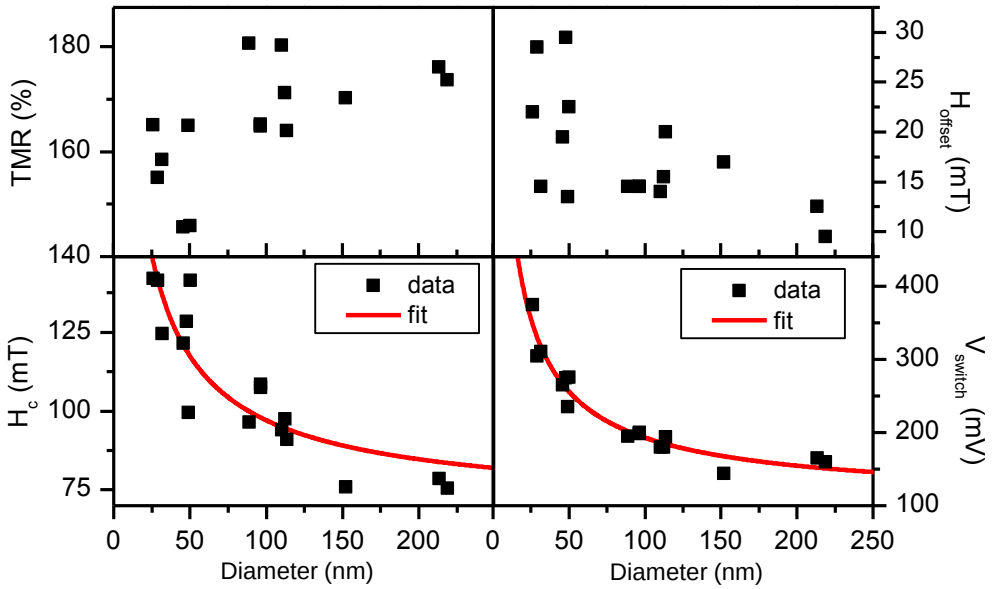

FIGURE 5.6: Size dependence of the properties extracted from the R(H) and the R(V) loops of POR19 devices with different diameters. The diameters are given by the electrical CD. The fit in the coercive field and switching voltage data corresponds to the size dependence as predicted by the demagnetizing factors (equation 5.2)

of the art section 2.1.2. The size dependence of the switching voltage is discussed in section 5.2.4.

Finally as a side remark, we can notice that in our experiment both a positive voltage and a positive field favor the AP state. While in our models when we introduced the generalized stimulus (equation 1.38) it was a positive voltage or a negative field that favored the AP state. This is simply a matter of field and voltage convention but we shall be careful about it when comparing our experimental data with the models.

5.2.4 Size dependence of the coercive field and switching voltage

The size dependence of the various device performances extracted from the static measurements are shown in figure 5.6. The TMR is slightly reduced for the smaller diameter. This is due to the damage on the MgO barrier during the patterning. The smaller is the device, the more edge effects are important and therefore the more the barrier is deteriorated.

The offset field is stronger overall for the small devices compared to the larger one and always favoring the AP state. As the offset field is the average of a more complex demagnetizing field profile along z, it is not surprising that it depends on size because of the change in the geometry. Even for the smaller devices H_{offset} remains below 30 mT, significantly smaller than the typical coercive fields.

The coercive field and the switching voltage are strongly correlated. This is understood from the simple macrospin picture, as at 0 K the coercive field is $H_{k,\,\text{eff}}^{\text{disk}}$ and the switching voltage is V_c which is proportional to $H_{k,\,\text{eff}}^{\text{disk}}$. The smaller is the device and the larger is the switching voltage. To be more quantitative we compare this trend to the size dependence predicted by the macrospin model at 0 K. Both H_c and

V_{switch} are predicted to be proportional to $H_k - (N_z - N_x)M_s$, where the demagnetizing factors of the disk depend on size. The exact demagnetizing factors are computed numerically, but a good estimation was proposed by Beleggia et al in reference [3]. The exact demagnetizing factors and the approximate formula are compared in figure 1.1. Equation 1.13 is thus a good estimation of the size dependence of H_c and V_{switch}. We fit our data with the function:

$$y = B + C\frac{3d}{2\pi x}[1 + \ln(\frac{d^2}{16x^2})] \tag{5.2}$$

where B and C are free parameters, d the thickness of the free layer (2.7 nm for POR19) and x the diameter for this equation. The fitting corresponds to the red lines in figure 5.6. The size dependence of the switching voltage extracted from our static measurement reminds the one predicted from the macrospin model at 0 K, having H_k and M_s as free parameters. The fitting is not as satisfying for our coercive field data, but we notice a larger variability from device to device for H_c compared to V_{switch} even around a single size, more statistics could allow a better fitting. Regardless, the good match obtained for V_{switch} has a strong implication: since the size dependence can be accounted for by demagnetizing effects, we can conclude that the patterning damage on the edges of the disk had little impact on the switching voltage or coercive field.

5.3 Ferromagnetic resonance measurements

5.3.1 Introduction on FMR

At low applied voltage, the magnetization dynamics inside the free layer is essentially given by the LLG equation (equation 1.24). The frequency of precession gives access to the effective field and the energy losses during this precession to the Gilbert damping. If we excite the magnetic body and look for resonances, we can access the effective field of the system knowing its γ_0. The linewidth of the resonance peak then gives the damping. Exciting our STTMRAM devices or stacks can therefore give access to key parameters of the system that are needed for our models. This is the principle of all FMR measurements.

How to excite the magnetic body? Two different methods were used during this PhD. In the VNA-FMR (for Vector Network Analyser FMR), the magnetic thin film is flipped on a coplanar waveguide. The coupling of the microwave photons to the magnetic body allows the study of the resonances of the magnetic body using a network analyser. This method has become the conventional FMR measurement to study magnetic thin films[71, 8, 61].

In a second method, the sample is excited after patterning directly by a high frequency voltage source. This so called voltage-FMR has the advantage of giving access to the properties after the patterning, allowing the study of its impact on device performances. However the signal to noise ratio is typically smaller than with the VNA-FMR method.

The FMR spectrum of a device is more complex than a single resonance corresponding to the macrospin mode of the free layer. In fact each layer can have numerous modes excited, each giving a different resonance frequency. These modes in a thin disks were predicted and measured through a ferromagnetic resonance force microscope in references [58, 78]. In practice the lowest energy mode corresponds to the macrospin mode and should be the one considered to study the effective field.

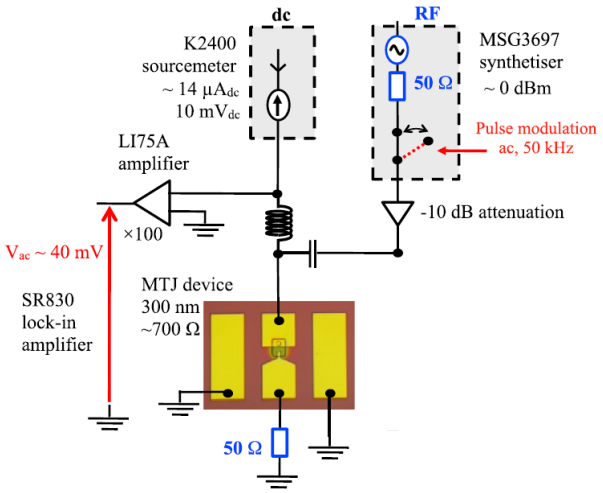

FIGURE 5.7: From reference [31]: sketch of the experimental set-up used in our voltage-FMR measurements. The instrument used as well as the typical experimental parameters values are given, in the case of a 300 nm device.

Both FMR methods excite the reference system additionally to the free layer. As the reference layer and the hard layer have typically much larger effective fields than the free layer (they are designed to be harder to reverse), it is usually easy to distinguish their resonances from the free layer ones.

During my PhD, I performed voltage-FMR measurement at device level on stacks older than POR19, with a focus on the impact of the diameter on device properties. I also collaborated with IMEC to set-up a VNA-FMR experiment. In this manuscript we study the switching path of the free layer, therefore we shall present our results of voltage-FMR in order to give our best estimation of the device parameters.

5.3.2 Voltage-FMR set-up

Description of the circuit

The voltage-FMR method that we performed is detailed in reference [31], we discuss here the main findings of this study. The experimental set-up is presented in figure 5.7. A high frequency voltage (written V_{rf}) is applied to the DUT by a synthetiser, this is the FMR excitation. This rf voltage is modulated at a much slower frequency (written ac frequency), such that the DUT is going from rf-excited to non-excited at the ac frequency. This modulation is performed at the reference frequency of a lock-in amplifier. The lock-in amplifier also amplifies and measures the ac-frequency voltage across the device V_{ac}, this is the raw signal. Additionally a static measurement sourcemeter is in parallel, applying a dc voltage to the DUT. As we will show this dc voltage can be used to tune the signal, but also to check the state of the DUT. Finally, before reaching the DUT the rf current goes through a -10 dB attenuation. This attenuation limits the standing waves within the circuit. To avoid the standing waves we work with a 50 Ω impedance matching and with high-frequency cables.

Origin of the signal

The lock-in measures and amplifies the ac component of the voltage across the DUT. This voltage consists of two contributions [31]:

$$V_{ac} = V_{1,ac} + V_{2,ac} \tag{5.3}$$

$$V_{1,ac} = \frac{V_{rf}}{R_{DUT} + 50} \frac{\delta R_{DUT}}{\delta M} \delta M_{rf} \tag{5.4}$$

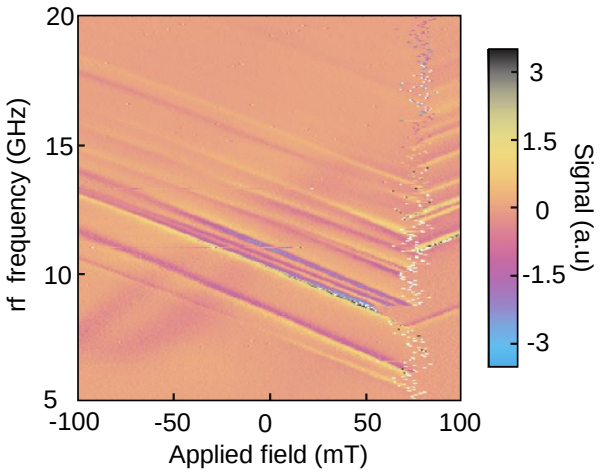

FIGURE 5.8: Voltage-FMR typical spectra, reconstructed from many field-loops performed at successive frequencies. The variation of the ac voltage with respect to the field $\frac{\delta V_{ac}}{\delta H}$ is plotted in the field-rf frequency space. For a 103 nm diameter device with a stack slightly different from POR19 (0.2 nm thinner free layer, different seed).

$$V_{2,ac} = \frac{V_{dc}}{R_{DUT} + 50} \frac{\delta R_{DUT}}{\delta M} \delta M_{ac} \tag{5.5}$$

where $\frac{\delta R_{DUT}}{\delta M}$ is the variation of the resistance induced by a variation of the magnetization of the free layer, δM_{rf} is the change of magnetization occurring at rf frequency and δM_{ac} the one occurring at ac frequency. The first voltage corresponds to variation of the resistance at the rf frequency (i.e. the rf precession resulting from linear susceptibility terms at the rf frequency), rectified at ac frequency by modulation. The second voltage corresponds to the change in resistance between an rf-excited and a non-excited device. This voltage is revealed by the dc current.

V_{ac} is proportional to $\frac{\delta R_{DUT}}{\delta M}$. But in our devices similar to POR19 this term is very small as highlighted by the flatness of the P and that AP levels in our R(H) loops (see figure 5.5.a). In theory such a device should present no signal, but in practice there is still some sensitivity left. It is found empirically that the signal is stronger in the AP state than in the P state. For this reason and to more easily distinguish the modes of the free layer and of the reference system, the measurement is performed for a device within the AP state.

Some non-magnetic artefacts remains in V_{ac} during the measurement. To remove such artefacts we consider the variation of V_{ac} for each field step at fixed frequency, suppressing the non-field sensitive component of the signal. Our final voltage-FMR spectra is therefore $\frac{\partial V_{ac}}{\partial H}$ plotted in the external field-applied rf frequency space. The field is swept while the frequency remains constant. Such a plot is presented in figure 5.8 for a stack older than POR19 and a device of 103 nm diameter.

5.3.3 Extracting the material parameters

Attributing each mode to a layer

The device of figure 5.8 has a 103 nm diameter. It was patterned on an older stack with a 2.5 nm free layer instead of the 2.7 one of POR19 and larger M_s. The seed was also different, which results in a weaker reference system. Three family of modes can be seen in the figure with different slopes. For fields between -100 mT and 75 mT, many thin modes are observed with a negative slope in the field-frequency space. They all present the same slope but different amplitude and line-shape. In the same field region, a very broad mode is observed with a positive slope. Finally in the 75 to 100 mT region, several thin modes are observed but this time with a positive slope.

From the dc part of the set-up, we monitor the resistance of the DUT while recording the spectra. From this we know that the MTJ is in the AP state in the -100 mT to 75 mT field region and in the P state in the 75 to 100 mT region. We conclude that for each field line we record at fixed frequency, the free layer switches around 75 mT. The slopes of the modes is given by the γ_0 of the considered material. The sign of the slope depends on the orientation of the considered layer with respect to the applied field: switching a layer changes the sign of the slope. From these information we conclude that the thin modes corresponds to the free layer modes as their slope changes sign when the free layer is reversed. The broad mode with a negative slope in the AP region is necessarily the reference layer mode, as its magnetization is in the opposite direction of the free layer in the AP state.

These findings are not surprising for two reasons: i) The free layer is expected to have a smaller anisotropy than the hard layer, which results in a smaller frequency at zero field. This can be observed by comparing the broad mode and the lower frequency thin mode of figure 5.8 at zero field. ii) The free layer is expected to have a smaller damping than the hard layer, this is once again confirmed by the fact that the free layer modes are the much thinner one. We will now be more quantitative and explain how anisotropy, damping and exchange can be extracted from such a spectra.

The anisotropy

The anisotropy is extracted from the frequency of the quasi-uniform mode at zero field. The frequency ω dependence on the applied field H_z is given by [27]:

$$\omega \approx \gamma_{0,i}[H_z + H_{k,\,\mathrm{eff}}^{\mathrm{disk}} + \frac{2A_{\mathrm{ex}}k_{m,l}^2}{\mu_0 M_s}] \tag{5.6}$$

where $\gamma_{0,i}$ is the gyromagnetic ratio of the material (CoFeB in the case of the free layer) and $k_{m,l}$ corresponds to the generalized wavevector of the considered mode. m and l correspond to the mode's wavenumber in the radial and vortex-like degrees of freedom. The different existing modes are studied in references [58, 78], they are discussed in the voltage-FMR context in reference [27].

From equation 5.6 we understand that we can directly access the effective anisotropy of the disk if we identify the quasi-uniform mode (in which $k \simeq 0$) and consider it at zero field. The macrospin mode is bound to be the lowest frequency one following this equation, but how to be certain that we indeed obtained a signal for the lowest frequency mode? There is a more reliable method to identify the macrospin mode than simply taking the lowest frequency one. This mode is expected not to be detectable at zero field because the flatness in the R(H) loops is maximum in this region. While the R(H) loops of the samples appeared relatively flat everywhere, this effect is clearly highlighted in reference [31] section III.D for other samples. Additionally to this vanishing around zero field, the quasi-uniform mode is also expected to have a weaker amplitude compared to the other free layer modes. Indeed the rf contribution $V_{1,\mathrm{ac}}$ to the ac voltage is zero for the quasi-uniform mode, because when the magnetization is uniformly aligned in the out-of-plane direction δM_{rf} is equal to zero (as the magnetization precesses around the effective field it does not change its z component and therefore do not affect the conductance of the DUT). For this reason the quasi-uniform mode is composed purely of $V_{2,\mathrm{ac}}$ and appears of weaker amplitude.

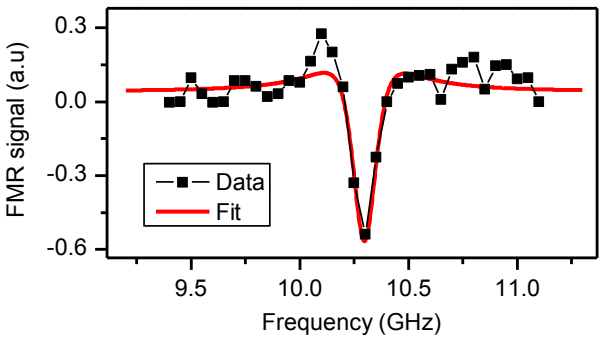

FIGURE 5.9: Extraction of the damping. The data represent a cut at a fixed applied field of -90 mT along the macrospin mode of figure 5.8. The fit is done with $\frac{d}{dH_z}\mathcal{R}e(\mathcal{X}_{xx})$, with $\mathcal{X}_{xx}$ the in-phase transverse susceptibility taken from equation 5.7. The fit is obtained for $\alpha = 0.010$

Notice that in figure 5.8 the lowest frequency free layer mode is indeed of lower amplitude than the other modes and vanishes near zero field. For these three reasons we are positive that it is the quasi-uniform mode. Its frequency at zero field is 7.75 GHz, the gyromagnetic ratio of CoFeB is taken as 29.4 GHz/T, which gives $H_{k,\,\mathrm{eff}}^{\mathrm{disk}} =$ 210 kA/m. To obtain the anisotropy of the stack after patterning several sizes must be compared, as we show in the following subsection.

The damping

The linewidth of each mode is related to the Gilbert damping α: the broader is a mode and the larger is the damping. To extract α from the linewidth, the lineshape must be predicted. Let us first consider only the macrospin mode. Then we can write the LLG equation and from this obtain the in-phase transverse susceptibility of the system $\mathcal{X}_{xx}$:

$$\mathcal{X}_{xx} = \frac{MsH'}{H'^2 - \omega'^2 + 2i\alpha H'\omega'} \tag{5.7}$$

Where $H' = H_{k,\,\mathrm{eff}}^{\mathrm{disk}} + H_z$ and $\omega' = \frac{\omega}{\gamma_0}$. The calculation leading to this expression is detailed in the appendix of reference [31]. The lineshape of the macrospin mode is the real part of this susceptibility as it only contain $V_{1,\mathrm{ac}}$, such that the predicted lineshape of our field-differentiated FMR signal is $\frac{d}{dH_z}\mathcal{R}e(\mathcal{X}_{xx})$. The exact expression of this function is cumbersome, it can also be found in the appendix of reference [27].

We isolate the fundamental mode from our data and we can extract a damping value from its linewidth by fitting $\frac{d}{dH_z}\mathcal{R}e(\mathcal{X}_{xx})$. For instance in figure 5.9 we fit the fundamental mode at a fixed applied field of -90 mT, to obtain a damping value of $\alpha = 0.010$. The same type of fitting could have been done at fixed frequency using the field dependence.

Obtaining a value of the damping from a single cut is of course not sufficient, especially given the signal to noise ratio in this type of measurement. The damping should be extracted all along the mode for better statistics. Furthermore the damping can also be extracted from the other modes following a more complex procedure detailed in reference [31]. The idea is to compensate the $V_{1,\mathrm{ac}}$ component of the higher order modes by performing measurements at opposite applied dc voltages, in order to obtain a purely $V_{2,\mathrm{ac}}$ signal. Then the lineshape of this mode can also be fitted by another function, giving damping values all along the mode.

During my PhD I did not use this complete method of studying the damping, but only used the fundamental mode. A complete result can be found in figure 6 of reference [31]. Following this study the 0.01 damping that we used during our theoretical work appears to be a reasonable value in our CoFeB free layers.

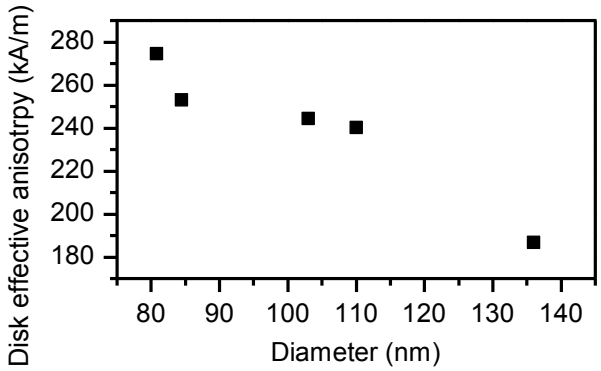

FIGURE 5.10: Effective anisotropy of the disk versus device diameter. The stack is the same as the one of figure 5.8. The diameter is taken as the electrical cd of the devices. The effective anisotropy of the disk is obtained from the frequency at zero field of the fundamental modes, using $\gamma_{0,CoFeB} = 29.4$ GHz/T.

The exchange stiffness

The exchange constant can also be in principle extracted from such voltage-FMR measurements. The numerous modes inside the free layer have been predicted and we know that the spacing between each of them is related to A_{ex} following equation 5.6. Then by measuring the spacing between the modes and by attributing a micromagnetic mode to each resonance, a value of A_{ex} is obtained. Such a method is discussed in reference [27] but was not used during this PhD. The previous study obtained a value of about 20 pJ/m in CoFeB based free layers, it is the value that we used in our calculations.

In a more recent study, the modes of thin CoFeB films were studied through Brillouin light scattering [11]. The obtained exchange stiffness is of about 18 pJ/m, in agreement with the voltage-FMR result.

5.3.4 Size dependence of the parameters

Here we briefly discuss the influence of the diameter of the device on the parameters of the free layer extracted by FMR.

We performed voltage-FMR measurement on an older stack with a 2.5 nm thick CoFeB-based free layer while varying the diameter between 80 and 150 nm. The effective anisotropy of the disks extracted from the lowest frequency mode at 0 field are shown in figure 5.10. As expected from the demagnetizing factors, the effective anisotropy of the disk increases as the diameter of the disk decreases. We do not have enough data for a quantitative comparison between this size dependence and the one predicted by the demagnetizing factors, similarly to what we did in figure 5.6. The reason for our lack of data is multifold: i) it is hard to obtain a signal to noise ratio significantly good on the smaller disks to identify the macrospin mode; ii) Each measurement can take up to a couple weeks; iii) We measured different stack composition and cannot compare two devices of different sizes but patterned on a different stack.

In our theoretical work, we used an anisotropy field $H_k = 1.566$ MA/m for a magnetization $M_s = 1.2$ MA/m. This anisotropy was extracted from VNA-FMR measurement on stacks with thinner free layers, it was our reference value when our micromagnetic simulation work started and therefore was kept for all the calculations for the sake of consistency. For POR19 the M_s is of about 0.8 MA/m (as discussed in the VSM measurement) and we expect the anisotropy to be closer to 1 MA/m. This value is taken from an effective anisotropy of 200 kA/m that was measured from voltage-FMR on very large devices (500 nm and more) patterned from more recent stacks.

The damping is expected not to depend on diameter. It is not affected by the demagnetizing effects unlike the effective anisotropy, but could be deteriorated by the patterning. We know from reference [27] and from our own measurements that the damping is of about 0.01. The value measured from VNA-FMR (namely with a great precision) on unpatterned films is 0.008. Therefore the patterning had little impact on damping. If the patterning has little impact on damping we expect it not to vary significantly with size. Our size dependence of the switching voltages shows that it is not impacted by edge damage (figure 5.6). Since the macrospin switching voltage depends on α this is an indication that α is not or not much dependent on size, but a more complete study based on voltage-FMR would of course be necessary to confirm this hypothesis.

Concerning the exchange constant it is also predicted not to depend on size. Performing a measurement of the exchange versus diameter from voltage-FMR measurement is a complex task that is yet to be done. We can only assume that it remains constant at 20 pJ/m.

5.4 Conclusion

In this chapter we have presented our STTMRAM devices and their basic properties. The stacks correspond to state-of-the-art magnetic tunnel junction with a strong reference system. They are patterned down to 25 nm and integrated specifically for our high-frequency electrical measurements.

We have shown R(H) and R(V) loops performed on these devices. From such measurements we can already discuss on the switching path. Indeed the macrospin model predicts well the size dependence of the critical switching field or voltage measured, just like in our micromagnetic simulations.

Finally we discussed the origin of each material parameters used along this manuscript. The magnetization is extracted from VSM loops performed at IMEC. The anisotropy is taken from VNA-FMR at film level and voltage-FMR at device level. The damping and the exchange are also obtained from voltage-FMR measurement performed by myself or before the beginning of this PhD.

Chapter 6

Time-resolved measurement of the free layer switching

In this chapter we present time-resolved measurements of the reversal of the free layer. These measurements were performed in Paris in 2019 towards the end of my PhD on POR19 samples from IMEC. The aim of this study is to unravel the switching path in our free layer in order to compare it with our different theoretical works. To do so the switching is studied while varying the voltage applied to the device or the diameter of the device. In this chapter we first detail our experimental set-up as well as the data processing necessary to extract the magnetization-induced signal. Then we propose a list of the different effects observed during our measurements. Finally we extract the incubation times and transition times of the switching and discuss the voltage and size dependence of the two delays.

6.1 Experimental methods

6.1.1 Scheme of the set-up

Time-resolved electrical measurements have already been presented in our state of the art, section 2.5.2. The principle is to reverse the free layer through STT by applying a voltage while the conductance is recorded by an oscilloscope. Figure 6.1 presents our experimental set-up. Let us first discuss broadly the role of each component before detailing them in the following subsection. The signal sent to the device is composed of two pulses generated by two distinct sources. The study pulse

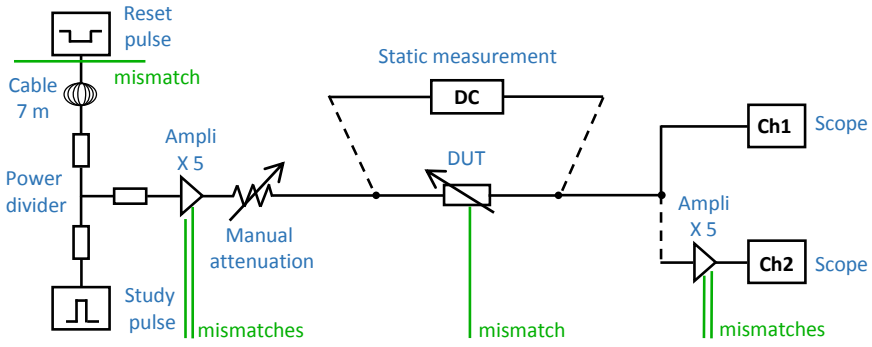

FIGURE 6.1: Electrical circuit used for our time-resolved measurements. The dc block is not detailed. In green are highlighted the impedance mismatches where reflections of the signal are expected. An external field in the z direction can be applied to the DUT and is controlled by a voltage source(not pictured here).

is the main pulse of our experiment. This pulse is going to reverse the free layer (from P to AP or AP to P) while the conductance is recorded. The second pulse is the reset-pulse. It is of weaker amplitude, opposite sign and longer duration than the study pulse. The aim of this pulse is to bring back the device in its initial configuration after it has been switched by the study pulse in order to prepare a second switching event. Since we are not studying the switching back, it is preferred to use a weak amplitude pulse to limit the stress induced on the device, hence the longer duration because the incubation time of the switching is longer at low voltages. The two pulses are combined in a power divider, their phases selected such that the reset pulse comes after the study pulse. The amplitude of the obtained signal is controlled by an amplifier followed by a manual attenuator. Using relays, the device under test (DUT) can be connected to this input or to a simple sourcemeter in order to perform the R(V) and R(H) loops presented in the previous chapter. The devices are connected by coplanar ground-signal-ground probes (from *picoprobe*). In the time-resolved configuration, the current flowing through the DUT is measured by our oscilloscope. This signal can be amplified for a better signal to noise ratio, but this induces an extra impedance mismatch hence we left the possibility to keep it un-amplified.

A part of the signal is reflected when there is an impedance mismatch. The signal therefore performs a back and forth motion within the circuit. This creates as many artefacts in the recorded signal that must be corrected. To reduce the mismatches we work at 50 Ω impedance as much as possible. Another strategy is to add a longer cable before a mismatch like presented in figure 6.1 in front of the reset pulse generator. This longer cable delays the reflected signal of a few tens of *ns* ensuring that it does not disturb the studied dynamics which is typically occurring in the first 20 ns or so. Moreover the reflected pulse is attenuated by the cable. We present reflection artefact and how to remove them in the data processing, figure 6.3.

6.1.2 Generating the input

We work with a 25 GHz oscilloscope. The oscilloscope uses internally a calibrating pulse with a very fast rise time. This calibrating pulse can also be an output of the oscilloscope and we use it as our study pulse. The main advantage of this study pulse is its rise time of about 20 ps, however we cannot control its duration and voltage directly from the scope output. The duration of the study pulse is of about 300 ns but it is not specified, such that it can vary between 300 and 400 ns from day to day. Having no control on the duration of the study pulse is of little consequences for our time-resolved measurement since we can directly access the switching time regardless of the pulse duration. The only issue is that an unnecessarily long pulse induces more stress to the device at high voltage.

However the applied voltage is an important parameter of our measurements and should be precisely controlled. The calibrating pulse has a fixed amplitude of 300 mV. To tune it we use an amplifier of 14 dB (x5) followed by an attenuator that can be manually tuned between -11 dB and 0 dB. The amplifier and attenuator were chosen such that the accessible voltage range corresponds to the one necessary for our study. Typically our devices present long switching time around -11 dB attenuation and breakdown at around -3 dB, this of course depending on their diameter.

The reset pulse is generated by a waveform generator (keysight 33600A). The pulse is set to have a 1 μs fixed duration, while we change its amplitude to match the voltage necessary for a reliable reset without unnecessary stress on the device. The reset pulse is sent at a 1 kHz repetition rate and the oscilloscope pauses to treat

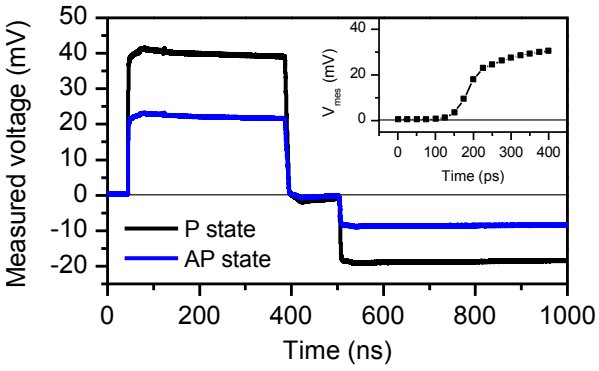

FIGURE 6.2: Study and reset pulses. The plot is the average over 1024 events of the study (positive) and reset (negative) pulses flowing through a device set in the P or the AP state. The device is of 114 nm diameter from POR19 stack, its state is fixed by a ±280 mT external field applied along z. The applied voltage is 531 mV. Such graphs are going to be used as references for normalization in our data processing. Inset: zoom in the rise time of the P state graph.

the data after recording a time trace for a few tens of ms, such that effectively after each study pulse a few tens of 1 μs long reset pulse are sent through the device. The two pulses are then combined through a power divider. The phase of the reset pulse is tuned in the waveform generator such that it starts right after the study pulse. This way both pulses can be observed in a single time trace to control easily their amplitude.

The amplifiers must be selected carefully. Indeed both pulses have initially a satisfying flatness, however some frequencies are bound to be filtered by the amplifier which deforms the pulses. The amplifier is chosen so to limit these deformations of the study pulse. The bandwidth must be broad: a low frequency cut degrades the flatness of the pulse while a high frequency cut its rise time. Typically the bandwidth of our amplifiers is between 1 MHz and 10 GHz. The noise figure is around 3 dB and the gain flat in frequency. Figure 6.2 shows the study and part of the reset pulse through a device fixed in the P or AP state. The rise time is slightly degraded after amplification, going from 20 ps to about 50 ps (see inset of figure 6.2). After this initial fast rise time the pulse amplitude keeps increasing at a much slower rate for about 100 to 200 ps until it gets to its maximum value. This slower increase is going to be removed from our signal by the data processing. We can also see that the study pulse is not perfectly flat because of the low frequency cut-off. This imperfect flatness is very little detrimental to our study because the typical magnetization dynamics are much faster and because we shall remove this artefact as well by normalising our signal using references in both states. The 50 ps typical rise time is still a satisfactory value to study FL dynamics whose typical frequency is of about 10 GHz.

6.1.3 Measuring the conductance

After amplification a certain voltage V_{app} is applied to the DUT when it is under the study pulse. The current across the device is read by the scope through a 50 Ohm impedance such that the measured voltage V_{mes} is given by:

$$V_{mes}(t) = V_{app}\frac{50\ \Omega}{R_{dut}(t) + 50\ \Omega} \tag{6.1}$$

Figure 6.2 shows the study pulse and part of the reference pulse when the device is set into a fixed P or AP state by a strong magnetic field along z. The conductance can be obtained from the measured voltage since we know the applied voltage from the attenuation. For instance in this figure the attenuation is -9 dB, giving a 531 mV

applied voltage and a 591 Ohm resistance in the P state. This value corresponds indeed to the one measured in the R(V) loop of the same device.

In practice the resistance of our devices is much larger than 50 Ohm and we make the assumption that $R_{dut}(t) \gg 50\ \Omega$. Within this assumption the measured voltage is proportional to the conductance of the device and we can obtain a normalized conductance versus time trace simply by normalizing $V_{mes}(t)$. We present our normalization method in the data processing section. This approximation is reasonable in the smaller devices while for devices of 200 nm and larger the resistance in the P state can be as low as 170 Ohm and the exact conductance must be recovered from equation 6.1.

The signal to noise ratio (SNR) depends on the voltage caliber of the scope. The best SNR is reached for 10 mV/division or less, therefore we shall zoom in the voltage range as much as possible while still observing the full dynamics. Regarding the temporal resolution of the scope, at best one point is recorded every 25 ps if we are reading several channels (40 GSamples/sec). If only one channel is recording it is possible to go up to 80 GSamples/sec. The oscilloscope also offers the possibility to interpolate more points up to one each 3 ps. This interpolation mode can be useful in the amplified channel to study the switching path, but of course no frequency above 20 GHz can be recorded in single channel configuration (Nyquist-Shannon sampling theorem). In practice we reduced artificially the bandwidth to 16.8 GHz, following the application notes of the oscilloscope vendor.

6.1.4 Chronology of a measurement on a single device

For each device we perform:

i) One R(H) and one R(V) loops. These loops are used to extract the offset field, the TMR ratio, the coercive field, the typical switching voltage range and the electrical diameter of the device. The results of the static measurements on POR19 were already discussed in the previous chapter. We perform the time-resolved measurement only on the devices presenting good static characterizations: a flat R(H) loop, TMR of 150 % or higher, hard to reverse reference system.

ii) The offset field is then corrected. At all time we apply the opposite of the offset field in order to ensure that the P to AP and AP to P switching are equivalent. The aim of this correction is to study a switching as close as possible from the voltage-only induced one studied in our micromagnetic simulations and domain wall motion models. This correction is never perfect in practice because the offset field varies slightly with applied voltage.

iii) We then sweep the voltage from -11 dB attenuation (422 mV) to -3 dB attenuation (1060 mV). We can only access 9 voltage points for each device with this set-up. For each voltage point we record the reference P state and AP state of the device. This is done by averaging 1024 pulses while the device is set into the P state or the AP state by a $\pm$280 mT external field applied along z (figure 6.2). These references will prove useful in the data processing. We then record 100 AP to P switching events through the amplified and through the un-amplified channel of the scope. Only the AP to P reversal was fully studied, the P to AP reversals were done on a few devices and present back-hopping at high voltages. The P to AP study is not discussed in this manuscript as it does not bring new findings in term of free layer dynamics. Our study on back-hopping can be found in reference [26] from other samples. The amplified data are taken while optimizing the time and voltage scale of the scope, in order to study efficiently the switching path. The un-amplified traces have more noise but less experimental artefacts, they are all taken within the same time and

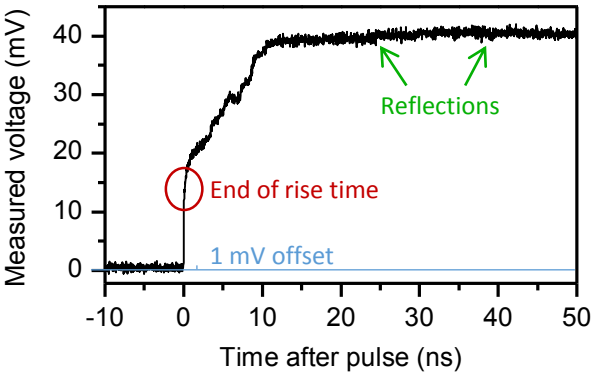

FIGURE 6.3: Typical time-resolved switching curve including some representative artefacts (raw data). The time trace shown is the raw measured voltage of 114 nm diameter from POR19 stack switching from AP to P under a 531 mV applied voltage. This is from the non-amplified channel. Pictured are three artefacts: i) The offset in voltage which is here of 1 mV (blue). ii) The end of the rise time (in red). iii) Reflections due to impedance mismatches (green). Here it is only slight reflections because we are in the non-amplified channel.

voltage caliber and are used to control our measurement. Finally an average over 1024 switching events and an histogram of all these events are recorded. For each voltage point we have at best 200 time traces we can extract characteristic delays from. We always start with the lower voltage and increase it gradually in order to have as much data as possible before any unexpected breakdown of the device.

These four steps were followed on numerous devices. Some of them encountered early breakdowns which prevent accessing the full data. We present here the full data that we obtained on POR19 devices of diameter 26, 48, 96, 114 and 152 nm.

6.2 Data processing

In this section we discuss our data processing. The aim is to extract a conductance versus time trace where only the magnetic part of the signal remains. Two tasks must be performed: defining the zero time (namely when does the study pulse start) and removing experimental artefacts. These artefacts include notably the decrease in voltage due to the low frequency cut of the amplifiers, the reflections due to impedance mismatches and the slower end of the rise time (figure 6.3). They are to be removed by normalizing the time traces with references taken in the P and the AP state.

6.2.1 Removing the voltage offset

There is a slight random offset voltage, essentially due to the $1/f$ noise of the amplifier(s). The measured voltage is supposed to be zero before the pulse (equation 6.1) but there is typically a 0 ± 1 mV signal as seen in figure 6.3. This offset must be removed because as we plan on normalizing the measured voltage to obtain a conductance versus time graph, we need to make sure that the measured voltage is directly proportional to the applied voltage, namely that there is no offset before normalizing.

In practice the offset is removed by averaging the signal before the beginning of the pulse and then subtracting this average value over the full time trace. For each single time trace the offset is recalculated and corrected.

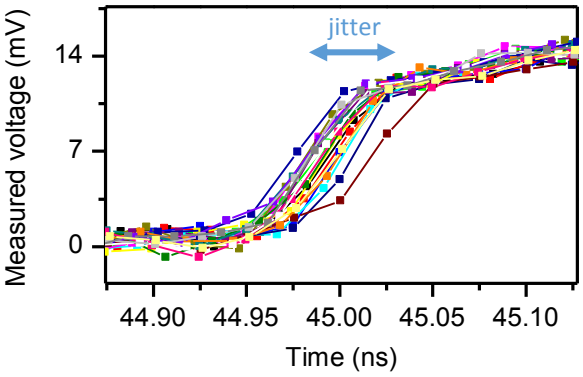

FIGURE 6.4: The jitter. The beginning of the pulse of 20 different time traces is plotted. The device and the voltage are the same as in figure 6.3. Here the beginning of the pulse vary up to 50 ps from one pulse to another. The beginning of the pulse presents a short first step followed by a slower increase of the pulse amplitude.

6.2.2 Defining the zero time

In the raw data the zero time is simply the moment at which the oscilloscope starts recording. This does not correspond to the beginning of the pulse, that we want to define as our zero time. Furthermore the time at which the pulse starts varies slightly from one pulse to another, we call this effect the jitter. Typically the beginning of the pulse varies of a few tens of ps, up to 300 ps in some cases. In figure 6.4 a weak jitter is pictured.

The jitter is not an issue for a direct observation of the switching path. It however becomes an issue when we extract characteristic delays from a time trace (switching time and incubation time). To remove the jitter we define a different zero time for each single time trace, which is taken as the time at which the pulses reaches 80 % of its final value before the beginning of the slower end of the rise time. This fluctuating definition of the zero time suppresses the jitter and ensures that all our switching events are under the same voltage at $t = 0$. We chose this 80 % value because we know that the switching events start with an incubation time. This incubation time is reduced very sharply when increasing the voltage. For this reason we can consider that the lower voltages applied to the device during the rise time have negligible effect on the magnetization compared to the final voltage and set our zero towards the end of the rise time. Moreover the slower end of the rise time corresponds to a weak voltage change compared to the faster initial increase.

In practice we first define the AP level at the end of the faster rise time by stacking together all our time traces, similarly to what is done in figure 6.4 but with our 100 curves. This is possible because of the clear change of rate in the signal between the faster and the slower part of the rise time. We then use a simple threshold code to start our data only after 80 % of the value at the end of the faster rise time has been reached and set the time to zero. With this method we generate a maximum mistake of 25 ps when defining the zero time (corresponding to our temporal resolution in the un-amplified data), which is satisfactory.

6.2.3 Normalizing the data

In this subsection we assume that we have two reliable references corresponding to the P and the AP state. As already stated these references are obtained by setting the device into P or AP state with a $\pm$ 280 mT external field and averaging the signal over 1024 pulses. In such references the pulse shape, the reflections and other non-magnetic artefacts are present. But no magnetic signal is present since the magnetization is fixed in one direction. We normalize our data using both the P reference

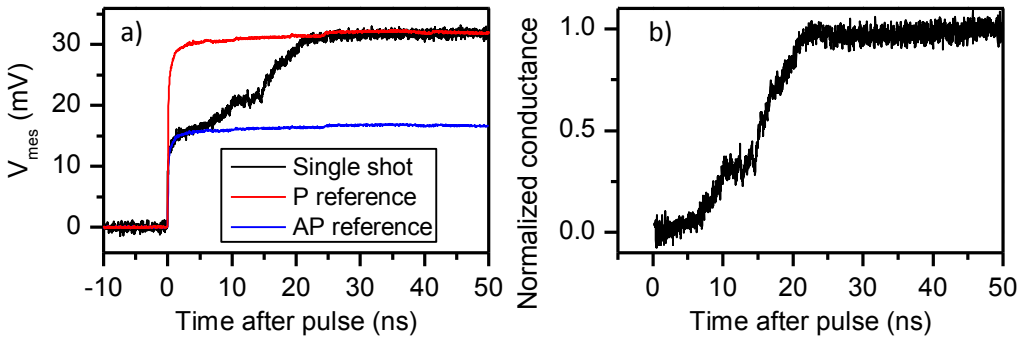

FIGURE 6.5: Normalizing our data. a) Measured voltage time trace for a device of 114 nm under 422 mV from the un-amplified channel. The time traces is plotted with the AP and P states references. b) The normalized conductance data obtained from this time trace and the two references following equation 6.2.

and the AP reference following the equation:

$$G_{\text{norm}}(t) = \frac{V_{\text{mes}}(t) - V_{\text{APref}}(t)}{V_{\text{Pref}}(t) - V_{\text{APref}}(t)} \tag{6.2}$$

Where $G_{\text{norm}}(t)$ is the normalized conductance. With this procedure artefacts occurring while the time trace is within the P state or the AP state are corrected. While if we used only one reference to normalize (for instance the P reference), then the artefact occurring in the AP state such as the slower end of the rise time are bound to be imperfectly corrected. G_{norm} then goes from 0 (AP state) to 1 (P state) in our AP to P switching. For devices of 200 nm and larger we first obtain the conductance versus time traces and references with equation 6.1 before normalizing. If this procedure corrects the artefact in the P and the AP states, it does not correct perfectly the one in the intermediates states that are reached while the magnetization is reversing, namely during the switching path. This is usually not an issue because typically the slower end of the rise time is finished before the magnetization reversal starts and the reflections occurs once it has ended. To correct artefacts during the intermediate states one would need a reference for each of these states which is impossible to obtain as the device cannot remains in these configuration for a long duration.

Figure 6.5.a presents a time trace with both its references. We can see the artefacts (slower end of the rise time and reflections) in both the time trace and its references. The final result is the normalized conductance versus time traces that shall be studied along this chapter.

This normalizing method has however a disadvantage. As the jitter is also present while we record the references, the rise time of the averaged reference is broadened by the jitter. For this reason the references are unreliable during the first 100 ps or so. When normalizing we end up dividing our measured voltage by a reference that is of lower value than expected because of the jitter, which creates unreliable data points. These data points are within the study pulse, but we move them out of our data range in order to analyse our normalized conductance time traces easier. Typically we show our final time traces starting at t = 100 ps or 200 ps to hide these poorly normalized data, as in figure 6.5 .b. This is not detrimental to our study of the switching path as the bad data are within the incubation time for all our diameters and voltages.

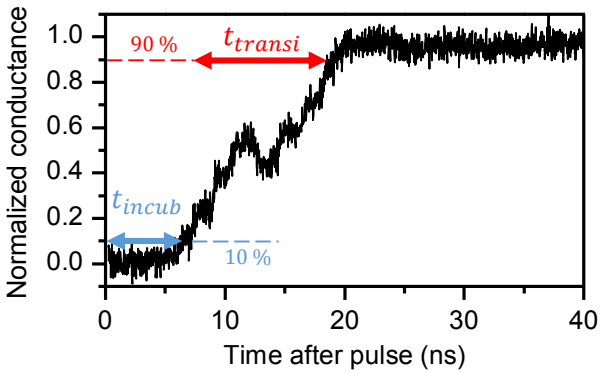

FIGURE 6.6: Extracting the delays with a threshold method. The time trace corresponds to 96 nm device under 473 mV. The delays are defined from ± 10 % of the final states.

6.2.4 Building a reliable AP reference

We have shown how to normalize the data from reliable P and AP references. However for a certain diameter and voltage range we cannot obtain a reliable AP reference when studying the AP to P reversal. This is due to the fact that at voltages above typically 600 mV (depending on diameter) the study pulse destabilizes the AP state that we are trying to fix with the external field. This is a fundamental issue in this measurement because we must necessarily obtain a reference of the state we are switching from, with a voltage sufficiently large to switch it.

In practice when the AP reference is unreliable, magnetic noise is observed in the time traces (oscillations of stronger amplitude and weaker frequency than the typical noise in the measurement). As a result the unreliable AP references are of higher conductance than expected from the device AP conductance. By looking at the magnetic noise it is easy to observe beyond which voltage the AP state is destabilized and the AP reference unreliable.

Now we explain how to build a reliable AP reference for the higher voltages from the one we could measure at the lower voltages. The most basic idea would be to multiply the reference at -11 dB attenuation in order to obtain a reference at higher voltage. However this is not sufficient because of the voltage dependence of the conductance in the AP state (seen in figure 5.5). This voltage dependence cannot be corrected directly because we cannot obtain a R(V) loop reaching the high voltage values of our time resolved measurements. This is due to the breakdown: in the dc measurement the voltage is applied much longer than our pulse length, which would kill the device for the higher voltage values.

To tackle this issue, we obtain the conductance of the AP state from the beginning of the pulse in a switching event. Since the beginning of the reversal is an incubation time, we assume that the first 100 ps of the switching correspond to a *pure* AP state. In practice the first 100 ps also correspond to the slower end of the rise time which is an artefact. Therefore we build a more reliable reference by fitting this slower increase of conductance by an arbitrary exponential function. Then from the fitting parameters we obtain precisely the conductance in the AP state at any voltage and build a reliable AP reference.

6.2.5 Extracting the delays

From our raw data we now obtained normalized conductance versus time single shots. These single shots can be directly used to discuss the switching path, as we shall do in section 6.3. To be more quantitative it is useful to decompose the switching measured into two delays, similarly to what was done in section 3.3.2 for our

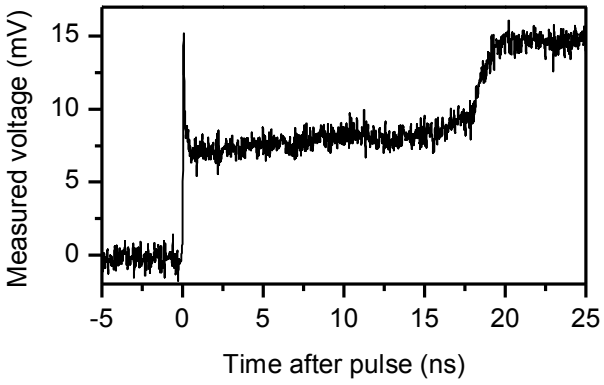

FIGURE 6.7: The capacitive spike for smaller devices. Pictured is a time trace taken from the amplified channel on a 26 nm device under 669 mV. The rise times comes with a strong capacitive spike, then the incubation time and the switching occurs normally.

micromagnetic simulations at finite temperature data, inspired from reference [44]. The incubation time t_{incub} is defined as the time needed for the device to be 10 % reversed and the transition time t_{transi} the time between 10 % and 90 % reversal.

The delays can be extracted with a simple threshold code, like pictured in figure 6.6. However in the time-resolved data it is more reliable to use a smoothing algorithm on the time traces before applying the threshold, because of the noise. The smoothing is done by a simple moving-averaging procedure. The window for the smoothing must be carefully selected: a too weak smoothing makes the delay extraction sensitive to noise, while a too strong smoothing is deforming the signal which impacts slightly the delays.

In practice we check manually which smoothing parameters is the best depending on diameter and applied voltage. Typically the smoothing window is 5 or 10 points long, being larger for the more noisy data. Finally the initial and final level are not always exactly 0 and 1 in our normalized data. This can be due to an imperfect reference, to a small contact issue with the probes, or to real magnetic effects. For this reason the final AP and P level are always defined manually by looking at all our normalized conductance data. The P state is always 0 ± 0.05 and the AP state 1 ± 0.05, but getting the exact value proved useful for a more reliable threshold extraction.

6.2.6 Issues for the smallest size

There is an additional experimental artefacts that we did not mention so far and that occurs only for the smaller diameter (26 and 48 nm in this set of data). In these highly resistive devices there is a capacitive spike right at the end of the rise time (see figure 6.7). For these smaller devices there is therefore a weaker signal to noise ratio due to the high resistance and an additional artefact. The capacitive spike is only a few tens of ps long and can be removed from our data without any issues. However it prevents us from using our fitting procedure to extract the AP conductance and build a reliable AP reference at all voltages. For this reason, the 26 and the 48 nm devices that are discussed in this manuscript where studied after only a P reference normalization. The artefact in the AP state in the time traces from these devices are not corrected as well as in the other devices.

The weak signal to noise ratio in these two devices also prevents us from using the threshold procedure that we just described. Indeed to obtain reliable delay we would need to smooth the data further, which deforms more and more the signal. To tackle this issue we extract the delays from a fitting procedure. Our conductance

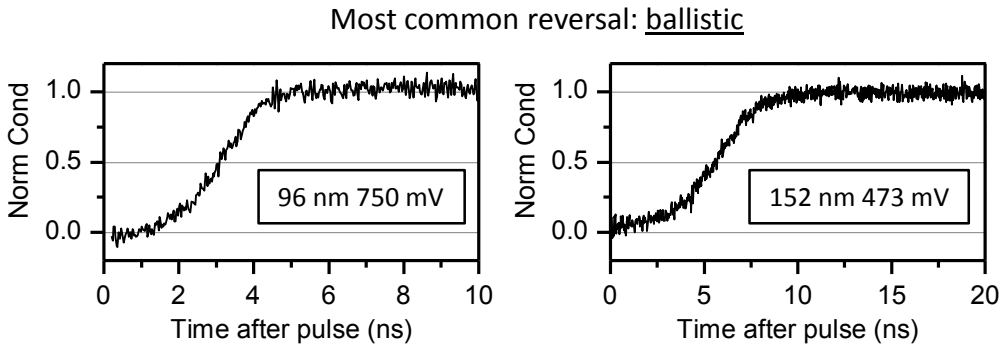

FIGURE 6.8: The ballistic reversal. Two time traces are shown for devices of 96 nm under 750 mV and 152 nm under 473 mV. The full data processing procedure was applied to obtain these traces. Note that the time scales are different highlighting a faster overall switching for the higher voltage graph.

versus time data are fitted with an ArcTan function, leaving 4 free parameters:

$$G_{\text{fit}}(t) = G_{\text{mid}} + G_{\text{HalfWidth}} \frac{2}{\pi} \text{ArcTan}\left(\frac{t - t_{\text{sw,fit}}}{0.5\Delta t_{\text{fit}}}\right) \tag{6.3}$$

From G_{mid} and $G_{\text{HalfWidth}}$ we obtain the initial and final values corresponding to the P and the AP state and check if they are consistent with what is observed manually. From $t_{\text{sw,fit}}$ and Δt_{fit} we obtain the two delays t_{incub} and t_{transi} from basic math on ArcTan function using the ± 10 % definition. Note that the fitting function has no physical meaning and the same result can be obtained with other functions such as the *error function* for instance.

6.3 Zoology of the switching events

In this section we give a qualitative overview of the switching observed in our time-resolved measurements while varying the diameter and the voltage. We identify 7 different types of events during the switching in total: ballistic reversal, small stops or move-back during a ballistic reversal, failed trials, pinning, strong move-back, oscillatory behaviour and finally magnetic noise in the P state. For each event we discuss their definition, their likelihood at different diameters and voltages, give a possible physical origin and give a typical figure. Then an overview of the switching events is shown.

6.3.1 The ballistic reversals

The most common time trace corresponds to a ballistic reversal. We define a ballistic reversal as a switching during which the normalized conductance is increasing monotonically. Ballistic reversals are shown in figure 6.8. These reversals are the preferred one in term of memory applications as all other switching events occurring during the transition time slow down the reversal. For this reason it is particularly interesting to identify the best region in the diameter-voltage space for ballistic reversals.

Ballistic reversals can be found at each voltage and diameter points that we measured. As seen in figure 6.17, the higher probability of ballistic reversals were obtained for the larger devices under high voltages.

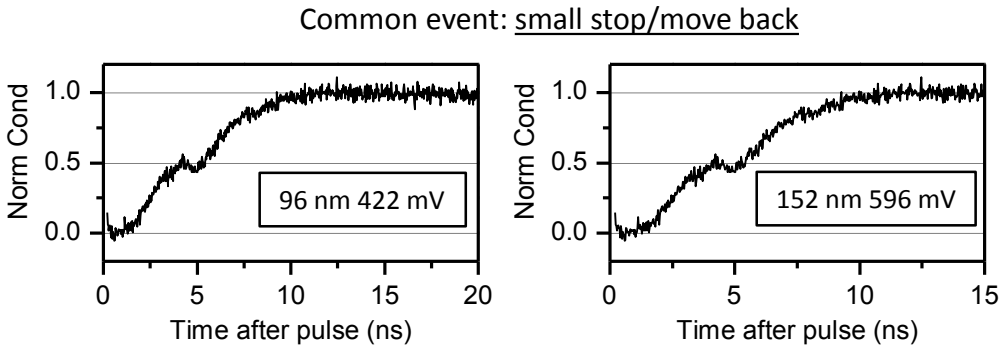

FIGURE 6.9: Small stops or moving-back during the switching. Two time traces are shown for devices of 96 nm under 422 mV and 152 nm under 596 mV. The full data processing procedure was applied to obtain these traces.

What is the physical origin of ballistic reversals ? We cannot give a single switching path leading to a ballistic reversal because both the macrospin switching and the domain wall based switching without strong Walker oscillations are expected to be somehow ballistic. This is seen in figure 3.4.b where both switching are compared for a simulated 40 nm device. The best way to indentify the switching path from a ballistic reversal is to look for a linearity in the time trace towards the center of the disk (namely around $G_{\text{norm}} = 0.5$). In figure 6.8 the central part of the graphs appears to be linear, which is a first indication of a domain wall-based reversal.

6.3.2 Small stops in the switching

During a ballistic reversal the normalized conductance sometimes stops or moves slightly back for less than a ns, we call these events small stops and small move-backs. In figure 6.9 we show two of such events occurring after 5 ns. These events can happen for values different from $G_{\text{norm}} = 0.5$ but they are typically not found for $G_{\text{norm}} < 0.2$.

Small stops and small move backs are common, they are found for each diameter and voltage we measured save for the 96 nm and 152 nm devices under 944 mV, in which 100 out of 100 measured time traces were ballistic. These events are more likely at low voltages compared to large voltages. Furthermore the typical stop is longer for a low voltage reversal that for a high voltage reversal on a given device.

There is not a single physical origin for the small stops and small move-back. In our micromagnetic simulations, thermal fluctuations are expected to induce such events in both macrospin and domain wall based reversal. That is a first possible physical origin for these short events: simple temperature-induced fluctuations of the magnetization of the free layer. The small stops can also correspond to very short pinning, then the stop occurs at the position of the pinning plateaus (to be defined in the following subsections). Several separate physical effects can cause such short events, which explains why they are almost always observed.

6.3.3 The failed trials before the switching

We call failed trial the event of the conductance going up and then back down to its initial state during the incubation time. The failed trials are not part of the transition time since the incubation time resumes after each one. Failed trials for different diameters and voltages are pictured in figure 6.10. The conductance can go up to

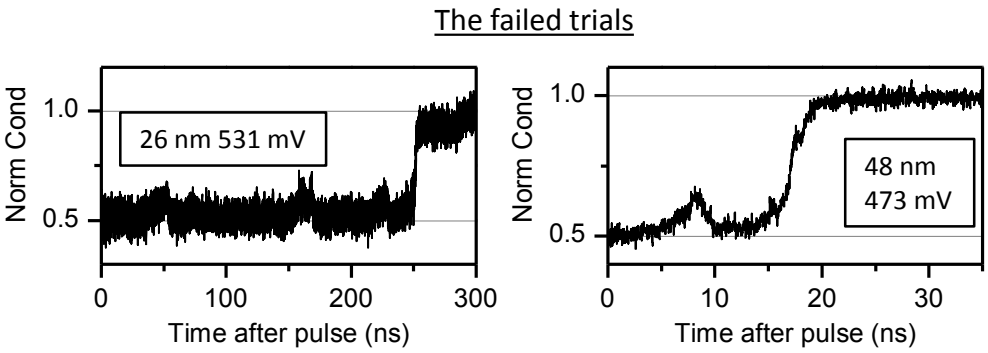

FIGURE 6.10: Failed trials. Two time traces are shown for devices of 26 nm under 531 mV and 48 nm under 473 mV. For these small devices the full data processing procedure cannot be applied and the conductance is only normalized by a P reference. Three fail trials are seen in the 26 nm device and one for the 48 nm one.

0.3 (namely a free layer 30 % reversed) before going back into incubation, but typical failed trials reach a maximum around 0.15. Several failed trials can occur during one incubation time, similarly to the 26 nm graph of figure 6.10.

Failed trials were measured in the 26 nm device for voltages of 750 mV or below and in the 48 nm device for voltages of 596 mV or below. No failed trials were found in the 96 nm device or the larger ones (figure 6.15). At low voltage the incubation time is longer and the failed trials are common (26 nm device in figure 6.10). While for the higher voltages the failed trials are rarer and occur right before the transition time (48 nm device in figure 6.10).

Failed trials were predicted in the incubation time of our micromagnetic simulations, as seen in figure 3.14. In the simulations these events correspond to an amplification of the macrospin precession which is then reduced again, due to the thermal fluctuations. The smaller devices presented more fluctuations than the larger one in the simulations because they are described by a smaller number of cell. The size dependence of the fluctuations in the simulations cannot be simply compared to the one of our time-resolved measurement. The existence of failed trials argue in favor of a macrospin first stage of the reversal, because of two reasons: i) In micromagnetic simulations the failed trials were only observed in the macrospin phase, they were not present in our initial domain wall simulations with temperature included. ii) If there is a nucleation of the domain wall, it induces a change in topology of the system and it would require another change to go back to the initial state and carry on the incubation time. For these reasons we believe that there is no nucleation of domain walls during the failed trials. But this does not prove that there is no nucleation during the successful reversal, especially since domain wall signatures such as pinning or oscillations are sometimes observed even in this diameter range.

6.3.4 Longer plateaus and pinning

The magnetization can get stuck around a fixed value in between the P and the AP state, this event is called a pinning. This name comes from the possible physical explanation which would be the pinning of a domain wall. While stuck in the plateau, the normalized conductance can present oscillations (figure 6.11.a) or even move to another pinning site before coming back. There can be several pinning positions

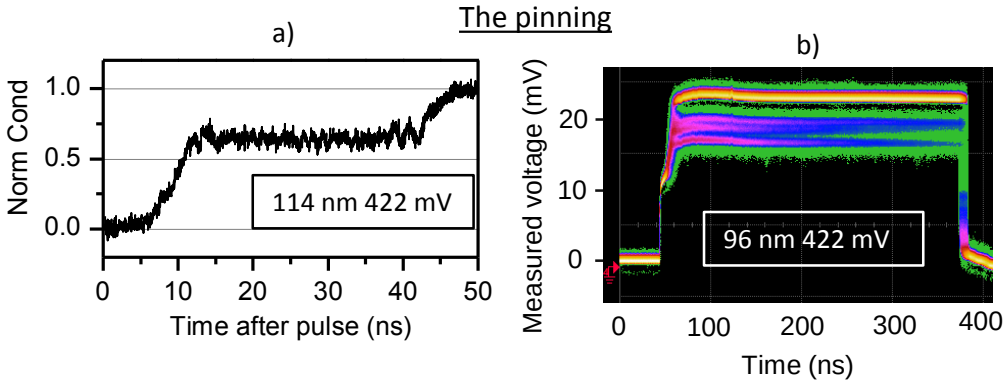

FIGURE 6.11: The pinning. a) Time trace for a 114 nm device under 422 mV. b) Histogram from 1024 study pulses stacked together, for a 96 nm device under 422 mV. The upper bright plateau is the P state while the pink and blue plateaus corresponds to three distinct pinning positions.

depending on the device measured, the pinning always occurs at these fixed positions. To identify the pinning positions we plot directly from the scope an histogram of 1024 study pulse stacked together, the color corresponding to the probability of presence (figure 6.11.b). We cannot extract the data of this histogram from the scope hence why we are showing only a screen print. No data processing was applied to this figure but it is still convenient to identify the pinning positions, three in this case.

Pinning was found in the devices of 96 nm or above but not in the 48 and 26 nm ones. It occurs only for the lower voltages value, as seen in figure 6.15. As the voltage is increased, the probability of a pinning occurring and the typical duration of the pinning decreases very sharply. Each pinning site can have its own probability of occurring regardless of the other pinning sites.

As the name suggest, the pinning is expected to be the consequence of the pinning of a domain wall at a fixed position. No macrospin scenario can explain such plateaus in the time traces. We expect the pinning to be due to defects in our free layer. The free layer is composed of CoFeB/Ta/CoFeB, with a very thin (3 angstroms) tantalum layer. We expect that this layer is not perfectly homogeneous, causing as a result a non-homogeneous free layer with holes in the exchange coupling between the two CoFeB layers. The domain wall once nucleated can get stuck at the hole position if it is not driven by a sufficiently strong voltage, which could correspond to the pinning. This hypothesis has been studied by ourselves and our partners at IMEC by looking at the pinning in different stacks coming soon. For proprietary stacks in which the exchange interaction is laterally much more uniform, the pinning was found to be essentially suppressed. Unfortunately the stack details fall under confidentially agreements and cannot be disclosed at the time of writing of this PhD manuscript. With this explanation of the pinning it is easy to understand why it was measured in the larger devices but not in the smaller one, as the probability of having a defect in the free layer grows as the square of the diameter. The oscillations seen at the pinning plateau would be trials of the domain wall to get de-pinned.

Finally if this hypothesis for the origin of pinning is correct, it has an implication on the domain wall nucleation. In our micromagnetic simulations the domain wall could nucleate anywhere around the edges of the disk. Let us assume that it is also the case in the measured device and that the defect is a point. Then the domain wall

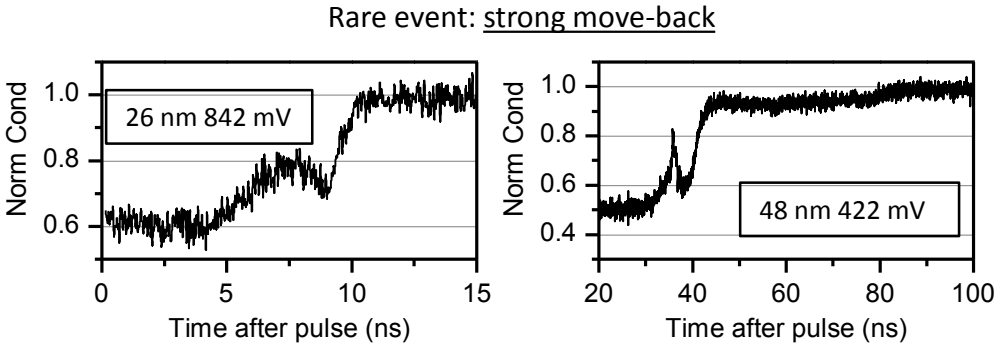

FIGURE 6.12: The strong move-back. Two time traces are shown for devices of 26 nm under 842 mV and 48 nm under 422 mV. For these small devices the full data processing procedure cannot be applied and the conductance is only normalized by a P reference. Notice the large difference in the time scale of the two graphs.

would encounter the defect for a continuous number of reversed domain size depending on the edge where the nucleation occurs, assuming that there is no rotation around the disk and that the defect is not at the center. Then there would not be a preferred position for the pinning plateaus in our conductance graphs. The fact that we have a finite number of pinning positions indicates that i) the nucleation always occurs at the same position and there are several defects, ii) Or the nucleation occurs at several different positions and there is one defect. As the defects necessarily break the circular symmetry of the system, we believe that there is a preferred pinning position and that the case i) is the most likely. The defects forces the nucleation around a fixed position and then pins the domain wall while it is crossing the disk.

6.3.5 Strong move-back during the switching

Sometimes the normalized conductance goes impressively backwards during the transition time before resuming a ballistic switching. We call these events strong move-backs. They can be seen for instance in figure 6.12. We differentiate the strong move-backs from the small stuck/small move-back because of their amplitude and the fact that they do not occur under the same conditions. We differentiate them from the failed trials because it happens during the transition time, and because the strong move-backs can occur even when more than 30 % of the free layer is reversed (as seen in the 48 nm device of figure 6.12).

The strong move-backs are observed for all the diameters at the lower voltage values we explored (422 or 473 mV). For higher voltages the strong move back are no longer present on the devices of 96 nm or larger, but can still be found for the devices of 26 and 48 nm. It is a rare event (typically 1 to 5 runs out of 100) whose probability decreases when the voltage increases.

Different physical effects could lead to a strong move-back. For instance it could be possible for a thermal fluctuation to cause such an event in a macrospin reversal, similarly to failed trials. However strong move-back are also found for diameter and voltages at which domain wall related effects are seen, such as oscillatory behaviour. For these conditions the strong move-backs could be due to the domain wall moving backwards because of a defect (it would be then related to pinning), or because of

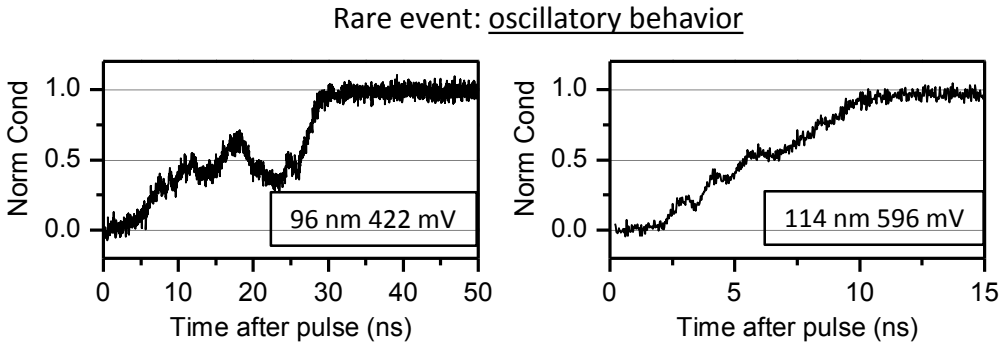

FIGURE 6.13: Oscillatory behaviour. Two time traces are shown for devices of 96 nm under 422 mV and 114 nm under 596 mV. Our full data processing was applied to obtain the graphs.

a strong walker oscillation around a $H_{\text{tot}} = 0$ position similarly to what was predicted in our domain wall dynamics models, while the rest of the weaker amplitude oscillations are lost under noise.

6.3.6 Oscillatory behaviour

Oscillatory behaviour is sometimes observed. We define it at several back and forth motion of the normalized conductance. The amplitude and the time scale of the back and forth motion can vary within one time trace, as observed in figure 6.13. The oscillatory behaviour does not necessarily happen around $G_{\text{norm}} = 0.5$.

Some form of oscillations were measured for all our diameters, even in the smallest one (figure 6.16.a). As for the other domain-wall related events, the probability to observe oscillatory behaviour decreases sharply as the voltage increases. Under certain voltages and diameters (for instance 96 nm 422 mV) it is a rather common event (more than 10 % of the reversals), while for smaller diameters or larger devices it is a rare event. The amplitude of the oscillations and the period decrease qualitatively if we increase the voltage or decrease the diameter, just like for the pinning and strong move-backs.

An oscillatory behaviour can be the consequence of different effects. It is a clear domain wall signature as we do not expect any oscillations to be observed in a macrospin configuration along the z component of the magnetization. It can be explained in some cases by the Walker oscillations that we predicted in our domain wall dynamics models. The oscillations seen in the larger devices notably can correspond to our predictions in term of size and voltage. However it is difficult to conclude that these are indeed Walker oscillations because there is also pinning in these devices that of course affect the domain wall dynamics. What we are measuring is a complex system with intrinsic domain wall dynamics on top of free layer defects. Moreover the oscillatory behaviour seen in the smaller devices cannot be explained by Walker oscillations of a domain wall because they are predicted to be of weak amplitude for these sizes. Then the oscillatory behaviour could be due to several small stop or strong move-back events occurring one after the other, explaining why it is a rarer event at small size.

6.3.7 Magnetic noise in the parallel state

The final event we discuss is not related to the switching path of the free layer and occurs after the transition and the incubation time. When the voltage is sufficiently

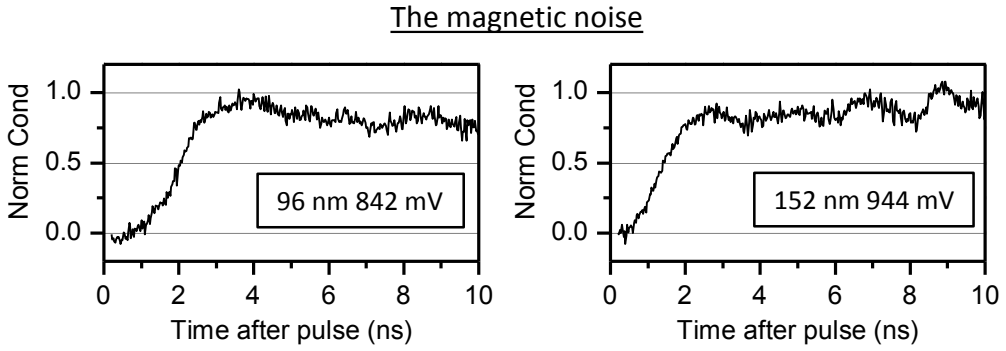

FIGURE 6.14: Magnetic noise in the P state. Two time traces are shown for devices of 96 nm under 842 mV and 152 nm under 944 mV. Our full data processing was applied to obtain the graphs.

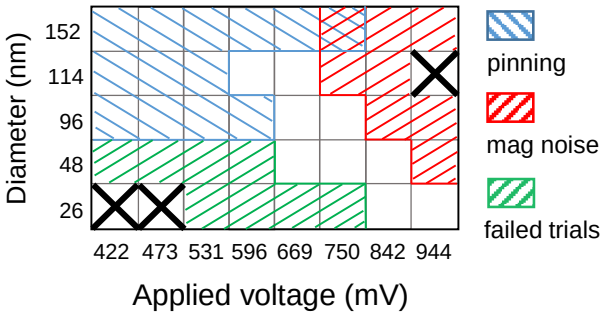

FIGURE 6.15: Map in the voltage-diameter space giving the conditions for pinning, magnetic noise and failed trials. The scale in diameter is not linear, the devices are sorted by size. The crossed out cells indicate that no data could be recorded (because of too slow dynamics or breakdown of the device).

strong some devices present magnetic noise in the P state and the normalized conductance does not reach a genuine 1. The magnetic noise is easy to distinguish from the standard noise of our measurement because it is non-white, of larger amplitude and always occurs when the final state is below 1 (figure 6.14).

The magnetic noise was reached before breakdown in all our devices of 48 nm or larger (figure 6.15). The larger is a device and the lower is the voltage necessary to observe magnetic noise. With a stronger voltage the effect is reinforced as the amplitude of the noise increases and the final state average value gets lower.

Having magnetic noise means that the magnetic tunnel junction is not perfectly in a parallel configuration and that the z component of the free layer or the reference layer is fluctuating. It happens at strong voltages favoring the P state therefore it is necessarily the reference layer that is unstable in this configuration. This instability of the reference layer was not seen in our R(V) loops because we did not apply dc voltages sufficiently strong, as the breakdown is occurring much easier in a dc measurement than with our 300 ns study pulse. The time-resolved measurement gives us more information than the simple dc measurements about the reference layer failure: the z component of its magnetization fluctuates rather than staying constant while it is tilted. We have shown that for the smaller devices the effective anisotropy of the free layer is stronger because of demagnetizing effects. This reasoning in theory holds true for the anisotropy of the reference system, such that the reference system is expected to be more robust for the smaller diameters than for the larger ones at a fixed voltage. This can explain why the magnetic noise is seen at larger voltages for the smaller diameters.

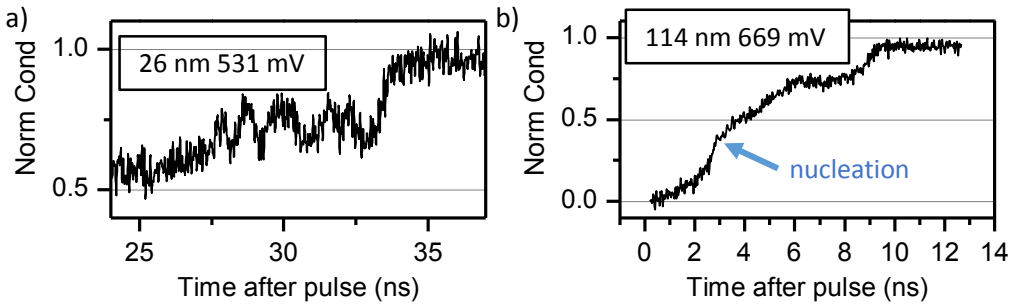

FIGURE 6.16: Domain wall signatures. a) Time trace for a 26 nm device under 531 mV. The full data processing was not applied and the normalization is only done by a P state reference. Here we see a clear domain wall signature. b) Time trace for a 114 nm device under 669 mV. The full data processing was applied. Several events are occurring, the arrow indicates what looks like a late nucleation of a domain wall.

6.3.8 Overview of the switching events

We have described three easy to distinguish events (pinning, failed trials and magnetic noise) and three different events that are harder to attribute to a single physical effect (small stops, strong move-backs and oscillatory behaviour). The three first events are found in the voltage and diameter conditions shown in figure 6.15. Even though we are lacking data between 48 and 96 nm, there is still clear trends on the voltage and diameter dependences of these three events. Another effect has not been discussed so far: the slope of the normalized conductance versus time graphs, namely the rate at which the device switches during the transition time, varies from one run to another. Even two ballistic reversals taken at the same voltage and diameter can have clearly different slopes and therefore different transition times (as seen in figure 6.18.b). We do not have a physical explanation for this effect.

We have seen clear domain wall-related effects, for all diameters. An example of oscillations seen in the 26 nm device is shown in figure 6.16.a, highlighting the fact that even the smallest device we could measured shows signs of non-homogeneity. The domain wall effects observed are: pinning, linear behaviour in the middle of the transition time, oscillations and strong move backs. The oscillations on the larger devices are reminiscent of the strong Walker oscillations we have predicted, but the pinning present in the same voltage and diameter range prevent us from reaching a clear conclusion. A similar study as been done towards the end of my PhD on pinning-less samples and is discussed in our conclusion and perspectives. The domain wall effects seen in the 26 and 48 nm devices are not explained by any of our models, it is unclear what is their physical origin.

Even though every reversal seems to include a domain wall, we have seen some macrospin signatures. Our micromagnetic simulations predicted that for devices larger than 20 nm the switching path is a macrospin phase followed by a nucleation of a domain wall and its motion. The failed trials found in our smaller devices are reminiscent of the one seen in the macrospin phase in the simulations of disks with similar diameters. Moreover the fact that these failed trials cannot go higher than a certain value is an indication that beyond a certain point we cannot as easily go back to the initial state. Does this point correspond to the nucleation of a domain wall ? While in most time traces there is not a clear change in the rate of switching, it can still be found in specific runs such as the one presented in figure 6.16.b. In this graph

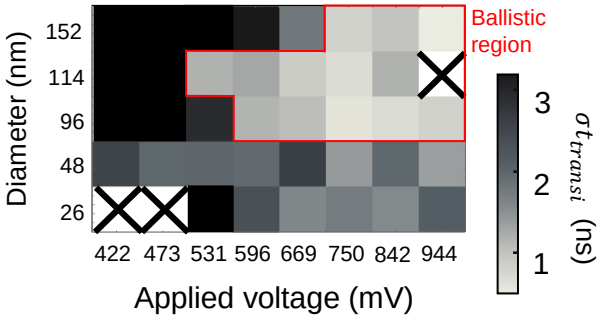

FIGURE 6.17: Standard deviation of the transition time in the voltage-diameter space. The scale in diameter is not linear, the devices are sorted by size. The crossed out cells indicates that no data could be recorded (because of too slow dynamics or breakdown of the device). When the standard deviation is low it indicates that the switching occurs mostly in a ballistic manner, allowing us to define a ballistic region.

the 114 nm device is switching in a non-linear fashion (as predicted by a macrospin model), before changing instantly its rate and starting a linear switching. Then the domain wall gets stuck by pinning before the end of the reversal. We believe that this change of rate corresponds to the nucleation of a domain wall, as it is similar to the one predicted in our micromagnetic simulations. The nucleation is not seen most of the time though. The reason for this could be that in most switching trials the nucleation occurs earlier than in figure 6.16.b and therefore the change of rate is not as clear in most cases. This figure would then correspond to a late nucleation. We have another strong argument indicating that the early stage of the reversal is macrospin at all sizes, this is discussed in section 6.5.2 as we look at the dependence of the incubation time on normalize voltage for different sizes.

Finally while it is hard to be quantitative about the probability of each events, we can still study the likelihood of a having a ballistic reversal by looking at the standard deviation of the transition time. Indeed a small standard deviation of the transition time indicated that the events slowing down the reversal are rare and not too detrimental. Typically if pinning, oscillatory behaviour or strong move-backs are present, the standard deviation is high. While if all the switching events measured are ballistic or only present small stops, it is lower. A map of the standard deviation of the switching time in the voltage-diameter space is shown in figure 6.17. We highlighted the region in which the standard deviation is the lowest, as it corresponds to the ballistic region. The most ballistic reversal is obtained for larger devices under a high voltage, which is not necessarily a good news for the scaling down of the STTMRAM devices. This is due to the unexplained domain wall effects on smaller sizes that are not reduced as sharply with voltage as the domain wall effects in the larger devices. This is also the reason for the almost non-dependence on size of the transition time discussed in section 6.4.2.

6.4 The measured transition time

So far we gave a qualitative view of the switching observed in our measurement. Now we discuss quantitatively the distributions of the transition time and the incubation time found at different voltages or diameters.

6.4.1 Overview of the transition time

The shape of the transition time distribution is directly related to the probability of occurrence of each events. For instance in figure 6.18 is pictured the transition time distribution in a case where pinning and other events slow down the transition

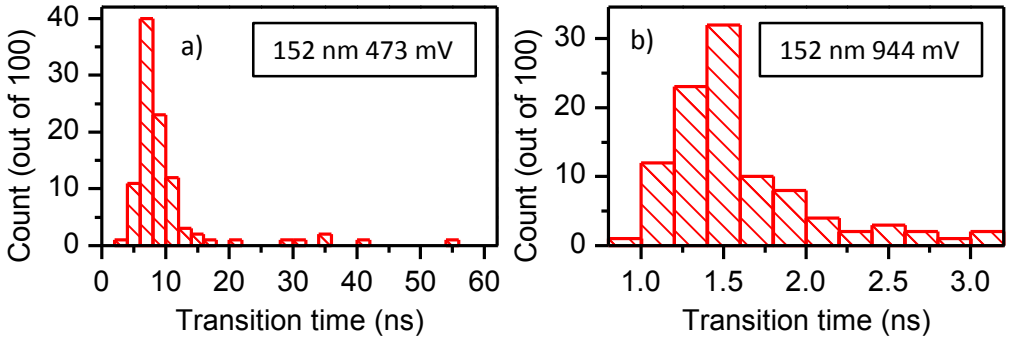

FIGURE 6.18: Typical transition time distributions. The data are taken from the 152 nm device under a) 473 or b) 944 mV. The transition time is obtained by the threshold method on 100 runs. The difference in time scale highlights that the distribution is much sharper at higher voltages.

and in a case where the switching is mostly ballistic. In panel a) we see that most transition times are of about 8 ns, but there are also around 10 events out of 100 of 20 ns or larger. These longer transition times correspond typically to pinning events. The higher voltage distributions such as panel b) are overall much sharper, centered around a lower value and no longer present points away from the main peak. This corresponds to the ballistic region that we could picture with the standard deviation of the transition time in figure 6.17. We can see that even for 100 ballistic switching events, the transition time can vary strongly (1 to 3 ns in this case) only from the variation of the slope that we previously discussed. For other voltages and diameters, the shape of the distribution depends on the different events that can slow down the reversal. But only the longer pinning events can be seen in the distributions as clearly as in figure 6.18.a. Most other events do not slow down the switching sufficiently to be distinguished from the main peak.

To study quantitatively the influence of size and voltage on the delays, we use their median value as a metric. We settle for the median instead of the mean because in some cases for the incubation time the switching does not start within our 300 ns study pulse window. In this case we know that the incubation time of this event is larger than 300 ns and we can incorporate it to the median as long as more that half of the switching are observed, but we cannot consider this event in a mean value. We suppose that there is no correlation between a longer incubation time and any specific switching event, therefore we can give a standard deviation of the transition time even from an incomplete data set. The median was used for the same reason in our micromagnetic simulations.

The median transition time dependence on size and voltage is pictured in figure 6.19. We can observe that there is a clear voltage dependence of the transition time at all voltages but no distinct size dependence. We shall discuss these two aspects.

But before let us remind briefly what are the expected diameter and voltage dependences in the macrospin and domain-wall models. In the macrospin scenario, the deterministic switching time is given by equation 2.2. It is easier to discuss the dependences by taking the approximate expression proposed by Sun 2.1:

$$t(m_z) = \frac{1+\alpha^2}{\alpha\gamma_0 H_{k,\,\mathrm{eff}}^{\mathrm{disk}}} \frac{1}{h-1} \ln\left(\frac{\theta}{\theta_0}\right) \tag{6.4}$$

The switching time is expected to vary as $(h-1)^{-1}$, namely the inverse transition

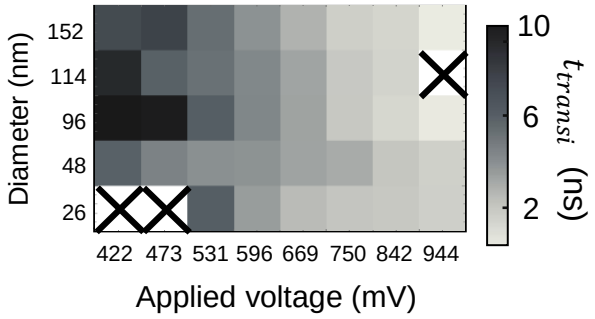

FIGURE 6.19: Median transition time in the voltage-diameter space. The scale in diameter is not linear, the devices are sorted by size. The crossed out cells indicates that no data could be recorded.

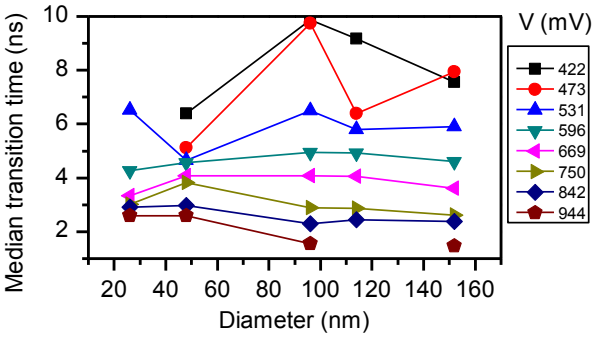

FIGURE 6.20: Size dependence of the median transition time. Each curve corresponds to a different applied voltage. This is the same data as in figure 6.19 but with a rigorous diameter scale this time.

time should depend linearly on voltage with a non-zero intercept. The diameter dependence is slightly more complex as both $H_{k,\,\mathrm{eff}}^{\mathrm{disk}}$ and h depend on diameter following the demagnetizing factors of the disk. At a given voltage decreasing the diameter increases the effective anisotropy which decreases h. As a result the smaller diameter are slower to reverse than the larger one at fixed voltage in the macrospin model.

For the domain wall based model, the switching time is given by the drift velocity term and by the possible strong Walker oscillations that can slow down the reversal. We disregard the strong oscillations since most of our measured reversal were ballistic and since we are considering the median of the transition time. Then the domain wall velocity simply follows equation 4.48:

$$\bar{\dot{q}} \approx \Delta(\sigma j - \alpha\gamma_0 H_{\mathrm{tot}}(q)) \tag{6.5}$$

In our measurement the offset field is compensated and the overall contribution of the other field terms (stretch and stray fields) to the drift velocity compensate, such that only the current term matters. The transition time in a pure domain wall reversal is then simply proportional to the voltage and to the diameter (linear dependence with zero intercept). This is valid without the strong Walker oscillations and at 0 K.

6.4.2 Median transition time versus diameter

The size dependence of the median transition time is shown in figure 6.20 for all the different applied voltages. It is found that changing the diameter of the device has little impact on the median transition time for all voltages. This is at first glance a surprising result. Indeed we know that domain walls are involved in the switching of all our devices. We also know from our calculations that overall the drift velocity of the domain walls is proportional to the applied voltage, and so regardless of the diameter of the device. Therefore we expect from our models the transition time to be proportional to the device diameter. This is clearly not the case here. As we have seen in the zoology of the switching, the transition time is a more complex data than

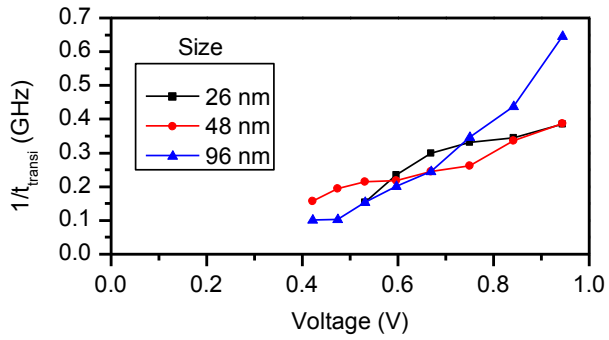

FIGURE 6.21: Inverse median transition time versus voltage for 3 different sizes. We are not showing the devices larger than 96 nm not to overload the figure, they behave qualitatively just like the 96 nm one.

a simple domain wall travel time because of the macrospin phase and because of the various events slowing down the reversal. We have also found that only for the larger devices at high voltages most of these events are suppressed, in the ballistic region. The larger is a device and the longer a domain wall must travel, but also the less likely it is to undergo an event slowing down the reversal: overall the *median* switching time ends up depending only little on diameter in this size range. This can be checked qualitatively by stacking together ballistic reversals under the same voltages for different sizes (not shown). Regarding the pinning it does not increase clearly the transition time at the lower voltages because we are looking at the median rather than the mean value. The same graph with a mean transition time instead of median would show greater values for the large diameters at low voltages.

In our micromagnetic simulations the transition time was in fact only slightly smaller for the 16 nm disk compared to the 40 nm one, as seen in figure 3.19. Only when going to 80 nm a clear increase of the transition time was predicted. This was due to the fact that for devices of 40 nm and smaller the domain wall motion was not occurring for sufficiently long compared to for larger devices. We studied only 3 sizes in our simulations and we cannot give a full transition time versus diameter graph, but it still indicates that the linear dependence of the transition time on voltage predicted in pure domain wall motion based switching is not expected in a more realistic model for the devices of 40 nm or less, even less in an actual measurement.

In others devices that are reported in reference [34] by our teams at C2N and IMEC, it was found that in ballistic reversals the transition time is indeed proportional to the voltage. These data concerned devices of 40 nm and larger for ballistic reversals. The weak dependence of the median transition time on diameter that we measured is related to the possible macrospin phase and to the numerous existing switching events, it does not necessarily hold true in other samples or in a larger size regime.

6.4.3 Median transition time versus voltage

In our micromagnetic simulations, it was found that the inverse of the transition time depends linearly on voltage. This was an interesting property because as seen in figure 3.19 it allows us to distinguish a switching based heavily on domain wall motion (80 nm case with the intercept close from zero) from the more macrospin-oriented reversals (intercept greater than zero). We try to plot the same graph from our measured transition time in figure 6.21. The devices of 114 and 142 nm are not pictured to make the figure easier to read, they present the same voltage dependence than the 96 nm device. First we can see that no device can be reasonably described by a linear dependence, apart maybe from the 48 nm one. In the case of the 96, 114 and 152 nm devices, the inverse median transition time increases with voltage faster

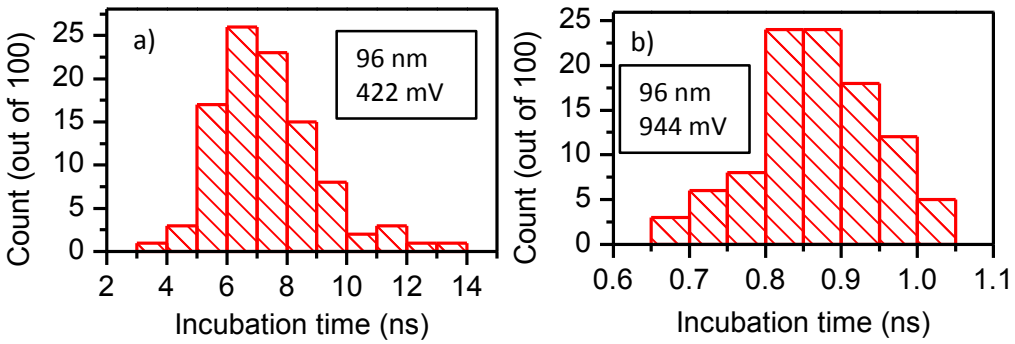

FIGURE 6.22: Typical incubation time distributions. The data are taken from the 96 nm device under a) 422 or b) 944 mV. The incubation time is obtained by the threshold method on 100 runs. The difference in time scale highlights that the distribution is much sharper at higher voltages.

than linearly. We cannot use the intercept to discuss the importance of domain walls in the reversal in these data.

Why is the linear dependence predicted in the micromagnetic simulations not observed in our measurements ? As we have seen each event slowing down the reversal has an impact that diminishes as we increase the voltage. Therefore increasing the voltage in our measured devices not only accelerates the macrospin and domain wall based dynamics, but also reduces the probability of having an event slowing down the reversal. This explains why the inverse transition time increases faster than linearly when we increase the voltage in a measured device. This picture helps us understand the voltage dependence for the devices of 96 nm and more. But for the 26 nm device the voltage dependence seems to be more complex. This can be related to the fact that the switching events occurring in this device are not well understood yet (oscillations and strong moving back were not expected in any of our models for this size).

The median transition time does not prove to be sufficient to describe the complex switching that we discussed in the zoology. This is due to the fact that many different physical effects end up affecting the median transition time in a similar manner (namely increasing it). This is not an issue in our forthcoming incubation time study where most of the physics is about thermal activation.

6.5 The measured incubation time

6.5.1 Overview of the incubation time

We now focus on the incubation time. Two characteristic incubation time distributions are shown in figure 6.22. The distribution is much sharper for the highest voltages and centered around a lower value. The shape of the distribution is slightly asymmetrical, similarly to what was described from our micromagnetic simulations. For all the voltages and diameter that we measured the distributions have the same shape as the one in the figure.

The median value of the incubation time versus diameter and voltage is represented in figure 6.23. The scale for the incubation time is logarithmic to better highlight the size and diameter influence. Contrary to the transition time map, there is this time a very clear diameter and voltage dependence of the incubation time. Increasing the voltage or the diameter reduces sharply the incubation time.

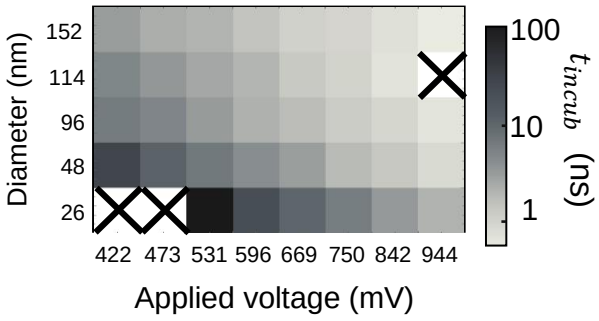

FIGURE 6.23: Median incubation time in the voltage-diameter space. The scale in diameter is not linear, the devices are sorted by size. The crossed out cells indicates that no data could be recorded. The color scale for the incubation time is logarithmic.

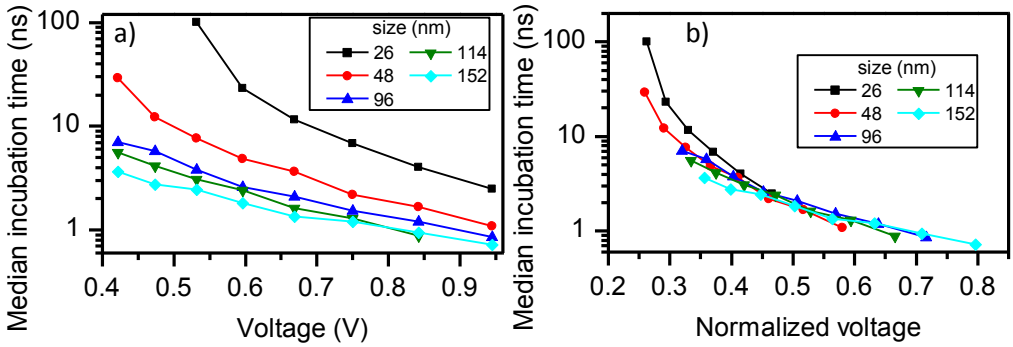

FIGURE 6.24: Voltage dependence of the median incubation time. a) Versus the applied voltage. b) Versus the voltage normalized to remove the demagnetizing effects following equation 6.7.

6.5.2 Incubation time size dependence versus macrospin model

The voltage dependence of the median incubation time is plotted for all the different diameters in figure 6.24.a in a log scale. We can notice that the voltage dependence is not the same for the larger devices compared to the 26 and 48 nm ones. Indeed in the two smaller devices under low voltages the incubation time is increased faster as the voltage is reduced, compared to the other devices.

Before discussing the voltage dependence, we try to normalize the voltage with the macrospin critical switching voltage, similarly to what we did in section 3.3.5 for our micromagnetic simulations. We cannot extract the macrospin critical switching voltage V_c directly from a measurement (we would need to cool down the devices as much as possible), therefore we normalize the voltage by the effective anisotropy of the disk. As a reminder the expression of V_c is 1.37:

$$V_c = \frac{2\alpha e \mathcal{A} R_\perp \mu_0 M_s d H_{k,\,\mathrm{eff}}^{\mathrm{disk}}}{P\hbar} \tag{6.6}$$

where $H_{k,\,\mathrm{eff}}^{\mathrm{disk}} = H_k - (N_z - N_x)M_s$ (from equation 1.11) is the effective anisotropy of the disk, which depends on size because of the demagnetizing factors. V_c depends on size only because of this demagnetizing term. We can therefore normalize the size dependence of the macrospin critical switching voltage by defining a new voltage V_{norm} as:

$$V_{\mathrm{norm}} = V_{\mathrm{app}} \frac{H_k - M_s}{H_k - (N_z - N_x)M_s} \tag{6.7}$$

The anisotropy field H_k is known from our FMR measurements, M_s from our VSM measurements and the demagnetizing factors of the disks taken from our free precession micromagnetic simulations (see figure 1.1) assuming that the electrical cd of

our devices is indeed the diameter of the disk. The size-normalized voltage dependence of the median incubation time is shown in figure 6.24.b. All the curves are now better stacked together. This shows that the size dependence of the incubation time is similar to the one predicted in the macrospin model by considering the demagnetizing factors of the disk. The incubation time gives us information on the initial stage of the switching, as it is about starting the reversal. Therefore this result is another hint of a macrospin initial stage of the switching in our devices at all sizes.

Two words of cautions are needed regarding this result. i) The match of figure 6.24.b is good for all our devices, save for the lower voltages points in the 26 nm device. The size dependence of the incubation time is not as well explained by the demagnetizing effects of the disk for the longer incubation delays than for the smaller ones. Reaching the long incubation time regime for the larger devices would have been interesting but we could not reduce further down the voltage with our initial set-up. ii) In the micromagnetic simulations we were surprised to observe that the incubation time increases indeed when the diameter is reduced, but not as much as predicted by the demagnetizing factors of the disk. The situation is a bit tricky since in the measurements the size dependence is well explained by a macrospin consideration of the demagnetizing effects, but in the simulations where we know that at 0 K the initial reversal is macrospin based the size dependence is not as strong as what is predicted by the same demagnetizing effects. One possible explanation would be that in the simulation it is a smaller volume that is initially excited due to thermal fluctuations (as we observed in subsection 3.3.3), while for some reason (larger exchange, missing ingredient in the simulations ...) it is the full volume being excited in the actual devices.

6.5.3 Incubation time size dependence versus subvolume model

A switching path different from the one we have presented so far is discussed in reference [96]: the subvolume excitation. The free layer is supposed to be composed of several subvolume of the same size, this subvolume size does not depend on the total diameter. It is then assumed that if one of the subvolumes switches, the full free layer is going to switch. Then the incubation time is not about starting a coherent precession in the full disk, but rather about starting a coherent precession in any of the subvolumes composing the free layer. This assumes that the subvolumes reversal starts with a coherent amplification, which is reasonable given their dimensions. In reference [96] the switching time of the free layer in the subvolume model is given by equation (13), written with our notations:

$$\frac{1}{t_{sw}} = \frac{P\gamma_0\hbar}{e\mu_0 M_s d A R_P} \frac{1}{\ln[(\frac{\pi}{2})^2 \frac{\Delta_{T,SV}}{N_a}] + \frac{5.0814}{N_a}} (V - V_{c,SV}) \tag{6.8}$$

where N_a is the number of subvolumes within the free layer, AR_P the RA product in the P state (does not depend on size), $\Delta_{T,SV}$ is the thermal stability of the subvolume and $V_{c,SV}$ the macrospin critical switching voltage of the subvolume. In this equation only the second term depends on the size of the free layer through N_a. This equation is valid if the applied voltage is larger than $V_{c,SV}$, which should be the case in most of our experimental data where the switching is faster than 10 ns.

Now let us assume that the size dependence of the incubation time in the subvolume model is the same as the size dependence of the switching time predicted by this equation. This assumption is reasonable since this holds true in the macrospin model. Then we can size-normalize our inverse incubation time versus voltage data

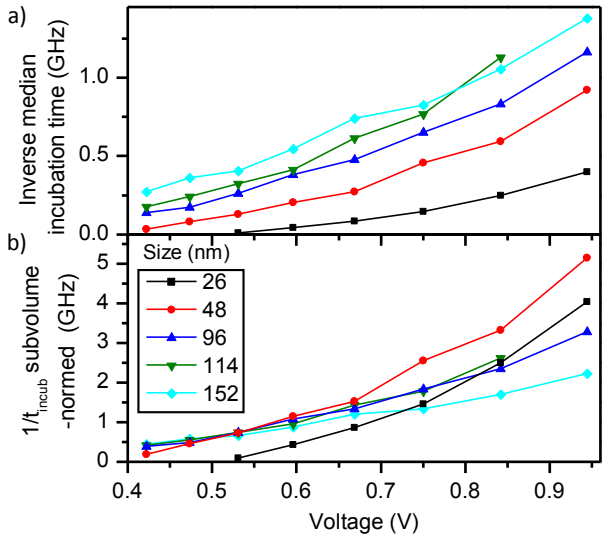

FIGURE 6.25: a) Inverse median incubation time versus voltage for all our devices. b) Same graph with the median incubation time normalized following the subvolume hypothesis of equation 6.8. According to this model the normalized inverse transition time should not depend on size.

by multiplying it by the size dependent second term of equation 6.8. The obtained subvolume-normalized inverse incubation time should not depend on size, namely all the graphs should be stacked.

We chose the following parameters: the subvolume is a disk of 26 nm diameter, in reference [96] the typical subvolume is 40 nm, but we suppose 26 nm in order to have a single subvolume for our smallest device. The thermal stability of the subvolume is 60, this is a reasonable value with our parameters for a disk of this dimension. The other quantities of equation 6.8 are not needed since we only focus on the size dependence.

The result of our normalization is shown in figure 6.25.b. The subvolume normalization stacked the devices together only for the lower voltage values and the 26 nm device does not fit with the other graphs. This result should be compared with our macrospin model normalization of figure 6.24. For the macrospin case also the 26 nm device was not stacked well with the other sizes, but in this case the high voltage data matched well. The amplification of a coherent precession in a subvolume hypothesis seems less likely than the fully coherent initial stage hypothesis.

6.5.4 Incubation time voltage dependence

We have already compared the size dependence of the incubation time in our time-resolved measurement with what was expected in the models (macrospin and micromagnetic simulations). We focus now on the voltage dependence of the incubation time.

Already from figure 6.24.a we can guess two regimes in the voltage dependence. The incubation time is increased much sharply when reaching low diameter and voltages compared to the high voltage or high diameter data. These two regimes do not correspond to the two regimes measured in write error rate measurement and that were attributed to going from an incubation time-dominated reversal to a transition-time dominated reversal, here we isolated the incubation contribution. We believe that if we could reach lower voltages, the two regimes would be also observed for the larger devices as it is for the 26 nm one (see figure 6.26).

As we have discussed in our state of the art, the incubation time is expected to depend on voltage as $\exp((1-h)^k)$ with k being 1 or 2. This approximate expression comes from a Fokker-Planck equation but is only valid when the reversal is a rare

	26 nm	48 nm	96 nm	114 nm	152 nm
Log	0.885	0.930	0.971	0.990	0.977
Inverse	0.947	0.942	0.970	0.953	0.977

TABLE 6.1: Adjusted R-squares obtained from fitting linearly the log of the median incubation time versus voltage, or the inverse median incubation time versus voltage.

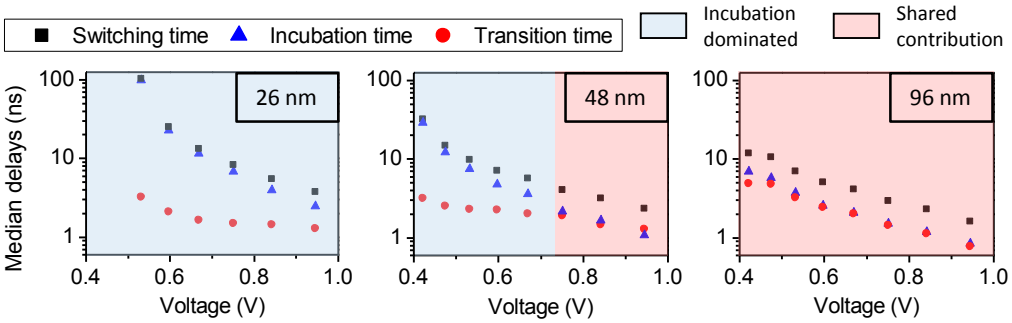

FIGURE 6.26: The contributions of each delays to the total switching time. The *transition time* that is represented is in fact half of the median of the transition time, the *incubation time* is the median of the incubation time and the *switching time* the sum of both. The colors highlight the regions where the incubation times dominates the switching dynamics and the regions where both delays contribute significantly. A single scale is used for the 26, 48 and 96 nm devices. The larger devices give graphs similar to the 96 nm one.

event, namely when the incubation time is long enough. We believe that this model is not relevant in most of our time-resolved data since we reach incubation times of less than a ns. As a result the only model we can compare our voltage dependence of the incubation time with is once again our micromagnetic simulations (or a numerically solved Fokker-Planck equation).

In our simulations we reported a linear dependence of the inverse median incubation time (figure 3.21), with an intercept much larger than 0 V. We present the same graph for our time resolved measurement in figure 6.25.a. These graphs cannot be satisfyingly fitted to a linear function. To be more quantitative we can compare the adjusted R-square that are obtained when fitting the inverse median incubation time versus voltage or the logarithm of the median incubation time versus voltage in table 6.1. The voltage dependence of the incubation time is better fitted by the inverse function for the two smaller devices and slightly better fitted by the log function in the larger devices. In our micromagnetic simulations the inverse fit was observed but not explained by any analytical models. While a linear dependence of the logarithm of the incubation time was indeed predicted, but not at all for this fast regime. We cannot conclude on the shape of the voltage dependence of the incubation time of our measurement. A study more focused on this aspect would be necessary to observe better the regime transition by going for much longer incubation times. We believe that under lower voltages the voltage dependence of the incubation time in the larger devices would be similar to the one observed at 26 and 48 nm.

6.6 Contribution of each delay and optimizing performances

In the final section of this chapter, we discuss the impact of our findings on the scaling down of STTMRAM devices. Let us define the switching time as the time needed for the device to be 50 % reversed. It is the relevant delay in term of memory applications, as if we stop the pulse anytime after switching time the device ends up reversed. This holds true for the ballistic type reversal (the most common) but not necessarily for more complex reversals such as the Walker oscillations in the center. Rigorously we should apply our extraction method again to obtain the switching time and a new transition time which correspond to 10 % to 50 % of the switching. In practice we make only a minute error by taking the half median transition time and the switching time median being the sum of the incubation time and half transition time medians. From this we can discuss which delay (incubation or transition) contributes the most to the full switching time of the reversal depending on diameter of voltage. This is shown in figure 6.26.

In the 26 nm device the switching time is essentially given by the incubation time for all the voltages measured. In the 48 nm device we are first in the incubation dominated region, but for voltages higher than about 700 mV both delays have a non-negligible contribution. For the 96 nm we are in the shared contribution region for all the voltage range, the transition time and the incubation time decreasing approximately at the same rate. In term of application we want to have the smallest device possible switching at the fastest speed possible. Here we can see that at the same voltage the smaller device is actually the slower to reverse. This is due to the fact that the incubation time is much larger in the 26 nm device than in the larger devices at fixed voltage. We have shown that this size dependence of the incubation time can be understood as an effect of the demagnetizing field which is varying with size. To a fixed voltage corresponds a smaller normalized voltage for the small device than for the large one. As we scale down the device the demagnetizing field is reduced and the device gets harder and slower to switch because of the incubation. This understanding assumes a macrospin initial stage.

This finding is important since it shows what should be improved to obtain faster switching on the smaller devices. A strategy could be to reduce the demagnetizing effect, but it depends only on the geometry, the anisotropy and the magnetization of the free layer. These material parameters already have many constraints in STTMRAM optimization. But as we can see the incubation time is decreasing sharply with voltage in the 26 nm device before we reach the breakdown region (about 1 V in our set-up). We could not go for higher voltages because in our set-up the pulse width is fixed of 300 ns and we must apply this pulse a few 1000 times for each data point to obtain our references. For this reason we apply a large stress on the device in our time-resolved measurements which is not necessary in the normal operating conditions of an STTMRAM device. If we only send pulses of 10 ns or smaller when writing down the device for instance, it is reasonable to go above 1 V. This is going to reduce greatly the incubation time and improve efficiently the switching time performances of the device.

6.7 Conclusions on time-resolved measurement

In this chapter we have presented the methods and the findings of our time-resolved measurements. These measurements gave us plenty of information on the switching path: i) signals characteristic of domain walls are indeed observed for all diameters.

For the smallest devices these effects are stronger than predicted by the models. For the largest devices, signatures of domain-wall dynamics were expected. But we cannot conclude on the existence of Walker oscillations from our data alone (see the perspectives of this manuscript for more convincing data from other samples). ii) Several signatures of a macrospin initial stage are reported. The failed trials correspond to the prediction from the micromagnetic simulations both in term of diameter and voltage range to observe them, and in term of how large they can be. Some changes of the switching rate that could be the signature of nucleations of domain walls are observed for larger devices. The size dependence of the incubation time corresponds to the one predicted by the macrospin model which is a last indication of a coherent first stage for the switching. We think that the switching path that we described during our micromagnetic simulations is relevant in actual devices.

We tried to understand quantitatively the size and voltage dependence of two characteristic delays: the incubation time and the transition time. Their size and voltage dependences were compared to our various models, with little success save for the size dependence of the incubation time. We think that this decomposition of the switching time into two delays shows clear limitations as to understand the physics of STTMRAM switching.

Finally we discussed the impact of our findings in term of memory applications. This highlight the great interest of performing time-resolved measurement of the switching, as understanding the origin of the switching time is impossible with a simple write error rate measurement. In the models of the switching time described in our state of the art the incubation time was supposed to be negligible as the switching time was given from a transition time. We have proven here that this approximation is not reasonable for all our voltages and diameters, especially for the smaller devices.

Chapter 7

Conclusions and perspectives

7.1 Conclusions

The aim of this manuscript was to understand the switching path in recent STTM-RAM devices. We have shown in the state of the art that before the beginning of this PhD it was already known that the switching included the nucleation and the motion of domain walls. It was also predicted that below a certain diameter the reversal was macrospin-like.

We computed numerically the switching of the free layer, considered as a thin disk perpendicularly magnetized. From these micromagnetic simulations we found indeed that there was a critical diameter for macrospin versus domain wall based reversal. However in our simulations the domain wall is nucleated only after a coherent phase. This switching path including both a macrospin phase and a domain wall motion is the one expected for devices between 100 and 20 nm under 300 K and a reasonable voltage, namely in standard STTMRAM devices. The micromagnetic simulations also allowed the study of the incubation time due to the thermal fluctuations. Finally they highlighted the existence of complex domain wall dynamics, which could not be understood fully from the domain wall models shown in our state of the art.

This led us to add an extra layer to the existing (q, ϕ) models for the domain wall motion. We simply derived the equations while taking into account the exact disk geometry and while including carefully the demagnetizing effects. The new terms arising from the geometry take the form of a new effective field along z, the stretch field. It is the result of the variation of the domain wall length which has an effect on the total elastic energy of the domain wall. This stretch field is position dependent. Consequently this field explains the complex domain wall dynamics observed in the simulations: there are Walker oscillations of varying amplitude and frequencies. These oscillations are predicted to be of great amplitude and low frequency where the total effective field seen by the domain wall is zero. Our model could also predict how to observe efficiently the strong Walker oscillations: the device should be of 60 nm and more, under a voltage as small as possible and the stray field coming from the rest of the stack onto the free layer should be carefully compensated. For the smaller devices we predicted a somehow ballistic reversal and we expect domain wall effects to be much harder to identify.

We dedicated a chapter to present our devices as well as their characterization in static measurements (VSM cycles, resistance-voltage loops) and in ferromagnetic resonance measurements. The devices are not optimized specifically for our study, they are state of the art PMA-STTMRAM that are designed for industrial applications. We then performed time-resolved electrical measurements of the switching. We did so while varying two key parameters for the switching path: the diameter

and the applied voltage. The measured switching path appeared to be more complex than the one predicted by our 2D free layer-only models. There is a combination of perfect free layer effects (such as domain wall nucleation and oscillations) and effects coming from the imperfections of the free layer or the rest of the system (pinning, magnetic noise). We found signatures of a macrospin initial stage: failed trials, potential late nucleations, size dependence of the incubation time following the macrospin model. As well as signatures of a domain wall being involved for all diameters: signal going strongly backwards or oscillating, pinning, linear behaviour. Because of these findings we believe that the switching path described in our micromagnetic simulations is indeed relevant: a coherent precession is amplified slowly by STT, once a certain critical angle is reached the nucleation occurs, the domain wall then sweeps across the device in a complex manner if the diameter is sufficiently large. Regarding the existence of the strong Walker oscillations, in a specific voltage and diameter condition similar oscillations were measured, but others effects such as pinning occur at the same time and prevent us from concluding clearly on their existence. Another explanation for the absence of clear Walker oscillations in our samples could be the stray field coming from the other layers onto the free layer. As we have discussed in our domain wall model chapters, it is expected to go up to 20 mT in-plane which is very detrimental for the strong Walker oscillations.

All along this PhD we also discussed the impact of our findings on the development of STTMRAM devices.

7.2 Perspectives

We have encountered in this manuscript some limitations of the incubation time/transition time dichotomy of the reversal. The incubation time for the larger devices necessarily includes the beginning of the amplification of the precession. The transition time fails to describe the complexity of the switching path, especially while looking only at its median value. I believe a study fully focussed on the incubation would be interesting, with a measurement covering both the very slow regime (ms scale) and the ultrafast regime.

While I was writing this manuscript the progress on the sample performance continued, and we received a new generation of devices. Thibaut Devolder and Olivier Bultynck, an IMEC PhD student, performed time-resolved measurements with the same set-up that I used but for these new devices. The new stack include a low moment, high volume novel free layer, resulting in weaker transport properties but in a better compensated stray field from the rest of the system. Moreover in the novel free layer, no pinning is found because there is not the detrimental Ta layer. As a result these samples are prime candidates for the strong Walker oscillations predicted by our models. They could indeed be observed as shown in figure 7.1. The three types of reversal predicted by our micromagnetic simulations and understood by our domain wall analytical models are found with similar likelihood. In this sample, unlike in our POR19 presented in this manuscript, the complex domain wall dynamics is the main effect impacting the reversal.

For the new generation devices in which the strong Walker oscillations are observed, the write error rate is directly related to the complex domain wall dynamics. Indeed when the domain wall is stuck around the center of the disk with a possible Bloch line included (figure 7.1.g), the reversal is greatly slowed down. Then if the pulse is not sufficiently long, this scenario corresponds to a write error rate. For this

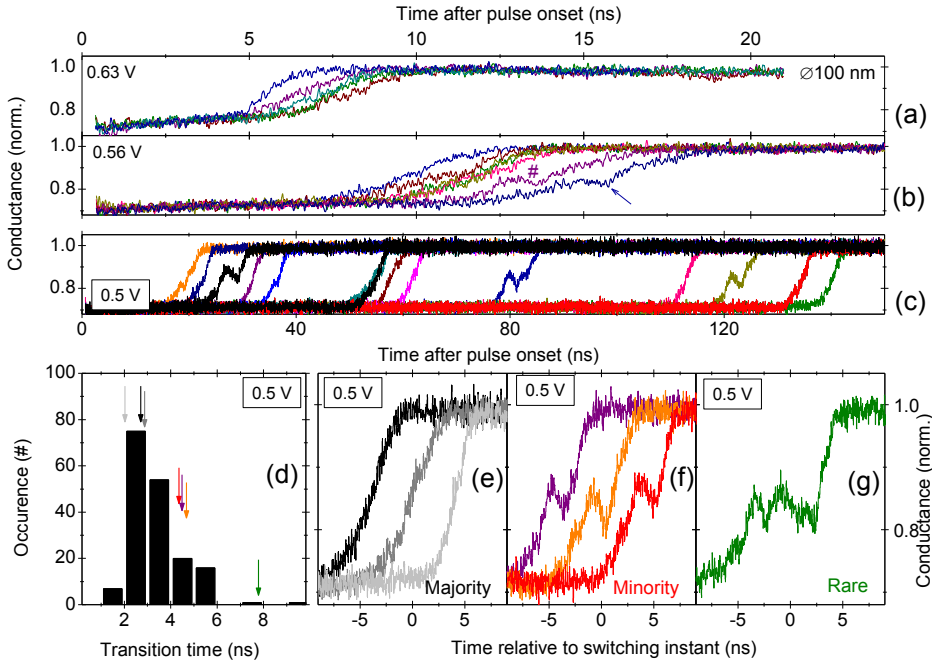

FIGURE 7.1: From our latest paper on domain wall dynamics. Time resolved measurement of the switching in a 100 nm high volume, low moment free layer sample. Several time traces are shown for a voltage of a) 630 mV, b) 560 mV or c) 500 mV. An histogram of the transition time d) is shown as well as three characteristic trials e-g) for the 500 mV voltage. The arrows in the histogram indicated the position of the different events within the transition time distribution.

reason it would be interesting to extend our domain wall model in order to give simple analytical expression for the likelihood of entering a Bloch line-type reversal. So far our model can predict the likelihood of entering strong oscillations (figure 4.14), but could only explain qualitatively the Bloch lines because of the 1D assumption.

We believe that some concepts that we developed, such as the stretch field or the retention pond, can be useful in different systems. It is straightforward to discuss the effect of DMI, or spin orbit torque for instance in our domain wall models. The stretch field which is rising from the elastic energy of the domain wall can be used as long as the domain wall length vary while it propagates, under the 1D assumption. It could be included in the modelling of spin-logic systems based on domain walls for instance. We have already discussed with the team from IMEC working on such devices about the implications of our findings.

Our work was focused on devices optimized for industrial applications. As a result an obvious perspective would be to improve the understanding of the switching in the smaller devices, which are preferred. Some effects measured in our time-resolved measurement are not well understood yet (the oscillations for the 26 nm device). Other geometries are also studied for STTMRAM free layers, such as the perpendicular shape anistropy-STTMRAM with an elongated free layer [111, 82]. The switching path in such systems could also be unravelled with methods similar to the one used in this manuscript.

Appendix A

Résumé en français

A.1 Introduction

Mes travaux de thèse se situent dans le contexte des mémoires magnétiques nouvelle génération, plus exactement les mémoires magnétiques à transfert de spin (STTMRAM). Pour obtenir un bit mémoire il doit être possible de stocker l'information, de la lire et enfin de l'écrire. Un dispositif STTMRAM est présenté dans la figure A.1 : l'information est stockée dans une couche mince ferromagnétique appelée la couche libre. La lecture de l'information se fait en tirant parti de la magnétorésistance à effet tunnel : la résistance du dispositif dépend de l'orientation relative des aimantations des deux couches magnétiques séparées par un isolant. Ainsi en fixant l'aimantation d'une des couches (appelée alors couche de référence), la direction de la couche libre est connue par une simple mesure de la résistance au travers du dispositif. Par exemple l'état aimantation parallèle (basse résistance) peut correspondre au 0 de notre bit, et l'état antiparallèle (forte résistance) au 1. Enfin pour écrire l'information, c'est-à-dire changer la direction de l'aimantation de la couche libre, les dispositifs STTMRAM tirent parti d'un autre effet appelé le transfert de spin [93] (STT). Le STT correspond au couple que peut exercer sur l'aimantation d'une couche un courant polarisé en spin traversant cette dernière. Dans nos dispositifs un courant électrique traverse l'empilement de couches. Ce courant se polarise en spin par STT dans la couche de référence, et c'est donc un courant polarisé qui est appliqué sur la couche libre, permettant de retourner son aimantation et écrivant ainsi l'information souhaitée selon le sens du courant.

Les dispositifs STTMRAM sont en réalité composés de nombreuses couches (figure A.6), ce complexe empilement est gravé sous la forme de pilier de quelques dizaines de nanomètres de diamètre. La couche libre est donc un disque de typiquement 2 nm d'épaisseur et de 20 à 200 nm de diamètre. Lorsque l'aimantation se retourne par STT, elle ne reste pas nécessairement homogène : plusieurs scénarios de retournement, appelés chemins de retournement, peuvent être imaginés. Des exemples de chemin de retournement sont présentés dans la figure A.2. La connaissance du chemin de retournement est importante, car de ce chemin dépendent

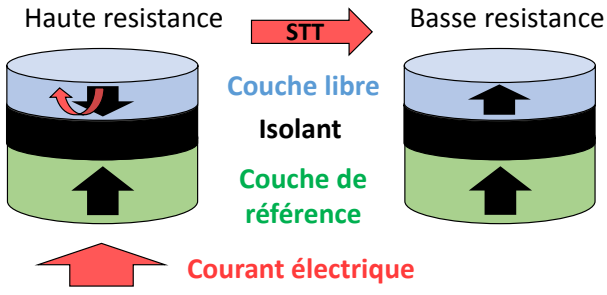

FIGURE A.1: Le principe des STTMRAM. Le dispositif représenté correspond à une géométrie hors-du-plan. L'information est lue par l'effet TMR et écrite par le STT.

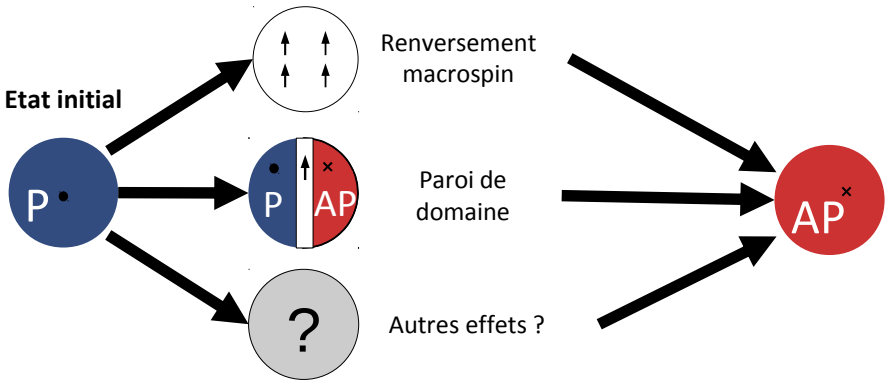

FIGURE A.2: Le chemin de retournement dans STTMRAM. Deux chemin possibles sont représentés, le renversement macrospin et le renversement basé sur une paroi de domaine.

les modèles utilisés pour prédire les performances des dispositifs STTMRAM. Une bonne connaissance de la dynamique de l'aimantation dans la couche libre aide au développement de mémoires plus rapides, plus petites, plus fiables. La question à laquelle j'ai essayé de répondre au cours de ma thèse est donc la suivante : quel est le chemin de retournement dans les mémoires magnétiques à transfert de spin ?

Pour répondre à cette question, je présente d'abord les concepts de base nécessaires à l'étude de la dynamique de l'aimantation dans la couche libre. Suit une présentation des connaissances de la communauté scientifique sur le chemin de retournement dans les STTMRAM avant le début de ma thèse. Les premiers résultats que je présente sont des simulations micromagnétiques du retournement. Puis un modèle analytique portant sur le déplacement des parois de domaines dans la couche libre. Alors s'ouvre la partie expérimentale de ce manuscrit : nos dispositifs sont d'abord présentés, puis des mesures électriques résolues en temps effectuées sur ces derniers.

A.2 Concepts de base

Énumérons les différentes énergies en jeu dans la couche libre :

- L'énergie de Zeeman. Elle correspond à la tendance qu'a l'aimantation de s'aligner le long d'un champ extérieur.
- L'énergie d'échange de Heisenberg. Dans un matériau ferromagnétique les spins adjacents ont tendance à rester parallèles sous cet effet, qui favorise donc une aimantation uniforme.
- L'énergie d'anisotropie. Cette énergie qui provient dans notre cas principalement de l'interface entre la couche libre et l'isolant favorise une aimantation hors du plan dans nos échantillons. Il s'agit d'une énergie clé car c'est elle qui donne la robustesse de l'aimantation de la couche libre, c'est-à-dire à quel point elle est facile ou dure à retourner.
- L'énergie démagnétisante. Cette énergie correspond au champ créé par l'aimantation de la couche libre, et qui agit sur elle-même. Ce terme est complexe à calculer et va jouer un rôle important dans notre système. Dans l'hypothèse d'un champ démagnétisant uniforme dû à une aimantation uniformément hors du plan,

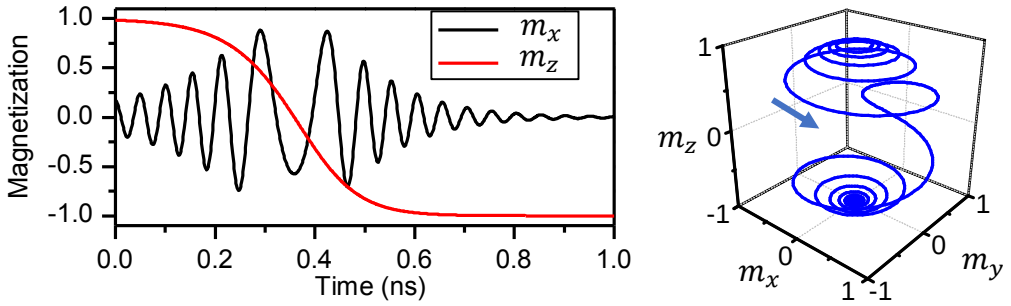

FIGURE A.3: La trajectoire macrospin. Le retournement tel que prédit par l'équation A.1 est présenté : a) une composante planaire et la composante hors-du-plan du l'aimantation b) la trajectoire en 3D. Les paramètres sont ceux de la table 1.1. La tension est 6 V et l'angle initial 10 degrés.

nous avons résolu exactement cette énergie de manière numérique à l'aide de simulation micromagnétiques. Ce champ démagnétisant dépend du diamètre de la couche libre.

Une fois les énergies connues, il faut discuter l'équation de base utilisée pour étudier la dynamique de l'aimantation sous l'effet d'un transfert de spin : l'équation de Landau-Lifshitz-Gilbert-Slonczewski (LLGS).

$$\frac{\mathrm{d}\overrightarrow{m}}{\mathrm{d}t} = -\gamma_0 \overrightarrow{m} \times \overrightarrow{H_{\mathrm{eff}}} + \alpha \overrightarrow{m} \times \frac{\mathrm{d}\overrightarrow{m}}{\mathrm{d}t} + \gamma_0 P \frac{V}{\mathcal{A} R_\perp} \frac{\hbar}{2e\mu_0 M_s d} \overrightarrow{m} \times (\overrightarrow{m} \times \overrightarrow{p}) \qquad \text{(A.1)}$$

Dans l'hypothèse dite macrospin d'un retournement homogène, cette équation décrit le retournemnt de la couche libre. Elle prédit que l'aimantation $\overrightarrow{m}$ précesse autour du champ effectif $\overrightarrow{H_{\mathrm{eff}}}$ dans lequel sont incluses toutes les énergies discutées plus haut (premier terme). Cette précession est accompagnée d'une relaxation visqueuse vers le champ effectif caractérisé par l'amortissement α (deuxième terme). Le dernier terme de l'équation correspond au STT qui a le même effet sur l'aimantation qu'un anti-amortissement : sous son action (s'il est suffisamment fort) l'aimantation quitte son état initial et se retourne tout en précessant. Les quantités de ce terme tiennent compte du transport dans le dispositif : V est la tension appliquée, $\mathcal{A}$ l'aire de la couche libre, $R_\perp$ sa résistance dans un état perpendiculaire, M_s son aimantation et d son épaisseur.

De cette équation on peut donc décrire un premier chemin de retournement : le retournement macrospin. La trajectoire que suit l'aimantation au cours d'un retournement macrospin est décrite dans la figure A.3.

A.3 État de l'art sur le chemin de retournement

Dans la littérature deux chemins de retournement sont principalement discutés : le retournement macrospin et le retournement basé sur le déplacement de parois de domaines. Une dépendance en taille du chemin de retournement est prédite : aux petites tailles le cas macrospin et aux plus grandes tailles le cas paroi de domaine. Le diamètre critique pour passer d'un chemin à l'autre peut être estimé par des considérations énergétiques [17].

Le modèle macrospin a été comparé à des mesures de diagramme de stabilité, c'est-à-dire des mesures des états que peut occuper un dispositif à une tension et un

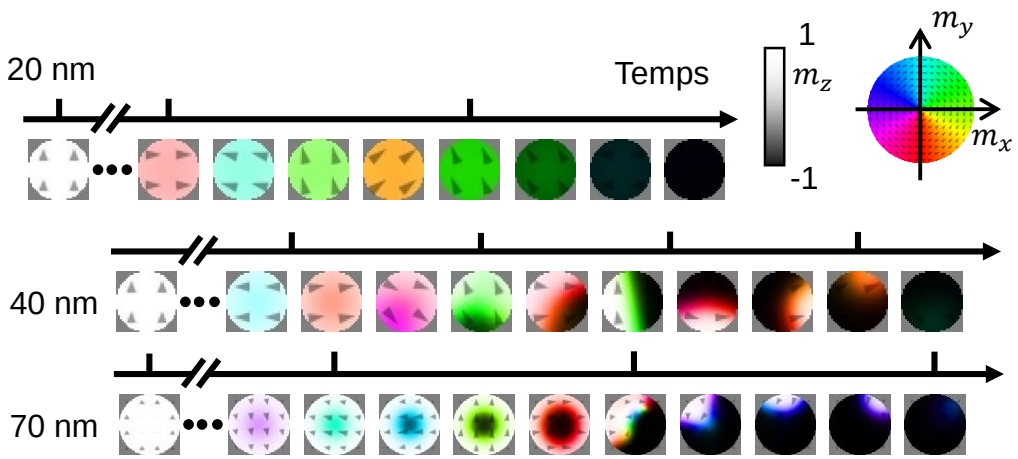

FIGURE A.4: Évolution temporelle de l'aimantation dans un disque aimanté perpendiculairement de 20, 40 ou 80 nm de diamètre. L'état initial est homogène, avec un angle de tilt arbitraire pour démarrer le retournement. La tension appliquée aux échantillons, normalisée par rapport à la taille, est de 1.21 fois leur tension critique.

champ donné. La comparaison ne peut être que qualitative et le modèle macrospin échoue à prédire exactement les limites de tels diagrammes [105, 95]. De même ce modèle a été comparé à des mesures de probabilité de retournement en fonction de la tension et de la durée de pulse, cette fois encore avec un succès uniquement qualitatif [2, 106]. Malgré ses limites le modèle macrospin est également utile pour inclure les fluctuations thermiques dans le système sous la forme d'un champ stochastique. L'équation de LLGS A.1 devient alors une équation de Fokker-Planck qui peut être résolue numériquement [13].

Un chemin de retournement basé sur le déplacement d'une paroi de domaine a aussi été étudié dans la littérature. En effet des parois de domaines ont été observées dans des mesures par dichroïsme circulaire magnétique de rayon X (XMCD) [6]. De même dans des mesures électriques résolues en temps du retournement certains effets n'ont pu être expliqué que par l'implication d'une paroi de domaine [44, 30]. Il est donc important de comprendre le déplacement des parois de domaine pour prédire le chemin de retournement. Les prédictions du modèle unidimensionnel de déplacement de parois ont été confronté aux observations expérimentales [22, 30]. Ceci mit en lumière la nécessité de modèles de parois plus complets pour comprendre leurs dynamiques au sein de la couche libre.

A.4 Simulations micromagnétiques du retournement

Nous avons effectué des simulations micromagnétiques du retournement de la couche libre en faisant varier le diamètre du système. La couche libre est découpée en une grille où chaque cellule présente une aimantation homogène, puis l'équation de LLGS est résolue dans toutes les cellules. Le chemin de retournement prédit par ce modèle est le suivant à 0 K : pour les dispositifs de 20 nm de diamètre ou moins le retournement est macrospin ; pour ceux entre 20 et 70 nm il y a d'abord une phase macrospin suivie par la nucléation d'une paroi de domaine et sa propagation ; au-delà de 70 nm après la phase macrospin un domaine se forme au centre du disque (appelé bulle), qui grossis et se transforme en paroi de domaine dès qu'elle entre en contact avec un bord. Ces chemins de retournement sont illustrés dans la figure A.4.

Nous avons inclus la température aux simulations micromagnétiques. Sous l'effet des fluctuations thermiques il y a un temps d'incubation stochastique avant que le retournement ne commence vraiment. La température impacte également le chemin de retournement : la taille critique pour un retournement macrospin est réduite; le retournement basé sur une phase macrospin suivie d'un déplacement de paroi est inchangé; pour les disques de moins de 100 nm de diamètre la bulle n'est pas stable à cause de la température et on retrouve une paroi de domaine après la phase macrospin. Ces simulations prédisent donc un chemin de retournement unique pour des dispositifs entre 20 et 100 nm a 300 K : amplification d'une precéssion cohérente, suivie de nucléation et propagation d'une paroi de domaine une fois un certain angle critique atteint. Les simulations ont aussi mis en lumière que le déplacement de parois de domaines peut être complexe pour les grandes tailles (typiquement audessus de 60 nm). Dans certains de nos chemins de retournement la paroi suit des oscillations de forte amplitude et faible fréquence autour du centre du disque. Nous allons donc améliorer les modèles existant de dynamique de paroi pour expliquer ces effets.

A.5 Dynamiques d'une paroi de domaine dans un disque

Notre modèle de déplacement de paroi se base sur ceux déjà existant : la paroi est décrite par seulement deux paramètres, sa position q et l'angle que fait la projection planaire de l'aimantation avec l'axe de la paroi ϕ (appellé angle de tilt). Elle est supposée rigide, droite, avec un angle de tilt constant selon sa longueur. Pour obtenir les équations qui décrivent la dynamique de la paroi, c'est-à-dire qui donnent l'évolution temporelle de q et ϕ, il faut intégrer les énergies discutées précédemment sur tout le volume puis résoudre l'équation de Lagrange sur q et ϕ. Les modèles existant précédemment considéraient la couche libre comme une bande infinie de largeur constante. Dans notre modèle nous avons simplement intégré les équations selon la géométrie circulaire de la couche libre. Nous avons également scindé les effets démagnétisant en plusieurs champs effectifs. Ainsi sont obtenus les équations décrivant la dynamique d'une paroi de domaine dans un disque :

$$-\dot{\phi} + \alpha \frac{\dot{q}}{\Delta} = -\gamma_0 \left[H_{\text{tot}}(q, \phi) \right] \tag{A.2}$$

$$\frac{\dot{q}}{\Delta} + \alpha \dot{\phi} = \gamma_0 \frac{H_{N \leftrightarrow B}}{2} \sin 2\phi + \sigma j \tag{A.3}$$

où $H_{N \leftrightarrow B}$ est la composante planaire du champ démagnétisant. σj est le terme de STT. $H_{\text{tot}}(q, \phi)$ est le champ magnétique hors-du-plan total vu par la paroi. Il comprend notamment le champ extérieur appliqué, une composante démagnétisante provenant des deux domaines, et surtout un nouveau champ appelé champ d'étirement. Le champ d'étirement provient de l'intégration le long du disque des énergies d'anisotropie et d'échange, son expression est la suivante :

$$H_{\text{stretch}}(q) \approx \frac{2\sqrt{A_{\text{ex}} K_{\text{eff}}}}{\mu_0 M_s} \frac{1}{S_{\text{DW}}(q)} \frac{\partial S_{\text{DW}}(q)}{\partial q} \tag{A.4}$$

Ou A_{ex} est la raideur d'échange, K_{eff} la constant d'anisotropie effective. $S_{\text{DW}}(q)$ est une surface effective de la paroi de domaine, elle dépend donc de sa position le long du disque. Le champ d'étirement traduit le fait que l'énergie d'élasticité de la paroi tend à rendre cette dernière aussi courte que possible. Quand la paroi se

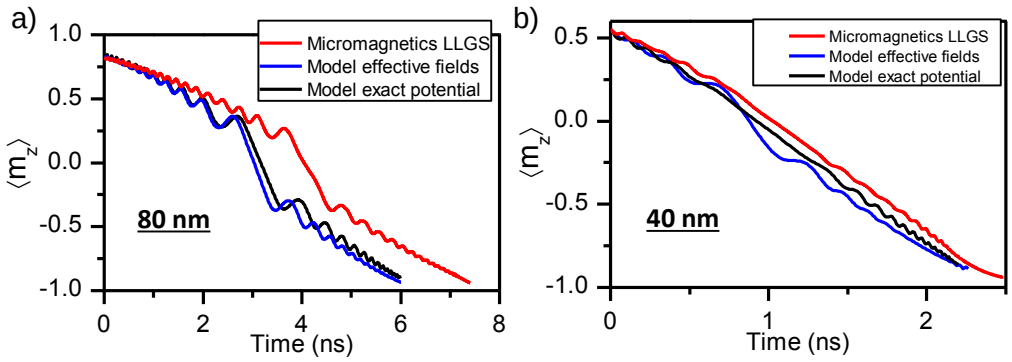

FIGURE A.5: Comparaison entre les simulations micromagnétiques et le modèle 1D de déplacement de paroi. Pour des disques de a) 80 ou b) 40 nm de diamètre. Les courbes du modèle sont obtenues par deux méthodes différentes : potentiel résolu analytiquement (comme c'est le cas dans les équations présentées ici) ou potentiel résolu numériquement. On peut remarquer dans le cas 80 nm le bon accord qualitatif entre le modèle, quel que soit la méthode, et les simulations.

déplace le long du disque sa longueur augmente puis diminue et ainsi son élasticité va d'abord s'opposer au retournement puis l'accélérer. Cet effet prend la forme d'un champ hors-du-plan lors de l'intégration des équations que l'on appelle le champ d'étirement. C'est un effet fort qui va jouer un rôle important dans la dynamique et expliquer les fortes oscillations observées dans nos simulations micromagnétiques.

Les équations A.2 et A.3 sont couplées. Si le champ total vu par la paroi est suffisamment grand (ce qui est le cas la majorité du temps dans notre système), q et ϕ suivent des oscillations couplées. La fréquence des oscillations est proportionnelle à H_{tot} et leur amplitude y est inversement proportionnelle. Additionnellement à ces oscillations, la paroi se déplace à une vitesse de dérive constante qui augmente linéairement avec la tension appliquée et avec αH_{tot}.

Les fortes oscillations sont donc des oscillations de Walker dont la fréquence tend vers zero et l'amplitude diverge lorsque la paroi d'approche du center de l'échantillon, car à cet endroit le champ d'étirement s'annule et change de signe. Nous comparons cet effet tel que prédit par le modèle à celui observé dans les simulations dans la figure A.5. On peut constater que le modèle analytique prédit bien les oscillations simulées.

Depuis notre modèle analytique nous pouvons également prédire la probabilité d'entrer dans de telles oscillations de Walker, et aussi sous quelles conditions les observer dans une mesure. Pour de fortes oscillations il faut un dispositif de 60 à 100 nm, sans aucun champ extérieur agissant sur la couche libre, avec une tension et donc un STT aussi faible que possible. Nous essaierons dans nos mesures résolues en temps de réunir ces conditions afin d'observer les oscillations de Walker.

A.6 Nos dispositifs et leurs caractérisations

Nos dispositifs de STTMRAM sont basés sur l'empilement décrit dans la figure A.6. La couche libre est entourée par deux couches de MgO pour augmenter l'anisotropie hors-du-plan. Le système de référence est composé de deux empilements couplés antiférromagnétiquement, la couche de référence (RL) et la couche dure (HL). Celles-ci forment un antiferromagnétique synthétique : le champ de fuite total créé par le

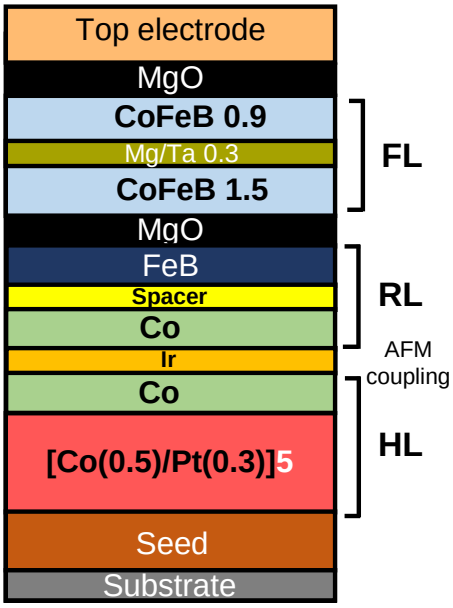

FIGURE A.6: Composition de l'empilement utilisé durant la majorité de ma thèse. La couche libre (FL), la couche de référence (RL) et la couche dure (HL) sont représentées. La RL et la HL forment ensemble l'antiferroaimant synthétique par leur couplage antiferromagnétique. Certains détails ne sont pas divulgués ici pour des raisons de confidentialité.

système de référence sur la couche libre est faible. La FL, la RL et la HL sont divisées en plusieurs sous-couches, dont les détails sont décrits dans le manuscrit en anglais.

Nos dispositifs ont d'abord été caractérisés pour obtenir les paramètres matériaux utilisés dans nos différent modèles. Nous avons effectué des cycles par magnétomètre à échantillon vibrant. Cette méthode permet d'obtenir l'aimantation M_s de la couche libre. Des cycles sont ensuite effectués en faisant varier le champ extérieur hors-du-plan ou la tension appliquée. De ces mesures on obtient les propriétés de transport du dispositif, ainsi que son diamètre électrique connu à partir de sa résistance et du produit résistance-surface de l'empilement complet. On supposera que ce diamètre électrique est le diamètre réel de la couche libre pour nos mesures suivantes.

Enfin la dernière mesure de caractérisation effectuée est une mesure de résonance ferromagnétique. Les fréquences des modes de la couche libre sont mesurées sur nos échantillons après gravure à l'aide de la méthode de résonance ferromagnétique par la tension [31]. De telles mesures nous pouvons obtenir l'anisotropie totale de la couche libre K_{eff}, ainsi que sa constante d'amortissement α.

A.7 Mesures électriques résolues en temps

Nous avons effectué des mesures électriques résolues en temps du retournement de la couche libre dans nos échantillons à l'aide d'un oscilloscope et d'amplificateurs. Ces mesures donnent des informations sur le chemin de retournement de la couche libre. Nous avons fait varier la tension appliquée (0.4 à 1 V) et le diamètre des dispositifs (26 à 152 nm). Pour chaque tension et diamètre, une centaine de retournements sont étudiés sous la forme de l'évolution temporelle de la conductance, normalisée par des références dans les états parallèle et antiparallèle. Des exemples de courbes sont présentés dans la figure A.7.

Tout d'abord même à une tension constante pour un même dispositif, les retournements n'ont pas lieu de la même manière. Il y a un temps d'incubation stochastique avant le début du retournement, et le retournement en lui-même peut présenter ou non certains évènements. Ces évènements sont les suivants :

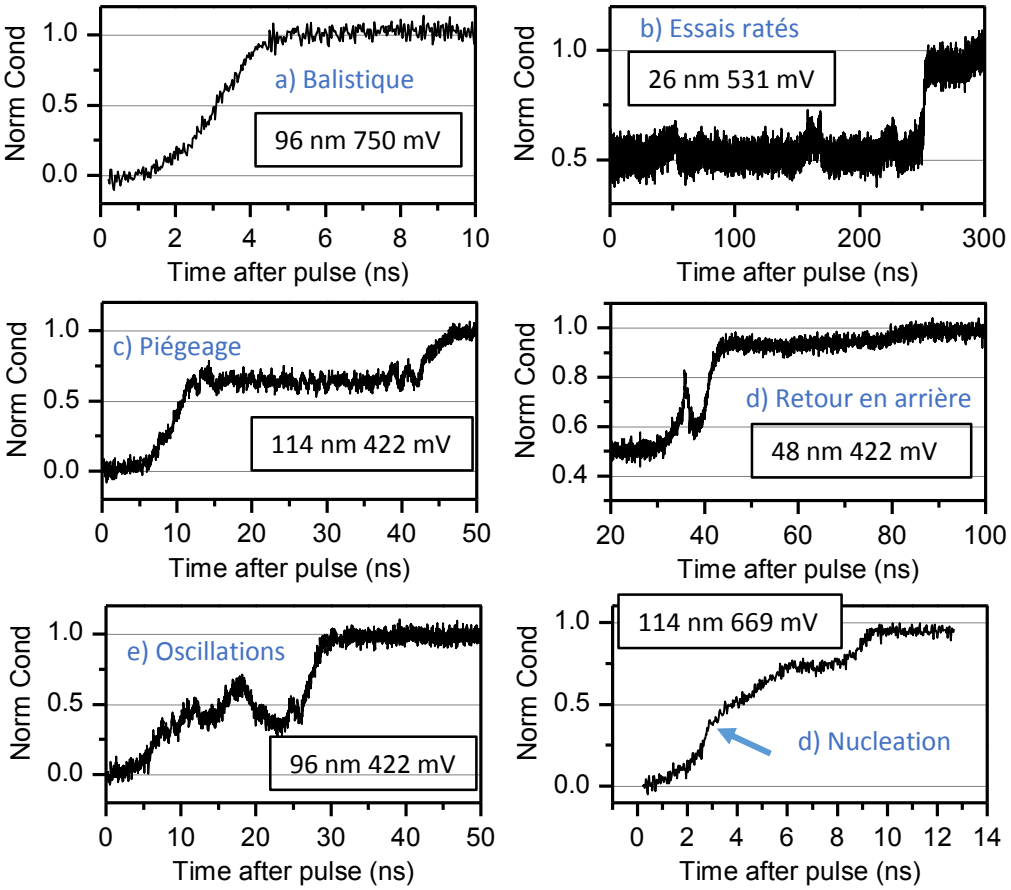

FIGURE A.7: Les différents évènements observés dans nos mesures résolues en temps. a) le retournement balistique. b) les essais ratés. c) le piégeage. d) les forts retours en arrière. e) les oscillations. f) les signatures de nucléation. Il ne s'agit que d'un exemple pour chaque évènement. Certains sont très courant et d'autre ne sont vus que pour un retournement sur 1000. Différentes tailles et tensions sont représentées (voir légende).

- Retournement balistique (figure A.7.a). Il s'agit du type de retournement le plus courant. Des retournements balistiques sont vus à toutes les tensions et tailles, mais ils sont plus probables aux fortes tensions.

- Pendant le temps d'incubation, le retournement commence parfois avant que la couche libre ne retourne dans son état initial (figure A.7.b). Nous appelons ces évènements des essais ratés. Ils sont vus aux petites tailles sous de faibles tensions seulement.

- Parfois la conductance reste une longue période de temps sur un plateau qui ne correspond ni à l'état initial ni à l'état final (figure A.7.c). Ces évènements sont appelés piégeage, car ils correspondent vraisemblablement au piégeage d'une paroi de domaine dans un défaut de la couche libre. Les piégeages sont observés pour les grand dispositifs sous de faibles tensions.

- Parfois la conductance peut retourner fortement en arrière au cours du retournement (figure A.7.d). Ceci est observé pour toutes les tailles, mais tend à disparaitre aux fortes tailles sous une forte tension.

- Le retournement se fait parfois après des oscillations du signal (figure A.7.e). Ceci est observé aux faibles tensions, principalement dans les grands dispositifs. Ces oscillations pourraient correspondre aux fortes oscillations de Walker prédites par nos modèles, mais il est difficile de trancher sur leur existence dans ces échantillons à cause du piégeage ayant lieu aux mêmes tailles et tensions.

- Enfin la vitesse à laquelle le retournement s'effectue varie d'un évènement de retournement à l'autre, et peut aussi varier au cours d'un même retournement (figure A.7.f). Ceci peut être interprété comme une nucléation de paroi de domaine car après le changement de pente, le retournement se fait linéairement comme prédit par nos modèles de déplacement de paroi dans les cas non-oscillant.

En plus d'étudier qualitativement ces différents évènements, nous avons extrait de chaque courbe un temps d'incubation et un temps de transition. Ces deux quantités ont pu être comparée quantitativement à nos modèles (macrospin ou déplacement de paroi). Le principal résultat issu de cette étude est que la dépendance en taille du temps d'incubation peut être bien décrite par le modèle macrospin. Ceci est une indication que la première étape du retournement est l'amplification d'une précession cohérente.

Nous avons donc au final des signatures de parois de domaines, et des signatures d'une première étape macrospin. Les signatures macrospin sont la dépendance en taille du temps d'incubation ainsi que les essais ratés. En effet les essais ratés ont été observés aux petites tailles dans nos simulations lorsque le début du retournement est macrospin, mais pas lorsque qu'une paroi de domaine est nucléée initialement. Les signatures de parois sont le piégeage, les forts retours en arrière, les oscillations et enfin les changements de rythme de retournement s'apparentant à des nucléations. Nous pensons donc que le chemin de retournement décrit dans nos simulations micromagnétiques, c'est-à-dire une phase d'amplification macrospin suivie par un déplacement de paroi de domaine, est également pertinent dans nos dispositifs mesurés.

Toutefois les fortes oscillations de Walker dans nos dispositifs n'ont pas été clairement mesuré sur ces échantillons. Mais dans des empilements différents où la couche

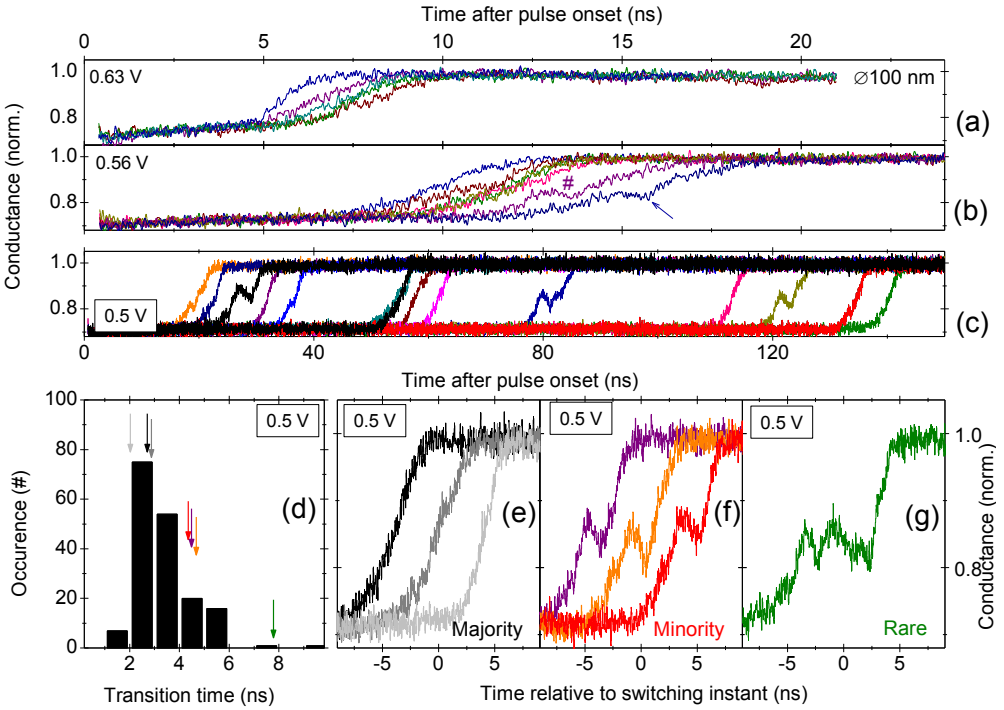

FIGURE A.8: Figure issue de notre dernier papier sur la dynamique de paroi. Mesures résolues en temps du retournement dans un échantillon à la couche libre sans piégeage et sans champ de fuite. La tension appliquée est a) 630 mV b) 560 mV ou c) 500 mV. Un histogramme des temps de transition est montré d) ainsi que trois évènements caractéristiques de cet histogramme. Les flèches de couleurs indiquent la position des trois évènements dans l'histogramme. Nous retrouvons des oscillations similaires à celles prédites dans nos modèles, avec la même probabilité d'existence.

libre ne contient pas de piégeage et où les champs de fuite du système de référence sont mieux compensés, ces fortes oscillations ont été récemment mesurées (voir figure A.8). Leur absence dans nos premiers 'échantillons peut s'expliquer par les champs de fuite du système de référence, comme notre modèle de dynamique de paroi peut prouver que leur présence supprime ces oscillations.

Nous pouvons donc conclure en disant que dans les dispositifs STTMRAM, la première étape du retournement est macrospin. Donc les modèles macrospin peuvent être utilisés pour discuter de l'activation du retournement et des tensions ou champs critiques. En revanche des parois de domaine sont impliquées dans le retournement pour toutes les tailles que nous avons pu mesurer (26 nm et plus). Le déplacement de ces parois n'est canonique seulement dans les échantillons où la couche libre présente peu de défauts et est sous un champ de fuite précisément compensé.

Bibliography

[1] Amikam Aharoni. "The nucleation problem". en. In: *Introduction to the Theory of Ferromagnetism*. International series of monographs on physics 1 (2001), p. 183. ISSN: 9780198508090. URL: https://global.oup.com/academic/product/introduction-to-the-theory-of-ferromagnetism-9780198508090?q=aharoni&lang=en&cc=fr.

[2] D. Bedau et al. "Spin-transfer pulse switching: From the dynamic to the thermally activated regime". en. In: *Applied Physics Letters* 97.26 (Dec. 2010), p. 262502. ISSN: 0003-6951, 1077-3118. DOI: 10.1063/1.3532960. URL: http://aip.scitation.org/doi/10.1063/1.3532960 (visited on 08/29/2018).

[3] M Beleggia, M De Graef, and Y T Millev. "The equivalent ellipsoid of a magnetized body". en. In: *Journal of Physics D: Applied Physics* 39.5 (Mar. 2006), pp. 891–899. ISSN: 0022-3727, 1361-6463. DOI: 10.1088/0022-3727/39/5/001. URL: http://stacks.iop.org/0022-3727/39/i=5/a=001?key=crossref.142cf7f4f2ffb3db89b2aa6c3de02b3b (visited on 07/02/2018).

[4] Mohamed Belmeguenai et al. "Interfacial Dzyaloshinskii-Moriya interaction in perpendicularly magnetized Pt/Co/AlO x ultrathin films measured by Brillouin light spectroscopy". en. In: *Physical Review B* 91.18 (May 2015), p. 180405. ISSN: 1098-0121, 1550-235X. DOI: 10.1103/PhysRevB.91.180405. URL: https://link.aps.org/doi/10.1103/PhysRevB.91.180405 (visited on 12/30/2019).

[5] K. Bernert et al. "Phase diagrams of MgO magnetic tunnel junctions including the perpendicular spin-transfer torque in different geometries". en. In: *Physical Review B* 89.13 (Apr. 2014). ISSN: 1098-0121, 1550-235X. DOI: 10.1103/PhysRevB.89.134415. URL: http://link.aps.org/doi/10.1103/PhysRevB.89.134415 (visited on 01/19/2017).

[6] David P. Bernstein et al. "Nonuniform switching of the perpendicular magnetization in a spin-torque-driven magnetic nanopillar". en. In: *Physical Review B* 83.18 (May 2011). ISSN: 1098-0121, 1550-235X. DOI: 10.1103/PhysRevB.83.180410. URL: https://link.aps.org/doi/10.1103/PhysRevB.83.180410 (visited on 07/06/2018).

[7] G. Bertotti et al. "Comparison of analytical solutions of Landau–Lifshitz equation for "damping" and "precessional" switchings". en. In: *Journal of Applied Physics* 93.10 (May 2003), pp. 6811–6813. ISSN: 0021-8979, 1089-7550. DOI: 10.1063/1.1557275. URL: http://aip.scitation.org/doi/10.1063/1.1557275 (visited on 09/05/2017).

[8] C. Bilzer et al. "Open-Circuit One-Port Network Analyzer Ferromagnetic Resonance". In: *IEEE Transactions on Magnetics* 44.11 (Nov. 2008), pp. 3265–3268. ISSN: 0018-9464. DOI: 10.1109/TMAG.2008.2004379. URL: http://ieeexplore.ieee.org/document/4717713/ (visited on 10/27/2017).

[9] Paul Bouquin et al. “Size dependence of spin-torque switching in perpendicular magnetic tunnel junctions”. en. In: *Applied Physics Letters* 113.22 (Nov. 2018), p. 222408. ISSN: 0003-6951, 1077-3118. DOI: 10.1063/1.5055741. URL: http://aip.scitation.org/doi/10.1063/1.5055741 (visited on 02/11/2019).

[10] P. Bruno. “Theory of interlayer magnetic coupling”. en. In: *Physical Review B* 52.1 (July 1995), pp. 411–439. ISSN: 0163-1829, 1095-3795. DOI: 10.1103/PhysRevB.52.411. URL: https://link.aps.org/doi/10.1103/PhysRevB.52.411 (visited on 03/04/2020).

[11] Tobias Böttcher et al. “Heisenberg Exchange and Dzyaloshinskii-Moriya Interaction in Ultrathin CoFeB Single and Multilayers”. en. In: *arXiv:2006.02690 [cond-mat]* (June 2020). arXiv: 2006.02690. URL: http://arxiv.org/abs/2006.02690 (visited on 06/29/2020).

[12] W. H. Butler et al. “Spin-dependent tunneling conductance of Fe | MgO | Fe sandwiches”. en. In: *Physical Review B* 63.5 (Jan. 2001), p. 054416. ISSN: 0163-1829, 1095-3795. DOI: 10.1103/PhysRevB.63.054416. URL: https://link.aps.org/doi/10.1103/PhysRevB.63.054416 (visited on 03/10/2020).

[13] W. H. Butler et al. “Switching Distributions for Perpendicular Spin-Torque Devices Within the Macrospin Approximation”. In: *IEEE Transactions on Magnetics* 48.12 (Dec. 2012), pp. 4684–4700. ISSN: 0018-9464, 1941-0069. DOI: 10.1109/TMAG.2012.2209122. URL: http://ieeexplore.ieee.org/document/6242414/ (visited on 02/20/2018).

[14] Kyo-Suk Chae, Tae-Hun Shim, and Jea-Gun Park. “Dependency of anti-ferromagnetic coupling strength on Ru spacer thickness of [Co/Pd] $_{n}$ -synthetic-anti-ferro-magnetic layer in perpendicular magnetic-tunnel-junctions fabricated on 12-inch TiN electrode wafer”. en. In: *Journal of Applied Physics* 116.3 (July 2014), p. 033904. ISSN: 0021-8979, 1089-7550. DOI: 10.1063/1.4887352. URL: http://aip.scitation.org/doi/10.1063/1.4887352 (visited on 03/04/2020).

[15] Yao-Jen Chang et al. “Perpendicular magnetic tunnel junctions with synthetic antiferromagnetic pinned layers based on [Co/Pd] multilayers”. en. In: *Journal of Applied Physics* 113.17 (May 2013), 17B909. ISSN: 0021-8979, 1089-7550. DOI: 10.1063/1.4799974. URL: http://aip.scitation.org/doi/10.1063/1.4799974 (visited on 03/04/2020).

[16] A. Chavent et al. “Steady State and Dynamics of Joule Heating in Magnetic Tunnel Junctions Observed via the Temperature Dependence of RKKY Coupling”. en. In: *Physical Review Applied* 6.3 (Sept. 2016), p. 034003. ISSN: 2331-7019. DOI: 10.1103/PhysRevApplied.6.034003. URL: https://link.aps.org/doi/10.1103/PhysRevApplied.6.034003 (visited on 06/24/2020).

[17] Gabriel D. Chaves-O’Flynn et al. “Thermal Stability of Magnetic States in Circular Thin-Film Nanomagnets with Large Perpendicular Magnetic Anisotropy”. en. In: *Physical Review Applied* 4.2 (Aug. 2015). ISSN: 2331-7019. DOI: 10.1103/PhysRevApplied.4.024010. URL: http://link.aps.org/doi/10.1103/PhysRevApplied.4.024010 (visited on 02/02/2017).

[18] D.-X. Chen, J.A. Brug, and R.B. Goldfarb. “Demagnetizing factors for cylinders”. en. In: *IEEE Transactions on Magnetics* 27.4 (July 1991), pp. 3601–3619. ISSN: 0018-9464, 1941-0069. DOI: 10.1109/20.102932. URL: http://ieeexplore.ieee.org/document/102932/ (visited on 10/15/2020).

[19] Ki Chul Chun et al. "A Scaling Roadmap and Performance Evaluation of In-Plane and Perpendicular MTJ Based STT-MRAMs for High-Density Cache Memory". en. In: *IEEE Journal of Solid-State Circuits* 48.2 (Feb. 2013), pp. 598–610. ISSN: 0018-9200, 1558-173X. DOI: 10.1109/JSSC.2012.2224256. URL: http://ieeexplore.ieee.org/document/6374706/ (visited on 03/04/2020).

[20] W. T. Coffey, D. A. Garanin, and D. J. Mccarthy. "Crossover formulas in the kramers theory of thermally activated escape rates-application to spin systems". en. In: *Advances in Chemical Physics*. Ed. by I. Prigogine and Stuart A. Rice. Hoboken, NJ, USA: John Wiley & Sons, Inc., Mar. 2007, pp. 483–765. ISBN: 978-0-470-14177-9 978-0-471-40542-9. DOI: 10.1002/9780470141779.ch5. URL: http://doi.wiley.com/10.1002/9780470141779.ch5 (visited on 11/29/2019).

[21] S. Couet et al. "Impact of Ta and W-based spacers in double MgO STT-MRAM free layers on perpendicular anisotropy and damping". en. In: *Applied Physics Letters* 111.15 (Oct. 2017), p. 152406. ISSN: 0003-6951, 1077-3118. DOI: 10.1063/1.5000992. URL: http://aip.scitation.org/doi/10.1063/1.5000992 (visited on 06/18/2018).

[22] J. Cucchiara et al. "Domain wall motion in nanopillar spin-valves with perpendicular anisotropy driven by spin-transfer torques". en. In: *Physical Review B* 86.21 (Dec. 2012). ISSN: 1098-0121, 1550-235X. DOI: 10.1103/PhysRevB.86.214429. URL: https://link.aps.org/doi/10.1103/PhysRevB.86.214429 (visited on 04/03/2018).

[23] L. Desplat et al. "Path sampling for collapse rates of metastable magnetic skyrmions and direct comparison with transition state theory". en. In: *arXiv:1905.04110 [cond-mat]* (May 2019). arXiv: 1905.04110. URL: http://arxiv.org/abs/1905.04110 (visited on 11/29/2019).

[24] Louise Desplat and Joo-Von Kim. "Entropy-reduced Retention Times in Magnetic Memory Elements: A Case of the Meyer-Neldel Compensation Rule". en. In: *Physical Review Letters* 125.10 (Sept. 2020), p. 107201. ISSN: 0031-9007, 1079-7114. DOI: 10.1103/PhysRevLett.125.107201. URL: https://link.aps.org/doi/10.1103/PhysRevLett.125.107201 (visited on 09/07/2020).

[25] T. Devolder et al. "Annealing stability of magnetic tunnel junctions based on dual MgO free layers and [Co/Ni] based thin synthetic antiferromagnet fixed system". en. In: *Journal of Applied Physics* 121.11 (Mar. 2017), p. 113904. ISSN: 0021-8979, 1089-7550. DOI: 10.1063/1.4978633. URL: http://aip.scitation.org/doi/10.1063/1.4978633 (visited on 03/22/2017).

[26] T. Devolder et al. "Back-hopping in Spin-Transfer-Torque switching of perpendicularly magnetized tunnel junctions". en. In: *arXiv:2006.05108 [cond-mat, physics:physics]* (June 2020). arXiv: 2006.05108. URL: http://arxiv.org/abs/2006.05108 (visited on 06/25/2020).

[27] T. Devolder et al. "Exchange stiffness in ultrathin perpendicularly magnetized CoFeB layers determined using the spectroscopy of electrically excited spin waves". en. In: *Journal of Applied Physics* 120.18 (Nov. 2016), p. 183902. ISSN: 0021-8979, 1089-7550. DOI: 10.1063/1.4967826. URL: http://aip.scitation.org/doi/10.1063/1.4967826 (visited on 02/21/2017).

[28] T. Devolder et al. "Instability threshold versus switching threshold in spin-transfer-induced magnetization switching". en. In: *Physical Review B* 71.18 (May 2005). ISSN: 1098-0121, 1550-235X. DOI: 10.1103/PhysRevB.71.184401. URL: https://link.aps.org/doi/10.1103/PhysRevB.71.184401 (visited on 07/02/2018).

[29] T. Devolder et al. "Offset fields in perpendicularly magnetized tunnel junctions". en. In: *Journal of Physics D: Applied Physics* (Apr. 2019). arXiv: 1904.10170. ISSN: 0022-3727, 1361-6463. DOI: 10.1088/1361-6463/ab1b07. URL: http://arxiv.org/abs/1904.10170 (visited on 04/24/2019).

[30] T. Devolder et al. "Time-resolved spin-torque switching in MgO-based perpendicularly magnetized tunnel junctions". en. In: *Physical Review B* 93.2 (Jan. 2016). ISSN: 2469-9950, 2469-9969. DOI: 10.1103/PhysRevB.93.024420. URL: https://link.aps.org/doi/10.1103/PhysRevB.93.024420 (visited on 04/03/2018).

[31] Thibaut Devolder. "Using rf voltage induced ferromagnetic resonance to study the spin-wave density of states and the Gilbert damping in perpendicularly magnetized disks". en. In: *Physical Review B* 96.10 (Sept. 2017). ISSN: 2469-9950, 2469-9969. DOI: 10.1103/PhysRevB.96.104413. URL: https://link.aps.org/doi/10.1103/PhysRevB.96.104413 (visited on 07/09/2018).

[32] Thibaut Devolder et al. "Effect of Tantalum Spacer Thickness and Deposition Conditions on the Properties of MgO/CoFeB/Ta/CoFeB/MgO Free Layers". en. In: *IEEE Magnetics Letters* 10 (2019), pp. 1–4. ISSN: 1949-307X, 1949-3088. DOI: 10.1109/LMAG.2019.2940572. URL: https://ieeexplore.ieee.org/document/8827935/ (visited on 04/10/2020).

[33] Thibaut Devolder et al. "Evolution of perpendicular magnetized tunnel junctions upon annealing". en. In: *Applied Physics Letters* 108.17 (Apr. 2016), p. 172409. ISSN: 0003-6951, 1077-3118. DOI: 10.1063/1.4948378. URL: http://aip.scitation.org/doi/10.1063/1.4948378 (visited on 03/05/2020).

[34] Thibaut Devolder et al. "Material Developments and Domain Wall-Based Nanosecond-Scale Switching Process in Perpendicularly Magnetized STT-MRAM Cells". en. In: *IEEE Transactions on Magnetics* 54.2 (Feb. 2018), pp. 1–9. ISSN: 0018-9464, 1941-0069. DOI: 10.1109/TMAG.2017.2739187. URL: http://ieeexplore.ieee.org/document/8017454/ (visited on 03/07/2019).

[35] R Dittrich et al. "A path method for finding energy barriers and minimum energy paths in complex micromagnetic systems". en. In: *Journal of Magnetism and Magnetic Materials* 250 (Sept. 2002), pp. 12–19. ISSN: 03048853. DOI: 10.1016/S0304-8853(02)00388-8. URL: https://linkinghub.elsevier.com/retrieve/pii/S0304885302003888 (visited on 11/29/2019).

[36] R. Dittrich et al. "Energy barriers in magnetic random access memory elements". en. In: *IEEE Transactions on Magnetics* 39.5 (Sept. 2003), pp. 2839–2841. ISSN: 0018-9464. DOI: 10.1109/TMAG.2003.816239. URL: http://ieeexplore.ieee.org/document/1233233/ (visited on 02/04/2020).

[37] I. Dzyaloshinsky. "A thermodynamic theory of "weak" ferromagnetism of antiferromagnetics". en. In: *Journal of Physics and Chemistry of Solids* 4.4 (Jan. 1958), pp. 241–255. ISSN: 00223697. DOI: 10.1016/0022-3697(58)90076-3. URL: https://linkinghub.elsevier.com/retrieve/pii/0022369758900763 (visited on 02/07/2020).

[38] Weinan E, Weiqing Ren, and Eric Vanden-Eijnden. "Energy landscape and thermally activated switching of submicron-sized ferromagnetic elements". en. In: *Journal of Applied Physics* 93.4 (Feb. 2003), pp. 2275–2282. ISSN: 0021-8979, 1089-7550. DOI: 10.1063/1.1536737. URL: http://aip.scitation.org/doi/10.1063/1.1536737 (visited on 02/04/2020).

[39] Weinan E, Weiqing Ren, and Eric Vanden-Eijnden. "String method for the study of rare events". en. In: *Physical Review B* 66.5 (Aug. 2002), p. 052301. ISSN: 0163-1829, 1095-3795. DOI: 10.1103/PhysRevB.66.052301. URL: https://link.aps.org/doi/10.1103/PhysRevB.66.052301 (visited on 11/29/2019).

[40] Satoru Emori et al. "Spin Hall torque magnetometry of Dzyaloshinskii domain walls". en. In: *Physical Review B* 90.18 (Nov. 2014), p. 184427. ISSN: 1098-0121, 1550-235X. DOI: 10.1103/PhysRevB.90.184427. URL: https://link.aps.org/doi/10.1103/PhysRevB.90.184427 (visited on 01/27/2020).

[41] Xuanyao Fong et al. "Spin-Transfer Torque Memories: Devices, Circuits, and Systems". en. In: *Proceedings of the IEEE* 104.7 (July 2016), pp. 1449–1488. ISSN: 0018-9219, 1558-2256. DOI: 10.1109/JPROC.2016.2521712. URL: http://ieeexplore.ieee.org/document/7448833/ (visited on 03/04/2020).

[42] J. H. Franken et al. "Tunable chiral spin texture in magnetic domain-walls". en. In: *Scientific Reports* 4.1 (May 2015), p. 5248. ISSN: 2045-2322. DOI: 10.1038/srep05248. URL: http://www.nature.com/articles/srep05248 (visited on 01/27/2020).

[43] C. Gourdon et al. "Domain-wall flexing instability and propagation in thin ferromagnetic films". en. In: *Physical Review B* 88.1 (July 2013), p. 014428. ISSN: 1098-0121, 1550-235X. DOI: 10.1103/PhysRevB.88.014428. URL: https://link.aps.org/doi/10.1103/PhysRevB.88.014428 (visited on 06/24/2020).

[44] Christian Hahn et al. "Time-resolved studies of the spin-transfer reversal mechanism in perpendicularly magnetized magnetic tunnel junctions". en. In: *Physical Review B* 94.21 (Dec. 2016), p. 4432. ISSN: 2469-9950, 2469-9969. DOI: 10.1103/PhysRevB.94.214432. URL: https://link.aps.org/doi/10.1103/PhysRevB.94.214432 (visited on 02/20/2018).

[45] J. He, J. Z. Sun, and S. Zhang. "Switching speed distribution of spin-torque-induced magnetic reversal". en. In: *Journal of Applied Physics* 101.9 (May 2007), 09A501. ISSN: 0021-8979, 1089-7550. DOI: 10.1063/1.2668365. URL: http://aip.scitation.org/doi/10.1063/1.2668365 (visited on 02/07/2019).

[46] Burkard Hillebrands and André Thiaville, eds. *Spin Dynamics in Confined Magnetic Structures III*. en. Vol. 101. Topics in Applied Physics. Springer Berlin Heidelberg, 2006. ISBN: 978-3-540-20108-3. DOI: 10.1007/b12462. URL: http://link.springer.com/10.1007/b12462 (visited on 01/09/2020).

[47] Keiji Hosotani et al. "Effect of Self-Heating on Time-Dependent Dielectric Breakdown in Ultrathin MgO Magnetic Tunnel Junctions for Spin Torque Transfer Switching Magnetic Random Access Memory". en. In: *Japanese Journal of Applied Physics* 49.4 (Apr. 2010), p. 04DD15. ISSN: 0021-4922, 1347-4065. DOI: 10.1143/JJAP.49.04DD15. URL: http://stacks.iop.org/1347-4065/49/04DD15 (visited on 11/29/2019).

[48] A. Hubert and R. Schäfer. *Magnetic Domains: The Analysis of Magnetic Microstructures*. Springer Berlin Heidelberg, 2008. ISBN: 978-3-540-85054-0. URL: https://books.google.fr/books?id=uRtqCQAAQBAJ.

[49] Alex Hubert and Rudolf Schäfer. "Domain Theory". In: *Magnetic Domains*. 1998, p. 306.

[50] S. Ikeda et al. "A perpendicular-anisotropy CoFeB–MgO magnetic tunnel junction". en. In: *Nature Materials* 9.9 (Sept. 2010), pp. 721–724. ISSN: 1476-1122, 1476-4660. DOI: 10.1038/nmat2804. URL: http://www.nature.com/articles/nmat2804 (visited on 06/22/2018).

[51] Peong-Hwa Jang et al. "Detrimental effect of interfacial Dzyaloshinskii-Moriya interaction on perpendicular spin-transfer-torque magnetic random access memory". en. In: *Applied Physics Letters* 107.20 (Nov. 2015), p. 202401. ISSN: 0003-6951, 1077-3118. DOI: 10.1063/1.4936089. URL: http://aip.scitation.org/doi/10.1063/1.4936089 (visited on 12/20/2019).

[52] Hannes Jónsson, Greg Mills, and Karsten W. Jacobsen. "Nudged elastic band method for finding minimum energy paths of transitions". en. In: *Classical and Quantum Dynamics in Condensed Phase Simulations*. LERICI, Villa Marigola: WORLD SCIENTIFIC, June 1998, pp. 385–404. ISBN: 978-981-02-3498-0 978-981-283-966-4. DOI: 10.1142/9789812839664_0016. URL: http://www.worldscientific.com/doi/abs/10.1142/9789812839664_0016 (visited on 10/19/2020).

[53] M T Johnson et al. "Magnetic anisotropy in metallic multilayers". en. In: *Reports on Progress in Physics* 59.11 (Nov. 1996), pp. 1409–1458. ISSN: 0034-4885, 1361-6633. DOI: 10.1088/0034-4885/59/11/002. URL: http://stacks.iop.org/0034-4885/59/i=11/a=002?key=crossref.ac0526de3bbf4bc7c58b0ea17472e03a (visited on 03/04/2020).

[54] M. Julliere. "Tunneling between ferromagnetic films". en. In: *Physics Letters A* 54.3 (Sept. 1975), pp. 225–226. ISSN: 03759601. DOI: 10.1016/0375-9601(75)90174-7. URL: http://linkinghub.elsevier.com/retrieve/pii/0375960175901747 (visited on 09/05/2017).

[55] A V Khvalkovskiy et al. "Basic principles of STT-MRAM cell operation in memory arrays". In: *Journal of Physics D: Applied Physics* 46.13 (Apr. 2013), p. 139601. ISSN: 0022-3727, 1361-6463. DOI: 10.1088/0022-3727/46/13/139601. URL: http://stacks.iop.org/0022-3727/46/i=13/a=139601?key=crossref.de8de76f28baa2dc01864ee7497afbcf (visited on 01/19/2017).

[56] S. I. Kiselev et al. "Microwave oscillations of a nanomagnet driven by a spin-polarized current". en. In: *Nature* 425.6956 (Sept. 2003), pp. 380–383. ISSN: 0028-0836, 1476-4687. DOI: 10.1038/nature01967. URL: http://www.nature.com/articles/nature01967 (visited on 07/02/2018).

[57] C. Kittel. "Ferromagnetic resonance". en. In: *Journal de Physique et le Radium* 12.3 (1951), pp. 291–302. ISSN: 0368-3842. DOI: 10.1051/jphysrad:01951001203029100. URL: http://www.edpsciences.org/10.1051/jphysrad:01951001203029100 (visited on 02/07/2020).

[58] O. Klein et al. "Ferromagnetic resonance force spectroscopy of individual submicron-size samples". en. In: *Physical Review B* 78.14 (Oct. 2008), p. 144410. ISSN: 1098-0121, 1550-235X. DOI: 10.1103/PhysRevB.78.144410. URL: https://link.aps.org/doi/10.1103/PhysRevB.78.144410 (visited on 04/07/2020).

[59] R. H. Koch, J. A. Katine, and J. Z. Sun. "Time-Resolved Reversal of Spin-Transfer Switching in a Nanomagnet". en. In: *Physical Review Letters* 92.8 (Feb. 2004). ISSN: 0031-9007, 1079-7114. DOI: 10.1103/PhysRevLett.92.088302. URL: https://link.aps.org/doi/10.1103/PhysRevLett.92.088302 (visited on 08/21/2018).

[60] Hitoshi Kubota et al. "Quantitative measurement of voltage dependence of spin-transfer torque in MgO-based magnetic tunnel junctions". en. In: *Nature Physics* 4.1 (Jan. 2008), pp. 37–41. ISSN: 1745-2473, 1745-2481. DOI: 10.1038/nphys784. URL: http://www.nature.com/articles/nphys784 (visited on 03/11/2020).

[61] Takahide Kubota et al. "Structure, exchange stiffness, and magnetic anisotropy of Co2MnAlxSi1-x Heusler compounds". en. In: *Journal of Applied Physics* 106.11 (Dec. 2009), p. 113907. ISSN: 0021-8979, 1089-7550. DOI: 10.1063/1.3265428. URL: http://aip.scitation.org/doi/10.1063/1.3265428 (visited on 04/08/2020).

[62] M. Lavanant et al. "State diagram of a perpendicular magnetic tunnel junction driven by spin transfer torque: A power dissipation approach". en. In: *Journal of Magnetism and Magnetic Materials* 428 (Apr. 2017), pp. 293–299. ISSN: 03048853. DOI: 10.1016/j.jmmm.2016.10.061. URL: http://linkinghub.elsevier.com/retrieve/pii/S0304885316311477 (visited on 02/08/2017).

[63] S. Le Gall et al. "State diagram of nanopillar spin valves with perpendicular magnetic anisotropy". en. In: *Physical Review B* 86.1 (July 2012). ISSN: 1098-0121, 1550-235X. DOI: 10.1103/PhysRevB.86.014419. URL: https://link.aps.org/doi/10.1103/PhysRevB.86.014419 (visited on 06/13/2018).

[64] A. Le Goff, V. Nikitin, and T. Devolder. "Spin-wave thermal population as temperature probe in magnetic tunnel junctions". en. In: *Journal of Applied Physics* 120.2 (July 2016), p. 023902. ISSN: 0021-8979, 1089-7550. DOI: 10.1063/1.4953680. URL: http://aip.scitation.org/doi/10.1063/1.4953680 (visited on 11/29/2019).

[65] Seung-Eun Lee, Tae-Hun Shim, and Jea-Gun Park. "Perpendicular magnetic tunnel junction (p-MTJ) spin-valves designed with a top Co2Fe6B2 free layer and a nanoscale-thick tungsten bridging and capping layer". en. In: *NPG Asia Materials* 8.11 (Nov. 2016), e324–e324. ISSN: 1884-4049, 1884-4057. DOI: 10.1038/am.2016.162. URL: http://www.nature.com/articles/am2016162 (visited on 03/05/2020).

[66] J. Leliaert et al. "Adaptively time stepping the stochastic Landau-Lifshitz-Gilbert equation at nonzero temperature: Implementation and validation in MuMax ^{3}". en. In: *AIP Advances* 7.12 (Dec. 2017), p. 125010. ISSN: 2158-3226. DOI: 10.1063/1.5003957. URL: http://aip.scitation.org/doi/10.1063/1.5003957 (visited on 06/11/2018).

[67] Z. Li and S. Zhang. "Magnetization dynamics with a spin-transfer torque". en. In: *Physical Review B* 68.2 (July 2003), p. 024404. ISSN: 0163-1829, 1095-3795. DOI: 10.1103/PhysRevB.68.024404. URL: https://link.aps.org/doi/10.1103/PhysRevB.68.024404 (visited on 02/06/2020).

[68] Zhi-Peng Li et al. "The study of origin of interfacial perpendicular magnetic anisotropy in ultra-thin CoFeB layer on the top of MgO based magnetic tunnel junction". en. In: *Applied Physics Letters* 109.18 (Oct. 2016), p. 182403. ISSN: 0003-6951, 1077-3118. DOI: 10.1063/1.4966891. URL: http://aip.scitation.org/doi/10.1063/1.4966891 (visited on 03/04/2020).

[69] E. Liu et al. "[Co/Ni]-CoFeB hybrid free layer stack materials for high density magnetic random access memory applications". en. In: *Applied Physics Letters* 108.13 (Mar. 2016), p. 132405. ISSN: 0003-6951, 1077-3118. DOI: 10.1063/1.

4945089. URL: http://aip.scitation.org/doi/10.1063/1.4945089 (visited on 03/04/2020).

[70] Enlong Liu et al. "Seed layer impact on structural and magnetic properties of [Co/Ni] multilayers with perpendicular magnetic anisotropy". en. In: *Journal of Applied Physics* 121.4 (Jan. 2017), p. 043905. ISSN: 0021-8979, 1089-7550. DOI: 10.1063/1.4974885. URL: http://aip.scitation.org/doi/10.1063/1.4974885 (visited on 03/27/2020).

[71] S Mizukami, Y Ando, and T Miyazaki. "Ferromagnetic resonance linewidth for NM/80NiFe/NM "lms (NM"Cu, Ta, Pd and Pt)". en. In: *Journal of Magnetism and Magnetic Materials* (2001), p. 3.

[72] Kotaro Mizunuma et al. "Size Dependence of Magnetic Properties of Nanoscale CoFeB–MgO Magnetic Tunnel Junctions with Perpendicular Magnetic Easy Axis Observed by Ferromagnetic Resonance". en. In: *Applied Physics Express* 6.6 (June 2013), p. 063002. ISSN: 1882-0778, 1882-0786. DOI: 10.7567/APEX.6.063002. URL: http://stacks.iop.org/1882-0786/6/i=6/a=063002?key=crossref.f9a60e0bbdc5da98ca4a160f4ab56065 (visited on 07/02/2018).

[73] J. S. Moodera et al. "Large Magnetoresistance at Room Temperature in Ferromagnetic Thin Film Tunnel Junctions". en. In: *Physical Review Letters* 74.16 (Apr. 1995), pp. 3273–3276. ISSN: 0031-9007, 1079-7114. DOI: 10.1103/PhysRevLett.74.3273. URL: https://link.aps.org/doi/10.1103/PhysRevLett.74.3273 (visited on 03/12/2020).

[74] Tôru Moriya. "Anisotropic Superexchange Interaction and Weak Ferromagnetism". en. In: *Physical Review* 120.1 (Oct. 1960), pp. 91–98. ISSN: 0031-899X. DOI: 10.1103/PhysRev.120.91. URL: https://link.aps.org/doi/10.1103/PhysRev.120.91 (visited on 02/07/2020).

[75] A Mougin et al. "Domain wall mobility, stability and Walker breakdown in magnetic nanowires". en. In: *Europhysics Letters (EPL)* 78.5 (June 2007), p. 57007. ISSN: 0295-5075, 1286-4854. DOI: 10.1209/0295-5075/78/57007. URL: http://stacks.iop.org/0295-5075/78/i=5/a=57007?key=crossref.80546d8cffe603aa65f0a30b93e7436d (visited on 02/19/2019).

[76] Sumanta Mukherjee et al. "Role of boron diffusion in CoFeB/MgO magnetic tunnel junctions". en. In: *Physical Review B* 91.8 (Feb. 2015), p. 085311. ISSN: 1098-0121, 1550-235X. DOI: 10.1103/PhysRevB.91.085311. URL: https://link.aps.org/doi/10.1103/PhysRevB.91.085311 (visited on 03/04/2020).

[77] Kamaram Munira and P. B. Visscher. "Calculation of energy-barrier lowering by incoherent switching in spin-transfer torque magnetoresistive random-access memory". en. In: *Journal of Applied Physics* 117.17 (May 2015), 17B710. ISSN: 0021-8979, 1089-7550. DOI: 10.1063/1.4908153. URL: http://aip.scitation.org/doi/10.1063/1.4908153 (visited on 02/02/2017).

[78] V. V. Naletov et al. "Identification and selection rules of the spin-wave eigenmodes in a normally magnetized nanopillar". en. In: *Physical Review B* 84.22 (Dec. 2011), p. 224423. ISSN: 1098-0121, 1550-235X. DOI: 10.1103/PhysRevB.84.224423. URL: https://link.aps.org/doi/10.1103/PhysRevB.84.224423 (visited on 04/07/2020).

[79] V. Novosad et al. "Novel magnetostrictive memory device". en. In: *Journal of Applied Physics* 87.9 (May 2000), pp. 6400–6402. ISSN: 0021-8979, 1089-7550. DOI: 10.1063/1.372719. URL: http://aip.scitation.org/doi/10.1063/1.372719 (visited on 12/30/2019).

[80] Janusz J. Nowak et al. "Dependence of Voltage and Size on Write Error Rates in Spin-Transfer Torque Magnetic Random-Access Memory". en. In: *IEEE Magnetics Letters* 7 (2016), pp. 1–4. ISSN: 1949-307X, 1949-3088. DOI: 10.1109/LMAG.2016.2539256. URL: http://ieeexplore.ieee.org/document/7428818/ (visited on 03/05/2020).

[81] J. A. Osborn. "Demagnetizing Factors of the General Ellipsoid". en. In: *Physical Review* 67.11-12 (June 1945), pp. 351–357. ISSN: 0031-899X. DOI: 10.1103/PhysRev.67.351. URL: https://link.aps.org/doi/10.1103/PhysRev.67.351 (visited on 02/19/2019).

[82] N. Perrissin. "Highly thermally stable sub 20nm mram based on perpandicular shape anisotropy". In: *ArXiv* (2018).

[83] D. Pinna, A. D. Kent, and D. L. Stein. "Spin-transfer torque magnetization reversal in uniaxial nanomagnets with thermal noise". In: *Journal of Applied Physics* 114.3 (2013), p. 033901. URL: http://aip.scitation.org/doi/abs/10.1063/1.4813488 (visited on 06/14/2017).

[84] Kwang-Su Ryu et al. "Chiral spin torque arising from proximity-induced magnetization". en. In: *Nature Communications* 5.1 (Sept. 2014), p. 3910. ISSN: 2041-1723. DOI: 10.1038/ncomms4910. URL: http://www.nature.com/articles/ncomms4910 (visited on 01/27/2020).

[85] J. Sampaio et al. "Disruptive effect of Dzyaloshinskii-Moriya interaction on the magnetic memory cell performance". en. In: *Applied Physics Letters* 108.11 (Mar. 2016), p. 112403. ISSN: 0003-6951, 1077-3118. DOI: 10.1063/1.4944419. URL: http://aip.scitation.org/doi/10.1063/1.4944419 (visited on 12/20/2019).

[86] L. San Emeterio Alvarez et al. "Field-current phase diagrams of in-plane spin transfer torque memory cells with low effective magnetization storage layers". en. In: *Journal of Applied Physics* 115.17 (May 2014), p. 17C713. ISSN: 0021-8979, 1089-7550. DOI: 10.1063/1.4862842. URL: http://aip.scitation.org/doi/10.1063/1.4862842 (visited on 02/19/2020).

[87] Jack C. Sankey et al. "Measurement of the spin-transfer-torque vector in magnetic tunnel junctions". en. In: *Nature Physics* 4.1 (Jan. 2008), pp. 67–71. ISSN: 1745-2473, 1745-2481. DOI: 10.1038/nphys783. URL: http://www.nature.com/articles/nphys783 (visited on 03/11/2020).

[88] H. Sato et al. "Perpendicular-anisotropy CoFeB-MgO magnetic tunnel junctions with a MgO/CoFeB/Ta/CoFeB/MgO recording structure". en. In: *Applied Physics Letters* 101.2 (July 2012), p. 022414. ISSN: 0003-6951, 1077-3118. DOI: 10.1063/1.4736727. URL: http://aip.scitation.org/doi/10.1063/1.4736727 (visited on 03/04/2020).

[89] G. Schütz et al. "Absorption of circularly polarized x rays in iron". en. In: *Physical Review Letters* 58.7 (Feb. 1987), pp. 737–740. ISSN: 0031-9007. DOI: 10.1103/PhysRevLett.58.737. URL: https://link.aps.org/doi/10.1103/PhysRevLett.58.737 (visited on 03/06/2020).

[90] J. C. Slonczewski. "Currents, torques, and polarization factors in magnetic tunnel junctions". en. In: *Physical Review B* 71.2 (Jan. 2005). ISSN: 1098-0121, 1550-235X. DOI: 10.1103/PhysRevB.71.024411. URL: https://link.aps.org/doi/10.1103/PhysRevB.71.024411 (visited on 05/24/2017).

[91] J. C. Slonczewski. "Theory of domain-wall motion in magnetic films and platelets". en. In: *Journal of Applied Physics* 44.4 (Apr. 1973), pp. 1759–1770. ISSN: 0021-8979, 1089-7550. DOI: 10.1063/1.1662444. URL: http://aip.scitation.org/doi/10.1063/1.1662444 (visited on 06/05/2019).

[92] J.C. Slonczewski and J.Z. Sun. "Theory of voltage-driven current and torque in magnetic tunnel junctions". en. In: *Journal of Magnetism and Magnetic Materials* 310.2 (Mar. 2007), pp. 169–175. ISSN: 03048853. DOI: 10.1016/j.jmmm.2006.10.507. URL: http://linkinghub.elsevier.com/retrieve/pii/S0304885306011371 (visited on 03/13/2017).

[93] John C. Slonczewski. "Current-driven excitation of magnetic multilayers". In: *Journal of Magnetism and Magnetic Materials* 159.1-2 (1996), pp. L1–L7. URL: http://www.sciencedirect.com/science/article/pii/0304885396000625 (visited on 03/23/2017).

[94] E. C. Stoner, F.R.S., and E. P. Wohlfarth. "A mechanism of magnetic hysteresis in heterogeneous alloys". en. In: *IEEE Transactions on Magnetics* 27.4 (1991), p. 3475. ISSN: 1471-2962. DOI: 10.1098/rsta.1948.0007. URL: http://rsta.royalsocietypublishing.org/content/240/826/599.

[95] N. Strelkov et al. "Stability phase diagram of a perpendicular magnetic tunnel junction in noncollinear geometry". en. In: *Physical Review B* 95.18 (May 2017), p. 184409. ISSN: 2469-9950, 2469-9969. DOI: 10.1103/PhysRevB.95.184409. URL: http://link.aps.org/doi/10.1103/PhysRevB.95.184409 (visited on 02/19/2020).

[96] J. Z. Sun et al. "Effect of subvolume excitation and spin-torque efficiency on magnetic switching". en. In: *Physical Review B* 84.6 (Aug. 2011). ISSN: 1098-0121, 1550-235X. DOI: 10.1103/PhysRevB.84.064413. URL: https://link.aps.org/doi/10.1103/PhysRevB.84.064413 (visited on 06/11/2018).

[97] Jonathan Z. Sun. "Spin-current interaction with a monodomain magnetic body: A model study". In: *Physical Review B* 62.1 (2000), p. 570. URL: https://journals.aps.org/prb/abstract/10.1103/PhysRevB.62.570 (visited on 03/16/2017).

[98] Jonathan Z. Sun et al. "Spin angular momentum transfer in a current-perpendicular spin-valve nanomagnet". en. In: ed. by Manijeh Razeghi and Gail J. Brown. San Jose, CA, United States, July 2004, p. 445. DOI: 10.1117/12.521195. URL: http://proceedings.spiedigitallibrary.org/proceeding.aspx?doi=10.1117/12.521195 (visited on 02/24/2020).

[99] J. Swerts et al. "BEOL compatible high tunnel magneto resistance perpendicular magnetic tunnel junctions using a sacrificial Mg layer as CoFeB free layer cap". en. In: *Applied Physics Letters* 106.26 (June 2015), p. 262407. ISSN: 0003-6951, 1077-3118. DOI: 10.1063/1.4923420. URL: http://aip.scitation.org/doi/10.1063/1.4923420 (visited on 03/27/2020).

[100] N. Tezuka et al. "Perpendicular Magnetic Tunnel Junctions With Low Resistance-Area Product: High Output Voltage and Bias Dependence of Magnetoresistance". en. In: *IEEE Magnetics Letters* 7 (2016), pp. 1–4. ISSN: 1949-307X, 1949-3088. DOI: 10.1109/LMAG.2016.2584582. URL: http://ieeexplore.ieee.org/document/7498675/ (visited on 03/05/2020).

[101] Ioannis Theodonis et al. "Anomalous Bias Dependence of Spin Torque in Magnetic Tunnel Junctions". en. In: *Physical Review Letters* 97.23 (Dec. 2006). ISSN: 0031-9007, 1079-7114. DOI: 10.1103/PhysRevLett.97.237205. URL: http://link.aps.org/doi/10.1103/PhysRevLett.97.237205 (visited on 02/23/2017).

[102] A Thiaville and J M Garc. "Domain wall dynamics in nanowires". en. In: *Journal of Magnetism and Magnetic Materials* (2002), p. 3.

[103] A Thiaville et al. "Micromagnetic understanding of current-driven domain wall motion in patterned nanowires". en. In: *Europhysics Letters (EPL)* 69.6 (Mar. 2005), pp. 990–996. ISSN: 0295-5075, 1286-4854. DOI: 10.1209/epl/i2004-10452-6. URL: http://stacks.iop.org/0295-5075/69/i=6/a=990?key=crossref.08cfdeef6135f63254ff9d17d22c1198 (visited on 10/03/2018).

[104] André Thiaville et al. "Dynamics of Dzyaloshinskii domain walls in ultrathin magnetic films". en. In: *EPL (Europhysics Letters)* 100.5 (Dec. 2012), p. 57002. ISSN: 0295-5075, 1286-4854. DOI: 10.1209/0295-5075/100/57002. URL: http://stacks.iop.org/0295-5075/100/i=5/a=57002?key=crossref.2efecb4b4825b9f99211cd2da9f0957b (visited on 07/06/2018).

[105] A. A. Timopheev et al. "Respective influence of in-plane and out-of-plane spin-transfer torques in magnetization switching of perpendicular magnetic tunnel junctions". en. In: *Physical Review B* 92.10 (Sept. 2015), p. 104430. ISSN: 1098-0121, 1550-235X. DOI: 10.1103/PhysRevB.92.104430. URL: https://link.aps.org/doi/10.1103/PhysRevB.92.104430 (visited on 03/17/2020).

[106] H. Tomita et al. "Unified understanding of both thermally assisted and precessional spin-transfer switching in perpendicularly magnetized giant magnetoresistive nanopillars". en. In: *Applied Physics Letters* 102.4 (Jan. 2013), p. 042409. ISSN: 0003-6951, 1077-3118. DOI: 10.1063/1.4789879. URL: http://aip.scitation.org/doi/10.1063/1.4789879 (visited on 03/17/2017).

[107] Larysa Tryputen et al. "Patterning of sub-50 nm perpendicular CoFeB/MgO-based magnetic tunnel junctions". en. In: *Nanotechnology* 27.18 (May 2016), p. 185302. ISSN: 0957-4484, 1361-6528. DOI: 10.1088/0957-4484/27/18/185302. URL: http://stacks.iop.org/0957-4484/27/i=18/a=185302?key=crossref.8965d690767a3352c61b2445fcbb3fe1 (visited on 03/05/2020).

[108] Meng-Chiau Tsai et al. "The intrinsic temperature dependence and the origin of the crossover of the coercivity in perpendicular MgO/CoFeB/Ta structures". en. In: *Journal of Applied Physics* 113.17 (May 2013), p. 17C118. ISSN: 0021-8979, 1089-7550. DOI: 10.1063/1.4799518. URL: http://aip.scitation.org/doi/10.1063/1.4799518 (visited on 11/29/2019).

[109] Arne Vansteenkiste et al. "The design and verification of MuMax3". en. In: *AIP Advances* 4.10 (Oct. 2014), p. 107133. ISSN: 2158-3226. DOI: 10.1063/1.4899186. URL: http://aip.scitation.org/doi/10.1063/1.4899186 (visited on 05/22/2017).

[110] P. B. Visscher, Kamaram Munira, and Robert J. Rosati. "Instability Mechanism for STT-MRAM switching". In: *arXiv preprint arXiv:1604.03992* (2016). URL: https://arxiv.org/abs/1604.03992 (visited on 04/04/2017).

[111] K. Watanabe et al. "Shape anisotropy revisited in single-digit nanometer magnetic tunnel junctions". In: *arXiv preprint arXiv:1712.08774* (2017).

[112] J.-E. Wegrowe and M.-C. Ciornei. "Magnetization dynamics, gyromagnetic relation, and inertial effects". en. In: *American Journal of Physics* 80.7 (July 2012), pp. 607–611. ISSN: 0002-9505, 1943-2909. DOI: 10.1119/1.4709188. URL: http://aapt.scitation.org/doi/10.1119/1.4709188 (visited on 01/16/2020).

[113] M. Wilczyński, J. Barnaś, and R. Świrkowicz. "Free-electron model of current-induced spin-transfer torque in magnetic tunnel junctions". en. In: *Physical Review B* 77.5 (Feb. 2008), p. 054434. ISSN: 1098-0121, 1550-235X. DOI: 10.1103/PhysRevB.77.054434. URL: https://link.aps.org/doi/10.1103/PhysRevB.77.054434 (visited on 03/11/2020).

[114] K. Yakushiji et al. "Ultrathin Co/Pt and Co/Pd superlattice films for MgO-based perpendicular magnetic tunnel junctions". en. In: *Applied Physics Letters* 97.23 (Dec. 2010), p. 232508. ISSN: 0003-6951, 1077-3118. DOI: 10.1063/1.3524230. URL: http://aip.scitation.org/doi/10.1063/1.3524230 (visited on 03/04/2020).

[115] Y. Yang et al. "Chemical diffusion: Another factor affecting the magnetoresistance ratio in Ta/CoFeB/MgO/CoFeB/Ta magnetic tunnel junction". en. In: *Applied Physics Letters* 101.1 (July 2012), p. 012406. ISSN: 0003-6951, 1077-3118. DOI: 10.1063/1.4732463. URL: http://aip.scitation.org/doi/10.1063/1.4732463 (visited on 03/04/2020).

[116] Hiroaki Yoda et al. "High efficient spin transfer torque writing on perpendicular magnetic tunnel junctions for high density MRAMs". en. In: *Current Applied Physics* 10.1 (Jan. 2010), e87–e89. ISSN: 15671739. DOI: 10.1016/j.cap.2009.12.021. URL: https://linkinghub.elsevier.com/retrieve/pii/S1567173909006087 (visited on 02/05/2020).

[117] Chun-Yeol You. "Micromagnetic Simulations for Spin Transfer Torque in Magnetic Multilayers". en. In: *Journal of Magnetics* 17.2 (June 2012), pp. 73–77. ISSN: 1226-1750. DOI: 10.4283/JMAG.2012.17.2.073. URL: http://koreascience.or.kr/journal/view.jsp?kj=E1MGAB&py=2012&vnc=v17n2&sp=73 (visited on 05/12/2017).

[118] Chun-Yeol You. "Switching current density reduction in perpendicular magnetic anisotropy spin transfer torque magnetic tunneling junctions". en. In: *Journal of Applied Physics* 115.4 (Jan. 2014), p. 043914. ISSN: 0021-8979, 1089-7550. DOI: 10.1063/1.4862963. URL: http://aip.scitation.org/doi/10.1063/1.4862963 (visited on 04/05/2017).

[119] L. You et al. "Co/Ni multilayers with perpendicular anisotropy for spintronic device applications". en. In: *Applied Physics Letters* 100.17 (Apr. 2012), p. 172411. ISSN: 0003-6951, 1077-3118. DOI: 10.1063/1.4704184. URL: http://aip.scitation.org/doi/10.1063/1.4704184 (visited on 03/04/2020).

[120] S Yuasa and D D Djayaprawira. "Giant tunnel magnetoresistance in magnetic tunnel junctions with a crystalline MgO(0 0 1) barrier". en. In: *Journal of Physics D: Applied Physics* 40.21 (Nov. 2007), R337–R354. ISSN: 0022-3727, 1361-6463. DOI: 10.1088/0022-3727/40/21/R01. URL: http://stacks.iop.org/0022-3727/40/i=21/a=R01?key=crossref.5e4ad43797a155e306a576b1744a6d26 (visited on 02/07/2020).

[121] S. Zhang, P. M. Levy, and A. Fert. "Mechanisms of Spin-Polarized Current-Driven Magnetization Switching". en. In: *Physical Review Letters* 88.23 (May 2002), p. 236601. ISSN: 0031-9007, 1079-7114. DOI: 10.1103/PhysRevLett.88.236601. URL: https://link.aps.org/doi/10.1103/PhysRevLett.88.236601 (visited on 02/10/2020).

université PARIS-SACLAY

ÉCOLE DOCTORALE
Physique et ingénierie : Electrons, Photons, Sciences du vivant (EOBE)

Titre : Les chemins de retournement dans les mémoires magnétiques à transfert de spin

Mots clés : électronique de spin, mesures hyperfréquences, micromagnétisme, paroi de domaine.

Résumé : Dans les mémoires magnétiques à transfert de spin, l'aimantation d'une couche mince ferromagnétique est retournée sous l'effet d'un courant polarisé. Au cours de ce manuscrit est étudiée la façon dont ce retournement s'opère, appelée chemin de retournement.
Après avoir posé les concepts théoriques de base nécessaires et effectué un état de l'art du chemin de retournement, je présente les résultats de nos simulations micromagnétiques. Nous avons étudié le chemin de retournement en fonction du diamètre du dispositif. Ces calculs numériques prédisent un retournement composé d'une phase cohérente suivie de la nucléation et de la propagation d'une paroi de domaine. Ce chemin de retournement est attendu pour les dispositifs the 20 à 100 nm à température ambiante, donc dans nos mesures à venir.
La propagation de paroi de domaine observée dans les simulations présente de complexes oscillations de Walker qui ne sont pas expliquées par les modèles de l'état de l'art. Aussi je présente un modèle de dynamique de paroi plus complet, où la géométrie exacte du système est prise en compte. Dans cette géométrie l'élasticité de la paroi donne naissance à un nouveau champ que nous appelons champ d'étirement.
Ce champ d'étirement joue un rôle capital dans la dynamique de paroi et va nous permettre de comprendre et de prédire les oscillations de Walker complexes.
Nos mesures sont effectuées pour des dispositifs de mémoires magnétiques à transfert de spin dernière génération, basé sur une jonction tunnel magnétique à anisotropie perpendiculaire. Le diamètre de nos dispositifs varie entre 26 et 200 nm. Nous effectuons des mesures de magnétométrie, de résonance ferromagnétique et des mesures électriques résolues en temps de la commutation.
Le chemin de retournement mesuré dans ces dernières présente les signatures d'une phase initiale cohérente suivie d'un déplacement de paroi de domaine, comme calculé dans nos simulations. Les fortes oscillations de Walker prédites par nos modèles sont observées pour des échantillons spécifiques où la couche libre présente peu de défauts, mais pas dans nos échantillons les plus standards. Ceci met en lumière l'intérêt de nos travaux analytiques dans la compréhension du retournement dans des dispositifs destinés aux applications industrielles.

Title : The switching paths of spin transfer torque magnetic random access memories

Keywords : spintronic, high-frequency measurements, micromagnetics, domain wall.

Abstract : In spin transfer torque random access memories (STTMRAM), the magnetization of a thin ferromagnetic layer is reversed under the action of a polarized spin current. Along this manuscript we study the switching path that the STTMRAM undergo.
First I present the basic theoretical concepts necessary for our forthcoming calculations. Then comes a state of the art of the switching path. The first results I present are micromagnetic simulations of the switching. We study the impact of the diameter of the device on the switching path. From these numerical calculations we predict for devices between 20 and 100 nm at room temperature a switching path composed of a coherent phased followed by a domain wall nucleation and motion. It is the switching path expected in our forthcoming measurements.
The domain wall dynamics observed in the micromagnetic simulations present complex Walker oscillations that are not understood from the domain wall models of the state of the art. Therefore, I present a more complete model for the domain wall dynamics within a STTMRAM which takes into account the exact geometry of the system.
In this geometry the elasticity terms act as a new effective field called the stretch field. The stretch field plays a key role in the wall dynamics and explains the complex Walker oscillations. The conditions under which these effects can be measured are also predicted by our new model.
Our measurements are performed on state-of-the-art STTMRAM based on perpendicular magnetic tunnel junction. The diameter of the devices varies between 26 and 200 nm. We characterize our devices by magnetometry, ferromagnetic resonance and electrical time-resolved measurements of the switching path.
The switching path in our time-resolved measurements presents the signatures of an initial coherent phase and of a domain wall motion. This is in agreement with the simulated switching path. The complex Walker oscillations predicted by our models are measured in specific devices with an ultrasoft free layer, but not in our most standard stack. This highlight the interest of our analytical models for understanding the behavior of application-oriented devices.

Université Paris-Saclay
Espace Technologique / Immeuble Discovery
Route de l'Orme aux Merisiers RD 128 / 91190 Saint-Aubin, France